École Polytechnique
Laboratoire d'Hydrodynamique

Thése présentée pour obtenir le grade de

Docteur de l'École Polytechnique

Spécialité : Mécanique

par

Nicolas DOVETTA

Data-based models for flow control

Modèles basés sur les données pour le contrôle d'écoulement

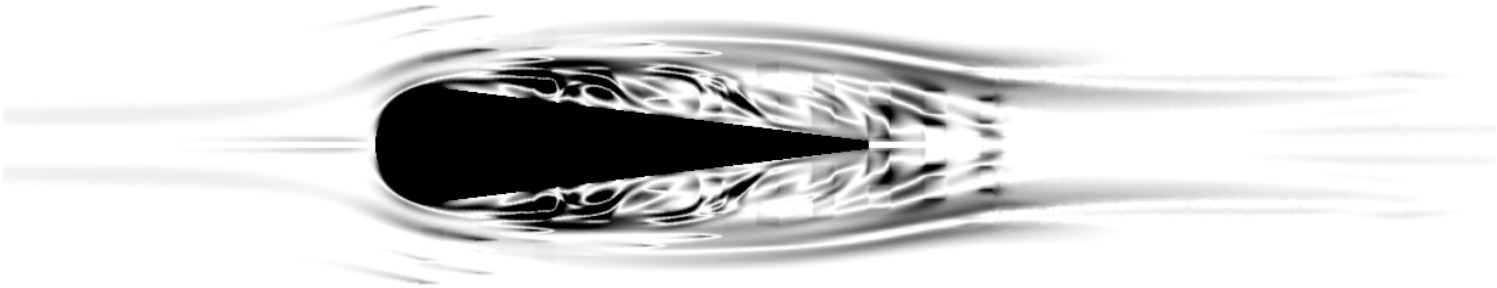

Thése présentée le 23 juin 2014 devant le jury composé de :

Rapporteurs :	Colm C. CAULFIELD	Cambridge university (UK)
	Angelo IOLLO	Université de Bordeaux
Directeurs de thèse :	Peter J. SCHMID	Imperial College
	Denis SIPP	ONERA
	Beverley J. MCKEON	Caltech
Examinateur :	Lionel MATHELIN	LIMSI

Data-based models for flow control

Abstract: This thesis presents two experimental data-based model design techniques: the system identification and the data-assimilation. The first allows the construction of a model, based on the system's input-output signals only. Several flow-control examples, using systyem identification, are described: flow inside a channel, and behind a cylinder. Data-assimilation is another data-based technique which makes use of a physical model. The assimilated model gives access to physics-based interpolation and extrapolation of a scattered data-set. Three examples of mean-velocity measurement assimilation are presented: a turbulent boundary layer, the flow around a cylinder, and the flow over an idealized airfoil. The impact of measurement uncertainty is demonstrated. An extension is developed for both methods to cope with corrupted data.

Keywords: flow control, system identification, data-assimilation, uncertainty propagation.

Modèles basés sur les données pour le contrôle d'écoulement

Résumé: Cette thèse est basé sur les méthodes de construction de modèles utilisant des données expérimentales. Deux groupes de méthodes sont étudiées, l'identification de systèmes et l'assimilation de données. La première permet de mettre en place une représentation pour un système donné en se basant sur l'histoire de ses entrées sorties. Cette représentation est calculée puis utilisée pour contrôler efficacement plusieurs exemples d'écoulements. La seconde, nécessite un modèle physique et met en oeuvre des mesures qui relève du vecteur d'état. Le modèle qui assimile les données offre un moyen d'extrapoler et d'interpoler ces dernières. Trois exemples d'assimilation de vitesses moyennes sont présentées, une couche limite turbulente, l'écoulement autour d'un cylindre et l'écoulement autour d'un profil d'aile idéalisé. Enfin plusieurs pistes pour la prise en compte d'incertitudes de mesures sont développés, pour l'assimilation de données et l'identification de systèmes.

Mots clefs: contrôle d'écoulement, identification de systèmes, assimilation de données, propagation d'incertitude.

Acknowledgments

It all started in November 2009 in Pr. P. Schmid office. I came as Pr P. Huerre suggested after I told him I wanted, for some reason, to start a PhD that could allow me to travel to the California Institute of Technology. Peter was welcoming the idea, the project seamed feasible to him especially since I was quite sure to get funding. After some discussion, and some time, he told me we were (and therefore I was) probably going to do some experimental flow control with Pr. B.J. McKeon, who was working at the aerospace laboratory of the institute. I guess I would have said "sounds good !", but at the time I probably said a French equivalent that I cannot remember today. Three years, or rather four, is a pretty long time. And this time contains so many events, thoughts, and reflections, that have impacted my life more than anything before. In these four years I have experienced the happiest moment I have leaved so far, but I've also been through most terrible. In those hours, the idea of dropping everything behind me has walked inside my mind too many times.

It turns out, I didn't.

For this I want to thank my dad for being strong minded, and of course my mom for being even more strong minded. I would like to thank my sister, my brother, my uncle Yves, my aunt Hélène, my grand parents (the four of them), my uncle Etienne, Alex, and Blandine, for being good at standing shoulder to shoulder. I also cannot thank enough the advices and comforting discussion from Catherine, Benoit-et-Marie, Gilles L., Sophie, and Michel, without whom I'd have certainly gone postal in the winter. I also don't think I would be writing acknowledgments today, without the heavy support provided by Clement and Eloise, without the cross-border train trips of Julien, without dream-team of friends from Lyon (plus extensions) Pilou, Marine, Fanny, Florent, Laurence, and the practical Daniel. I surely doubt that I would have make it any further, without the approximately 1359 coffee-break surrounded by, Dany and his chouquettes, Sabine and her ragots, Fabien and his Tanks T., Matthieu and his office (no wait, this was mine ?), Xavier and his Ouzo, Silvia and not her Ouzo, Etienne and his bubbles, Clement and his fluid-structure interactions (yes it sounds weird), Marine and her dorade, Miguel and not his dorade, Cristina para ella eau la qu'est talle, Franz and his cocktails, Dimitry and his nuit du styx, Alex and his boats, Ryan and his question remarks and concerns, Bruno and his housewarming party, and of course Catherine and her cross-continent plane trips.

Apart from all that, this thesis would not have been completed without going through some data-based model for flow control. And for this I surely cannot thank enough Peter for enthusiasm towards the different parts of the project, his brilliants ideas on every single existing topic, for understanding the spirit of my botched English, and of course for having strong nerves, without ever wrecking mines too much. I will not be able to thank Beverley enough either, for opening such a welcoming group and laboratory to Fabien and I, for the enormous amalgamation of ideas and thoughts and remarks that were every single time priceless, but also for dealing with my strange lifestyle. I also cannot thank enough Denis, for his welcome

at the ONERA, for his numerous tips, ideas and reflections that made big parts of this project possible. Finally, the defense would not have been possible without the comity members, I want to sincerely thank Angelo Iollo, Colm Caufield and Lionel Mathelin for coming to my presentation, reading and correcting the manuscript, but also and more importantly for their questions and instructive remarks on my thesis.

As this chapter of my life closes, let me thank all of you once more for filling it with many good memories.

Contents

Chapter 1

Introduction

Contents

Man-made and natural systems that are governed by internal or external fluid flow can often be described by these flows' base-flow and perturbation dynamics. Instabilities and noise amplification often limit performance, operational range, and robustness in these systems. Improving flow conditions under these circumstances often involves active or passive flow control techniques. The ability to control and manipulate fluid flows comes with a broad spectrum of applications, ranging, for example, from noise reduction around airfoils and in jet engines to mixing enhancement in chemical processes. While natural fluid systems make extensive use of general flow control techniques, the application of fluid manipulation in many industrial settings offers technological advantages that can hardly be overestimated.

Early attempts in flow control research date back to the beginning of the 20^{th} century when the first patents were published after 1920, and when Prandtl already experimented with boundary-layer control devices (see Wygnanski, 2006). However, further progress in flow control has slowed, while general control theory applied to electronic and mechanical systems developed rapidly and occupied an increasingly larger part in the academic community. This rise was accompanied by the founding of the International Federation of Automatic Control in 1957, and the creation of leading control journals such as *Automatica* and the *Journal of Electronics and Control* (continued as *Journal of Control* after 1965). Even though flow control rose simultaneously during this period with first dedicated books and articles published around 1960 (see Lachmann, 1961; Chang, 1976), the discipline of flow control advanced far slower and more reluctantly. The reason for this developmental delay may be associated with the far greater complexity of fluid systems. Fluid systems are characterized by many different spatial and temporal scales and a substantial number of degrees of freedom.

Control and guidance for mechanical and industrial systems, such as robots or chemical processes, has seen a major growth after 1960 (see Qin & Badgwell, 2003) with many important developments in control algorithms and model design: comparative advances for flow control applications were rather slow. The simultaneous development of Micro-Electro-Mechanical Systems (MEMS) and the rise of efficient computer algorithms in the late 80's set the stage for confronting flow control related problems and therefore triggered increased interest in flow control research (see Bewley, 2001).

Today, flow control is an active research field which greatly benefits from the earlier developments of general control theory. Even though the technological gap between general control theory and flow control methods is gradually narrowing, there remains a great deal of important control technology that has yet to be adapted to flow control applications. This present thesis aims at decreasing this technological gap by employing system-identification techniques (see Ljung, 1987), data-assimilation schemes (see Ghil & Malanotte-Rizzoli, 1991) and model predictive control design (see Camacho & Bordons, 2004), and by critically assessing the performance, robustness, and applicability of these techniques to fluid systems. This chapter presents a broad overview of flow control techniques; the remaining thesis will then focus on model design algorithm for flow control based on data.

1.1 Classification of flow control methods

Drag reduction, lift enhancement, mixing augmentation, heat transfer improvement, and flow-induced noise suppression are but a few applications that demonstrate the variety and range of flow control objectives. Equally, the manner in which we manipulate the flow or extract information from it adds even more to this variety. For this reason, there exists a great number of flow control configurations, which calls for a classification according to an appropriate criterion (see Kral, 2000). Among

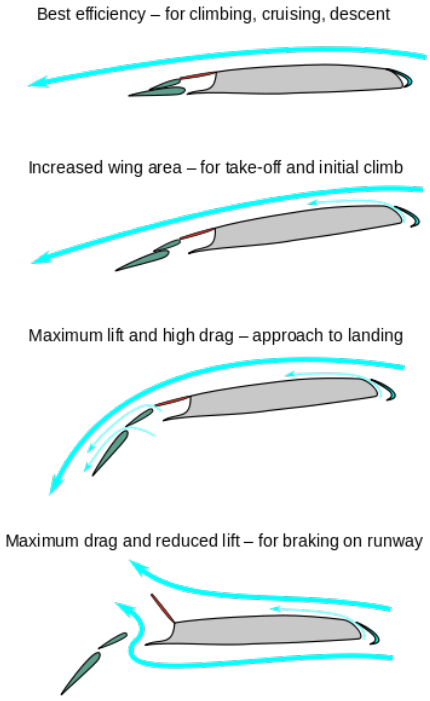

Figure 1.1: Geometric shaping of commercial airfoils during different flight conditions.

the many possible classification criteria we choose energy expenditure to categorize different flow control layouts. Flow control methods are referred to as active if energy is transferred to the system; in contrast, if no external energy is injected into the system, the corresponding configuration is labeled as passive.

1.1.1 Passive control

Geometric modification, the use of fixed, mechanical vortex generators and the placement of riblets on a surface are examples of passive flow control. A familiar illustration of passive control technologies can be observed on most commercial aircrafts in the form of flaps which modify the lift and drag characteristics by changing the airfoil shape (see figure 1.1). Additionally, vortex generators are often encountered on top of the engines (see figure 1.2); they also manipulate the local mean flow field to avoid adverse flow conditions. A review of passive flow control techniques is given in Gad-el Hak *et al.* (1998).

The passive approach has been found effective in many flow-control problems, for example, in delaying transition (see Cossu, 2007), in manipulating a flow's thermal transport (see Allan *et al.*, 2006), or in reducing drag by shape optimization (see Owen *et al.*, 2001). Despite its effectiveness, we can often improve control performance through an *actuation* device which injects energy into the fluid system. In practice, both strategies (passive and active) can be brought to bear on a single

Figure 1.2: Vortex generators on a commercial aircraft.

application where the advantages of either technique can be exploited efficiently.

1.1.2 Active control

Methods based on the injection of external energy into a fluid system have appeared nearly twenty years ago and have been developed considerably since then. These active control methods may be divided into two sub-categories (see Kral, 2000).

In the first case, energy is given to the fluid system regardless of the current flow state. In this sense, the control is *predetermined* and applied without on-line modification. Predetermined control is also known as open-loop control. Many examples of successful predetermined control can be found: Corke *et al.* (2010) (see figure 1.3) for separation control using plasma actuators, and Gonzalez *et al.* (2010) and Wallace & McKeon (2012) for separation control using a dynamic roughness element which oscillates at a constant frequency in a boundary layer.

Predetermined control assumes that the control law is effective regardless of the evolving fluid state and thus cannot cope with complex control objectives. For instance, it is known that a shear layer amplifies time-periodic disturbances near its convectively unstable frequencies (see Huerre & Monkewitz, 1985). A fixed control law cannot adapt to varying flow conditions and therefore to varying disturbance amplifications; it thus becomes ineffective in suppressing instabilities or amplifications in time-varying flows. To achieve reasonable control performance, the control law has to adjust to the current state of the fluid system, which leads to the concept of *interactive* control.

In *interactive* control, information about the flow's state is extracted via sensors, and an appropriate control law is determined for the control unit based on this extracted information. The *controller* then produces a signal which gets passed onto the *actuators* and injects engery into the fluid system to achieve a given control objective. The terms closed-loop control, feedback control and feedforward control are specific types of interactive control which are commonly used in the flow control literature.

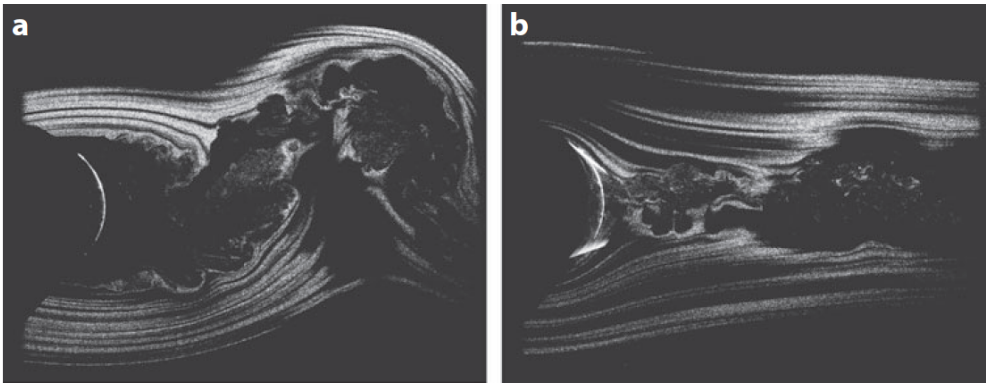

Figure 1.3: Flow past a cylinder at $R_e = 33000$. (a) uncontrolled, (b) controlled by plasma actuators aiming at separation control.

1.2 Focus on interactive control

In interactive control, the control law uses information about the fluid state and adjusts the control signal accordingly in order to satisfy a user-specified control objective. The essential components of interactive flow control are thus: (i) a model which accurately describes the temporal evolution of the flow state, (ii) an objective function quantifying the performance and success of the applied control, and (iii) a control unit forcing the fluid system in a prescribed manner. The goal of interactive control design is to determine an optimal control strategy, with respect to the objective function, based on the model's prediction of the state evolution. These three components will be discussed in more detail below.

1.2.1 Objective functional

The choice of an objective for flow control is closely linked to the concept of a utility function which can be thought of as a mapping of relevant state variables which describe the fluid system onto an ordered space of scalar quantities. In this context, the ordered space represents a hierarchy of performance measures that allows a ranking from minimal to maximal. Even though it may appear straightforward to define control objectives, such as "the system should be stable", or "the flow over a bluff body should not separate", it is non-trivial to recast these objectives into a quantitative utility function. The degree of success (or failure) to formulate the utility function directly and significantly impacts the effectiveness and efficiency of the designed controller.

For example, choosing separation avoidance around an airfoil as our control objective, a quantitative expression of utility is hard to find. A controller may be built to reattach the flow by minimizing the distance between the separation and reattachment point. Alternatively, it may be built to maximize the integrated wall shear stress along the airfoil. Either case will result in substantially different optimal actuator placements, optimal control laws, and ultimate performances. Moreover,

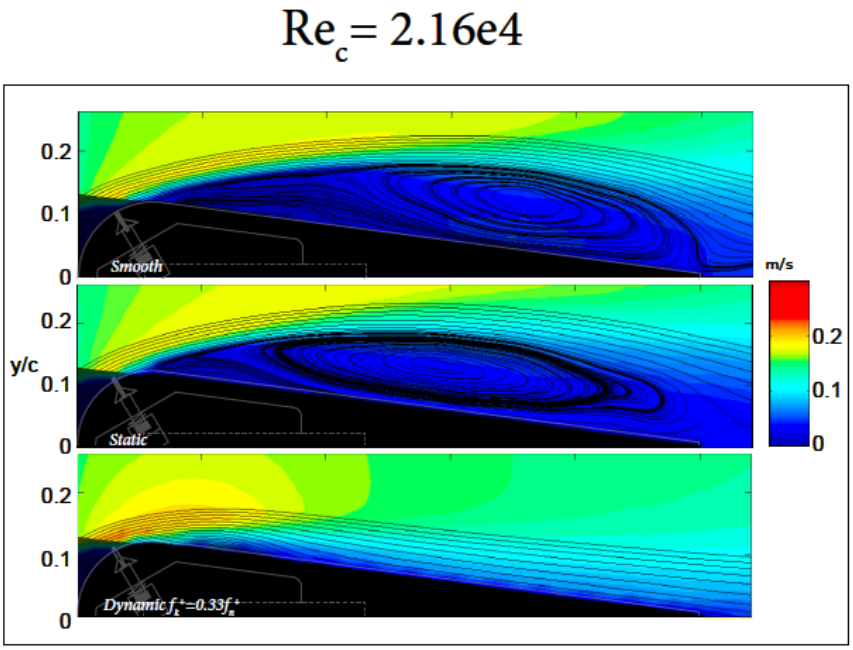

Figure 1.4: Separation control on an idealized airfoil using a predetermined control strategy, from Gonzalez *et al.* (2010). The colored contours represent the mean velocity; stream lines are also plotted to visualize the recirculation bubble. (top) uncontrolled flow around a smooth airfoil; (middle) flow around the airfoil with a static roughness element; (bottom) flow around the airfoil with a periodically activated roughness element. In the latter case the flow reattaches.

the utility function or control objective has to be based on quantities that can be readily measured or extracted from the flow fields. For example, figure 1.4 shows a controlled recirculation bubble using predetermined control. In this particular set-up neither the reattachment point nor the lift can be measured to sufficient accuracy and therefore cannot be used to evaluate the controller's performance. A proxy quantity that can be extracted from the experiment has to be used instead, for example, time-resolved PIV measurements in this case.

1.2.2 Model

The underlying model for our flow control design represents the mapping of a dynamic input to a responsive output. In some, but not all, cases this input-output mapping passes through a state-vector that often has a physical interpretation, such as a flow state. Not surprisingly, the fidelity of this model crucially affects the ultimate performance of the controlled system. The term *model* is rather general: it spans a range of complexity from simple models based on physical intuition to non-linear sophisticated numerical models with millions of degrees of freedom. Again, a classification is desirable.

One criterion for classification is based on the source of the model's derivation. A model is said to be *physics-based*, if it mostly stems from an application of first-principle physical conservation laws. In contrast, a model is said to be *data-based*, if its main characteristics have been derived from an observation of data. A typical physics-based model can be determined from the Navier-Stokes system of equations, with the only data-based input related to the geometry and the boundary conditions. On the other hand, an example of a data-based model is one that is system-identified from data sequences, with the only physics-based input contained in the structure and order of the model to be identified (*e.g.* linear, non-linear, fuzzy, auto-regressive, neural networks). In most cases, there does not exist a purely data-based or purely physics-based model but rather a hybrid model of various degrees of either component.

The amount of data-based input into a model design process is closely related to its specific application. If the boundary conditions, the flow domain and the underlying physics are well established, a physics-based model may be more suitable. In contrast, in the presence of uncertainties regarding the geometry, the external disturbance environment, or even the underlying physics, a data-based design procedure using observed measurements may be more appropriate.

A physics-based approach has been successfully applied in flow-control problems, which resulted in a large body of literature, see for example Moin & Bewley (1994); Gerber *et al.* (2006); Barbagallo *et al.* (2009, 2012); Illingworth *et al.* (2011); Semeraro *et al.* (2011).

In this thesis we focus on the data-based approach and consider two particular methods: (i) a technique based on system identification and (ii) a procedure using data assimilation. Sections 1.3 and 1.4 describe these two methods, their characteristics, their applicability, and their distinct features.

1.2.3 Controller design

Once the objective functional has been selected and the model has been determined, the control design can be formulated as an optimization problem: find a control strategy that maximizes (or minimizes) the objective functional taking into account the model behavior. In a first step, an appropriate space of admissible controllers has to be defined. Examples include proportional controllers or controllers described by a non-linear auto-regressive transfer function of given order.

The range of admissible controllers may impact the attainable control optimum. If our controllers are restricted to proportional scalar controllers, the optimization procedure may be fast and straightforward, but the performance may likely be poor. A balance has to be struck between (i) a complex or high-dimensional controller which may be highly effective, but difficult to identify and expensive to apply on-line, and (ii) a simple or low-dimensional controller which may be easy to identify and apply on-line, but inadequate in terms of performance.

1.3 Model design by system identification

Historically, system-identification techniques became popular in the 1980's after Ljung pioneered this field and produced a large body of literature and an identification toolbox in MATLAB® (see Ljung, 1988, and references therein) that made it easy and convenient for industrial and academic applications. Following his work, it is difficult to give a better definition of a *system* than the one offered in the introduction of *System identification: Theory for the user* (Ljung, 1987).

> In loose terms a *system* is an object in which variables of different kinds interact and produce observable signals. The observable signals that are of interest to us are usually called *outputs*. The system is also affected by external stimuli. External signals that can be manipulated by the observer are called *input*. Others are called *disturbances* and can be divided into those that are directly measured and those that are only observed through their influence on the output.

System identification refers to a family of techniques that identify the system behavior from input-output data sequences. These input-output relationships link the actuation (input) to the different sensors (output), and the observable disturbances to the variables of interest (output-output relationship). The result of system identification consists of a *model* that approximately describes the observable system behavior.

Three user-supplied ingredients are required for system identification: (i) a model structure, (ii) a learning and testing data sequence, and (iii) a fitting criterion. In effect, system identification represents an optimization problem where we find the best realization within our chosen model-structure which reproduces the data sequence according to a fitting criterion.

1.3.1 Model structure

The model structure provides a set of admissible models, and the optimization will identify a final model within this set. For this reason, a first decision has to be made as to the precise type of model. Possible choices include, for example, state-space models, frequency-domain transfer functions, continuous models, non-linear Hammerstein-Wiener models, or auto-regressive models (ARX, ARMA, ARMarkov, ARMAX, ARARX ARARMAX, OE Output Error, BJ Box-Jenkins, etc).

Each structure is particularly geared towards representing a specific type of system behavior. For example, finite impulse response (FIR) models are particularly apt at capturing delays and transient short-time behavior and are thus appropriate for convection-dominated and stable flows. In contrast, non-linear Hammerstein-Wiener models allow for input and output non-linearities, together with a linear transfer function to represent the state-vector dynamics; they are particularly suited for configurations with anemometry sensors and non-linear synthetic jets acting on a linear fluid system. Within the fluid mechanics community, many different

structures have been used for control design purposes, among them : Cortelezzi & Speyer (1998); Juillet *et al.* (2013) using state-space models, Kegerise *et al.* (2002) using finite- and infinite-impulse response models, and Williams *et al.* (2010) using non-linear block models.

After a particular structure has been chosen, the order of the model needs to be determined. The order of a model represents the number of degrees of freedom. A Finite Impulse Response (FIR) structure of order 150 (*i.e.*, with 150 Markov parameters), contains 150 degrees of freedom, whereas a single-input single-output (SISO) state-space model of order two contains eight degrees of freedom. Higher-order models with more degrees of freedom are more likely to match complex data sequences and thus can represent more complex system behavior, but are more difficult to identify in a robust manner.

It is advantageous to supplement the choice of model and the choice of order by physical arguments about the flow behavior of the system under investigation. Inherent or assumed linear behavior should lead to an admissible set of linear models. For example, a double pendulum can be described most appropriately by a second-order ARX model. In the absence of physical arguments, a more mathematical approach can be taken which favors among a suite of potential candidates a relevant model by evaluating and ranking a robustness measured such as the Akaike Information Criterion (AIC, see Akaike, 1974) or Minimum Description Length (MDL, see Rissanen, 1983). This will simultaneously determine the best order of the model.

1.3.2 Data sequence

The data sequence used in the identification is the observable part of the system's behavior, and therefore should be used to its fullest extent. In some cases, the data sequences are given *a priori* and may cause limitations in the quality and robustness of the identified model. A better situation is given when a user-designed input sequence can be implemented that can be judiciously tailored to account for a particular system behavior or for specific flow or model characteristics. More particularly, if the length of the data sequence and the choice of sampling time are under the control of the user, a more information-rich data sequence can be generated which will yield a better model. For example, for identification techniques based on a discrete Fourier transform (DFT), the length of the data sequence should exceed the larger characteristic time-scale while the sampling time should fall below half the smallest characteristic time-scale (conforming with the Nyquist-limit criterion).

Choosing an appropriate input sequence for system identification is a non-trivial problem which remains at the center of many discussions within the system-identification community (see Mehra, 1974; Kalaba & Spingarn, 1982). Common input signals in system identification are: the step function, a sum of trigonometric functions, Auto-Regressive with Moving-Averges (ARMA) sequences, and Pseudo-Random Binary Signals (PRBS). The preference for a specific input signal is, among others, governed by the noise-to-signal ratio, the data-sequence length, and the frequency response of the system (see Ljung, 1987, for details).

Broad-band signals are often most effective, if the system response is not fully known. While white-noise forcing may cause a broad-band driving of the unknown system, in practice it is often damaging to the actuator hardware. A pseudo-random binary signal (PRBS) is a good compromise as its spectrum is sufficiently broad-band, but its impact on the actuator is less harmful.

1.3.3 Fitting criterion

After the model structure and order have been chosen, and the input-output data sequence has been recorded, the model parameters can be determined as the final part of the identification procedure. An optimization problem can be formulated based on a user-specified utility. Ideally, this utility should include information about the controlled system and should produce an efficient control strategy. In other words, the reproduction of the data sequence by the model is less relevant than the controller's performance. However, this goal is rarely achievable and alternative formulations have to be resorted to in practice. Common choices for the fitting criterion include the distance between a measured output and its estimation by the model which is taken as a prerequisite for a proper controller performance. Most often this distance is based on classic norms such as average square distance or maximal distance. In the end, the identified model is the minimizer of the fitting criterion.

1.3.4 Optimization for system identification

The actual model-identification step is an optimization problem: we find a model, within the selected model structure family, which minimizes the fitting criterion. The solution of this optimization problem calls for an algorithm which should be closely related to the underlying model structure, as suggested in Ljung (1976, 2002). If a full solution of the optimization problem is sought, the available techniques fall under the category of Prediction-Error-Methods (PEM). Alternatively, if only an approximate, and thus sub-optimal, solution is attempted, subspace identification algorithms are often the method of choice, among others.

If the model structure is linear and the fitting criterion is explicitly and linearly dependent on the model parameters (which holds true for Auto-Regressive with eXogeneous parameters – ARX – and Finite Impulse Response – FIR – models, but not for ARMA models with eXogeneous parameters, state-space, or Output Error models), the optimization simply reduces to a linear least-squares minimization. In this case, the problem can be written in terms of an under-parametrized problem (involving rectangular matrices), which can easily be solved using the Moore-Penrose pseudo-inverse. In all other cases (*e.g.* for general forms of the fitting criterion or for non-linear model structures), non-linear optimization algorithms have to be considered. Typical algorithms, in the latter category, include the Newton-Raphson method, gradient-based methods, or grid-search algorithms. Despite the considerable effort expended by these non-linear optimization algorithms, only local minima

may be attained, at the expense of slow convergence, and substantial computational cost. In addition, the first initial guess crucially affects the final convergence and consequently the optimal solution.

Typically, for state-space model structures, PEM identification is prohibitively expensive and yields only local minima. In this case, subspace identification, see Katayama (2005), presents a more affordable alternative and provides suboptimal results which are nonetheless preferred. Whenever possible, a linear formulation is advantageous since the model parameters are more efficient to compute, and the associated identification algorithms show a more robust performance.

1.3.5 System identification for flow control

In figure 1.5 the main steps and components of the system-identification procedure are presented. The figure attempts to indicate how physics-based and data-based information contribute at various stages of the overall algorithm (see the associated colormap). We observe modules that are purely physics- or data-based, together with modules of a hybrid nature that include physical insight as well as observed measurements. A clear distinction between physics-driven or data-driven design is case-dependent and has to be assessed according to the flow details. This latter ambiguity is maybe best summarized by again quoting Ljung (1988) — this time from his recommendation taken from the user's guide to Matlab's system-identification toolbox:

> Step 1, Looking at the Data: Plot the data. Look at it carefully. Try to see the dynamics with your own eyes.

System identification is certainly a model design technique which can be applied to a complex system with rather little knowledge of its physical behavior or response characteristics. This advantage makes system-identification techniques attractive for a wide range of general control problems. For this reason, we find applications of system identification in process control, control of HVAC (Heating, Ventilation and Air Conditioning), and robotics, among many others fields.

For this reason, it has developed into a mature application field with a substantial body of literature covering specific applications or high-performance algorithmic improvements. In contrast, system identification is a rather recent technique to manipulate wall-bounded shear flows, and this thesis attempts to make a contribution towards the applicability, implementation, and performance evaluation of system-identified flow control design.

1.4 Model design by data assimilation

Conceptually, there is little difference between data assimilation and system identification. Both techniques rely on an underlying model, observed data, and a fitting criterion. In our case, system identification aims at providing a *predictive dynamical model* around which an effective control strategy can be built, whereas data

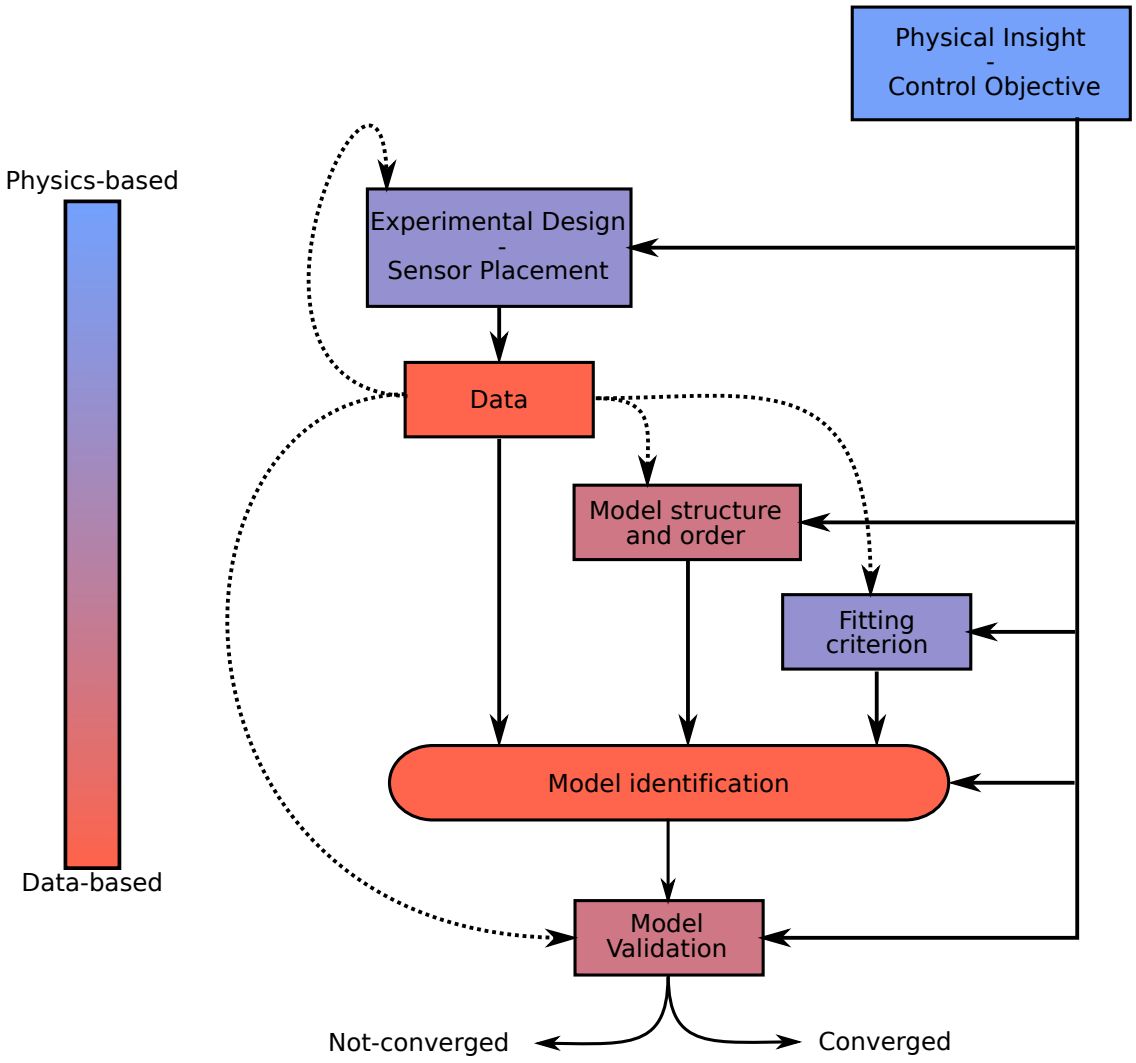

Figure 1.5: Data-based and physics-based components of the system-identification procedure

assimilation will be used to *extend under-sampled observations* while satisfying a physics-based constraint. Beyond the scope of this thesis, these two concepts are far closer than what might be implied from the following chapters, and the difference between them may often come down to linguistic details.

Considering the applications covered in this thesis, we can make the following heuristic observations. In system identification, the parametric model structure contains various mathematical assumptions such as linearity, causality, input-output cross-correlation length. In data assimilation, the parametric model-structure contains significantly more physical constraints such as incompressibility, or conservation of momentum, energy or passive scalars. In system identification, the dynamical model links a few input signals to a few output signals. In data assimilation, a limited number of measurements is related to a substantially larger number of extrapolated output variables. Even though data assimilation is based on the same three ingredients as introduced for system identification, namely a model, observed data, and a fitting criterion, in what follows we will briefly outline the main characteristics and significance of these ingredients and point out relevant differences.

1.4.1 Model and its compliance

The model underlying data assimilation is commonly based on physical principles expressed in terms of governing equations. In order to assimilate data, this model has to be properly parameterized. Examples for this parametrization include the initial conditions for time varying problems, material properties such as compressibility or viscosity, or boundary conditions. A set of parameters is then used to drive a given model output towards the observed data. In many cases the parameters are difficult to obtain experimentally. For example, for turbulent flows, modeled by the Reynolds-Averaged Navier-Stokes equations, the Reynolds stress tensor is difficult to model or measure at a reasonable cost. It can however be recovered via data assimilation by matching more accessible variables to their equivalent measurements. In this respect, non-measurable and non-observable quantities can be determined from measured data by observing the constraints given by the model.

This way, we may distinguish between three distinct data-recovery applications: (i) the interpolatory computation based on coarsely-sampled or scattered data, (ii) the extrapolatory extension of measured data beyond their domain of measurement, and (iii) the calculation of state-vector components from partial or composite measurements.

1.4.2 Data measurements

Whereas for system identification there exists a great deal of flexibility in processing various data-types (for example, the raw current output from a hot-film sensor), data-assimilation techniques are more stringent, as they can only process data for which a model equation is available. In order to process secondary data signals, it is necessary to convert them into variables that are tracked by the governing equations.

This conversion often involves an empirical model and proper calibration.

1.4.3 Fitting criterion

As before, the fitting criterion represents the objective of the optimization problem. For the data-assimilation case, this commonly involves the residual norm accounting for the mismatch between measured and model-reconstructed data. In its simplest case, a standard L_2-norm is used, but a more sophisticated spatial or componentwise weighting can be straightforwardly accommodated. The latter technique is often applied to increase the accuracy near critical points such as, a separation point, a reattachment location, and actuator position, or any other location with increased demands on accuracy.

1.4.4 Optimization procedure

A non-linear governing equation as a constraint on the data-assimilation procedure leads to a non-linear optimization problem. With it come typical issues such as, increased computational costs, low convergence rates, convergence towards local rather than global minima, and increased sensitivity to initial starting vectors. Many of these disadvantages and challenges can be overcome with some numerical effort, as evidenced by a long list of research articles, see for example Thévenin & Janiga (2008); Mohammadi & Pironneau (2004), and references therein.

1.5 Impact of measurement uncertainties on data-based models

In both system identification and data assimilation, the quality of the data plays an important role. As the data quality impacts nearly all design steps, any uncertainty in the data will influence the identified model parameters or the recovered variables, and will ultimately affect the performance and robustness margins of the controller (for system identification) or the accuracy and validity of the reconstructed flow fields (for data assimilation). System identification and data assimilation are particularly attractive for processing experimental or real-life data; but these data are often contaminated by deterministic or stochastic perturbations of unknown origin. It is thus important to address the issue of how data uncertainty propagates through the entire system-identification or data-assimilation process and manifests itself in the respective output models.

A common procedure to deal with the influence of noise in the data is filtering. This technique is most effective, if the frequency content and nature of the noise source is known or can be rather accurately estimated. For system identification, the filtering of incoming noise is inherent for *under-parameterized* models, *i.e.* models whose order is too low to recover the learning data-set accurately. In this case, the identified model acts as a filter.

Due to the importance of uncertainty propagation during system-identification or data-assimilation calculations, we develop and present a framework for the sensitivity analysis of the model-design algorithm with respect to noise sources in the processed data.

1.6 Outline

Chapter 2: System identification for flow control This chapter presents a particular system-identification algorithm for control design of convection-dominated flows. A finite-impulse response (FIR) model is postulated and identified from input-output data sequences, after which a controller is designed based on a disturbance-rejection approach and a feed-forward controller set-up.

Both Single Input Single Output (SISO) and Multiple Input Multiple Output (MIMO) configurations are treated. The control performance is compared to the Linear Quadratic Gaussian (LQG) design framework, and the theoretical equivalence of the two algorithms for convection-dominated flows is demonstrated.

A second part focuses on the robustness of system-identification algorithms. Measurement uncertainty is taken into account and its impact on the final model is quantitatively estimated. As the identified model is used to estimate the controller performance, the influence of measurement disturbances on the controller is quantified as well.

Chapter 3: Linear control of an open shear layer, the limits of linear identification? The third chapter applies the technique developed in chapter 2 to control an experimental flow over an idealized airfoil at $Re_c = 12500$. First, the controllability of the flow with respect to a disturbance-rejection algorithm is assessed. The amplifier behavior of the shear layer and oscillator behavior of the von Karman vortices have been found to be uncoupled. The convection-dominated shear layer is then assumed to be controllable by a feed-forward disturbance-rejection algorithm aiming at suppressing disturbances near the reattachment point of the recirculation bubble. While this control approach could successfully achieve this goal for numerical simulations of the linearized Navier-Stokes equations, the same approach applied to an equivalent experimental set-up failed to stabilize the flow due to inherent non-linearities at the chosen chord-based Reynolds number.

Chapter 4: Data assimilation of mean flows The last chapter focuses on model design by data-assimilation algorithms. A theoretical framework for data assimilation based on the Reynolds-Averaged Navier-Stokes equations is developed using a direct-adjoint optimization algorithm to find a model that optimally complies with the measured data. Three test cases have been considered: an experimental turbulent pipe flow, a numerical simulation of flow around a cylinder, and experimental flow around an idealized airfoil in a water tunnel. For the last example, measurement uncertainties had a significant impact on the assimilated model, and

a theoretical technique to cope with measurement-noise for data-assimilation applications is presented. All three aspects of data assimilation, *i.e.* interpolatory, extrapolatory and recovery of state vector components, have been included.

Chapter 2

System identification for flow control

Contents

2.1 Introduction

As stated before, system identification is a data-oriented model design strategy, which recovers the coefficients of a user-specified parameterized model structure form observed input-output data sequences, with rather little physical insight required from the user. It has been successfully implemented in many different applications areas, but its impact on flow control problems is still in its infancy. Even though a few encouraging studies already exist in the fluid dynamics literature (see Rathnasingham, 1997; Weyer, 2001; Kegerise *et al.*, 2002), the full potential of system identification for flow control problems may not yet have been realized.

This chapter describes a system-identification algorithm together with a control design based on disturbance rejection. Once the performance of such a controller has been demonstrated, we develop a quantitative framework for the propagation of uncertainties stemming from the data through the identification procedure and assess the impact of uncertainties in the data on the final model robustness.

Previous research (see Barbagallo *et al.*, 2012; Hervé *et al.*, 2012; Juillet *et al.*, 2013) pointed towards an inherent difficulty in controlling shear flows dominated by convection, their studies provided the motivation for a further and more detailed look into control design for this type of flow. Additional past research also demonstrated that standard control design algorithms such as state space identification and LQG compensators seemed overly complicated for and unadapted to the control of convectively dominated flows. Furthermore, a large number of linear control strategies, summarized under the term *model predictive control* (MPC, see Camacho & Bordons, 2004), suggests a renewed investigation to find a proper design approach

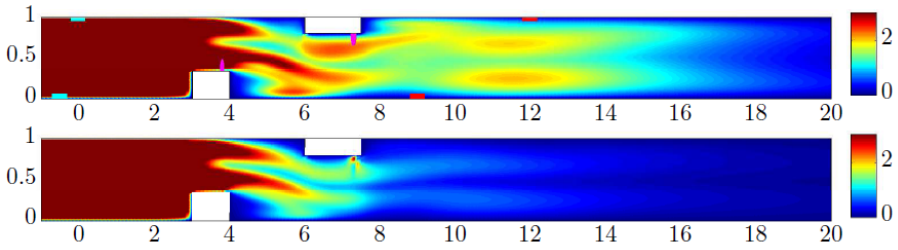

Figure 2.1: Contours of averaged perturbation energy for an excitation by three upstream noise sources. Above, uncontrolled case; Below, controlled case.

for amplifier flows. Even though these techniques have been extended to non-linear settings, we will limit ourselves to the control of linear systems by linear means.

Despite a great variety of underlying models, we will choose a simple Finite Impulse Response filter (FIR) to represent the perturbation dynamics. This choice has been motivated by the realization that convection in a finite domain is an intrinsically finite-time process, characterized by the transit time of perturbations through the domain given by the location of the noise source and the placement of actuators and sensors. The FIR model represents a convenient compromise between model simplicity and thus ease of identification, and flexibility to capture all relevant phenomenon of the flow (convection, delays, *etc*).

With the model structure chosen, we introduce a control design based on disturbance rejection. To this end, a feed-forward approach is used that introduces a properly designed control input based on upstream measurements of the incoming perturbations such that, at a specified location downstream, the two signals (incoming perturbations and control) destructively interfere. The design of the control strategy relies on a ratio of transfer functions and can be equally applied to single input-output or multiple input-output configurations.

This technique has been applied to flow through an obstructed channel and has been successful in suppressing disturbances arising from upstream noise sources. The control results have been encouraging in terms of achieved performance (see figure 2.1) and have been found robust to off-design conditions. Since the entire system identification and control-design procedure has been based on measured data, which is readily available in physical experiments, this approach shows potential for an application under realistic conditions.

Since system identification and subsequently flow control design heavily rely on data-sequences, the data quality, fidelity and ability to represent pertinent flow features seem crucial to a successful control design. In effect, we have to assume that data, particularly data from experimental settings, contain both deterministic and stochastic components whose origin is not part of the fluid system. These perturbations contaminate the data-sequence, and it is important to assess which impact they may have on the ultimate control performance as well as on robustness margins. A common technique to deal with data-contamination is pre-filtering.

While certain components of undesirable noise can be eliminated by filtering, this procedure also impacts frequencies and times scales of physically relevant processes.

It appears difficult to make a clear distinction between relevant flow features and undesirable noise sources, especially since they may appear on the same time- or frequency-scale. For this reason, it may be more advantages to consider the propagation of disturbances at all frequencies (modeled by white noise) through the full identification and control-design process and to quantify the influence of all frequencies on the final performance and robustness measures. In return, we can recover time signals that are responsible for the most severe deterioration of control robustness; a subsequent Fourier transform will give the spectral signature of the most dangerous data-contamination.

The second article in this chapter is a study of error propagation stemming from the data through all procedural steps of the system identification process. The mapping of uncertainties in the resulting model to robustness margins of the controller is also given and taken as a quality measure of the design process. For simplicity a ARMarkov Least-Squares (LS) identification scheme is chosen to illustrate the algorithmic steps, but alternative and more complex underlying models can be treated within the same framework. With ARMarkov/LS model fully identified, we construct a general controller and quantify its performance and robustness limits.

As a motivational example, we consider the linear Ginzburg-Landau equation controlled by an optimal LQG controller using a localized volume force. The control objective is given by

$$J = \sum_{k=0}^{\infty} \|y(k)\|_2^2 + \ell \|u(k)\|_2^2, \tag{2.1}$$

with $y(k)$ as the output signal, $u(k)$ as the applied control, and ℓ as a user-specified parameter that represents the cost of control, but mathematically acts as a regularizing parameter in the optimization problem of the control design. We choose governing parameters for the Ginzburg-Landau equation that assure an asymptotically stable behavior. For this case, two limiting values of ℓ have to be considered. For $\ell \to \infty$, we penalize the control term in J such that ultimately no control effort will be expended and $u(k) = 0$. This limit is referred to as the small gain limit. For $\ell \to 0$, we apply a control signal without restrictions on its amplitude. This limit is referred to as the large gain limit. For the Ginzburg-Landau equation the eigenvalues of the closed-loop (compensated) system are displayed in figure 2.2. In the limit $\ell \to \infty$, we recover the eigenvalues of the uncontrolled system. As the parameter ℓ is reduced, the closed-loop system becomes even more stable, even though some individual eigenvalues (for example, eigenvalue 3 in figure 2.2) move towards the unstable half-space, in our case the exterior of the unit disk. In the large gain limit ($\ell \to 0$, with no penalty on the control), the nominal control performance, defined as the performance of the compensated *true* system that corresponds to our identified model, is expected to improve, as control energy is expended more liberally. However, due to data-inaccuracies the error bars around this nominal performance increase drastically as ℓ tends to zero which can ultimately cause significantly re-

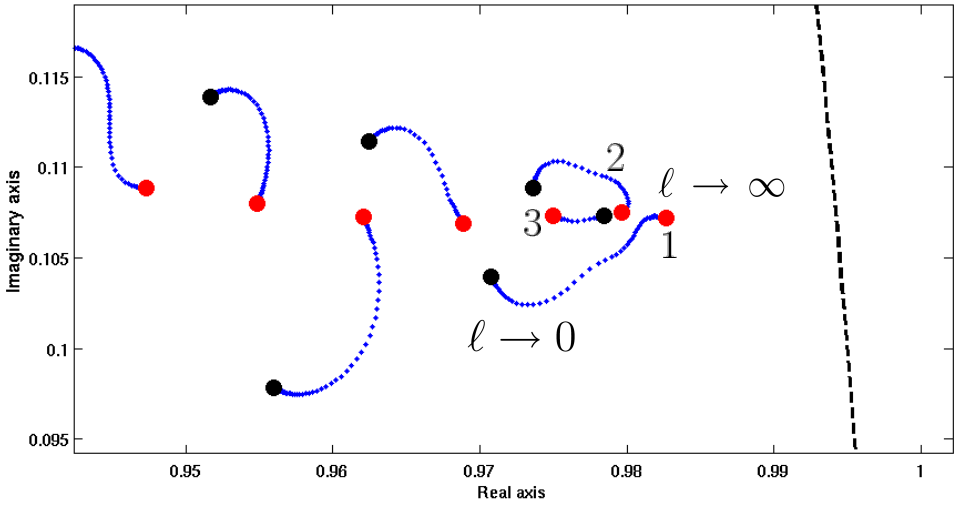

Figure 2.2: Eigenvalues of the controlled Linear Ginzburg-Landau system. Red uncontrolled system; black infinite gain limit for the controlled system; blue controlled system with a gain between the two limits

duced stability margins or, in the worse case, control failure by instabilities. This behavior is reflected in the loss of stability of the third eigenvalue in figure 2.2. This simple example clearly demonstrates the importance of studying the propagation of uncertainties and data-inaccuracies (*i.e.* the error bars around the nominal control performance) during the identification and control design process.

An alternative and common way of visualizing robustness margins for closed-loop systems is the Nyquist diagram, *i.e.* a frequency-parameterized curve in the complex plane describing the open-loop transfer function of the system. The closeness of the curve to the point $(-1, 0)$ in the complex plane can be used to determine the positive and negative gain margins; through a similar procedure the phase margin can be calculated.

Figure 2.3 displays a nominal Nyquist curve in the complex plane (black solid line), together with the 95% likelihood-bands (about two standard deviations). From this figure it can be seen that even a small contamination in the data can result in a markedly reduced gain margin, as indicated by the arrows. In our case, we observe a 50% reduction in the gain margin for data perturbations that result in a model within two standard deviations of the nominal value.

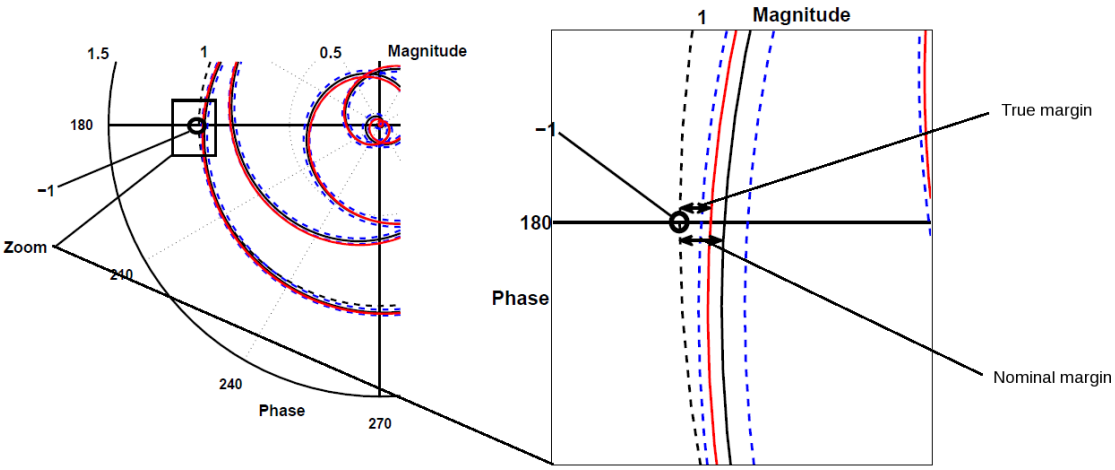

Figure 2.3: Nyquist plot of the Open-Loop Transfer Function. Exact model: solid red line; nominal model: solid black line; and 95% likelihood bands centered around the nominal value: dashed blue line. The arrows show the nominal and true gain margins.

2.2 Article 1: Data-based model-predictive control design for convectively dominated flows

Under consideration for publication in J. Fluid Mech. 1

Data-based model-predictive control design for convectively unstable flows

NICOLAS DOVETTA, FABIEN JUILLET AND PETER J. SCHMID

Laboratoire d'Hydrodynamique (LadHyX), Ecole Polytechnique, 91128 Palaiseau, France

(Received)

Convection-dominated or convectively unstable flows are characterized by the amplification of disturbances over a broad range of scales as they propagate in the downstream direction. Controlling this type of flows favors a feedforward configuration that actuates on the flow based on information provided by an upstream sensor. A simple and effective identification and control procedure, based on model-predictive concepts, is proposed that extracts the proper transfer functions from input-output data-sequences which are then used to design disturbance-rejection control laws. It provides a less complex and more efficient alternative to commonly applied LQG-methods. This technique is applied to a simple model problem as well as a two-dimensional obstructed channel flow; in both cases, satisfactory control performance can be demonstrated. Since the implementation of this technique merely requires input-output measurements, it is not only applicable to numerical, but also to experimental data.

Key words:

1. Introduction

It has long been acknowledged that flow control is a key technology in fluid systems to reduce drag, suppress instabilities, enhance efficiencies or increase operational envelopes, to name but a few potential applications. For this reason, flow control has attracted a great deal of attention. The current state of this discipline is characterized by a wide range of techniques and approaches brought to bear on specific flow configurations. In particular, linear control has received strong interest as evidenced by a large body of literature (see, e.g., Kim & Bewley 2007; Williams & Rowley 2006; Bagheri & Henningson 2011). It most readily applies to flow situations that are either globally stable or only sightly supercritical, such that a linearization about a steady equilibrium point can be justified.

The choice of a successful control strategy critically depends on the type of flow behavior. For example, relying solely on downstream sensors to control upstream-generated perturbations in a convection-dominated flow would appear futile. These types of flow — which will be considered in this article — are indeed more suited for feedforward than for feedback control (Juillet *et al.* 2013). Common techniques to design feedforward control strategies fall under the category of Model Predictive Control (MPC; Qin & Badgwell 2003; Gerber *et al.* 2006), examples of which are the Model Predictive Heuristic Controller algorithm, originally developed in Richalet *et al.* (1978) but also well presented in Camacho & Bordons (2004) and Zheng (2010), and the step-response-based Dynamic Matrix

Controller (DMC; see Cutler & Ramaker 1980). Even the familiar Linear Quadratic Gaussian (LQG) control (Kalman 1960) can be interpreted within the MPC framework (see, e.g., Qin & Badgwell 2003; Camacho & Bordons 2004). This latter technique has been used extensively in the flow control literature due to its theoretical foundation and provable optimality. Using LQG control for convection-dominated flow, where a feedforward control seems more appropriate and practical, is rather cumbersome: first, two Riccati equations for the control and Kalman gains need to be solved, and, second, a model for the system noise is required. Whereas the former can be resolved by efficient algorithms and model reduction efforts, the latter poses a far greater challenge that is not easily overcome but, nonetheless, is a deciding factor for the ultimate control performance. In contrast, a Model Predictive Heuristic Controller (MPHC) is significantly simpler to design as only a least-squares problem is required. At the root of this technique, finite-impulse responses are used to describe the fluid system. These impulse responses are commonly obtained from system-identification algorithms.

System identification is concerned with the extraction of a model of the fluid system from input-output data sequences only. Typical system identification techniques are subspace identification techniques (van Overschee & de Moor 1996; Katayama 2005) or classical least-squares fitting techniques (Ljung 1987). Among the subspace identification techniques, the Canonical Variate Analysis algorithm (CVA; Larimore 1983, 1990), the Multiple-inputs and multiple-outputs Output-Error State sPace algorithm (MOESP; Verhaegen & Deprettere 1991) and the Numerical algorithms for Subspace State Space System IDentification (N4SID; van Overschee & de Moor 1994) are the most widely used. All these techniques identify the system directly in its state-space form. Alternatively, a specific model for the system can be prescribed: for instance, a simple Finite Impulse Response model (FIR), an AutoRegressive model with eXogeneous inputs (ARX; Huang & Kim 2008)) or an AutoRegressive Moving-Average model with eXogeneous inputs (ARMAX; Hervé *et al.* 2012). The unknown coefficients in the chosen model are then determined by fitting the true output measurements to the ones predicted by the model, using a least squares algorithm. In convection-dominated flows, long delays are typical due to the physical separation of the input and output components. For this reason, describing this type of systems by finite impulses responses may be more appropriate than enforcing a state-space form, even though the latter may resemble more closely a familiar "governing equation"-format.

In a second step, the controller can be designed using a disturbance rejection argument based on the identified finite impulse response (FIR) model. Regularization techniques may be necessary for a robust control performance. Alternatively, a state-space model may be recovered from the FIR-model via a procedural step referred to as system realization, after which a controller can be designed using Riccati-techniques.

In this article, a multiple-input multiple-output (MIMO) data-based control design procedure, particularly suited for convection dominated flows, is proposed and validated. The procedure is linear and is intended to control flows that are globally stable, but react sensitively to external perturbations and noise sources. Typical examples in this category are pipe or channel flows, boundary layers, co-flow mixing layers or homogeneous jets, at subcritical Reynolds numbers, but any shear flow that is mainly governed by a convective process can benefit from the control setup and design illustrated in this article.

After a short introduction to disturbance rejection by feedforward techniques, the finite-impulse-response (FIR) least-squares identification procedure is presented. First, a single-input single-output (SISO) model predictive heuristic control algorithm is obtained for the design of an optimal control law, which is subsequently extended to accommodate multiple-input and multiple-output (MIMO) signals. Then, this algorithm is applied to

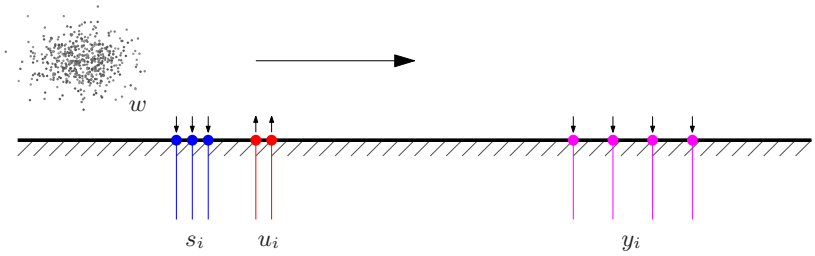

FIGURE 1. Feedforward control setup for convectively dominated flows. An unknown disturbance environment w is convected past the spy-sensors s_i which estimate the characteristics of w. The actuators u_i then manipulate the flow such that the control-objective, given by the downstream sensors y_i, is met.

a convection-dominated flow modeled by the linear Ginzburg-Landau equation. Possible extensions and implementation details of the technique are mentioned at the end of the section. The algorithm, in its MIMO-form, is then applied to a two-dimensional, linearized finite-element simulation of a channel flow with two obstructions and its effectiveness is evaluated. Attention is also directed towards user-specified weights for the input and output signals. Summarizing remarks conclude this article.

2. Control design based on data-sequences

Convectively dominated flows are characterized by information propagation largely in the downstream direction. Consequently, a control setup, respecting this feature, has to be designed in a feedforward configuration. The goal of flow control efforts is the reduction of disturbance levels measured by downstream sensors y, also referred to as cost sensors. Since the source of these disturbances is assumed to be mainly upstream, actuators u have to be placed upstream of the sensors. To complete the control setup, spy-sensors s will be placed upstream of the actuators. Their role is the detection and estimation of the incoming disturbance environment – information that is valuable for an effective control design u to accomplish our cost objective (measured by y). The resulting configuration of spy-sensors, actuators and cost-sensors is depicted in figure 1.

The fluid system is then characterized by two sets of input (the known actuator signals u and the unknown disturbance environment w) and two sets of output (the measurements y yielding the control objective and measurements s providing information about the incoming disturbances w). For the sake of simplicity, but without loss of generality, only single input- and output-signals are assumed; a generalization to multiple inputs and outputs will be addressed later.

The setup above can be formulated in the terms of transfer functions according to

$$y = \mathsf{G}_{wy} w + \mathsf{G}_{uy} u \tag{2.1}$$

which describes the dependency of the downstream cost measurement y on the disturbance environment w and the control u. Similarly,the spy-sensor output s is expressed in terms of the true disturbance environment w by writing

$$s = \mathsf{G}_{ws} w. \tag{2.2}$$

Owing to the convective nature of the flow, no influence of the control u on the spy-sensor s is assumed. Ultimately, we wish to determine a transfer function C_{su} which links

information from our spy-measurements s to the actuation u, i.e.

$$u = \mathsf{C}_{su} s. \tag{2.3}$$

This latter transfer function has to be designed such that our cost-objective is satisfied. In our case, we wish to minimize the disturbance energy at the cost-sensor location and thus choose $y = 0$ (for all times) as our control objective. Upon substitution of (2.3) and (2.2) into (2.1), we arrive at an expression linking the output y to the input w according to

$$y = (\mathsf{G}_{wy} + \mathsf{G}_{uy}\mathsf{C}_{su}\mathsf{G}_{ws})\, w. \tag{2.4}$$

For a controller that suppresses the output signal y for all times and independent of the disturbance environment w, we have to require the expression in the parenthesis to be identically zero which yields a control law u of the form

$$u = -\mathsf{G}_{uy}^{-1}\mathsf{G}_{wy}\mathsf{G}_{ws}^{-1} s \equiv \mathsf{C}_{su} s. \tag{2.5}$$

At this point, a discussion about the existence of the inverse transfer functions, their minimal-phase properties and their compliance with causality is postponed to a later section. Instead, we proceed by introducing techniques to identify the involved transfer functions from input-output data sequences. Any transfer function requiring information about the unknown disturbance environment w, such as G_{wy} and G_{ws}, cannot be determined under realistic conditions. Coincidentally, the control design (2.5) only requires the *composite* transfer function $\mathsf{G}_{wy}\mathsf{G}_{ws}^{-1}$. Using relation (2.2) between w and s we have

$$y = \mathsf{G}_{uy} u + \mathsf{G}_{wy}\mathsf{G}_{ws}^{-1} s. \tag{2.6}$$

Since the signals u, s and y are readily accessible (e.g. from an experiment) we can determine the two transfer functions G_{uy} and $\mathsf{G}_{wy}\mathsf{G}_{ws}^{-1}$. Their identification by processing finite-impulse responses (in the temporal rather than frequency domain) is the focus of the next section.

2.1. *Finite-impulse responses (FIR)*

To take advantage of a data-based approach, an input-output data sequence of N samples will be recorded from which the transfer functions will be determined. This latter process can be divided into two steps: a model-structure for the system's impulse responses has to be chosen first, after which a fitting procedure will determine the inherent parameters of the selected model.

It is important to choose an input signal u that properly excites the inherent frequencies of the system and thus provides a complete input-output map that accurately represents the response behavior of the system to a range of harmonic excitations. To this end, a pseudo-random binary signal (PRBS), a chirp signal or, simply, white noise are appropriate and common choices of a frequency-rich input signal.

2.1.1. *FIR model structure*

Among the many options to represent a transfer function of a linear system, one of the most straightforward is the finite-impulse response description. For discrete times, this description links the present output to past inputs in the form

$$y = \mathsf{G}_{uy} u \qquad \Rightarrow \qquad y(k) = \sum_{j=0}^{\infty} H_j u(k-j) \tag{2.7}$$

where $y(k)$ is a short-form for $y(k\Delta t)$ with Δt as the discrete time-step, and H_j stands for the j^{th} impulse response coefficient (also referred to as the j^{th} Markov parameter).

Under the assumption that, after a sufficient time, the influence of past actuation on the present measurement is negligible, we can truncate the above expression and arrive at the Finite Impulse Response (FIR) model of order μ

$$y(k) = \sum_{j=0}^{\mu-1} H_j u(k-j) \tag{2.8}$$

where only the μ first Markov parameters are accounted for. For single input and single output signals, the Markov parameters are scalar; for n_u input signals u and n_y measurement signals y the Markov parameters will be $n_y \times n_u$ matrices.

For our control configuration (see figure 1) two transfer functions need to be identified: G_{uy} and $\mathsf{G}_{wy}\mathsf{G}_{ws}^{-1}$. Consequently, two sets of Markov parameters, denoted by H^u and H^s, describe the FIR input-output relation,

$$y(k) = \sum_{j=0}^{\mu_u-1} H_j^u u(k-j) + \sum_{j=0}^{\mu_s-1} H_j^s s(k-j). \tag{2.9}$$

Even though each term of the FIR model can have a different order, for the sake of simplicity, we will take $\mu_u = \mu_s = \mu$ for the remainder of this study.

2.1.2. *Least-squares identification*

Denoting by $\widehat{y}(k; H^u, H^s)$ the output predicted by the identified model, the identification error E may be written as the L_2-norm distance between the exact (measured) output y and its estimation, i.e.,

$$E(H^u, H^s) = \frac{1}{N} \sum_{k=1}^{N} \left\| y(k) - \widehat{y}(k; H^u, H^s) \right\|_2 . \tag{2.10}$$

The identification procedure then corresponds to the minimization of E, resulting in the set of Markov parameters H^u, H^s. Among the many different ways to solve this optimization problem, the pseudo-inverse is used to arrive at the solution. In vector form the identification error can be written as

$$E = \frac{1}{N} \left\| Y - \mathcal{H}\Phi \right\|_2 \tag{2.11}$$

with

$$Y = \left(y(\mu),\ y(\mu+1),\ \ldots,\ y(N) \right) \tag{2.12a}$$

$$\mathcal{H} = \left(H_0^u,\ \ldots,\ H_{\mu-1}^u,\ H_0^s,\ \ldots,\ H_{\mu-1}^s \right) \tag{2.12b}$$

$$\Phi = \left(\begin{array}{cccc} u(\mu) & u(\mu+1) & \cdots & u(N) \\ u(\mu-1) & u(\mu) & \cdots & u(N-1) \\ \vdots & \vdots & & \vdots \\ u(0) & u(1) & \cdots & u(N-\mu) \\ \hline s(\mu) & s(\mu+1) & \cdots & s(N) \\ s(\mu-1) & s(\mu) & \cdots & s(N-1) \\ \vdots & \vdots & & \vdots \\ s(0) & s(1) & \cdots & s(N-\mu) \end{array} \right) . \tag{2.12c}$$

Based on this formulation, the set of Markov parameters which minimizes the L_2-identification error is obtained using the pseudo-inverse of the data matrix Φ according to

$$\mathcal{H} = Y\Phi^{\dagger}. \tag{2.13}$$

Using the identified Markov parameters $\mathcal{H}$ we can form the two sought-after transfer functions G_{uy} and $\mathsf{G}_{wy}\mathsf{G}_{ws}^{-1}$ based on our FIR-representation and determine the controller according to $u = -\mathsf{G}_{uy}^{-1}\mathsf{G}_{wy}\mathsf{G}_{ws}^{-1}s = \mathsf{C}_{su}s$. Thus, the remaining step is to apply the inverse of G_{uy} (by left multiplication) to the composite transfer function $\mathsf{G}_{wy}\mathsf{G}_{ws}^{-1}$; this final step is the focus of the next section.

2.2. *Disturbance rejection control design*

For realistic cases the inversion of the transfer function G_{uy} may be complicated by the fact that for some frequencies the modulus of the transfer function is nearly zero, resulting in excessively large control amplitudes following the inversion. Regularization techniques have to be employed to avoid these situations. The idea is to invert the transfer function only for frequencies where the transfer-function modulus is above a pre-set threshold value. This technique is equivalent to singular-value thresholding when forming the pseudo-inverse of the transfer function. In our case, the transfer function is expressed as a finite-impulse response in the time domain, and the algorithm of Model Predictive Heuristic Control (MPHC) (see, e.g., Camacho & Bordons 2004) is most conveniently applied to arrive at a regularized inverse and a robust expression for the transfer function $\mathsf{G}_{uy}^{-1}\mathsf{G}_{wy}\mathsf{G}_{ws}^{-1}$. The MPHC approach determines the Markov parameters of the transfer function C_{su} using a variational principle: we seek a signal u which minimizes the cost functional J given by

$$\text{(SISO)} \qquad J = \sum_{k=0}^{\mu-1} y(k)^2 + \alpha \sum_{k=0}^{\mu-1} u(k)^2, \tag{2.14a}$$

$$\text{(MIMO)} \qquad J = \frac{1}{2}\sum_{k=0}^{\mu-1}\sum_{i=1}^{n_o} \beta_i y_i(k)^2 + \frac{1}{2}\sum_{k=0}^{\mu-1}\sum_{j=1}^{n_i} \alpha_j u_j(k)^2. \tag{2.14b}$$

The first cost functional is relevant for a single-input-single-output (SISO) configuration, whereas the second expression allows for multiple-input and multiple-output signals (MIMO), where n_o and n_i are respectively the number of cost-sensors and the number of actuators. In either case, the aim is to compute a signal u which will cancel an impulse in s. Furthermore, the cost functional covers a time span of μ time steps (the length of the impulse response from s to reach y) and represents a balance between the compensated signal and its associated control. The balancing constant α (for the SISO-case) accounting for the relative weight of the control cost and the measured signal is an analog to the threshold value for the frequency cut-off (in the frequency domain). In the MIMO-case, the cost of the different actuators α_j and the weights for the measured signals β_i allow a great deal of flexibility to account for special features of the physical system under consideration.

2.2.1. *Optimal actuation: single input, single output (SISO)*

Starting with the cost functional for the SISO-case, we use the additional fact that the signal s is given by an impulse and that y is given by (2.9) and obtain

$$J = \sum_{k=0}^{\mu-1} \left(H_k^s + \sum_{j=0}^{\mu-1} H_j^u u(k-j) \right)^2 + \alpha \sum_{k=0}^{\mu-1} u(k)^2. \tag{2.15}$$

Introducing the impulse response coefficients (Markov parameters) corresponding to the transfer function C_{su} as L_k we can write

$$u(k) = \sum_{j=0}^{\mu-1} L_j s(k-j). \tag{2.16}$$

Again, for the special case of an impulse in s, that is $s(0) = 1$ and $s(k) = 0$ for $k > 0$, we arrive at the simplified relation

$$u(k) = L_{k-1}. \tag{2.17}$$

Returning to (2.15) we obtain, using (2.17), an expression for the cost functional J in terms of Markov parameters only. We have

$$J = \sum_{k=0}^{\mu-1} \left(H_k^s + \sum_{j=0}^{\mu-1} H_j^u L_{k-j-1} \right)^2 + \alpha \sum_{k=0}^{\mu-1} L_k^2. \tag{2.18}$$

The desired transfer function C_{su} has to be causal which requires that for $k < 0$, the Markov parameters L_k have to be identically zero. We proceed by defining the transposed (upper triangular) Toeplitz matrix T^T containing the Markov parameters of G_{uy}, i.e.,

$$\mathsf{T}^T = \begin{pmatrix} H_0^u & H_1^u & \cdots & H_\mu^u \\ & H_0^u & \cdots & H_{\mu-1}^u \\ & & \ddots & \vdots \\ & & & H_0^u \end{pmatrix}. \tag{2.19}$$

Furthermore, we introduce S as the vector of Markov parameters of G_{sy},

$$\mathsf{S} = (H_0^s, H_1^s, \ldots, H_{\mu-1}^s)^T, \tag{2.20}$$

and L as the vector of (unknown) Markov parameters of the desired transfer function C_{su}, that is,

$$\mathsf{L} = (L_0, L_1, \ldots, L_{\mu-1})^T, \tag{2.21}$$

and can then reformulate the cost functional J in the more compact form

$$J(\mathsf{L}) = \|\mathsf{S} + \mathsf{T}\mathsf{L}\|^2 + \alpha \|\mathsf{L}\|^2 \quad \rightarrow \quad \min \tag{2.22}$$

which attains its minimum for (see appendix A)

$$\mathsf{L} = -(\mathsf{T}^T\mathsf{T} + \alpha \mathsf{I})^{-1} \mathsf{T}^T \mathsf{S}. \tag{2.23}$$

We recognize the expression $(\mathsf{T}^T\mathsf{T} + \alpha\mathsf{I})^{-1}\mathsf{T}^T$ as a Tikhonov regularization of the pseudo-inverse of the Toeplitz matrix T, where α acts as the Tikhonov regularization parameter that avoids large coefficients in L stemming from the ill-posedness of the original problem. Low values of α enforce a low frequency-cutoff threshold and result in large-amplitude actuation; large values of α yield low-amplitude (but maybe ineffective) actuation.

The desired transfer function of the controller is determined directly from (2.23): the Markov parameters H^u and H^s have been identified earlier, which makes the computation of L straightforward. With L determined, the optimal control for disturbance rejection is given by the application of the transfer function to the measured signal s according to

$$u(k) = \sum_{j=0}^{\mu-1} L_j s(k-j). \tag{2.24}$$

This expression concludes the computational procedure for the design of a controller — from measured data-sequences — that optimally acts on the flow to suppress the signal energy downstream.

2.2.2. *Optimal actuation: multiple inputs, multiple outputs (MIMO)*

This generalization to multiple inputs and/or outputs is very similar to the previous SISO case; the optimization procedure is equivalent, but the derivation of the cost functional with respect to the unknown Markov parameters is rather arduous. Starting with the cost functional

$$J = \frac{1}{2}\sum_{k=1}^{\mu}\sum_{i=1}^{n_o} \beta_i y_i(k)^2 + \frac{1}{2}\sum_{k=1}^{\mu}\sum_{j=1}^{n_i} \alpha_j u_j(k)^2 \tag{2.25}$$

which, upon analogous substitution of the Markov parameters, becomes

$$J = \frac{1}{2}\sum_{i=1}^{n_o}\beta_i \left(\sum_{k=1}^{n_s} \left\| \mathsf{S}_{ki} + \sum_{j=1}^{n_i} \mathsf{T}_{ij} L_{jk} \right\|^2 \right) + \frac{1}{2}\sum_{j=1}^{n_i}\alpha_j \left(\sum_{k=1}^{n_s} \|L_{jk}\|^2 \right). \tag{2.26}$$

In this expression, T_{ij} denotes the transpose Toeplitz matrix of the Markov parameters of the transfer function from the control u_j to the sensor y_i, and S_{ki} stands for the vector of Markov parameters of the transfer function from the spy sensor s_k to the cost sensor y_i. Finally, the terms L_{jk} represent the Markov parameters of the controller (from spy s_k to actuation u_j), the quantities that have to be determined.

As before, it is convenient to formulate the minimization problem for J in matrix form which then allows a simple solution in terms of a pseudo-inverse. For this reason, we introduce

$$J_k(L_{1k}, L_{2k}, \ldots, L_{n_s k}) = \frac{1}{2}\sum_{i=1}^{n_o}\beta_i \left(\left\| \mathsf{S}_{ki} + \sum_{j=1}^{n_i} \mathsf{T}_{ij} L_{kj} \right\|^2 \right) + \frac{1}{2}\sum_{j=1}^{n_i}\alpha_j \left(\|L_{jk}\|^2 \right) \tag{2.27}$$

which simplifies (2.26) to

$$J = \sum_{k=1}^{n_s} J_k(L_{1k}, L_{2k}, \ldots, L_{n_i k}). \tag{2.28}$$

From this we conclude that the minimization of J with respect to L_{ij} is equivalent to the minimization of each individual J_k with respect to L_{ik} and that the controller associated with each spy sensor can be designed independently. We proceed by defining

$$\underline{\mathsf{T}} = \begin{pmatrix} \mathsf{T}_{11} & \mathsf{T}_{12} & \ldots & \mathsf{T}_{1,n_i} \\ \mathsf{T}_{21} & \mathsf{T}_{22} & \ldots & \mathsf{T}_{2,i} \\ \vdots & \vdots & \ddots & \vdots \\ \mathsf{T}_{n_o,1} & \mathsf{T}_{n_o,2} & \ldots & \mathsf{T}_{n_o,n_i} \end{pmatrix} \tag{2.29a}$$

(2.29*b*)

$$\underline{S}_k = \begin{pmatrix} S_{k,1} \\ S_{k,2} \\ \vdots \\ S_{k,n_o} \end{pmatrix} \qquad \underline{L}_k = \begin{pmatrix} L_{k,1} \\ L_{k,2} \\ \vdots \\ L_{k,n_i} \end{pmatrix} \tag{2.29c}$$

which brings the individual cost functionals (2.27) into the compact form

$$J_k = \|\mathsf{B}(\underline{S}_k + \underline{\mathsf{T}}\,\underline{L}_k)\|^2 + \|\mathsf{A}\underline{L}_k\|^2. \tag{2.30}$$

with

$$\mathsf{B} = \begin{pmatrix} \sqrt{\beta_1} I_\mu & 0 & \dots & 0 \\ 0 & \sqrt{\beta_2} I_\mu & \ddots & \vdots \\ \vdots & \ddots & \ddots & 0 \\ 0 & \dots & 0 & \sqrt{\beta_{n_o}} I_\mu \end{pmatrix} \qquad \mathsf{A} = \begin{pmatrix} \sqrt{\alpha_1} I_\mu & 0 & \dots & 0 \\ 0 & \sqrt{\alpha_2} I_\mu & \ddots & \vdots \\ \vdots & \ddots & \ddots & 0 \\ 0 & \dots & 0 & \sqrt{\alpha_{n_i}} I_\mu \end{pmatrix}. \tag{2.31}$$

including the weight measures β_k and α_k. The minimization of J_k with respect to the controller Markov parameters $\underline{L}_k$ is then simply a matter of linear algebra resulting in

$$\underline{L}_k = -(\underline{\mathsf{T}}^T \mathsf{B}^2 \underline{\mathsf{T}} + \mathsf{A}^2)^{-1} \underline{\mathsf{T}}^T \mathsf{B}^2 \underline{S}_k. \tag{2.32}$$

The solution of this optimization is similar to the SISO case, except for the appearance of weight matrices A and B accounting for the specific balance of terms in the cost functional. In a last step, the control laws for each actuator u_j $(j = 1, ..., n_i)$ can be written as

$$u_j(p) = \sum_{k=1}^{n_s} \sum_{i=0}^{\mu-1} L_{kj} s_k(i-p) \tag{2.33}$$

which concludes the design process for the MIMO case.

2.3. *Validation on a simple example*

Before applying the above control design strategy to a more realistic flow case, we will first validate its effectiveness on a simple, yet fluid-related model problem. The key steps in the design of a SISO, model-predictive control strategy can be summarized as follows: (i) We force the system with a broadband control signal u and record the resulting output signals s (representing the unknown upstream disturbance environment) and y, as well as the control input u. (ii) From these data-sequences, we identify the impulse response coefficients (Markov parameters) based on a FIR-model using a least-squares technique (see equ. (2.13)). (iii) Based on the identified transfer functions G_{uy} and $\mathsf{G}_{wy}\mathsf{G}_{ws}^{-1}$, we determine the impulse response coefficients (Markov parameters) L_k of the control transfer function C_{su} using a variational approach with (2.23) as the cost functional. (iv) Using the coefficients L_k and (2.24), an optimal control law results linking the input signals s to an actuator signal u that optimally suppresses the cost-sensor energy given by y.

These procedural steps will be followed for the design of a disturbance rejection control law for the Ginzburg-Landau equation. This equation is a popular choice for benchmarking control schemes, since it contains advective, dissipative, dispersive and unstable terms, thus mimicking (with a substantially reduced number of degrees of freedom) the fundamental, underlying processes of many fluid systems. For our case, the parameters of the equation have been chosen to replicate the behavior of a convectively dominated

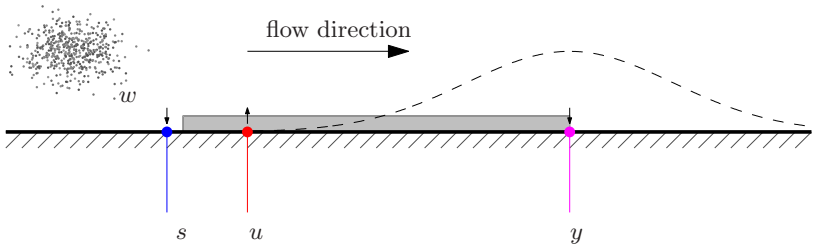

FIGURE 2. Setup of a control problem for the Ginzburg-Landau equation.

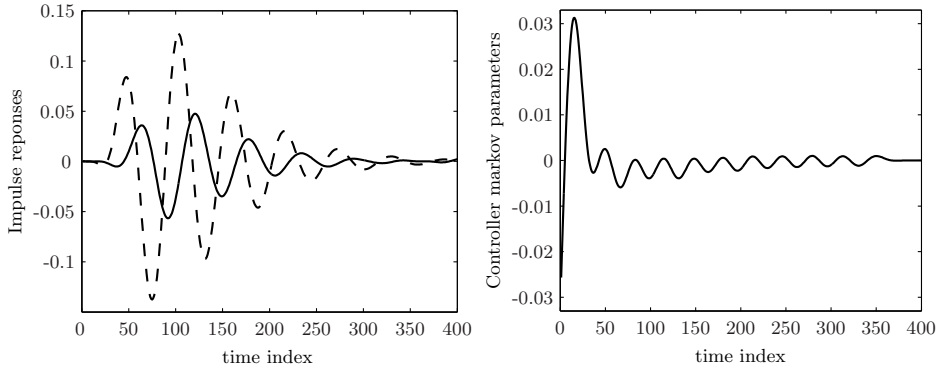

FIGURE 3. Left :Identified impulses responses, G_{uy} (dashed) and $\mathsf{G}_{wy}\mathsf{G}_{ws}^{-1}$ (plain). Right : computed impulse response of the controller C_{su}.

(amplifier) flow (see Roussopoulos & Monkewitz 1996). We have

$$\frac{\partial \psi}{\partial t} - \omega_{kk} k_0 \frac{\partial \psi}{\partial z} - \frac{i}{2}\omega_{kk}\frac{\partial^2 \psi}{\partial z^2} + i\left(\omega_0 + \omega_{kk}\frac{k_0^2}{2}\right)\psi = 0. \tag{2.34}$$

The layout of the control problem based on the Ginzburg-Landau equation is shown in figure 2. The upstream noise disturbance w is convected in the streamwise x-direction and is measured by the sensor s. The actuation u aims at reducing this disturbance so that the signal y at the cost sensor location is minimized. The dotted line symbolizes the spatial disturbance energy distribution for the uncontrolled case.

Working through the design procedure, the identified FIR representation of G_{uy} and $\mathsf{G}_{wy}\mathsf{G}_{ws}^{-1}$ are displayed in figure 3; quantitatively, the residuals from the identification of G_{uy} and $\mathsf{G}_{wy}\mathsf{G}_{ws}^{-1}$ are less than 0.5% in either case. It is noteworthy that the controller's transfer function approximates a delay combined with an opposition action. Finally, figure 4 shows space-time diagrams of the energy magnitude (starting with an impulse applied at the noise location) with the controller switched off (figure 4(a)) or on (figure 4(b)). The controller efficiency (for $\alpha = 0.01$) is approximately 97%. After applying control, the signal measured by the cost sensor is only a 1/20-th of the uncontrolled signal.

2.4. *Additional remarks, implementation issues and extensions of the method*

We recall that finding the optimal model-predictive controller for disturbance rejection is equivalent to computing the transfer function $\mathsf{C}_{su} = -\mathsf{G}_{uy}^{-1}\mathsf{G}_{wy}\mathsf{G}_{ws}^{-1}$ which links the sensors measurements s to the actuator signal according to $u = \mathsf{C}_{su}s$. For this procedure to yield feasible results, causality constraints have to be respected. For purely convective flows the transfer functions introduced above can be thought of as approximations of

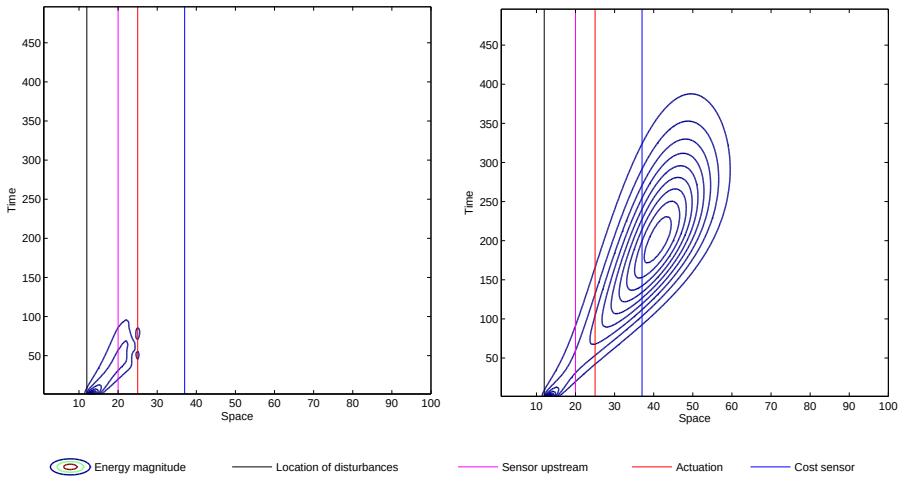

FIGURE 4. Controlled (left) and uncontrolled (right) impulse response (from the noise source) in a space-time diagram.

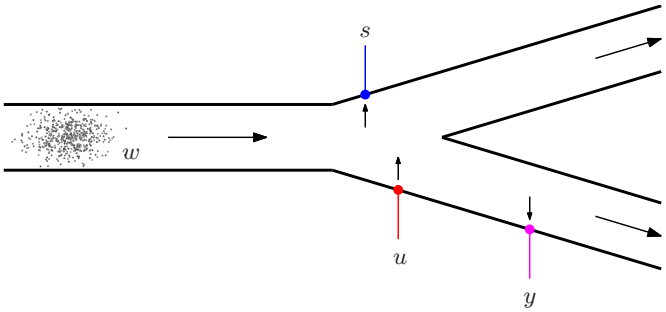

FIGURE 5. Example of a feedforward configuration that satisfies the causality constraint and hence is controllable by the proposed algorithm.

delay operators; for example, G_{uy} corresponds to a forward translation over τ_{uy} time units while G_{ws}^{-1} can be represented as a translation backward in time. The final control transfer function C_{su} is thus describes a time delay of $\tau_{su} = -\tau_{uy} + \tau_{wy} - \tau_{ws}$ which is only sensible if it is positive, or if $\tau_{wy} > \tau_{uy} + \tau_{ws}$. This causality constraint, expressed in terms of time delays for convective systems, has implications for the placement of sensors and actuators to ensure an effective control configuration. A feedforward configuration for a more complex geometric setup (e.g., the one displayed in figure 5) can be treated analogously by the technique introduced above, as long as this constraint is accounted for.

It is worth pointing out that the transfer function $\mathsf{C}_{su} = -\mathsf{G}_{uy}^{-1}\mathsf{G}_{wy}\mathsf{G}_{ws}^{-1}$ can be computed by a variety of algorithms: in the time domain, in the frequency domain, or using other model structure, such as state-space representations. All those techniques are mutually consistent and should give equivalent results, even though the individual implementation details may vary. We have chosen the MPHC-approach for its simplicity, ease of implementation and effectiveness. In a similar vein, the computation of the impulse response coefficients can also be accomplished with a wide range of available methods, such as, for example, ARX (Gerencsér *et al.* 2009), ARMarkov (Akers & Bernstein 1997),

subspace identification (Katayama 2005) or any other linear system identification algorithm (see Ljung 1987). The overall procedure, however, is identical to the one introduced above, even though slight variations in the convergence rate or statistical properties of the errors are conceivable.

Under the assumption of a pure feedforward configuration (the information only travel in one direction), stability — but not performance — of the controlled system is assured. If this assumption is violated, however, robustness issues arise. In this case, a feedback from the controller u to the sensor s can be modeled by a transfer function of the form

$$s = \mathsf{G}_{ws} w + \mathsf{G}_{us} u = \frac{\mathsf{G}_{ws}}{1 - \mathsf{G}_{us}\mathsf{C}_{su}} w. \tag{2.35}$$

The non-zero term G_{us} can give rise to divergences in the sensor s which subsequently impact the control signal u. This divergence occurs when $\mathsf{G}_{us}\mathsf{C}_{su}$ approaches unity; the minimum distance to this singularity can be interpreted as a robustness margin of the controlled system. A more detailed analysis of robustness margins can be found in Dovetta *et al.* (2011).

An implementation concern stems from the signal delay caused by the convective nature of the flow: due to causality, signals generated upstream will have an impact on measurements downstream after a delay that can be estimated by the convection speed and the distance between upstream and downstream signal location. This delay can be accounted for explicitly in the computation of the respective transfer functions. In this manner, one avoids the calculation of unnecessary zero Markov parameters that reflect the time delay in the various impulse responses.

Placing multiple spy sensors in a MIMO configuration appears to be a prudent way of extracting more information about the unknown upstream disturbance environment and is expected to improve the effectiveness and performance of the disturbance rejection control. However, the cost of this procedure has to be taken into consideration, since we aim at a real-time implementation of the feedforward control which may become prohibitive with a large number of sensors. In this latter case, redundant information from the spy sensors should be removed. Even though this objective poses a non-trivial problem, various approximate options exist. The multiple signals could be combined via a linear combination to yield a smaller number of filtered (noise-reduced) spy signals. Alternatively, the estimation error for all combinatorial sensor configurations can be computed and only the most performing combinations could be retained. A far more efficient approach is based on the sequential evaluation of the rms-difference between the estimated signal $\hat{s}_2(s_1)$ based on retained spy sensors s_1 and the true signal s_2 at the same location. If this value falls below a given threshold (for example, related to the measurement noise), the sensor s_2 is eliminated, since most of its contribution is already captured by s_1.

3. Application to two-dimensional obstructed channel flow

We intend to test the proposed control design technique MPHC on a more challenging case and chose a configuration depicted in figure 6 with a MIMO setup. The two-dimensional channel has two rectangular-shaped obstructions that cause flow separation and recirculation regions. Nonetheless, the flow is convectively dominated and is thus a suitable application of feedforward control. Included in figure 6 is also the location of the sensors s_1 and s_2, the actuators u_1 and u_2, as well as the performance sensors y_1 and y_2. Causality constraints have been observed in the placement of these elements. The flow is excited upstream with multiple high-dimensional broad-band noise sources.

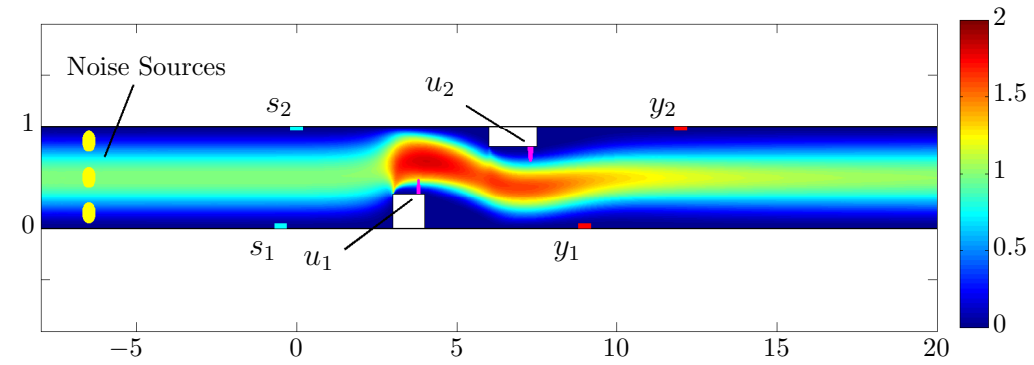

FIGURE 6. Flow in an obstructed two-dimensional channel; the base flow is visualized by the streamwise velocity, and the location of sensors and actuators is indicated.

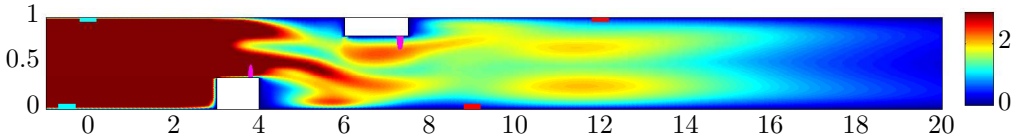

FIGURE 7. Contours of averaged perturbation norm, in response to excitation by the three upstream noise sources.

Our numerical experiment is is based on the Navier-Stokes equations linearized about a steady base flow. Upstream perturbations are initially damped, but are then re-amplified (due to a Kelvin-Helmholtz instability) in the shear regions near and downstream of the obstructions. The response of the flow to excitation by the noise sources, measured by the average perturbation norm, is shown in figure 7; the aim of our control efforts is the minimization of the fluctuating signals measured by the sensors y_1 and y_2.

3.1. *Identification and control*

Numerical experiments have been performed with a white noise actuator signal, from which all necessary impulse responses have been identified using (2.13). Four of the total eight identified impulse responses are shown in figure 8. In particular, the identified impulses responses from the spy sensors s_1 and s_2 to the cost sensor y_2 (see figure 8(b)) appear far noisier compared to its equivalent in the Ginzburg-Landau case. Part of this phenomenon can be attributed to the more complex flow configuration yielding more complex transfer functions G_{wy} and G_{ws}, which also reflects into the product $\mathsf{G}_{wy}\mathsf{G}_{ws}^{-1}$. A second reason is more of a numerical nature: by the time the broad-band noise w reaches the location of the respective spy sensors it has lost a substantial part of its frequency content, causing the input $s_{1,2}$ into the identification algorithm to be not as rich in frequency as desired. The resulting least-squares problem can thus be ill-conditioned. To compensate for this difficulty, lower cut-off thresholds for the truncation of the singular values of Φ in (2.13) have to be chosen. As a consequence, small oscillations can appear in the FIR representation of the associated transfer function, evident in figure 8(b).

With all necessary transfer functions identified, a control strategy can be designed to minimized the signals at y_1 and y_2. For simplicity, the weight coefficients for the actuators and performance sensors have been chosen as $\alpha_1 = \alpha_2 = 0.01$ and $\beta_1 = \beta_2 = 0.5$. The controller designed with these parameters has been attached to the numerical simulation, and the controlled flow is represented in figure 9, visualized by the averaged perturbation

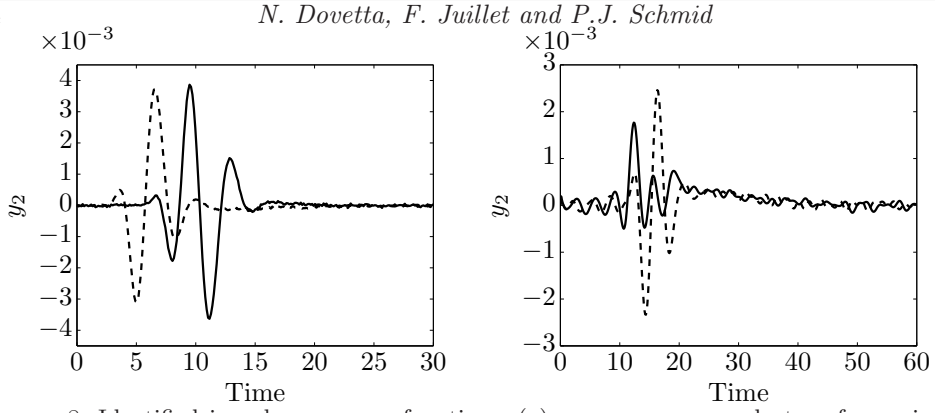

FIGURE 8. Identified impulse response functions: (a) response measured at y_2 for an impulse generated in u_1 (continuous line) and u_2 (dashed line); (b) response measured at y_2 for an impulse in s_1 (continuous line) and s_2 (dashed line).

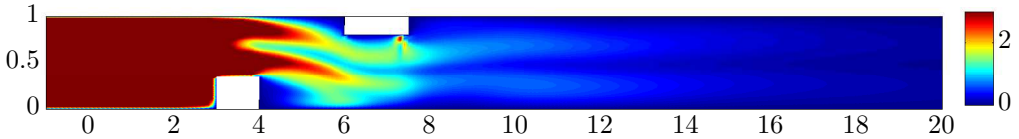

FIGURE 9. Averaged perturbation norm of the controlled flow in an obstructed channel flow.

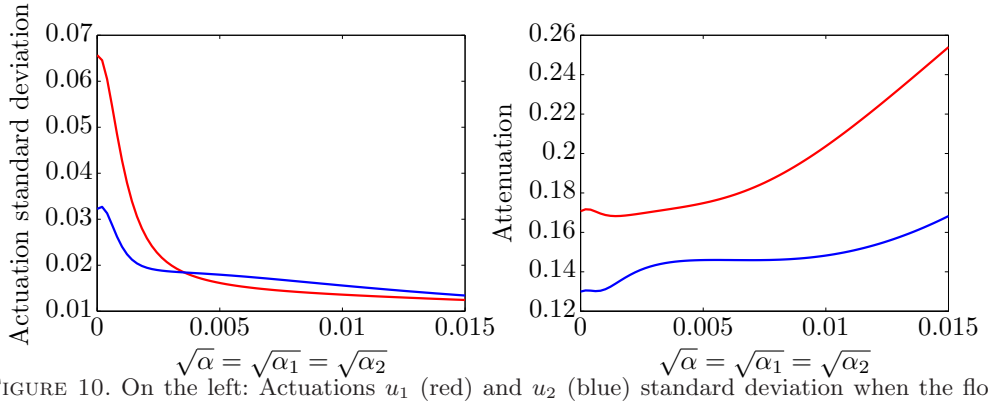

FIGURE 10. On the left: Actuations u_1 (red) and u_2 (blue) standard deviation when the flow is designed for actuation penalty weights $\alpha_1 = \alpha_2 \equiv \alpha$ varying from 0 to 0.015. On the right: Corresponding attenuation on y_1 (red) and y_2 (blue).

norm. The perturbation flow has been drastically reduced, which is apparent from a comparison with the contour plots of the uncontrolled flow in figure 7 (the same colormap has been used). More quantitatively, the rms-value of the signals y_1 and y_2 has been reduced by more than 80%.

The effectiveness of the disturbance-rejection feedforward control is very encouraging; we will next explore the flexibility of our MIMO setup and investigate the influence of the different weights parameters α_i and β_i (see expression (2.14)) on the performance of the MIMO control strategy.

3.2. *Influence of the actuator weigths α_1 and α_2*

The weights α on the actuator signal in the objective functional (2.14) takes into account the cost of control. Large values of α penalize any control effort and yield parsimonious actuation, while small values of α produce more liberally expended control signals.

Figure 10 displays the standard deviations of the actuator and sensor signal as a

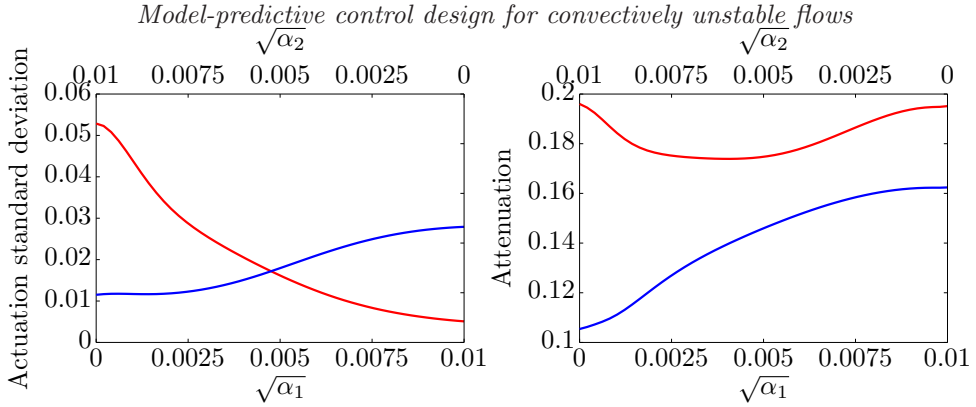

FIGURE 11. On the left: Actuations u_1 (red) and u_2 (blue) standard deviation when the flow is designed for actuation penalty weights $\alpha_1 = 0.01 - \alpha_2$ varying from 0 to 0.01. On the right: Corresponding attenuation on y_1 (red) and y_2 (blue).

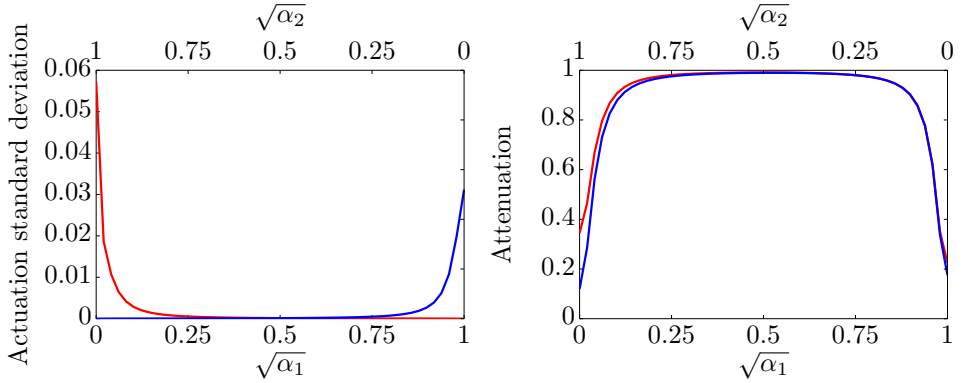

FIGURE 12. On the left: Actuations u_1 (red) and u_2 (blue) standard deviation when the flow is designed for actuation penalty weights $\alpha_1 = 1 - \alpha_2$ varying from 0 to 1. On the right: Corresponding attenuation on y_1 (red) and y_2 (blue).

function of the weight α. We observe that the more expensive the control efforts, the less control will be expended and the more fluctuations can be expected at the objective sensor locations and *vice versa*. More interestingly, we set the sum of the actuation penalizations to a constant and vary the relative weight between the two. Figures 11 and 12 show two cases of tuning the actuation penalties: with $\sum \alpha_i = 0.01$ and $\sum \alpha_i = 1$, respectively. In figure 11, even though the different actuators are more or less active, depending on the penalty distribution, the disturbance attenuation recorded by the two objective sensors remains in approximately the same range. We conclude that the two actuators are *independently* able of significantly reducing the energy of the flow perturbations. In figure 12, the overall cost of the actuation is substantially larger when compared to the sensor signal. Consequently, for $\alpha_1 \simeq \alpha_2$, each actuation is too expensive, and the controller nearly shuts down. On the other hand, if one of the actuation signal becomes cheap, it is able to control the flow by itself; the controller increases its signal, and we converge to the performance of a single-actuator configuration. Next, we investigate the effect of the sensor weights which discriminates the different outputs.

3.3. *Influence of objective sensor weights β_1 and β_2*

The penalization of the actuations is set to $\alpha_i = 0.005$, and $\beta_1 = 1 - \beta_2$ varies from 0 to 1. In figure 13 the standard deviations of the control signals and the attentuation of the sensor signals are represented. The control efficiency is influenced, as expected, by the

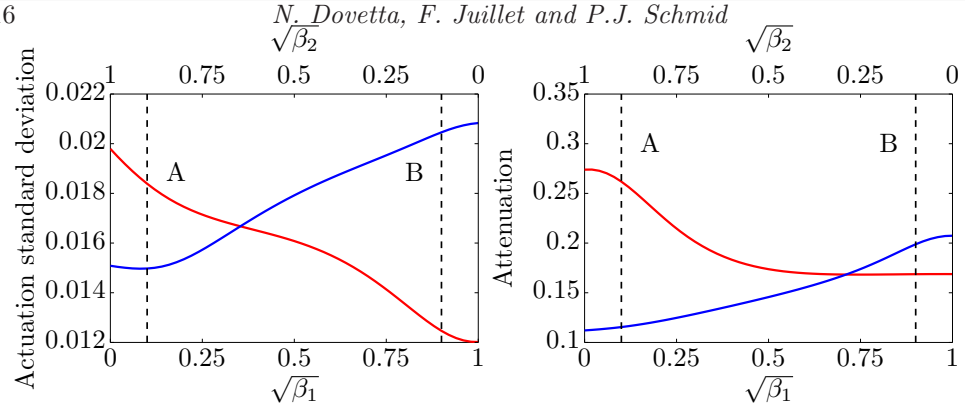

FIGURE 13. On the left: Actuations u_1 (red) and u_2 (blue) standard deviation when the flow is designed for objective sensor weigths $\beta_1 = 1-\beta_2$ varying from 0 to 1. On the right: Corresponding attenuation of y_1 (red) and y_2 (blue).

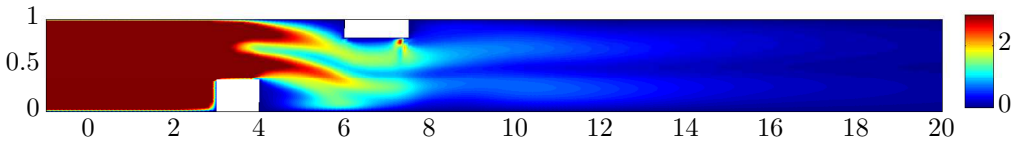

FIGURE 14. Controlled perturbation norm (case A)

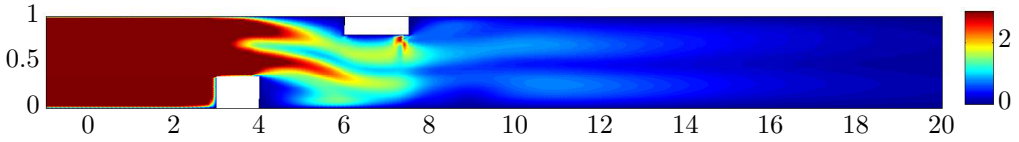

FIGURE 15. Controlled perturbation norm (case B)

variation of the weight coefficients. However, even if one coefficient is set to zero (i.e., the controller is not designed to reduce the fluctuations measured by the corresponding sensor), the attenuation in the associated sensor signal is still significant; for instance, the signal measured at y_1 has its standard deviation reduced by 73% compared to the uncontrolled case, even when $\beta_1 = 0$. This means that the flow responds more globally to a certain perturbation and that it suffices to control this perturbation based on at least one sensor measurement and still reap remarkable benefits at the other sensors.

To see the impact of the weight coefficients on the flow behavior, the controlled perturbation norm is presented for two cases (referred to as A and B; see figure 13) in figures 14 and 15. Both controllers significantly reduce the perturbation norm over the entire downstream flow field. However, closer inspection of the difference between the two compensated perturbation norms (figure 16) reveals slightly different behavior in the two cases. Hence, the MIMO algorithm together with the weight coefficients can be used to design control schemes that will change the flow behavior such that some regions of the flow are more or less sensitive to external perturbation as the cost functional is minimized.

4. Summary and conclusion

A data-based identification and control design algorithm for fluid flows that are dominated by convection has been presented. The identification step is based on a simple finite-impulse-response model, whose unknown coefficients can be determined by a least-

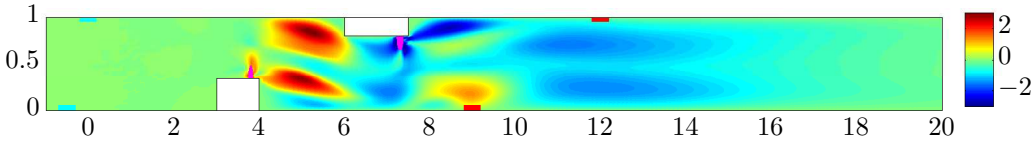

FIGURE 16. Difference between the averaged perturbations for case A and B. Regions in blue are more effectively controlled by the compensator A whereas regions in red are better controlled by the compensator B.

squares match of the true and model-predicted output sequence, as the model is driven by frequency-rich input signals. Noise sources are captured by a sensor located upstream of the actuator. The two identified transfer functions (Markov parameters) between (i) upstream and downstream sensors and (ii) actuator and downstream sensor are then used to compute a control strategy based on disturbance rejection. This yields a transfer function between upstream sensor and actuator, thus providing a control strategy. The SISO-case has been tested on a simple Ginzburg-Landau model, while the MIMO-version has been applied to control two-dimensional channel flow over two rectangular obstructions. In both cases, an effective and efficient control performance could be achieved.

The presented approach is particularly suited for convection-dominated flows where it provides a simpler and far more efficient alternative to the more commonly used LQG-technique (for a relation between the proposed and LQG-approach, see appendix B). It is also noteworthy that the entire design process only relies on flow measurements and thus is equally applicable to numerical simulations and experimental data. Future work will explore the implementation of the FIR-based model-predictive heuristic controller to experimental data aiming at the suppression of upstream generated disturbances in convectively dominated shear flows.

Appendix A. Minimization of the cost functional

More details are given on the minimization of the cost functional J with respect to the Markov parameters L of the controller. The mathematical problem can be stated as

$$J(L) = \|S + \mathsf{T}L\|^2 + \alpha\|L\|^2 \quad \rightarrow \quad \min \tag{A 1}$$

which can be rewritten, using the norm-related scalar product, as

$$J(L) = \langle S + \mathsf{T}L, S + \mathsf{T}L\rangle + \alpha\langle L, L\rangle. \tag{A 2}$$

Using the bilinearity property, the latter expression can be expanded as

$$J(L) = \langle S, S\rangle + 2\langle \mathsf{T}L, S\rangle + \langle \mathsf{T}L, \mathsf{T}L\rangle + \alpha\langle L, L\rangle. \tag{A 3}$$

A minimum is obtained when the first variation of J with respect to L vanishes, i.e.,

$$\frac{\partial J}{\partial L}\delta L = J(L + \delta L) - J(L) = 2\langle \delta L, \mathsf{T}^T S\rangle + 2\langle \delta L, \mathsf{T}^T\mathsf{T}L\rangle + 2\alpha\langle \delta L, L\rangle = 0. \tag{A 4}$$

The last expression has to hold for all variations δL, which leads to

$$\mathsf{T}^T S + \mathsf{T}^T\mathsf{T}L + \alpha L = 0 \tag{A 5}$$

which, after rearrangement, results in an explicit expression for L that renders J minimal. We finally arrive at

$$L = -(\mathsf{T}^T\mathsf{T} + \alpha\mathsf{I})^{-1}\mathsf{T}^T S. \tag{A 6}$$

Appendix B. Equivalence between finite and infinite time-horizon control design for convective systems

We will consider the infinite time-horizon cost functional

$$J_\infty = \lim_{N\to\infty} \frac{1}{N} \left(\sum_{k=0}^{N} y(k)^2 + \alpha \sum_{k=0}^{N} u(k)^2 \right). \tag{B 1}$$

This cost functional is minimized by the LQG controller based on a state-space representation of a system that has been identified by its finite impulse responses. The disturbances are taken as white in time, and the system is assumed to be convectively dominated. This allows the formulation of the system's behavior by a set of finite-impulse responses (FIR) of length μ. Substituting this formulation back into (B 1) we obtain

$$J_\infty = \lim_{N\to\infty} \left[\frac{1}{N} \sum_{k=0}^{N} \left(\sum_{j=0}^{\mu-1} H_j^u \sum_{i=0}^{\mu-1} L_i s(k-j-i) + \sum_{j=0}^{\mu-1} H_j^s s(k-j) \right)^2 + \alpha \frac{1}{N} \sum_{k=0}^{N} \left(\sum_{i=0}^{\mu-1} L_i s(k-i) \right)^2 \right] \tag{B 2}$$

which, after rearranging the sums, yields

$$J_\infty = \lim_{N\to\infty} \left[\frac{1}{N} \sum_{k=0}^{N} \left(\left(\sum_{j=0}^{\mu-1} \left(\sum_{i=0}^{\mu-1} H_j^u L_i s(k-j-i) + H_j^s s(k-j) \right) \right)^2 + \alpha \left(\sum_{i=0}^{\mu-1} L_i s(k-i) \right)^2 \right) \right]. \tag{B 3}$$

Introducing $\mathbf{S}_{k-2\mu}^{k} = (s(k), s(k-1), \ldots, s(k-2\mu+2))$, as well as two linear operators $(\mathcal{A}, \mathcal{B})$ corresponding to the above quadratic forms, we arrive at a compact formulation according to

$$J_\infty = \lim_{N\to\infty} \frac{1}{N} \sum_{k=0}^{N} \left(\|\mathcal{A}\mathbf{S}_{k-2\mu}^{k}\|^2 + \alpha \|\mathcal{B}\mathbf{S}_{k-2\mu}^{k}\|^2 \right), \tag{B 4}$$

and, using the definition of the operator scalar product, we obtain

$$J_\infty = \lim_{N\to\infty} \left[\mathrm{trace} \left(\mathcal{A} \frac{1}{N} \sum_{k=0}^{N} \left(\mathbf{S}_{k-2\mu}^{k} {\mathbf{S}_{k-2\mu}^{k}}^T \right) \mathcal{A}^T \right) + \alpha \ \mathrm{trace} \left(\mathcal{B} \frac{1}{N} \sum_{k=0}^{N} \left(\mathbf{S}_{k-2\mu}^{k} {\mathbf{S}_{k-2\mu}^{k}}^T \right) \mathcal{B}^T \right) \right]. \tag{B 5}$$

In the above expression, we notice that $(\sum_{k=0}^{N} \mathbf{S}_{k-2\mu}^{k} {\mathbf{S}_{k-2\mu}^{k}}^T)/N = \sigma\mathcal{I}$ with $\mathcal{I}$ as the identity matrix of size 2μ and σ denoting a scalar, which follows from the fact that the noise has been taken as white. We thus have

$$J_\infty/\sigma = \|\mathcal{A}\|^2 + \alpha\|\mathcal{B}\|^2. \tag{B 6}$$

Based on the definition of $J(L)$, and the expressions for the two linear operators above, we recognize that the infinite time-horizon cost functional is proportional to the finite

time-horizon cost functional (which our disturbance-rejection algorithm optimizes)

$$J_\infty/\sigma = 2\mu J(L) = 2\mu \left(\|S + \mathcal{T}L\|^2 + \alpha \|L\|^2 \right). \tag{B 7}$$

We conclude that, if the system, driven by white noise, is convectively dominated, then the controller that minimizes an infinite time-horizon cost functional is equivalent to a controller that stems from a (sufficiently long) finite time-horizon optimization.

REFERENCES

Akers, J.C. & Bernstein, D.S. 1997 Armarkov least-squares identification. In *Proceedings of the American Control Conference*, pp. 186–190. Albuquerque, New Mexico, USA.

Bagheri, S. & Henningson, D.S. 2011 Transition delay using control theory. *Phil. Trans. R. Soc. A* **369**, 1365–1381.

Camacho, E.F. & Bordons, C. 2004 *Model Predictive Control*, 2nd edn. *Advanced Textbooks in Control and Signal Processing* XXII. Springer Verlag.

Cutler, C.R. & Ramaker, B.L. 1980 Dynamic matrix control – a computer control algorithm. *Proc. Joint Autom. Control Conf.* .

Dovetta, N., Schmid, P., Sipp, D. & McKeon, B. 2011 Application of system-identification by ARMarkov and sensitivity analysis to noise-amplifier models. In *64th Annual Meeting of the APS Division of Fluid Dynamics*, , vol. 56.

Gerber, A.G., Dubay, R. & Healy, A. 2006 CFD-based predictive control of melt temperature in plastic injection molding. *Appl. Math. Model.* **30** (9), 884–903.

Gerencsér, L., Hjalmarsson, H. & Mårtensson, J. 2009 Identification of ARX systems with non-stationary inputs - asymptotic analysis with application to adaptive input design. *Automatica* **45**, 623–633.

Hervé, A., Sipp, D., Schmid, P.J. & Samuelides, M. 2012 A physics-based approach to flow control using system identification. *J. Fluid Mech.* **702**, 26–58.

Huang, S.-C. & Kim, J. 2008 Control and system identification of a separated flow. *Phys. Fluids* **20** (10), 101509.

Juillet, F., Schmid, P.J. & Huerre, P. 2013 Control of amplifier flow using subspace identification techniques. *J. Fluid Mech.* **725**, 522–565.

Kalman, R.E. 1960 A new approach to linear filtering and prediction problems. *Trans. ASME J. Basic Eng.* **87**, 35–45.

Katayama, T. 2005 *Subspace Methods for System Identification*. Springer Verlag.

Kim, J. & Bewley, T.R. 2007 A linear systems approach to flow control. *Ann. Rev. Fluid Mech.* **39**, 383–417.

Larimore, W.E. 1983 System identification, reduced order filtering and modeling via canonical variate analysis. *Proc. Conf. Dec. Control* .

Larimore, W.E. 1990 Canonical variate analysis in identification, filtering and adaptive control. *Proc.* 29^{th} *Conf. Dec. Control, Honolulu, Hawaii* .

Ljung, L. 1987 *System Identification: Theory for the User*. Prentice-Hall, Inc.

van Overschee, P. & de Moor, B. 1994 N4SID: subspace algorithms for the identification of combined deterministic-stochastic systems. *Automatica* **30**, 75–93.

van Overschee, P. & de Moor, B. 1996 *Subspace Identification for Linear Systems*. Kluwer Academic Publishers.

Qin, S.J. & Badgwell, T.A. 2003 A survey of industrial model predictive control technology. *Control Eng. Pract.* **11**, 733–764.

Richalet, J., Rault, A., Testud, J.L. & Papon, J. 1978 Model predictive heuristic control: applications to industrial processes. *Automatica* **14**, 413–428.

Roussopoulos, K. & Monkewitz, P. A. 1996 Nonlinear modelling of vortex shedding control in cylinder wakes. *Physica D* **97**, 264–273.

Verhaegen, M. & Deprettere, E. 1991 A fast, recursive MIMO state space model identification algorithm. *Proc.* 30^{th} *IEEE Conf. Dec. Control* pp. 1349–1354.

Williams, D.R. & Rowley, C.W. 2006 Recent progress in closed-loop control of cavity tones. *AIAA Paper* **712**, 2006.

Zheng, T. 2010 *Model Predictive Control*. Sciyo Publishing.

2.3 Article 2: Uncertainty propagation in the design process of data-based flow controllers

Under consideration for publication in J. Fluid Mech. 1

Uncertainty propagation in model extraction by system identification and its implication on control design

NICOLAS DOVETTA[1]†,
PETER J. SCHMID[2] AND DENIS SIPP[3]

[1]Laboratoire d'Hydrodynamique (LadHyX), Ecole Polytechnique, 91128 Palaiseau, France
[2]Dept. of Mathematics, Imperial College London, London SW7 2AZ, United Kingdom
[3]ONERA DAFE, 8rue des Vertugadins, 92190 Meudon, France

(Received ?; revised ?; accepted ?. - To be entered by editorial office)

In data-based control design, system-identification techniques are used to extract low-dimensional representations of the input-output map between actuators and sensors from observed data-signals. Under realistic conditions, noise in the signals is present and is expected to influence the identified system representation. For the subsequent design of the controller, it is important to gauge the sensitivity of the system representation to noise in the observed data; this information will impact the robustness of the controller and influence the stability margins for a closed-loop configuration. Commonly, Monte-Carlo analysis has been used to quantify the effect of data-noise on the system identification and control design, but in fluid systems, this approach is often prohibitively expensive, both for numerical simulations and physical experiments. Instead, we present a framework for the estimation of statistical properties of identified system representations given an uncertainty in the processed data. The ARMarkov/LS identification procedure has been chosen to illustrate this framework and to obtain error bounds on the identified system parameters based on the signal-to-noise ratio of the input-output data sequence. Multiple simulations (as in Monte-Carlo techniques) are not necessary, which makes the proposed technique affordable and efficient even for large-scale flow control problems. The procedure is illustrated on the control design for flow over an idealized airfoil with a trailing-edge splitter plate.

Key words: uncertainty, ARMarkov model, system identification, flow control, sensitivity analysis

1. Introduction

Flow control is an attractive and promising technology as it aims at altering and improving inherent flow behavior by externally applied forces. Reducing drag, suppressing instabilities, extending parameter envelopes or enhancing mixing are only a few objectives that could be accomplished by flow control strategies. Despite its potential for technological advances, the design of flow control schemes still poses significant challenges, principally among them the modelling of the flow behavior and the accurate description of the disturbance environment.

† Email address for correspondence: nicolas.dovetta@ladhyx.polytechnique.fr

Model-based approaches, based on a prescribed set of equations and an *a priori* assumption on the characteristics of the noise environment, have been successfully applied to numerical simulations and have demonstrated their effectiveness within the range of design assumptions. For applications in experiments, in the absence of sufficient information on the disturbance environment, a different approach may be more appropriate that does not impose a preconceived model but rather extracts information for the control design, such as transfer functions, directly from measured (noise-contaminated) data. Techniques in this category rely on system identification methods to obtain representations of the flow's input-output behavior; they fall into two major families: subspace identification and Markov-parameter/realization techniques. Whereas the former exploits the low-rank nature of the control signal space to arrive at approximate system matrices via oblique projections (see, e.g., Katayama 2005), the latter first determines the discrete impulse responses (Markov parameters) of the flow which are then, in a second step, used to derive a state-space model.

System identification has been an active field of research for many decades and has matured into a well-established discipline of system theory. Even though many techniques and algorithms are available, the use of system-identification techniques in the design of flow control strategies is rather recent (see Kim 2003; Hervé *et al.* 2012; Juillet *et al.* 2013). For the identification of a reduced-order model that will form the basis of our control design, a two-step process, referred to as the separation principle, is often advocated (see, e.g., Hjalmarsson 2005). It consists of a high-order identification of a preliminary model that best fits the available data, which is subsequently transformed into a low-order representation by model-reduction techniques. The two-step approach ensures favorable statistical properties, since the asymptotic efficiency of the high-order system can be shown to be inherited by the low-order system; furthermore, the thus reduced low-order system is optimal within the constraints given by the high-order system.

Following this separation principle, we choose a Markov parameter/realization technique in this study. In particular, we use a ARMarkov/LS technique to convert measured data-sequences into discrete impulse responses (Markov parameters) by assuming an underlying auto-regressive model that explicitly contains the Markov parameters; the parameters of the auto-regressive model are determined by a least-squares (LS) matching to the measured data. The Markov parameters are then used in the Eigensystem Realization Algorithm (ERA) to arrive at a state-space representation of the model, which in turn can be used to design a control law by standard techniques. The ARMarkov/LS procedure has originally been proposed by Akers & Bernstein (1997), and many subsequent studies (see Van Pelt & Bernstein 1998; Kamrunnahar *et al.* 2000; Fledderjohn *et al.* 2010) have confirmed it as a very efficient technique to obtain the Markov parameters of a system. The ERA state-space realization step has been developed by Juang & Pappa (1985), has been studied extensively (see Lew *et al.* 1993) and has recently been applied to flow control problems in the form of an adjoint-free model reduction procedure (see Ma *et al.* 2011).

One of the advantages and appeal of data-based control design using system identification techniques are its applicability to realistic flow situations, where the only information about the system to be controlled consists of (low-dimensional) measurements. This advantage is, however, off-set by the uncertainty these signals introduce into the design process, since the processed data will surely be contaminated by background and measurement noise and ultimately affect the control performance. In particular, for a practical control design, it is important to quantify the noise in the data and how it propagates through the procedural steps of the system identification and control design to ultimately influence the control performance and its internal stability margins. A sen-

sitivity analysis of this type is the focus of this article. Due to the separation principle, we can break apart the error in the identification step into a variance estimation of the identified model and a bias estimation of the reduced-order model. This distinction is valid as long as the model reduction step is robust, i.e., shows a negligible sensitivity of the model parameters to noise in the underlying data.

Computing estimates of the variance and bias error with respect to variations in the model parameters for an identification-realization algorithm has been the topic of previous articles in the identification/realization literature. For example, the model-order criteria of Akaike (1974) and Rissanen (1983) apply penalization techniques to a repeatability estimate to arrive at an objective model order (see Ljung 1987). In the study of Longman *et al.* (1991), the model parameters for the ERA-step have been chosen based on statistical information of the identified variables. Besides its obvious benefits for control and stability calculations, the quantification of the variance and bias of the identification-realization parameters can also be used as a model structure falsification criterion (see Hjalmarsson 2005).

This paper is concerned with the propagation of uncertainties and stochastic fluctuations in the processed data through a multi-step procedure based on system identification, state-space realization and optimal control design. In particular, we wish to quantify how small perturbations in the data will ultimately affect closed-loop control performance and degrade internal stability margins. We start in section § 2 by presenting the ARMarkov/LS/ERA identification-realization algorithm for a single-input single-output (SISO) system. Section § 3 will then concentrate on a perturbation technique to derive estimates of the error between the real and identified model; this section naturally divides into two parts: quantifying the ARMarkov/LS-identification error and deriving an ERA error estimate. A validation of these error estimates is presented in section § 4, where we consider a one-dimensional (thus computationally tractable) model problem that mimics noise-amplifier flows. Numerical simulations of flow over a backward-facing step will be used to illustrate the introduced techniques on a more realistic flow configuration and to demonstrate the utility of sensitivity measures in the analysis of closed-loop control problems based on system identification and realization. Conclusions are presented in § 5.

2. From data-sequences to control performance

We start by developing the essential steps in the design of a efficient and robust control strategy, starting from input-output data sequences. These steps will consist of (i) a system identification process, which matches the coefficients of a given model structure using observed input-output signals, (ii) a design of a feedback or feed-forward controller, and (iii) the assessment of gain and phase margins of the compensated system.

2.1. *General framework for linear time-invariant systems (LTI)*

We choose a discrete-time state-space representation to describe the flow-control setup for a linear time-invariant (LTI) system and consider a single input and single output (i.e., a SISO-system). We have

$$\mathbf{x}(k+1) = \mathsf{A}\mathbf{x}(k) + \mathsf{B}u(k) + \mathsf{E}_x w_x(k), \tag{2.1a}$$

$$y(k) = \mathsf{C}\mathbf{x}(k) + \mathsf{D}u(k) + \mathsf{E}_y w_y(k), \tag{2.1b}$$

where k denotes the discrete time index, $\mathbf{x}(k)$ represents the state vector, $u(k)$ is the control, $y(k)$ stands for the measurement, and $w_x(k)$ and $w_y(k)$ are the state noise and

measurement uncertainties, respectively. The system matrix is given by A, the actuation is modeled by B, and the sensors by C. The spatial distribution of the noise is contained in the matrices E_x and E_y, for the state vector and measurements, respectively. Finally, D describes the instantaneous effect of the actuation on the measurement. For a system of order n, the system matrix A is $n \times n$, the actuation matrix B is $n \times 1$, the sensor matrix C is $1 \times n$, and D is a scalar. Finally, $\mathsf{E}_x, \mathsf{E}_y$, w_x and w_y are matrices and vectors of dimensions that correspond to the order of the noise.

The impulse response of the above system (2.1), in the case of vanishing noise matrices, can be defined as a sequence of scalars. This sequence is also referred to as the Markov parameters H_j. From the state-space representation (2.1) an explicit form of the Markov parameters can be derived according to

$$\mathsf{H}_0 = \mathsf{D}, \tag{2.2a}$$

$$\mathsf{H}_j = \mathsf{C}\mathsf{A}^{j-1}\mathsf{B}, \qquad j \geqslant 1. \tag{2.2b}$$

Based on these Markov parameters, we can formulate regressive or auto-regressive representations of the system's input-output behavior that do not involve the state-vector $\mathbf{x}(k)$. Rather, the output at k can be determined solely as functions of past inputs and outputs. The definition (2.2) of the Markov parameters H_j then allows us to formulate a regressive representation of general LTI-systems as a discrete transfer function from the input u to the output y. We obtain

$$y(k) = \sum_{j=0}^{\infty} \mathsf{H}_j u(k-j). \tag{2.3}$$

An approximation of this model, assuming that after a certain time the effects of the actuations are negligible, is the well-known Finite Impulse Response (FIR) model of order μ. We have

$$y(k) = \sum_{j=0}^{\mu-1} \mathsf{H}_j u(k-j). \tag{2.4}$$

A more sophisticated representation is applying an auto-regressive term to the signal y which yields the well-known ARMA (auto-regressive-moving-average) model

$$y(k) = \sum_{j=1}^{n} -\mathsf{N}_j y(k-j) + \sum_{j=0}^{n} \mathsf{M}_j u(k-j) \tag{2.5}$$

where M_j and N_j are coefficients to be determined. Akers & Bernstein (1997) showed that the Markov parameters can be extracted from the ARMA representation via the following recursive algorithm. Using (2.5) and the definition of the measurement y we obtain, after repeated substitution, the following auto-regressive representation that explicitly isolates μ Markov parameters (referred to as μ-ARMarkov):

$$y(k) = \sum_{j=1}^{n} -\mathsf{N}_j y(k-\mu-j+1) + \sum_{j=1}^{\mu} \mathsf{H}_{j-1} u(k-j+1) + \sum_{j=1}^{n} \mathsf{Q}_j u(k-\mu-j+1). \tag{2.6}$$

To proceed, the μ-ARMarkov model may be written as a linear relation between $y(k)$, a vector $\phi(k)$ and the model parameters, grouped into the vector W, according to

$$y(k) = \phi(k)\mathsf{W}, \tag{2.7}$$

where $\phi(k)$ and W are given as

$$\phi(k) = [y(k-\mu), \ldots, y(k-\mu-n+1), u(k), \ldots, u(k-\mu-n+1)]\,, \tag{2.8}$$

and

$$\mathsf{W}^T = [-\mathsf{N}_1\ ,\ \ldots\ ,\ -\mathsf{N}_n\ ,\ \mathsf{H}_0\ ,\ \ldots\ ,\ \mathsf{H}_{\mu-1}\ ,\ \mathsf{Q}_0\ ,\ \ldots\ ,\ \mathsf{Q}_n]\,. \tag{2.9}$$

Equation (2.7) is a compact form of the auto-regressive representation of equation (2.6) where $\phi(k)$ contains the input-output sequence just before the k^{th} time index and W contains the ARMarkov parameters. The transfer functions based on the z-transform of the above models (FIR, ARMA and μ-ARMarkov) are given in the appendix for completeness. The following section presents the algorithm proposed by Akers & Bernstein (1997) to identify the μ-ARMarkov parameters (in W) from input-output data sequences. Once the Markov parameters are identified (as a part of the vector W), the system behavior is predicted using the FIR model (2.4). The other coefficients (*i.e.* N_i and Q_i) — even though ultimately not used — are to account for noise in the data-set and thus yield more accurate Markov parameters (see Hjalmarsson 2005; Kamrunnahar *et al.* 2000).

2.2. *From data to an identified system: ARMarkov/Least Squares*

This section shows how the coefficients of the ARMarkov model are obtained from data-sequences via a least-squares minimization. Many alternative techniques exist to identify model coefficients, in particular, for the ARMarkov representation. While details are kept to a minimum in what follows, the interested reader is referred to Ljung (1987); Hjalmarsson (2005) for more information about the mathematical and algorithmic principles underlying system identification.

2.2.1. *The Least-Squares (LS) algorithm*

Given an input-output data-set, a system identification procedure is concerned with finding a model that can reproduce the output (y) sequence using the input (u) sequence. Formally, $y(k)$ is the array of measured outputs at time k, W denotes a set of parameters that describe the model, and $\widehat{y}(k|\mathsf{W})$ stands for the output computed using the input sequence and the model parameterized by W. The goal is to find W such that the sequence $\widehat{y}(k|\mathsf{W})$ best matches $y(k)$. Thus, the ARMarkov/LS-identification consists of minimizing J given by

$$J(\mathsf{W}) = \frac{1}{N}\sum_{k=1}^{N}(y(k) - \widehat{y}(k|\mathsf{W}))^2, \tag{2.10}$$

with N as the number of data points. For ARMarkov, the relationship between $\widehat{y}(k|\mathsf{W})$ and W is explicit and given by (2.7). Substituting into (2.10) yields

$$J(\mathsf{W}) = \|\mathsf{Y} - \mathsf{\Phi W}\|_2^2 \tag{2.11}$$

with

$$\mathsf{Y} = \begin{pmatrix} y(1) \\ y(2) \\ \vdots \\ y(N) \end{pmatrix} \qquad \text{and} \qquad \mathsf{\Phi}^T = \begin{pmatrix} \phi(1) \\ \phi(2) \\ \vdots \\ \phi(N) \end{pmatrix}. \tag{2.12}$$

The minimization of $J(\mathsf{W})$ may be solved using the pseudo-inverse to obtain

$$\mathsf{W} = \mathsf{\Phi}^{\dagger}\mathsf{Y}. \tag{2.13}$$

The coefficient vector W contains the Markov parameters H_j. The pseudo-inverse is often computed using Moore's definition

$$\mathbf{\Phi}^{\dagger} \equiv \lim_{\epsilon \to 0} (\mathbf{\Phi}^T \mathbf{\Phi} + \epsilon \mathsf{I})^{-1} \mathbf{\Phi}^T \tag{2.14}$$

which minimizes a regularized cost functional $\widetilde{J}(\mathsf{W})$ of the form

$$\widetilde{J}(\mathsf{W}) = \lim_{\epsilon \to 0} \|\mathsf{Y} - \mathsf{W}\mathbf{\Phi}\|_2^2 + \epsilon \|\mathsf{W}\|_2^2 \tag{2.15}$$

The parameter ϵ can be set to machine precision, but it can also be used to enforce regularization of an otherwise ill-posed problem, as $\mathbf{\Phi}$ is often rank-deficient. $\mathbf{\Phi}$ contains the input-output data-sequence: when the input does not consist of a broad-band signal, the resulting least-squares problem becomes ill-posed. In this case, the use of Moore's pseudo-inverse definition allows us to implement a Tikhonov regularization of the problem ($\epsilon \neq 0$, Fleming (2011)). This way, the norm of W remains bounded which, in turn, avoids numerical problems when using the identified model. In the different test cases presented in this paper, regularization is always applied with ϵ ranging from 10^{-5} to 10^{-16} (machine precision). The choice of ϵ is depends on the application and the ill-posedness of the data-sequence ($\mathbf{\Phi}$).

In order to have W represent the system's dynamics rather than measurement noise, the minimization problem should be strongly under-parametrized, i.e., $2n + \mu \ll N$. In the limiting case of $2n + \mu = N$, the input-output data sequence (u, y) will be exactly matched by the reconstructed data $(u, \widehat{y})$. In this case, the model parameters in W are strongly noise-dependent and will unlikely be consistent with another set of data. In our examples, the parameters are chosen such that $2n + \mu < N/5$; this choice is related to the AIC criterion defined below (see equation (2.16)). Even so, the model parameters in W are still dependent on noise, where the majority of this dependence is contained in the auto-regressive part of W. For this reason, only the Markov parameters are kept (see Hjalmarsson 2005; Kamrunnahar *et al.* 2000), to minimize the noise dependence. The ARMarkov/LS procedure identifies all coefficients of the ARMarkov representation, but only a finite impulse response (FIR, i.e., the set of Markov parameters) transfer function is kept. Still, with all these precautions to identify a model that faithfully represents the system dynamics, the Markov parameters are influenced by noise, especially in realistic data-set where the noise-to-signal ratio may be rather high. The uncertainty propagation analysis aims at quantitatively estimating this dependence in order to improve the prediction of a controller's performance.

2.2.2. *Choice of data sequence*

As we saw, the choice of the spectral content of the inputs has a significant impact on the statistical property of the identified model, as it is related to the well-posedness of the minimization problem. For the examples given in this article the input will be chosen as a Pseudo-Random Binary Signal (PRBS): it is broad-band, widely used and actuator-friendly. For details on the choice and implications of the input signals, the reader is referred to the studies of Gerencser *et al.* (2009); Brighenti *et al.* (2009); Mehra (1974).

2.2.3. *Model order and its link to model estimation error*

The order of the model constitutes a crucial choice that has to be made in the identification process. For an ARMarkov model the order is $2n + \mu$, while for a FIR model the order is simply μ. As shown previously, the model order is constrained, on one hand, by the length of the data sequence $2n + \mu \ll N$. On the other hand, we have that $2n + \mu$

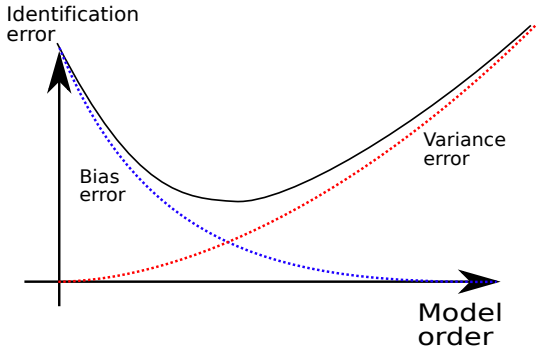

FIGURE 1. Sketch of the variance and bias error contribution to the total estimation error, as a function of the model order.

(and in particular μ since only a FIR is kept from the identification) has to be large with respect to the order of the model that describes the dynamics between the input and the output. A model order has to be chosen to balance these two criteria. Figure 1 graphically illustrates this balance that has to be struck. The bias error is related to an under-modelling of the dynamics, while the variance error is caused by a data-sequence which is too small compared to the model order. An *adequate* model order can be found by various means. The very common Akaike criterion is chosen for our work (see Akaike 1974). For model orders higher than Akaike's criterion, see 2.16, the model error is assumed to be mostly due to variance error; for model orders below Akaike's value, the model error is mostly due to bias error. In our case, the Akaike criterion reads

$$\mathsf{AIC} = \log(J(\mathsf{W})) + \frac{2}{N}\mathrm{card}(\mathsf{W}). \tag{2.16}$$

This value can be computed *a posteriori*, once a model has been determined. The optimal model according to Akaike has a minimal AIC-value. The criterion contains two terms. The first term $\log(J(\mathsf{W}))$ characterizes the residual minimization error, which is meant to represent the bias error of the identified model. Indeed, if the model order is sufficiently high, the problem becomes over-parameterized and $J(\mathsf{W})$ consequently tends to zero. However, if the model order is rather low, the problem is over-constrained and $J(\mathsf{W})$ may not vanish. The second term in (2.16) denotes an index that is correlated to the variance error. It increases linearly with the number of parameters in the model and penalizes over-parameterization. For our ARMarkov-model, the cardinality card(W) is the number of parameters $2n + \mu$. The model order that minimizes AIC is taken as the optimal order for the identification procedure.

The uncertainty propagation developed later allows us to estimate the variance error; the bias error, however, is far harder to estimate, particularly, when the noise-to-signal ratio is high. In order to take advantage of the variance error estimation, it is essential to choose a model order that is sufficiently high. What constitutes a sufficiently high model order is difficult to define theoretically based on only the data sequence. For the remainder of the article, we base the model order on the minimal value of AIC given in (2.16).

2.3. *From identified system to controller design*

Once a model of appropriate order has been identified, a control strategy can be defined. Among the various choices to manipulate the flow, we will concentrate on two of the most common approaches: simple feedback control and simple feed-forward control. Both strategies are outlined in figure 2 in the form of a block diagram; they cover the most

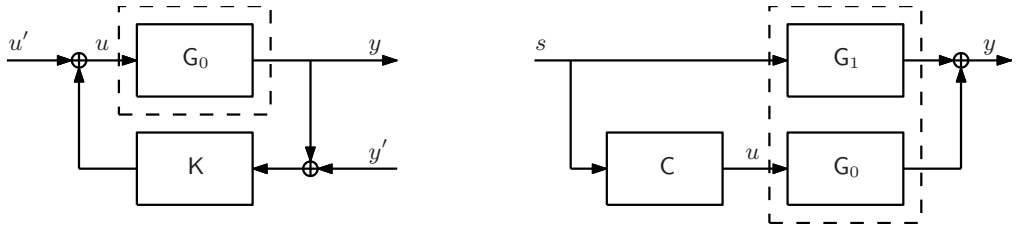

FIGURE 2. Feed-back (left) and feed-forward (right) control layout. G_i are transfer functions inherent to the system, K and C are the transfer functions of the respective controllers. The respective physical systems are enclosed by dashed lines.

widely studied structures to control oscillatory and convectively dominated fluid flows. In these configurations, y represents the signal from the objective sensor which enters a user-specified objective function, and u is the control variable, i.e., the signal passed to the actuator. In the feed-forward configuration, an additional sensor is present, which provides information about incoming disturbances and acts as a proxy for the (upstream) disturbance environment. In either configuration, G_i stands for a transfer function describing the fluid behavior between input and output signals; the transfer functions of the respective controllers are denoted by K and C, respectively. For the feedback setup, we also account for environmental noise sources, indicated by uc and y', which will influence the stability of the controller. Before describing performance and stability criteria, we briefly outline common design algorithms for the two control configurations.

2.3.1. *Feedback controllers*

One of the most commonly applied strategy for feedback control is the infinite-time-horizon LQG/LQR control. After the identified system has been converted to a state-space representation, for example, by using the Eigenvalue Realization Algorithm (ERA; Juang & Pappa 1985), a Kalman filter (for the optimal state-estimation from measurements) and a proportional controller (which minimizes the control objective) can be designed. A large body of literature gives details of this design process; a data-based feedback approach applied to a fluid system can be found, e.g., in Illingworth *et al.* (2011).

Regardless of the details of the designed controller, transfer functions of the feedback-controlled system can be expressed explicitly. They will be referred to as the closed-loop transfer function (CLTF) throughout this paper. The CLTF describing the influence of the noise signal uc on the output y reads

$$\mathsf{T}_{CL} = \frac{\mathsf{G}_0}{1 + \mathsf{G}_0\mathsf{K}}, \tag{2.17}$$

while the closed-loop transfer function linking the noise signal y' to the same output is given by

$$\mathsf{T}'_{CL} = \frac{\mathsf{K}\mathsf{G}_0}{1 + \mathsf{G}_0\mathsf{K}}. \tag{2.18}$$

2.3.2. *Feed-forward controllers*

This type of control is commonly applied to flows with a strongly convective behavior, where disturbances originating upstream are to be compensated. In this setup, an upstream sensor detects the incoming disturbances, after which an actuator counteracts

them to create a nearly disturbance-free environment farther downstream (at the location of the objective sensor). General algorithms to design such controllers fall within the category of Model Predictive Controllers (MPC). Following the diagram in figure 2(b), the mapping between the measured incoming perturbations s and the output (objective) sensor y is given by the transfer function G_1. An equivalent link between the actuator signal u and the same output sensor y can be established and described by the tranfer function G_0. The goal of the control design is then to construct a controller transfer function C such that the signal passing through C and G_0 destructively interferes with the signal passing though G_1. It is straightforward to show that $\mathsf{C} = -\mathsf{G}_0^{-1}\mathsf{G}_1$ provides a control law that accomplishes this task. As before, the transfer function of a system controlled by a feed-forward controller (from the upstream to the downstream sensor) can be stated explicitly. We will refer to it as the controlled-system transfer function (CSTF), given by

$$\mathsf{T}_{CS} = \mathsf{G}_1 + \mathsf{C}\mathsf{G}_0. \tag{2.19}$$

2.4. *From controller design to performance and stability: Nyquist and Bode plot analysis*

The two transfer functions can be used to determine performance and stability measures. However, one has to keep in mind that the true transfer functions are not known; only their identified variants are available. To formally differentiate the exact and identified transfer functions, we introduce G_i for the exact (but experimentally inaccessible) transfer function and $\widehat{\mathsf{G}}_i$ for the nominal (identified) transfer function. Differences between these two tranfer functions can be traced back to uncertainties or noise in the processed data.

For performance and stability studies, a simple substitution of G_i by $\widehat{\mathsf{G}}_i$ in (2.17) and (2.19) and a small-difference expansion can be applied for a first estimate of the influences of data corruption. In some high noise-to-signal cases, however, a different approach, involving a better approximation of the identification error, is called for. In the following section, we give a brief summary of stability criteria for feedback (the Nyquist criterion) and feed-forward controller. Only stability issues will be dealt with in this article; uncertainty propagation, as introduced here, however is not limited to this output criterion.

2.4.1. *The Nyquist stability criterion for feed-back controllers*

Considering the expression for the $CLTF$ and $CLTF'$ in (2.17) and (2.18), the closed-loop transfer functions are singular when $\mathsf{G}_0\mathsf{K} = -1$. This singularity is linked to the instability of the controlled system. The Nyquist plot is a representation of the open-loop transfer function (OLTF) as a parameterized curve (by frequency) in the complex plane. The phase and gain margins defined by the Nyquist plot are measures that quantify the distance of the open-loop transfer function $\mathsf{G}_0\mathsf{K}$ to the point -1 in the complex plane. The phase margin is the maximally admissible phase variation of the system before stability is lost; the gain margin is the maximally admissible gain variation for the system to lose stability. The Nyquist curve can be recovered from the discrete-time transfer function (a function of z) by a transformation to a continuous-time transfer function (a function of the frequency ω) via $z = e^{i\omega T_e}$, where T_e stands for the sampling time step of the data sequence.

Figure 3 shows an example of a Nyquist plot. In this figure gives a graphical definition of the phase and gain margins, as well as a potential reduction in the margins due to general uncertainties. For small noise-to-signal ratio the phase and gain margins can be satisfactorily estimated from the nominal system. As soon as uncertainties become more prevalent, the stability margins computed from the nominal system increasingly differ

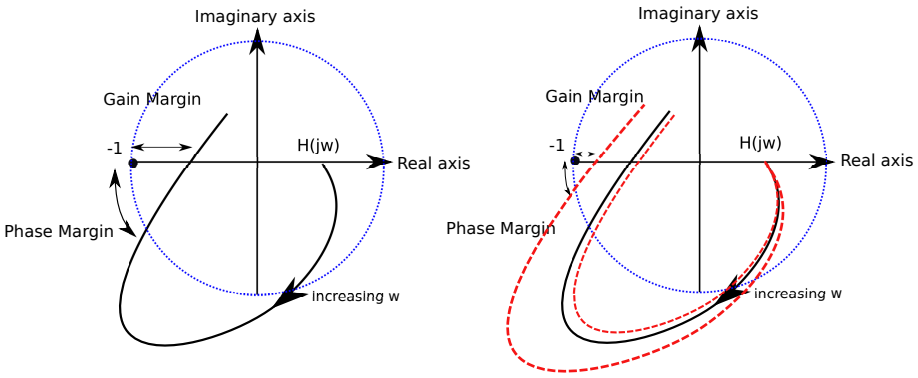

FIGURE 3. Nyquist plot of the $OLTF$, showing phase and gain margins, based on the nominal system (left) and the nominal system with uncertainty bounds (right).

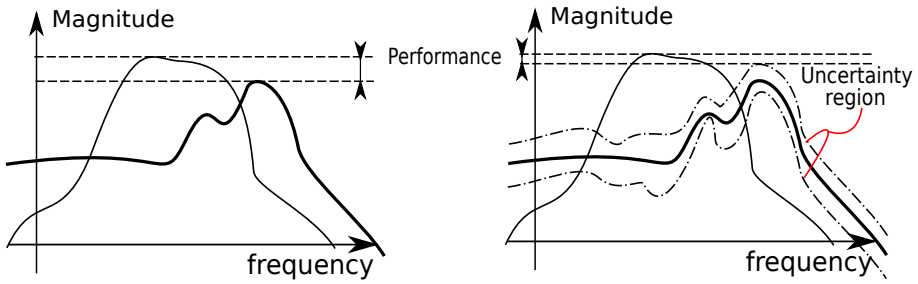

FIGURE 4. Bode diagram of the uncontrolled (thin black) and controlled (thick black) transfer function, showing H_∞-based performance of nominal system (left) and the nominal system with uncertainty bounds (right).

from the realized margins. In this latter case, uncertainty has to be directly taken into account to properly correct the margins.

2.4.2. *Performance analysis for feed-forward disturbance rejection controllers*

For feed-forward control configurations and strictly convective systems (*i.e.*, with no feedback from the downstream input u to the upstream sensor s), the controller cannot be unstable. In this case, performance is of principal concern and constitutes the criterion for our analysis of uncertainty propagation. Performance will be defined using the maximum value of the $CSTF$ (i.e., its H_∞ norm). A controller is deemed effective if the maximum value of the transfer function without control is larger than the maximum value of the $CSTF$. Figure 4 provides a sketch of this criterion. In this figure, the uncontrolled and the controlled transfer function of the system are plotted, and the performance measure of the controller is evaluated. Similar to the feedback configuration, uncertainty bounds about the nominal transfer function may yield a pronounced reduction of this nominal performance.

3. Uncertainty propagation for the ARMarkov/LS-identification process

We proceed by developing procedures to estimate uncertainty bounds in the identified system stemming from uncertainty in the processed data. In our case, we assume that the standard deviation of the data is known. First, the uncertainty propagation is demon-

strated for the ARMarkov/LS identification algorithm, where the impact on the model parameters (Markov parameters and auto-regressive parameters) is quantified. This is followed by establishing a link between the uncertainty in the Markov parameter and the resulting uncertainty bounds in the Bode and Nyquist diagrams. Monte-Carlo variance estimation is then used, on a simple test case, to validate the uncertainty propagation results by alternative means.

$$\mathsf{T}'_{CL} = \frac{\mathsf{K}\mathsf{G}_0}{1 + \mathsf{G}_0\mathsf{K}}. \tag{3.1}$$

3.1. *Variance error: linear perturbation analysis of the least-squares algorithm*

Contrary to Monte-Carlo techniques, we seek an explicit expression linking statistical information (such as the standard deviation) of the input data to an equivalent statistical measure of the Markov parameters. The uncertainty in the data is assumed to be additive; multiplicative uncertainty propagation analyses can be found in Skogestad & Postlethwaite (2001), but will not be considered here. In addition, we restrict ourselves to sufficiently small measurement uncertainty in order to justify a first-order perturbation approach. The original data sequence, described by the vector Y, is perturbed as follows

$$\widetilde{\mathsf{Y}} = \mathsf{Y} + \delta\mathsf{Y}. \tag{3.2}$$

The influence of the perturbation $\delta\mathsf{Y}$ on the identified parameters (contained in W) can be quantified using (2.13). We note that, since $\mathsf{\Phi}$ contains past measurements, the size N of the total data sequence differs from the number of equation $N - n + 1$. For this reason, two notations must be put forth: the vector of output data Y of size N, and the solution Y_t of the least-squares problem of size $N - n + 1$

$$(\mathsf{W} + \delta\mathsf{W}) = (\mathsf{\Phi} + \delta\mathsf{\Phi})^{\dagger} \,.\, (\mathsf{Y}_t + \delta\mathsf{Y}_t)\,. \tag{3.3}$$

The resulting perturbations $\delta\mathsf{W}$ of the model parameters W is sought as a function of the perturbation $\delta\mathsf{Y}$ in the data Y. Under the previously mentioned assumption of small perturbations $\delta\mathsf{Y}$, we linearize the above expression and derive a first-order perturbation solution for $\delta\mathsf{W}$. This step is equivalent to linearizing the pseudo-inverse term $(\mathsf{\Phi} + \delta\mathsf{\Phi})^{\dagger}$, a complex problem that has been the object of many past studies (see Wedin 1973; Stewart 1977, 1990). Before proceeding, we have to state the following underlying hypothesis and assumption: $\mathrm{rank}(\mathsf{\Phi}) = \mathrm{rank}(\widetilde{\mathsf{\Phi}})$ which states that the rank of $\mathsf{\Phi}$ is not affected by the additive perturbation $\delta\mathsf{\Phi}$. This statement is true for sufficiently small $\delta\mathsf{Y}$; in fact, the rank preservation defines the size of the admissible perturbations $\delta\mathsf{Y}$.

Under this assumption, we can give an explicit expression for the model parameter perturbations $\delta\mathsf{W}$ (see Stewart 1977)

$$\delta\mathsf{W} \approx \mathsf{\Phi}^{\dagger}\delta\mathsf{Y}_t + \left(-\mathsf{\Phi}^{\dagger}\mathsf{P}_{\mathsf{\Phi}}\delta\mathsf{\Phi}\mathsf{R}_{\mathsf{\Phi}}\mathsf{\Phi}^{\dagger} + (\mathsf{\Phi}^T\mathsf{\Phi})^{\dagger}\mathsf{R}_{\mathsf{\Phi}}\delta\mathsf{\Phi}^T\mathsf{P}^{\perp}_{\mathsf{\Phi}} - \mathsf{R}^{\perp}_{\mathsf{\Phi}}\delta\mathsf{\Phi}^T\mathsf{P}_{\mathsf{\Phi}}(\mathsf{\Phi}\mathsf{\Phi}^T)^{\dagger}\right)\mathsf{Y}_t, \tag{3.4}$$

where

$$\mathsf{P}_{\mathsf{\Phi}} \equiv \mathsf{\Phi}\mathsf{\Phi}^{\dagger}, \qquad \mathsf{R}_{\mathsf{\Phi}} \equiv \mathsf{\Phi}^{\dagger}\mathsf{\Phi}, \tag{3.5a}$$

$$\mathsf{P}^{\perp}_{\mathsf{\Phi}} \equiv \mathsf{I} - \mathsf{P}_{\mathsf{\Phi}}, \qquad \mathsf{R}^{\perp}_{\mathsf{\Phi}} \equiv \mathsf{I} - \mathsf{R}_{\mathsf{\Phi}}. \tag{3.5b}$$

The matrix $\delta\mathsf{\Phi}$ contains perturbations of the data-sequence. By definition, it can be directly expressed in terms of $\delta y(k)$ for $k \in [1,\ N]$ according to

$$\delta\Phi = \begin{pmatrix} \delta y(n) & \delta y(n-1) & \dots & \delta y(1) & 0 & \dots & 0 \\ \delta y(n+1) & \delta y(n) & \dots & \delta y(2) & 0 & \dots & 0 \\ \vdots & \vdots & & \vdots & \vdots & \ddots & \vdots \\ \delta y(N) & \delta y(N-1) & \dots & \delta y(N-n+1) & 0 & \dots & 0 \end{pmatrix} \Phi \tag{3.6}$$

or, in a more compact form,

$$\delta\Phi = \sum_{k=1}^{N} \mathsf{E}(k)\delta y(k) \tag{3.7}$$

where we have introduced the operator $\mathsf{E}(k)_{i,j}$ as

$$\mathsf{E}(k)_{i,j} = \begin{cases} 1 & \text{if } i-j+n=k \text{ and } j<n, \\ 0 & \text{elsewhere.} \end{cases} \tag{3.8}$$

With this definition, we can reformulate the above relation between the data perturbations and the model parameter perturbations and state it in the form

$$\delta\mathsf{W} \approx \Phi^{\dagger}\delta\mathsf{Y}_t + \sum_{k=1}^{N} \left(-\Phi^{\dagger}\mathsf{P}_{\Phi}\mathsf{E}(k)\mathsf{R}_{\Phi}\Phi^{\dagger} + (\Phi^T\Phi)^{\dagger}\mathsf{R}_{\Phi}\mathsf{E}(k)^T\mathsf{P}_{\Phi}^{\perp} - \mathsf{R}_{\Phi}^{\perp}\mathsf{E}(k)^T\mathsf{P}_{\Phi}(\Phi\Phi^T)^{\dagger}\right)\mathsf{Y}_t\delta y(k). \tag{3.9}$$

Finally, this expression is equivalent to

$$\delta\mathsf{W} = \mathcal{L}\ \delta\mathsf{Y} \tag{3.10}$$

where $\mathcal{L}$ can be interpreted as the Jacobian of W with respect to Y. Consequently, the gradient of each component of W with respect to a specific perturbation in the processed data can be extracted from $\mathcal{L}$. We recall that only the Markov parameters H_i are relevant for the representation of the system-identified model. With the definition of W, the propagation of data-uncertainties into each Markov parameter can be found from (3.10). If we introduce the notation $\mathcal{L}_i$ as the i^{th} row of the Jacobian $\mathcal{L}$, we obtain

$$\delta\mathsf{H}_i = \mathcal{L}_{i+n}\ \delta\mathsf{Y}, \qquad i = 0, \dots, \mu-1. \tag{3.11}$$

With the above link between the data perturbations and Markov parameter perturbations, we can now establish a mapping between statistical properties of the two perturbations. To this end, let $\sigma_{\delta y}$ and $\sigma_{\delta\mathsf{H}_i}$ denote, respectively, the standard deviation of the measurement noise and of the i^{th} Markov parameter. Further introducing the noise standard deviation $\delta\mathsf{Y}^T\delta\mathsf{Y} = N\sigma_{\delta y}^2$, we can state

$$\sigma_{\mathsf{H}_i} = \sigma_{\delta y}\sqrt{\mathcal{L}_{i+n}\mathcal{L}_{i+n}^T}. \tag{3.12}$$

This final expression (3.12) describes the first-order uncertainty mapping (in terms of the standard deviation) from the output data sequence to the identified Markov parameters; given the noise standard deviation, it is now possible to determine uncertainty bounds for each Markov parameter. These bounds are associated with statistical probabilities: if the measurement noise is Gaussian, the i^{th} Markov parameter falls within the range $\mathsf{H}_i \pm \sigma_{\mathsf{H}_i}$ with a 68.2% probability or is contained within $\mathsf{H}_i \pm 2\sigma_{\mathsf{H}_i}$ with a 95% probability. However, evaluating the 95% probability range of a specific Markov parameter is not an effective way of probing the potential impact of data uncertainty on the controlled-system behavior. Rather, a direct influence on stability or performance criteria is sought. As stated in section § 2.4, we will limit our stability and performance assessment to criteria that can be straightforwardly extracted from Nyquist or Bode plots.

Two approaches to extend the uncertainty analysis to apply to stability and performance measures come to mind. First, the numerical procedures to compute the criteria and corresponding margins can be linearized about a nominal set of Markov parameters, after which the Jacobian of these criteria/margins with respect to data uncertainty can be extracted. Such a linearization, however, is rather cumbersome owing to the complex steps in computing the criteria and margins; for instance, the stability phase margin in the Nyquist diagram of a feedback controller requires to (i) compute a transfer function, (ii) find the frequency for which the gain in one, and (iii) determine the minimal phase between this frequency and the singularity at $z = -1$ in the complex plane. Each of these three steps needs to be linearized to arrive at sensitivity measures. An alternative, and more attractive, technique to extend the uncertainty analysis to stability and performance measures is based on a Monte-Carlo approach. We recall that the Monte-Carlo method has been dismissed as an option for determining the uncertainty propagation from measurement errors to Markov parameters. Our reasoning came from the prohibitively large dimensionality of the space that defines the measurement uncertainty, and ultimately led us to the linearization approach. For the sensitivity measure of stability and performance quantities, however, the situation is reversed: the number of Markov parameters μ is substantially smaller than the number N of measurement points (for example, $N \approx 10^4$ whereas $\mu \approx 10^2$), and Monte-Carlo techniques thus become a viable option. In short, once the uncertainty of the identified Markov parameters is known (using linearization of the least squares identification), a more appealing Monte-Carlo procedure may be used for the final step of the uncertainty analysis — from Markov-parameter perturbations to performance/stability margins. The uncertainty regions around the nominal Nyquist and Bode diagram are thus computed using a large number of possible systems taken within the uncertainty bounds of the identified Markov parameters (see equation (3.12)).

In summary, for a given set of perturbed data, a Nyquist or Bode plot including uncertainty bounds may be computed as follows: (i) solve the nominal problem for W, using the pseudo-inverse of Φ, according to (2.13); (ii) compute the Jacobian Matrix $\mathcal{L}$ defined in (3.10) using the nominal solution; (iii) compute the standard deviation of each Markov parameter based on (3.12); (iv) generate a large number (order μ) of transfer functions using Markov parameters that are given by their mean (nominal value) and standard deviation (from the above uncertainty propagation); (v) compute the standard deviation of the Nyquist or Bode plots, or any other stability or performance criterion, from this set of transfer functions. In the following section we apply the above procedure to several test cases of controllers.

4. Application to a test flow

We consider a linear numerical simulation of flow over an idealized airfoil followed by an infinite plate. The airfoil consists of a circular body of radius R and two straight segments joining at the trailing edge. The Reynolds number based on R is $Re = 400$, the radius $R = 0.5$ and the chord length is 4.6 non-dimensional units; see figure 5 for a sketch of the flow configuration. With a unit inflow velocity, the viscosity is chosen to correspond to the inverse Reynolds number $\nu = 1/Re$. The flow domain is meshed by a two-dimensional unstructured grid of about $5 \cdot 10^5$ nodes. First, a stable base flow is computed using a Newton iterative solver. Then, equations for the temporal evolution of perturbations (u, v, p) around this base flow are formulated and spatially discretized using finite elements (in our case, P_2-P_1 Taylor-Hood elements). The pressure field is computed using the Uzawa algorithm with a Cahouet-Chabart preconditioner (see Glowinski 2003). The time discretization is semi-implicit based on a second-order backward-differentiation

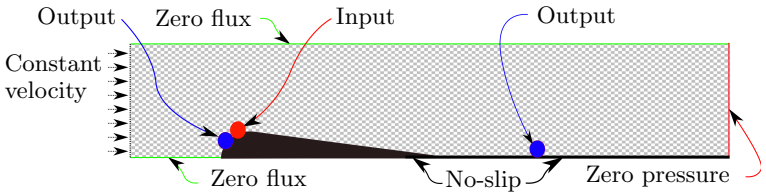

FIGURE 5. Numerical domain and boundary condition for the case of flow over an idealized airfoil.

scheme. We choose a time step of $\Delta t = 0.003$ for the simulations. Data sequences generated by the simulations are extracted with a time-step of $dt = 0.075$, before being subjected to the identification algorithms. The length of the sampled data is $N = 1500$, and the entire measurement sequence is used in the identification algorithms. Two simulations are performed: the first contains an upstream source of noise (one radius R upstream of the leading edge) that creates fluctuations in the flow field which are detected by both sensors; in the second simulation, a broad-band pseudo-random binary signal (PRBS) is applied to the input which mostly affects the downstream sensor. Artificial measurement perturbations are added to the downstream sensor, using a white Gaussian noise with the same variance as the noise-free signal variance (*i.e.*, we consider a 100% noise contamination). All identified nominal transfer functions will be found using the ARMarkov identification algorithm with the set of parameters $\mu = 200$, $n = 20$ and $N = 1500$. Based on the given noise standard deviation, the standard deviation of each Markov parameter is estimated using the uncertainty propagation algorithm given by (3.12). Finally, exact transfer functions are also identified from longer noise-free data signals (with $N = 4000$). These latter signals are assumed unobtainable in realistic experiments; they are computed here solely for a performance evaluation of the uncertainty propagation algorithm.

With the nominal transfer function and the different controller transfer functions known, it is then possible to estimate the performance and stability of a given controlled system. The next subsections focus on two control setups: a feedback and a feed-forward configuration. It will be shown that the exact performance and stability is quite different from the nominal values, and that this difference is well predicted by the uncertainty propagation technique.

4.1. *Feedback control*

We first consider a feedback configuration for flow over the idealized airfoil. The developed framework applies to the block diagram shown in figure 2(a) where, in the present case, y denotes the signal from the downstream sensor and u stands for the upstream control input. From the realistic (i.e., noise-contaminated) data sequence, the nominal transfer function (Markov parameters) is identified using the ARMarkov/LS idenification algorithm. The number of identified Markov parameters is set to $\mu = 200$, which is about 1.4 times the AIC value of $\mu = 144$. The nominal system together with the noise standard deviation then provides an estimate of the standard deviation of the identified Markov parameters. This latter standard deviation can be interpreted as uncertainty bands about the nominal transfer function.

For demonstration purposes, we assume a proportional feedback controller with $\mathsf{K} = 0.025$. The stability of the closed-loop system is determined by the distance of the open-loop transfer function $\mathsf{G}_0\mathsf{K}$ to the point -1; see (2.17). Figures 6(a) and (b) show the Nyquist plots of the exact OLTF, the nominal OLTF and the uncertainty bounds associated with twice the standard deviation at each frequency. These bounds correspond to

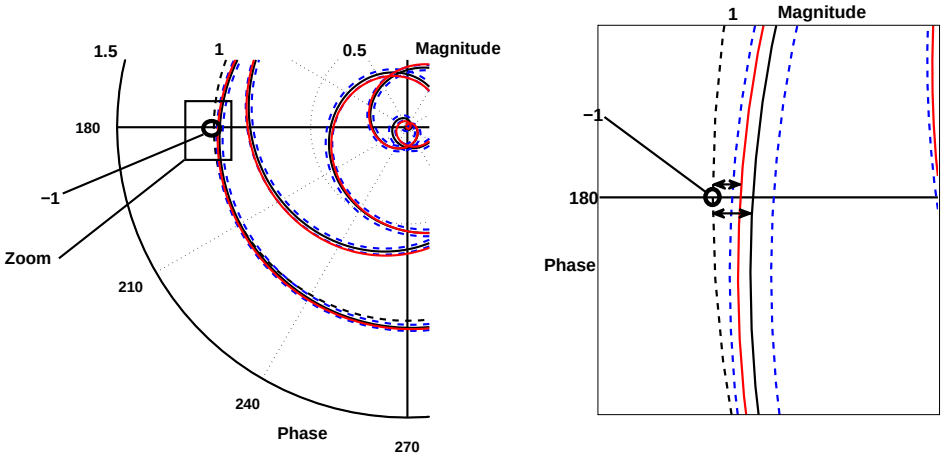

FIGURE 6. Nyquist plot of the Open Loop Transfer Function (OLTF): (red) exact, (black) nominal value; the 95%-likelihood bounds around the nominal value are given by dashed-blue lines. (b) Magnified detail of the OLTF in (a) near the point $z = -1$ with arrows showing the nominal and real gain margins.

a confidence interval of 95%, i.e., in only 5% of cases does the real OLTF fall outside these bounds. Furthermore, the nominal transfer function of the controlled system shows a gain margin of $\mathsf{GM} = 0.033$ which overestimates the real gain margin by more than 40% ($\mathsf{GM} = 0.023$). Our uncertainty propagation algorithm gives estimates for the gain margin of more than $\mathsf{GM} = 0.017$ with a probability of 95%, and more than $\mathsf{GM} = 0.025$ with a probability of 68.2%. According to the same algorithm, the standard deviation of the gain margin is about $\sigma_{\mathsf{GM}} = 0.008$. In contrast, the singularity at -1 is nearly four standard deviations away from the nominal transfer function, which — according to the gain margin criterion and under the assumption of Gaussian noise — suggests that in only 0.1% of all cases should we expect an unstable feedback-controlled system. A similar comparison may be performed using the phase margin: the nominal margin is $\mathsf{PM} = 29^o$, the exact phase margin is $\mathsf{PM} = 21^o$, while the 95%-likelihood margin is determined as $\mathsf{PM} = 13^o$.

In this feedback control example, compared to the nominal transfer function, the real transfer function tends to overestimate the stability margins of the closed-loop system. The uncertainty propagation technique allows a quantitative estimation of the error bounds which results in a more realistic estimation of these margins.

4.2. *Feed-forward control*

In feed-forward control applications, the control performance is often measured by the maximum magnitude of the controlled system transfer function (CSTF). In this case, the input signal comes from the upstream sensor (see figure 5). As before, this controlled system transfer function can be estimated with the nominal identifications and compared to the real transfer function. Figures 7(a) and (b) show the transfer function of the exact system without control, the nominal controlled system and the exact system. This time, the performance of the controller seems to be positive (note the reduction of the maximal amplitude) with the nominal estimation. However, a closer look reveals that the real system behaves worse with control than without. This can be predicted using the 95%-uncertainty bounds which show the probable lack of performance of the controlled system.

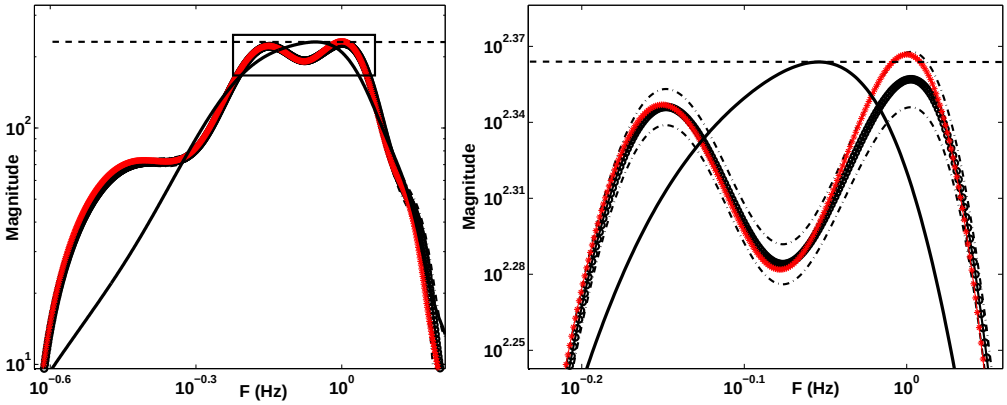

FIGURE 7. Bode diagram of the uncontrolled system (black line), the nominal CSTF (black thick line), and the exact CSTF (red); the error bounds around the nominal CSTF are shown by black mix-dashed lines. The maximum amplitude of the uncontrolled system is represented by a dashed horizontal line. (b) Magnified view of (a) for a limited frequency range.

5. Conclusions

The identification error due to measurement uncertainty can have an important effect on the stability margins and performance bounds of any data-based controller. In this study, an uncertainty propagation technique has been developed and applied to two types of control architectures: feedback and feed-forward control. In both cases, the nominal prediction overestimate either the controller's performance or stability margins. When input-data uncertainty is taken into account, more accurate predictions can be made. Even though uncertainty propagation may be treated via Monte-Carlo analysis, the related computational costs are often prohibitive. In contrast, a linearization of the identification algorithm provides statistical information about the identified transfer function, requiring only one single experiment and thus overcoming the previous computational bottleneck. Estimating *a priori* the performance and stability characteristics of a given controller, using the data-sequences from which the controller has been designed, may lead to a better design of control strategies. In fact, controllers are commonly built to be optimal in the nominal sense. Being able to give a robust definition of optimality with respect to uncertainty should allow the construction of control setups that are more relevant for implementation in experiments or more suited for the control of flows under realistic conditions.

Appendix A. Transfer functions for linear time-invariant systems

Three different models have been introduced in section § 2.1. For completeness sake, we present the transfer functions of these models which can be obtained by taking the z-transform of the equivalent discrete-time models.

For the finite-impulse response (FIR) model we obtain the transfer function

$$\mathsf{G}(z) = \mathsf{H}_0 + \mathsf{H}_1 z^{-1} + \ldots + \mathsf{H}_{\mu-1} z^{1-\mu}. \tag{A 1}$$

with H_i as the Markov parameters (discrete impulse response). The transfer function is simply a sum of monomials in z^{-1}. Following the same procedure, the more complicated

auto-regressive moving average (ARMA) model yields the transfer function

$$\mathsf{G}(z) = \frac{\mathsf{M}_0 + \mathsf{M}_1 z^{-1} + \ldots + \mathsf{M}_n z^{-n}}{1 + \mathsf{N}_1 z^{-1} + \ldots + \mathsf{N}_n z^{-n}} \tag{A 2}$$

which represents a rational function in z^{-1} to approximate the transfer function of the identified system. The third and final model, the ARMarkov model, has the transfer function

$$\mathsf{G}(z) = \frac{\mathsf{H}_0 + \mathsf{H}_1 z^{-1} + \ldots + \mathsf{H}_{\mu-1} z^{-(\mu-1)} + z^{-\mu}(\mathsf{Q}_0 + \mathsf{Q}_1 z^{-1} + \ldots + \mathsf{Q}_n z^{-n})}{1 + z^{-\mu}(\mathsf{N}_1 z^{-1} + \ldots + \mathsf{N}_n z^{-n})} \tag{A 3}$$

which also represent a rational approximation of the system response but, contrary to the previous ARMA model, contains the first μ Markov parameters H_i explicitly.

Appendix B. Validation using Monte-Carlo simulation

We will validate the perturbation framework introduced in the main text using Monte-Carlo simulations. In particular, we wish to assess the dependence of the perturbative approach on the signal-to-noise ratio of the processed data. To this end, we introduce the parameter γ defined as $\gamma = \sigma_{\delta y}/\sigma_y$, measuring the standard deviation of the perturbations with respect to the standard deviation of the unperturbed data. For efficiency reasons, we choose as our test case a system that can be solved quickly, yet still has characteristics of a full-scale fluid system. In particular, the chosen system should produce data-sequences reminiscent of many fluid systems: with a range of certain frequencies amplified by the flow, while other frequencies damped, and with a delay between input and output signals mimicking advection.

The selected test case consists of incompressible flow around a cylinder ($Re = 40$), modeled by the linear Ginzburg-Landau equation. An actuator is placed about half a radius upstream of the cylinder, and the sensor is located in the stable wake; both employ or provide signals of the normal-velocity component. The linear Ginzburg-Landau model equation is solved numerically using finite differences on a one-dimensional equispaced mesh of $N = 100$ grid points. The relatively small dimensionality of the system facilitates the convergence of the Monte-Carlo variance estimation. The flow behaves as a filter with delay, and the power spectral density of the output signal (given white-noise input) is plotted in figure 8 (solid line); it shows amplification of lower frequencies (around 25 mHz) and a strong damping of higher frequencies. The input sequence has been generated with a Pseudo-Random Binary Signal (PRBS) algorithm. A total of 500 noise-free numerical experiments have been performed, resulting in 500 independent noise-free input-output data sequences with each sequence containing 1000 measurement-points sampled at 1 Hz (i.e., about 50 times the characteristic time scale of the system). The length of each sequence represents 25 characteristic time units. This length and the sampling frequency are adequate to accurately identify the system behavior (see section 2.2).

After establishing the base-line data-sequences, we add noise to each of the 500 experiments. In general, three different approaches can be distinguished. The added noise could be (i) broadband and affect all frequencies nearly equally. Alternatively, it could be strongly colored with (ii) higher amplitudes near the system's natural frequency or (iii) with higher amplitudes at higher frequencies that do not correspond to physically observed frequencies. Often, the system's characteristic frequency can be estimated, which allows the application of low-pass filters to eliminate the noise for the third case. In the first two cases, low-pass filtering will not succeed in eliminating the noise components in the data. For this reason, we will focus on these cases.

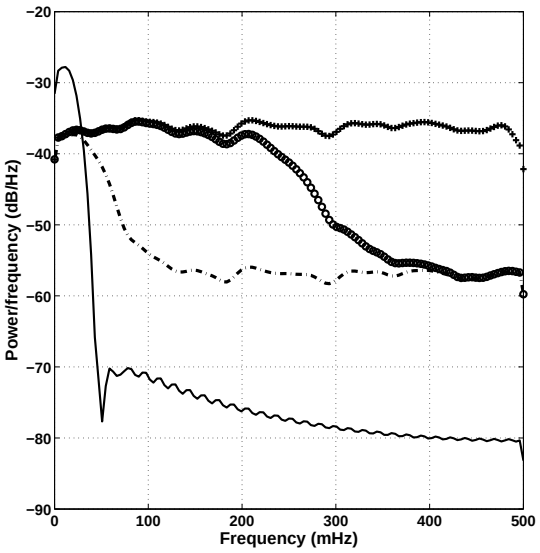

FIGURE 8. Power spectral density of the different measurement disturbances: crosses denote the white noise, circles show the colored noise 1, the dashed-line displays the colored noise 2. The spectrum of the noise-free output signal is represented by the solid line.

Three different measurement disturbances will be considered: white noise and two colored noise distributions with a pronounced amplitude near the system's characteristic frequencies. Their power spectra are presented in figure 8 together with the output power spectrum. These noise spectra cannot be simply filtered and are likely to influence the value of the identified Markov parameters. Their noise-to-signal ratio γ is set by choosing the noise amplitude. For each of the three noise spectra and for every considered noise-to-signal ratio, we compare the statistical information estimated by the Monte-Carlo approach to the same information computed by the uncertainty algorithm of the main text. The mean standard deviation of the identified Markov parameter (mean(σ_{H})) is the objective for this test case; it has to be compared to the average of the Markov parameter value which is one. If mean(σ_{H}) $= 10^{-2}$, the variance error is estimated to be on average one percent for each Markov parameter.

First, 500 noisy data-sequences are used to estimate the standard deviation of the identified Markov parameters (the Monte-Carlo approach). Then, one single input-output data-sequence and the noise standard deviation are used to estimate the standard deviation of the identified Markov parameters (using the uncertainty propagation approach). For the Monte-Carlo estimation, each of the 500 perturbed input-output data-sequences is used in the ARMarkov/LS identification algorithm, yielding the corresponding Markov parameters; from these 500 sets of Markov parameters, their means and standard deviations can easily be determined. For the uncertainty propagation, one arbitrarily perturbed data-sequence is taken as input to the algorithm of section 3. Equation (3.12) produces the standard deviation of the Markov parameters based on the noise standard deviation, from which the mean can be computed. The parameters for the different algorithms are $N = 1000$, $\mu = 400$, $n = 40$, and ϵ is set to machine precision. The corresponding AIC is not given, since its value varies with each noise-to-signal ratio and each color of noise. Figure 9 shows the results of the standard deviation estimates for each algorithm

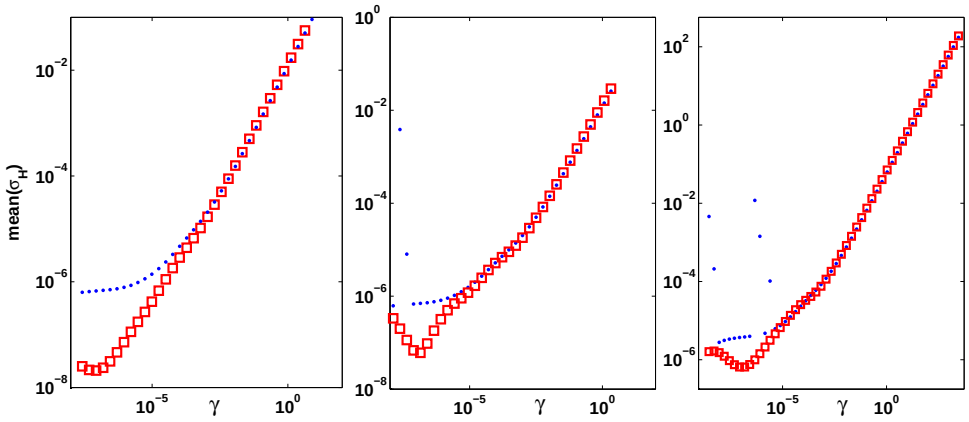

FIGURE 9. Monte-Carlo (blue dots) and uncertainty propagation (red squares) estimates of the standard deviation of the identified Markov parameters as a function of the noise-to-signal ratio. (left) white noise; (middle) low-pass filtered noise 1; (right) low-pass filtered noise 2.

(Monte-Carlo and uncertainty propagation) and for each noise-spectrum/noise-to-signal ratio.

As can be deduced from figure 9, the three different noise spectra (measurement disturbances) affect the standard deviation of the Markov parameters in a similar manner. Independent of the noise spectrum, the Monte-Carlo and uncertainty propagation approaches give identical estimates for high noise-to-signal ratios, thus validating the uncertainty propagation algorithm for sufficiently high values of γ. According to these experiments, accurate estimates of the standard deviation of the Markov parameters can be expected for noise-to-signal ratios γ between 10^{-5} and 2 (very noisy signal). For low values of γ ($\ll 10^{-5}$), two reasons may explain the discrepancy between the Monte-Carlo results and the uncertainty propagation. First, the standard deviation may be influenced by round-off errors which become important at 10^{-8} due to the square root dependence of the standard deviation. Secondly, with only 500 samples available, the Monte-Carlo algorithm may only be converged up to 10^{-6}. In any event, realistic data-sequences taken from fluid systems are rarely contaminated by noise of less than 0.001%.

This simple test case illustrates that uncertainty propagation provides accurate and valuable estimates of the Markov-parameter variance error for realistic noise-to-signal ratios.

REFERENCES

AKAIKE, H. 1974 Fitting autoregressive models for prediction. *IEEE Trans. Autom. Contr.* **19**, 716–723.

AKERS, J.C. & BERNSTEIN, D.S. 1997 ARMarkov least-squares identification. In *Proc. Amer. Contr. Conf*. Albuquerque, NM.

BRIGHENTI, C., WAHLBERG, B. & ROJAS, C.R. 2009 Input design using Markov chains for system identification. In *Joint 48th IEEE Conf. Dec. and Contr. and 28th Chin. Contr. Conf.*, pp. 1557–1562. Shanghai, P.R. China.

FLEDDERJOHN, M.S., HOLZEL, M.S., PALANTHANDALAM-MADAPUSI, H.J., FUENTES, R.J. & BERNSTEIN, D.S. 2010 A comparison of least squares algorithm for estimating Markov parameters. In *Amer. Control Conf. (ACC)*, pp. 3735–3740. Baltimore, MD.

FLEMING, J. 2011 Generalized Tikhonov regularization: Basic theory and comprehensive results on convergence rates. PhD thesis, Techn. Univ. Chemnitz.

Gerencser, L., Hjalmarsson, H. & Martensson, J. 2009 Identification of ARX systems with non-stationary inputs – asymptotic analysis with application to adaptive input design. *Automatica* **45**, 623–633.

Glowinski, R. 2003 Finite element methods for incompressible viscous flow. In *Handbook of Numerical Analysis*, , vol. 9, pp. 3–1176. Elsevier.

Hervé, A., Sipp, D., Schmid, P.J. & Samuelides, M. 2012 A physics-based approach to flow control using system identification. *J. Fluid Mech.* **702**, 26–58.

Hjalmarsson, H. 2005 From experiment design to closed-loop control. *Automatica* **41**, 393–438.

Illingworth, S.J., Morgans, A.S. & Rowley, C.W. 2011 Feedback control of flow resonances using balanced reduced-order models. *J. Sound Vibr.* **330** (8), 1567–1581.

Juang, J.N. & Pappa, R.S. 1985 Eigensystem Realization Algorithm for modal parameter identification and model reduction. *J. Guid. Contr. Dyn.* **8** (5), 620–627.

Juillet, F., Schmid, P.J. & Huerre, P. 2013 Control of amplifier flows using subspace identification. *J. Fluid Mech.* **725**, 522–565.

Kamrunnahar, M., Huang, B. & Fisher, D.G. 2000 Estimation of Markov parameters and time-delay/interactor matrix. *Chem. Eng. Sci.* **55** (17), 3353–3363.

Katayama, T. 2005 *Subspace Methods for System Identification*. Springer-Verlag.

Kim, J. 2003 Control of turbulent boundary layers. *Phys. Fluids* **15** (5), 1093–1105.

Lew, J.-S., Juang, J.-N. & Longman, R.W. 1993 Comparison of several system identification methods for flexible structures. *J. Sound Vibr.* **167** (3), 461–480.

Ljung, L. 1987 *System Identification: Theory for the User*. Prentice-Hall, Inc.

Longman, R.W., Lew, J.-S., Tseng, D.-H. & Juang, J.-N. 1991 Variance and bias computation for improved modal identification using ERA/DC. *Amer. Control Conf.* pp. 3013–3018.

Ma, Z., Ahuja, S. & Rowley, C.W. 2011 Reduced order models for control of fluids using the Eigenvalue Realization Algorithm. *Theor. Comp. Fluid Dyn.* **25** (1), 233–247.

Mehra, R.K. 1974 Optimal inputs for linear system identification. *IEEE Trans. Autom. Contr.* **19** (3), 192–200.

Rissanen, J. 1983 A universal prior for integers and estimation by minimum description length. *The Annals of Stat.* **11** (2), 416–431.

Skogestad, S. & Postlethwaite, I. 2001 *Multivariable Feedback Control – Analysis and Design*. John Wiley and Sons, Ltd.

Stewart, G.W. 1977 On the perturbation of pseudo-inverses, projection and linear least squares problems. *SIAM Rev.* **19** (4), 634–662.

Stewart, G.W. 1990 Perturbation theory and least squares with errors in the variables. *Contemp. Math.* **112** (4).

Van Pelt, T. & Bernstein, D.S. 1998 Least squares identification using μ-Markov parameterizations. In *Proc. 37th IEEE Conf. Dec. and Contr. 1998*, , vol. 1, pp. 618–619.

Wedin, P.A. 1973 Perturbation theory for pseudo-inverses. *BIT Num. Math.* **13** (2), 217–232.

Chapter 3

Experimental flow over an airfoil: reaching the limit of linear identification

Contents

3.1 Introduction

The identification and control design techniques developed and previously applied to numerical simulations are now applied to and tested on an experimental case: flow over an idealized airfoil. This type of flow consists of an oscillatory component given by the shedding of the von Karman vortices into the wake, as well as a noise-amplifier component represented by the shear layer associated with the separation bubble forming on top of the airfoil. Only the noise-amplifier part can be properly treated by the technique introduced earlier; for this reason, we have to ensure ultimate controllability with model predictive control by establishing an uncoupling of the two competing instability mechanisms. Once controllability is assured, the system-identification and control design algorithm described in chapter 2 is applied. It consists of two components: (i) a system-identification technique that constructs a finite impulse response (FIR) model for the perturbation dynamics, and (ii) a disturbance-rejection model predictive controller (MPC) that aims at controlling perturbations that are convected and amplified in the shear layer.

When applied to a numerical simulation of the linearized Navier-Stokes equations (for the same flow configuration), this technique successfully reduces the amplification of external disturbances (see figure 3.1).

Encouraged by these results, the same controller-design procedure is applied to an experimental setting of the same flow configuration (idealized airfoil at $Re_c = 12500$). However, it has been observed that the identification step fails at extracting a sufficiently accurate model, which subsequently compromises the performance of the associated controller. Non-linearities in the flow dynamics are thought to be the cause of this lack of performance, as, by design, they are not sufficiently captured

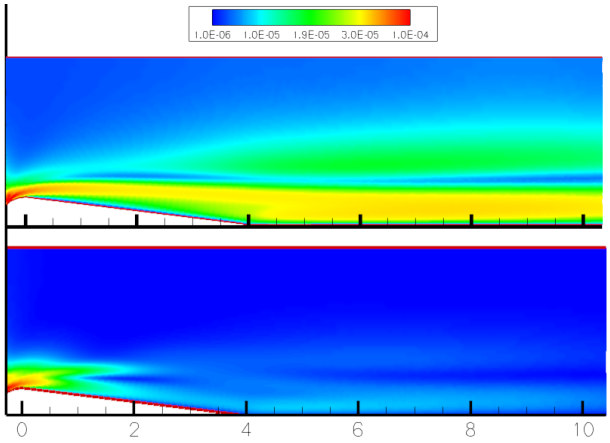

Figure 3.1: Numerical simulations of the linearized Navier-Stokes equations for flow around an idealized airfoil (chord Reynolds number $Re_c = 2000$, uncontrolled (top) and controlled (below) configurations. The colormap shows the local kinetic perturbation energy. Applying a disturbance rejection controller effectively reduces the fluctuation intensity.

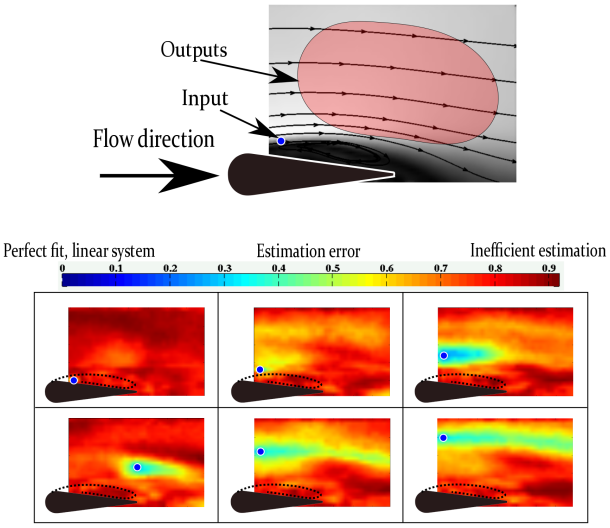

Figure 3.2: Linear identification error, the blue point is the chosen input, the rest of the field is the output-set.

by the linear system-identification technique. To further investigate this breakdown in performance, several point-to-field (single-input multiple-output, SIMO) system-identifications have been performed, and their respective identification error is plotted in figure 3.2. The color-contours represent the identification error from a single input location (blue dot) to the entire flow field. The measures give an indication of the parts of the flow that can be *linearly* identified based on information from the single measurement point. For a successful identification and control,

this identification error has to be sufficiently small to expect our technique to give reasonable control performance. As can be seen in figure 3.2, the size and spatial distribution of the identification error does not bode well for a successful control of the shear layer disturbances.

3.2 Experimental report

Experimental flow over an airfoil: reaching the limit of linear identification

N. Dovetta[a], B.J. McKeon[b], P.J. Schmid[a]

a. *LadHyX, Ecole Polytechnique, Palaiseau*
b. *GALCIT, California Institute of Technology, Pasadena (USA)*

1 Introduction

Noisy measurements, non-linearities and upstream residual turbulence are a few examples of challenges inherent to *experimental* flow control problems. For these flows, the controllers have to cope with output signals that are corrupted by measurement noise, and on-line actuation has to be sufficiently fast to control the equally fast dynamics.

While many experimental cases of successful oscillator-flow manipulation using feedback control exist (*e.g.* [17]), very few experimental disturbance-rejection studies have been reported with good performance [14, 9].

In this work, the controller design procedure developed in [6] is applied to an experiment. The procedure is composed of : (i) a linear ARMarkov system-identification [1] model design algorithm that identifies the impulse response of the system from input-output data-sequences, and (ii) a Model Predictive Heuristic Control (MPHC) design-algorithm [5] which computes an optimal disturbance-rejection controller from impulse responses of the system. Flow over an idealized airfoil is considered, and the control design aims at reducing the fluctuations propagating through the shear layer and bounding the recirculation bubble over the airfoil.

First, the flow-behavior around the airfoil is characterized. The identification and control design procedure is then applied to reduce the level of fluctuations close to the reattachment point. As the identification-step of the algorithm fails at predicting the temporal evolution of the shear-layer, the final section of this report explains the reasons for this unsuccessful controller design attempt.

2 Description of the test case and experimental set-up

The idealized airfoil (Figure 1) has already been studied by Prof. McKeon's group ; this profile showed promising potential for flow control applications since a predetermined control design has successfully be implemented to reattach the flow over the airfoil (see Figure 2 and reference [8, 16]).

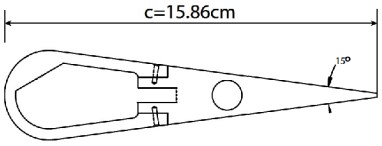

FIG. 1 – Idealized airfoil profile with a circular leading edge and a planar trailing edge. The actuation device is not plotted.

The profile is 50.8 cm wide (spanwise), 15.86 cm long (streamwise), and 3.43 cm thick. It is composed of a circular leading edge followed by a straight body. The shape has a rather specific impact on the separation bubble as it triggers detachment at the jump in curvature (for the range of Reynolds number considered).

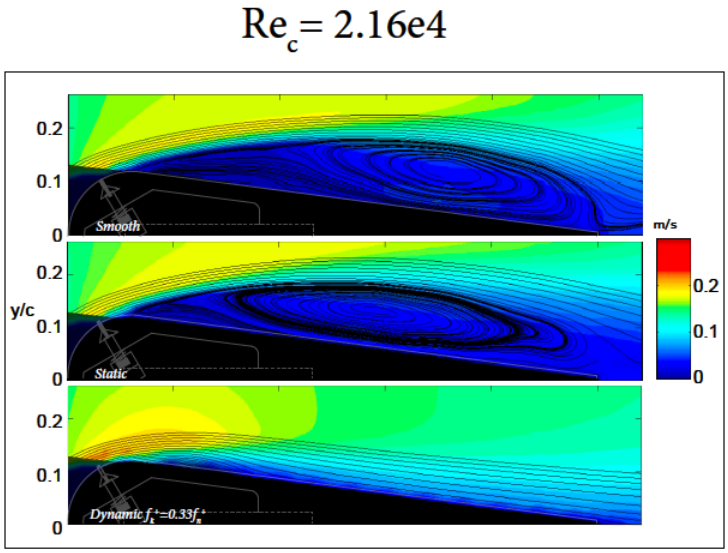

FIG. 2 – From [8], predetermined separation control. The colormap visualizes the mean velocity; stream lines are also plotted to highlight the recirculation bubble. The top plot shows the flow around a smooth airfoil; the middle plot shows the flow around the airfoil with static actuation; the bottom plot shows the flow around the airfoil with predetermined periodic actuation. In the latter case, the predetermined control successfully reattaches the flow.

Facility : The experiment is performed in a free-surface water facility (see figure 14 and [12, 7]). It has a test section length of 1.6 m, a width of 0.46 m and a depth of 0.50 m. The flow is preconditioned by a perforated plate, a honey comb, three turbulence-reducing screens and a $4:1$ fifth-order polynomial contraction. The water temperature is 23 degrees Celsius ($\nu = 0.943 \cdot 10^{-6}$). The tunnel's flow velocity ranges from $5.4 cms^{-}1$ to $45 cms^{-}1$. (For our profile, the width-based and chord-based Reynolds number in this tunnel falls within the intervals $Re_w = [2000; 16000]$ or $Re_c = [10000; 80000]$).

Three types of measurements are available : dye visualization, Particle Image Velocimetry (PIV), and hot-film Constant Temperature Anemometry (CTA). In addition , numerical simulations are performed.

Dye visualization : Dye was put in the flow near the leading edge, near the middle of the profile's spanwise dimension, using a tube of 5 mm diameter. The dye is an eatable colorant of density slightly higher than water, but the effect of density variation is rather small and has thus been neglected.

Particle Image Velocimetry : PIV measurements were made using a LaVision time-resolved 2D PIV set-up with one Photron Fastcam APX-RS high-speed camera equipped with a Nikon lens of 50 mm focal length and a $1:1.2$ aperture. The camera was synchronized with a high speed controller at 83 Hz, with a resolution of 1024×512 pixels squared, and calibrated at 5.25 pixels per mm. The camera frequency is chosen to guarantee a freestream particle-displacement of about 7 pixels between every snapshot. The seeding particles are hollow glass spheres (reference 110P8 with an average diameter $11.7 \mu m$ and a specific gravity of 1.1); the seeding density is about 0.1 particles per square pixel. The particles are illuminated by a 2 mm thick laser sheet provided by a Photonics DM20-527 solid-state laser. To avoid large uncertainty near the illuminated profile due to surface reflection, the image intensity is calibrated using white image subtraction (normalization of the image intensity using the average light distribution) and background image subtraction. The white and background images are

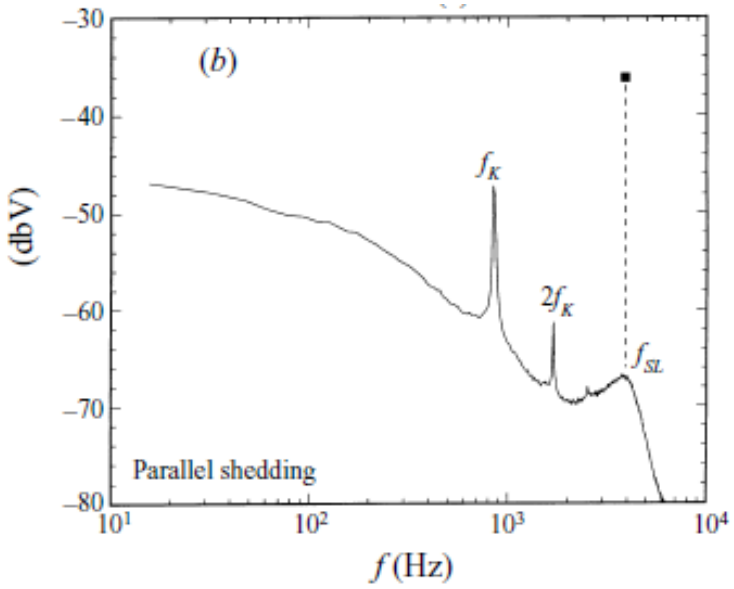

FIG. 3 – From [13], velocity fluctuations within the shear layer at $Re = 2500$. The measurements are made at $x/D = 1$ and $y/D = 0.8$.

taken before each run and averaged over 100 snapshots.

3 Shear layer behavior

Two instability mechanisms are acting on this profile : the shear-layer, convective instability on both sides of the idealized airfoil, and the von-Karman street, absolute instability starting at the trailing edge of the profile. These two phenomena may be coupled : the shear-layer beating frequency may be locked to the frequency of the von-Karman instability, in which case a disturbance-rejection controller is likely to perform rather poorly. If shear-layer and von-Karman vortices are uncoupled (*i.e.*, their characteristic frequencies are distinct from each other), a disturbance-rejection controller may efficiently reduce perturbations that are convected and amplified in the shear layer.

Literature about bluff body flow [13, 18] shows that even though von-Karman vortices perturb the flow at a specific frequency, the shear layer may still behave independently. Indeed, frequency locking will occur only if the characteristic frequency of the shear layer is close to the characteristic frequency of the vortices (or its first harmonics). If the shear layer frequency is locked onto the vortex-street frequency, the flow is globally oscillating, in which case feed-forward control will be ineffective. However, if the two frequencies are distinct, the shear layer may behave as a noise amplifier and therefore be a suitable candidate for MPHC control [6]. Figure 3 shows the spectrum of velocity fluctuations behind a cylinder at a Reynolds number of $Re = 2500$, with f_K as the von-Karman street frequency and f_{SL} as the shear-layer frequency. This spectrum shows that the two dynamics are likely uncoupled, because their frequencies are separated by almost one order of magnitude. The shape of the amplification further supports this argument, as the peaks at f_K and $2f_K$ have a rather sharp shape which highlights the associated oscillatory behavior ; in contrast, the smooth peak at f_{SL} corresponds to what is commonly observed for noise-amplifier behavior (see [3]). Another study from [18] has demonstrated similar results for flow around an airfoil at a chord-based Reynolds number of $Re = 10^4$ (see figure 4).

In summary, the flow around bluff bodies or around thick airfoils may present two types of instabilities that have distinct dynamics, if they are uncoupled. In this case, the shear layers behave as noise-amplifiers and thus fit into a disturbance-rejection control framework.

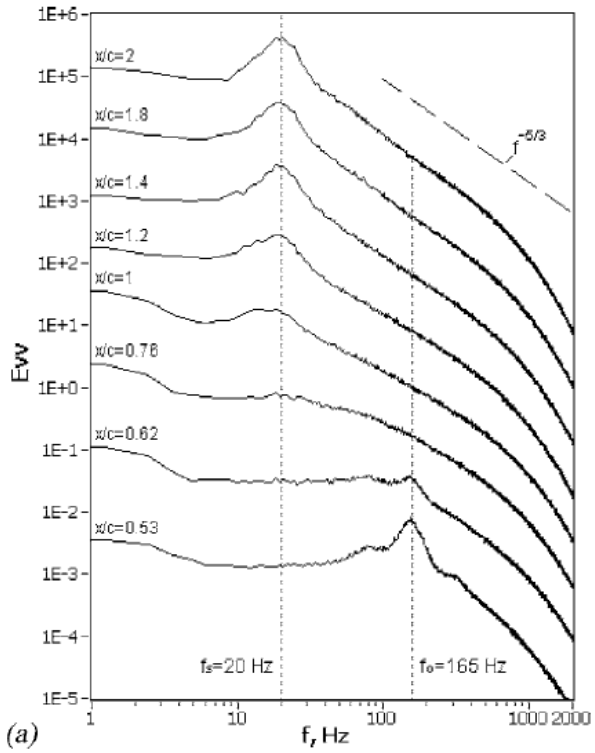

FIG. 4 – From [18], spectra of the fluctuating lateral-velocity component at $Re_c = 10^4$. The amplitude of each successive spectrum is increased by one order of magnitude.

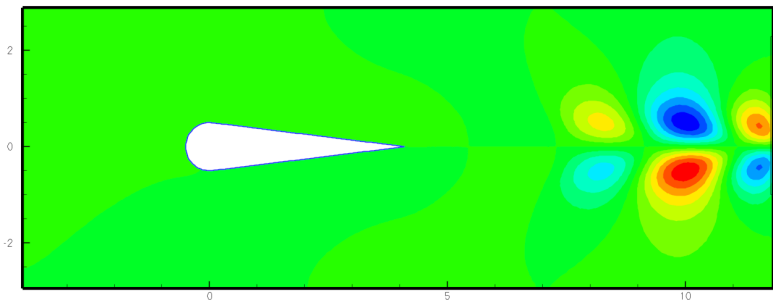

FIG. 5 – First unstable linear mode. The mode represents the von-Karman instability, apparent about one-and-a-half chord lengths from the airfoil.

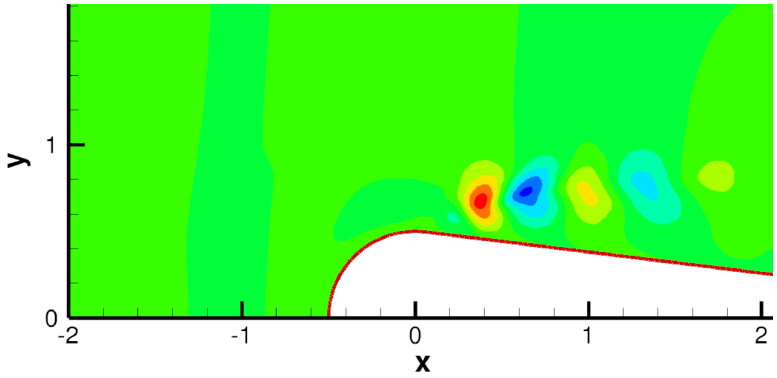

FIG. 6 – Impulse response of the shear layer computed from the linearized Navier-Stokes equation. The shear layer convects and amplifies the initial perturbation due to a Kelvin-Helmholtz instability.

The last part of this section demonstrates the non-coupling character of the instability mechanisms on our idealized airfoil, which motivates the application of feedforward MPC to its shear layer.

Numerical simulations : First, the steady, two-dimensional, laminar solution of the Navier-Stokes equation (i.e., the base flow) is computed using a finite-element discretization of the equations on a triangular mesh. Newton's algorithm is applied to find the base flow at increasing Reynolds number, exploiting continuity of the problem. Any base flow at chord-based Reynolds numbers higher than $Re_c = 1600$ is linearly unstable, and the most amplified mode shows von-Karman structures (see figure 5) oscillating at a Strouhal number of 0.23. The lowest experimental Reynolds number is $Re_c = 10000$; hence, regardless of the selected velocity, von-Karman shedding certainly appears in the wake of the airfoil in our facility.

To evaluate the frequency at which the shear layer is amplifying incoming disturbances, the numerical domain is truncated (see figure 6). Above a Reynolds number of $Re_c = 1600$, the shear layer becomes convectively unstable, and the Strouhal number of the most amplified frequency is approximately 1. From linear numerical simulations of flow about the idealized airfoil we conclude that the instability mechanisms are uncoupled ; however, these numerical studies are describing the flow at much lower Reynolds numbers than what can be realized in our experimental facility.

Spectrum using PIV data : Time-resolved PIV data have been recorded by R. Wallace ([16]). Using Dynamic Mode Decomposition (DMD ; see [15]) on this set of data provides the frequency

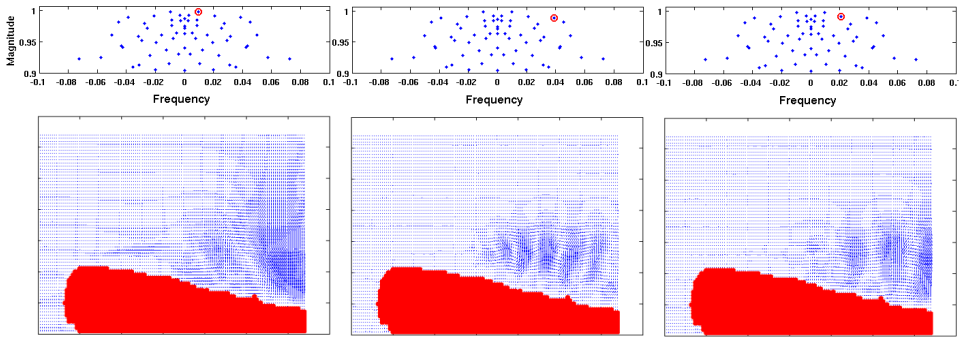

FIG. 7 – Eigenvalues and corresponding modes from a dynamic mode decomposition (DMD) of the TR-PIV data around the airfoil. The circled eigenvalue corresponds to the eigenmode plotted below.

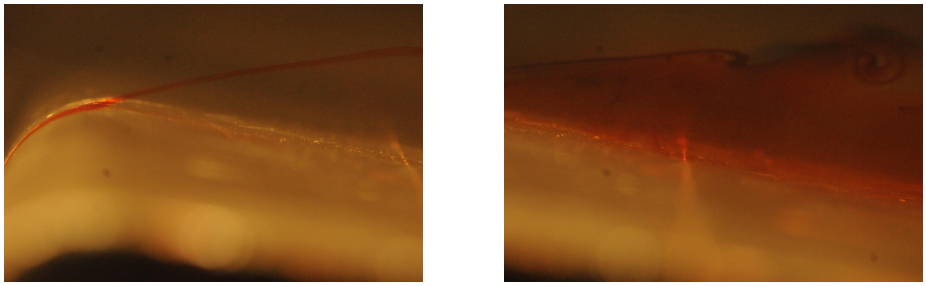

FIG. 8 – Dye streaks in the shear layer for flow around an airfoil with a splitter plate ; the chord-based Reynolds number is $Re_c = 10000$.

content and associated flow features, in our case for $Re_c = 11000$. Figure 7 shows the eigenvalues and some eigenvectors of the DMD-companion matrix. Three fields are plotted corresponding to three frequencies circled (in red) in the spectrum. The first (left) mode shows a large flow structure, which could be caused by the von-Karman street ; the corresponding Strouhal number is about 0.15. The two other structures plotted are localized in the shear layer ; their respective Strouhal numbers are 0.61 (middle) and 0.32 (right). This seems to correspond to the results found at higher Reynolds numbers, even on different profiles in [18].

The frequencies and modes found with DMD suggest a separation of behavior between the shear layer and the vortex street. Therefore, a feed-forward controller may successfully control perturbations growing in the shear layer.

Flow features using dye visualization : In order to confirm the above behavior, flow visualizations with dye coloration have been performed. Figures 8 and 9 show the flow marked with dye coloration for two different Reynolds numbers. The shear-layer structures are clearly identifiable. Their characteristic frequency may be qualitatively evaluated, yielding their shape and average velocity in the shear layer. The results agree with the Strouhal number found with the DMD.

Besides confirming the results from the DMD, the dye pictures show the separation point, which is, as expected, at the jump in curvature of the airfoil. The upstream sensor has to be placed just ahead of this separation to detect upstream perturbations before they enter the convectively unstable shear layer.

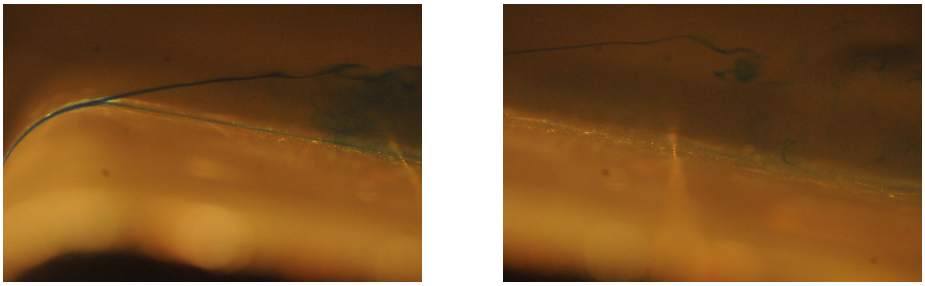

FIG. 9 – Dye streaks in the shear layer for flow around an airfoil with a splitter plate ; the chord-based Reynolds number is $Re_c = 25000$.

Conclusions on the shear layer behavior : The shear layer appears to be uncoupled from von-Karman vortices. This has been observed in several studies [13, 18] and is confirmed by the spectral and numerical analysis performed on our profile : the frequencies of the two phenomena are distinct and separated. Additionally, the dye visualization confirmed the location of separation as the position of the curvature jump. Since the shear layer starts at the separation point, perturbations that grow in the shear layer are most easily detected by a sensor just upstream of the separation point (as shown in figure 13).

4 Limits of linear system identification

The controller design algorithm is described in more detail in [6]. It is first briefly summarized here and then applied to both numerical and real experiment.

4.1 System identification and control design algorithm

The goal of the controller is to reduce the disturbance levels in the shear layer. The disturbance level is represented by a scalar signal y denoting the deviation of a measurement from its mean ; $y = 0$ is achieved for a steady flow. This scalar information is either coming from a hot-film on the airfoil or from PIV-measurements of a large area of the flow field. Actuation is denoted by u and is placed near the separation point. The spy-sensor s is either a hot-film placed upstream of the actuator, or an upstream point measurement from PIV. Its role is to detect the incoming disturbance for an effective control design.

The fluid system is governed by two input signals (the known actuator signal u and the unknown disturbance environment w) and two output signals (the measurements y and s). The following linear model is assumed to be representative of the flow's input-output relationship.

$$y = \mathsf{G}_{wy} w + \mathsf{G}_{uy} u \tag{1}$$
$$s = \mathsf{G}_{ws} w. \tag{2}$$

The control u is assumed to have no influence on the spy-sensor s, due to the convective behavior of the flow. The controller-structure is taken as the set of linear transfer functions from the spy sensor to the actuation ; it is a feedforward set-up.

$$u = \mathsf{C}_{su} s. \tag{3}$$

This transfer function has to be designed to reduce the shear layer disturbances. In our case, we wish to reach $y = 0$ at all times, which gives

$$u = -\mathsf{G}_{uy}^{-1} \mathsf{G}_{wy} \mathsf{G}_{ws}^{-1} s \equiv \mathsf{C}_{su} s. \tag{4}$$

Since w is unknown, the transfer functions G_{wy} and G_{ws} cannot be determined. Using relation (2) between w and s, y may be written without referring to w

$$y = \mathsf{G}_{uy}u + \mathsf{G}_{wy}\mathsf{G}_{ws}^{-1}s. \tag{5}$$

Since the signals u, s and y are measurable, the two transfer functions G_{uy} and $\mathsf{G}_{wy}\mathsf{G}_{ws}^{-1}$ are identifiable. The next section describes the chosen identification algorithm.

4.1.1 Finite-impulse response model

To take advantage of a data-based approach (due to its feasibility in an experimental setup), an input-output data sequence of N samples will be recorded from which the transfer functions will be determined. This latter process can be divided into two steps : (i) a model-structure for the system's impulse responses has to be chosen first, after which (ii) a fitting procedure will determine the inherent parameters of the selected model.

It is important to choose an input signal u that properly excites the inherent frequencies of the system and thus provides a complete input-output map that accurately represents the response behavior of the system to a range of harmonic excitations. To this end, a pseudo-random binary signal (PRBS), a chirp signal or, simply, white noise are appropriate and common choices of a frequency-rich input signal.

FIR model structure : A Finite Impulse Response model links the present output to past inputs in the form

$$y = \mathsf{G}_{uy}u \quad \Rightarrow \quad y(k) = \sum_{j=0}^{\mu-1} H_j u(k-j) \tag{6}$$

where $y(k)$ is a short-form for $y(k\Delta t)$ with Δt as the discrete time-step, H_j stands for the j^{th} impulse response coefficient (also referred to as the j^{th} Markov parameter), and μ is the length of the impulse (order of the model). H^u and H^s are the Markov parameters associated with the two transfer functions to be identify : G_{uy} and $\mathsf{G}_{wy}\mathsf{G}_{ws}^{-1}$.

$$y(k) = \sum_{j=0}^{\mu-1} H_j^u u(k-j) + \sum_{j=0}^{\mu-1} H_j^s s(k-j). \tag{7}$$

Least-squares identification : Denoting by $\widehat{y}(k; H^u, H^s)$ the output predicted by the identified model, the identification error E may be written as the 2-norm distance between the exact (measured) output y and its estimation :

$$E(H^u, H^s, Z_N) = \frac{1}{N}\sum_{k=1}^{N} \|y(k) - \widehat{y}(k; H^u, H^s)\|_2 \tag{8}$$

where Z_N stands for a compound vector containing the input and output signals, i.e., $Z_N = (u(k)_{k=1,N},\ y(k)_{k=1,N}$, The identification procedure then corresponds to the minimization of E, resulting in

$$(H^u, H^s) = \arg\min_{H^u, H^s} E(H^u, H^s, Z_N). \tag{9}$$

Details about the optimization algorithm may be found in [6]. The identification problem may be split : first no actuation is given to the flow and the Markov parameters H^s are identified ; then, the parameters H^u are identified using the actuated configuration.

Using the identified Markov parameters $H^{s,u}$ the two transfer functions G_{uy} and $\mathsf{G}_{wy}\mathsf{G}_{ws}^{-1}$ are formed. The final step consists of multiplying the inverse of G_{uy} to the transfer function $\mathsf{G}_{wy}\mathsf{G}_{ws}^{-1}$.

4.1.2 Disturbance-rejection control design

Model Predictive Heuristic Control (MPHC) [5] is applied to arrive at a regularized inverse and a robust expression for the transfer function $\mathsf{G}_{uy}^{-1}\mathsf{G}_{wy}\mathsf{G}_{ws}^{-1}$. The MPHC approach determines the Markov parameters of the transfer function C_{su} such that the signal u minimizes the cost functional J given by

$$J = \sum_{k=0}^{\mu-1} y(k)^2 + \alpha \sum_{k=0}^{\mu-1} u(k)^2 \tag{10}$$

where the scalar α balances the control cost and the measured objective signal — a penalization that prevents excessively large values for the control u.

In its impulse response form, the transfer function C_{su} can be written

$$u(k) = \sum_{j=0}^{\mu-1} L_j s(k-j), \tag{11}$$

with L_k as the k^{th} Markov parameter. MPHC consists of building the transposed (upper triangular) Toeplitz matrix $\mathcal{T}^T$ containing the Markov parameters of G_{uy}, i.e.,

$$\mathcal{T}^T = \begin{pmatrix} H_0^u & H_1^u & \cdots & H_\mu^u \\ & H_0^u & \cdots & H_{\mu-1}^u \\ & & \ddots & \vdots \\ & & & H_0^u \end{pmatrix}. \tag{12}$$

Then, by introducing S as the vector of Markov parameters of G_{sy},

$$S = (H_0^s, H_1^s, \ldots, H_{\mu-1}^s)^T, \tag{13}$$

and L as the vector of (unknown) Markov parameters of the desired transfer function C_{su}

$$L = (L_0, L_1, \ldots, L_{\mu-1})^T, \tag{14}$$

the cost functional J may be reformulated in the more compact form

$$J(L) = \|S + \mathcal{T}L\|^2 + \alpha\|L\|^2 \quad \rightarrow \quad \min \tag{15}$$

which attains its minimum for (see [6])

$$L = -(\mathcal{T}^T\mathcal{T} + \alpha I)^{-1}\mathcal{T}^T S. \tag{16}$$

The desired transfer function of the controller is determined directly from (16). The Markov parameters H^u and H^s have been identified earlier, which makes the computation of L straightforward and leads to the controller's transfer function according to

$$u(k) = \sum_{j=0}^{\mu-1} L_j s(k-j). \tag{17}$$

This expression concludes the computational procedure for the design of a controller using the MPHC framework.

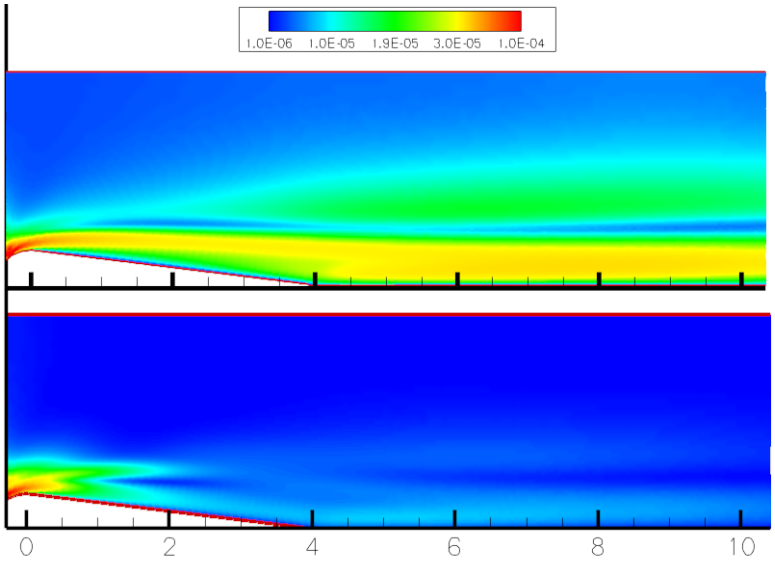

FIG. 10 – Uncontrolled (top) and controlled (below) flow around the airfoil. The colormap shows the fluctuations' intensity about the base flow. Applying a disturbance-rejection controller reduces the fluctuation intensity.

4.2 Numerical simulation

The simulation is based on the linearized Navier-Stokes equations for the evolution of perturbations around the mean flow. The Reynolds number is $Re_c = 1600$. Actuation and sensor placement correspond to the set-up used the previous section. The controller is computed using the previously defined MPHC algorithm. Figure 10 shows the amplitude of the fluctuation around the mean flow of the streamwise component. The uncontrolled case (on top) shows yellow and red contours behind the airfoil where the fluctuations are high compared to the freestream values. When the control is applied, the bulk of the fluctuations are damped to a rather low level. The fluctuation energy is diminished to about 10% of its initial value. Despite this encouraging result, we have to keep in mind the idealized nature of the flow : linear governing equations, convectively dominated flow, and the absence of measurement disturbances.

4.3 Experimental shear layer

We aim at controlling disturbances traveling into the shear layer using a data-based model. The model describes the effect of the control input and the effect of the incoming disturbances on the flow. The most challenging step is the identification of the incoming disturbances; indeed, the optimization problem is often ill-posed due to the narrow spectral content of the upstream sensor. Because the input spectrum is chosen broad, which makes the identification problem well-posed.

First, incoming disturbances and output data-sequences from the hot-films were recorded and analyzed. No linear system can predict the evolution of the sensor downstream solely from the upstream sensor information — even after employing different pre-processing operations (filtering, removing the mean, extracting only the frequency at which the shear layer responds). Since the identification fails at predicting the evolution of the flow between the leading and trailing edge, an intermediary step is designed which consists of using PIV measurements as incoming disturbances and as output. Because PIV measurements contain the velocity everywhere in the measured flow field, we can assess the conditions when flow structures become too nonlinear to be identified by a linear model. A Single Input Multiple-Output (SIMO) linear system identification is designed to identify a transfer function

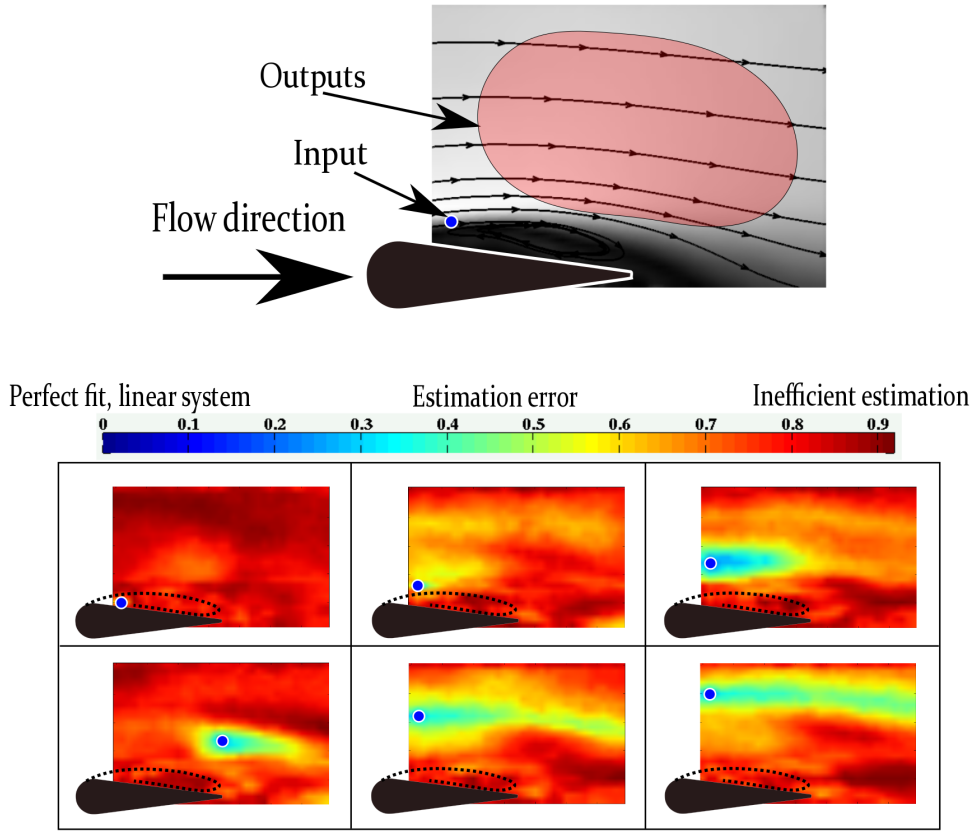

FIG. 11 – Linear identification error, the blue point is the chose input, the rest of the field represents the set of outputs.

between one location (the input) and the rest of the flow field (the output). For each of these transfer functions, an estimation error E_r is computed ; it is a measure of the accuracy of the identified model

$$E_r = \frac{\sum_{k=1}^{N} \|y(k) - \widehat{y}(k; H^s)\|_2}{\sum_{k=1}^{N} \|y(k)\|_2}. \tag{18}$$

Given a point in the flow field (the input), a map can be determined which identifies the regions (the outputs) that are linearly related to that point. Figure 11 shows different colormaps, which represent the estimation error from linear identification. For each of these colormaps, one point is chosen to be the input, the rest of the field are outputs. If the flow can be estimated by a linear system and by knowing the input, our linear-control framework may produce satisfactory results. If, on the other hand, the flow cannot be estimated linearly, our control design efforts will certainly fail. It appears that fluctuation can be predicted as they propagate in the freestream. It is also shown (on the first two colormaps) that the estimation of fluctuations is rather inaccurate near the recirculation bubble and on the shear layer. This figure provides evidence that our controller, based on this particular sensor set-up, will likely fail. This, however, does not imply that no controller is capable of reducing the fluctuations in the shear layer ; only our specific configuration will be unsuccessful.

5 Conclusions and perspectives

In this study, an analysis of the flow over an idealized airfoil has been conducted. The unstable shear layer has been found to be convectively dominated. However, identification of its behavior using linear

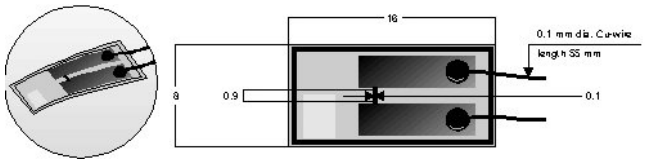

FIG. 12 – Drawing of glue-on films for anemometry measures. The conductance of the film varies with its temperature, directly linked to the velocity thermal conduction of the fluid.

system identification failed, as an estimation error analysis showed.

Identification of the linear part of the flow : Looking at [14], it appears that, even though the turbulent boundary layer is nonlinear, linear identification and control can be effectively applied.

The sensor-actuator placement in their work is much more compact, and nonlinear effects do not negatively influence the identification process. As was shown in figure 11, linear identification decreases in accuracy with the distance to the input. Moving input and output closer together (as in [14]) allows an efficient control.

Non-linear identification : Nonlinear identification and control may also be employed to bypass the accuracy problem. A Hammerstein-Wiener nonlinear system showed some significant improvement in identification accuracy (not plotted here) and seems to provide a favorable framework for shear layer control beyond a linear approach. Identification may be performed using Ljung's classical PEM method [11], or using different identification algorithms [2]. Nonlinear control design has already been developed (see, e.g., [4]), which would facilitate an effort towards such flow control applications.

A Constant temperature anemometry

The anemometry makes use of the convective heat-transfer phenomenon : velocity variations around the probe change the probe's temperature. This temperature variation produces a change in the electrical resistance of the probe. This resistance variation can then be sensed with a constant-temperature anemometer composed of a Wheatstone bridge and a servo amplifier. Finally, the analog electric tension from the amplifier may be acquired via an analog/digital card. As may be expected, the relationship between the acquired tension and the velocity around the probe is nonlinear. An example of this issue is the relationship for hot-wires that may be described by a 5^{th}-order power-law as shown in [10] :

$$U = C_0 + C_1 E + C_2 E^2 + C_3 E^3 + C_4 E^4 + C_5 E^5. \tag{19}$$

The hot-films used in our experiment (see figure 12) are a special version of the flush-mounting probes, where the sensor is deposited on a 50 μm thick Kapton foil. The sensor is $0.9 \times 0.1\text{mm}^2$ and connected to gold-plated lead areas (middle of the figure 12). The film is glued directly onto the wall where time-resolved information about the velocity is required. Even if this type of sensors is primarily intended for qualitative measurements of transition and separation points, it is used here for the acquisition of time-varying data-sequences. A typical mounting of the sensor onto the airfoil is shown in figure **??** where the film is placed on the leading edge, near the separation point. The airfoil, with sensors, in the tunnel is shown in figure 13. In our experiment, two Dantec glue-on hot-films with nominal resistance of 9.8 and 11 Ohms are used, placed at the leading and trailing edge of the profile.

Références

[1] J.C. Akers and D.S. Bernstein. Armarkov least-squares identification. In *Proceedings of the American Control Conference*, pages 186–190, Albuquerque, New Mexico, USA, 1997.

[2] Er-Wei Bai. An optimal two-stage identification algorithm for hammerstein–wiener nonlinear systems. *Automatica*, 34(3) :333–338, 1998.

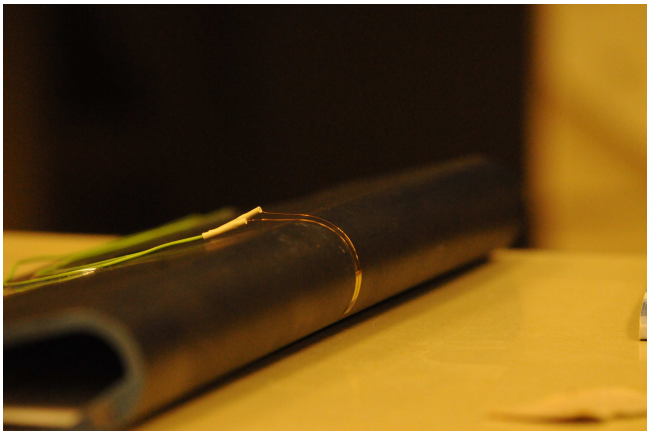

FIG. 13 – Hot-film placement on the airfoil. Bboundary layer perturbations are sensed on the leading edge. The wires are placed on the uncontrolled side.

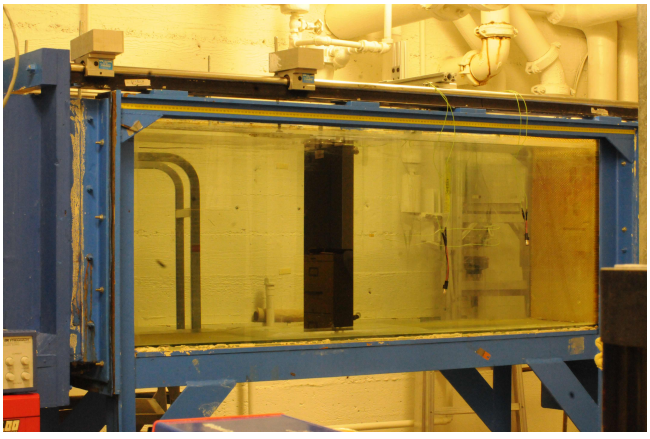

FIG. 14 – Image of the airfoil in the tunnel. The flow is from left to right.

[3] George Keith Batchelor, Henry Keith Moffatt, and MG Worster. *Perspectives in fluid dynamics : a collective introduction to current research*. Cambridge University Press, 2002.

[4] HHJ Bloemen, TJJ Van Den Boom, and HB Verbruggen. Model-based predictive control for hammerstein - wiener systems. *International Journal of Control*, 74(5) :482–495, 2001.

[5] E.F. Camacho and C. Bordons. *Model Predictive Control*. Number XXII in Advanced Textbooks in Control and Signal Processing. 2nd edition, 2004.

[6] Nicolas Dovetta, Fabien Juillet, and Peter J Schmid. Data-based model-predictive control design for convectively unstable flows. *Underconsideration for publication in Journal of Fluid Mechanics*, 2013.

[7] M. Gharib. *The effect of flow oscillations on cavity drag, and a technique for their control*. PhD thesis, California Institute of Technology, 1983.

[8] C. Gonzalez, J.-F. Bruhat, B. Wainfan, and B.J. McKeon. Control of laminar separation on an idealized airfoil using periodic dynamic roughness actuation. In *Gallery of Fluid Motion Poster 26*. Long Beach, CA, 63rd meeting of the american physical society division of fluid dynamics edition, November 2010.

[9] Fabien Juillet, Peter J Schmid, and Patrick Huerre. Control of amplifier flows using subspace identification techniques. *Journal of Fluid Mechanics*, 725 :522–565, 2013.

[10] Louis Vessot King. On the convection of heat from small cylinders in a stream of fluid : determination of the convection constants of small platinum wires, with applications to hot-wire anemometry. *Proceedings of the Royal Society of London. Series A*, 90(622) :563–570, 1914.

[11] L. Ljung. *System identification Theory for the user*. Prentice-Hall, Inc., Englewood Cliffs, New Jersey, 1987.

[12] A. Norman and B. J. McKeon. Effect of sting size on the wake of a sphere at subcritical reynolds numbers. *38th Fluid Dynamics Conference and Exhibit*, (2012-4183), June 2008.

[13] A. Prasad and C.H.K. Williamson. The instability of the shear layer separating from a bluff body. *Journal of Fluid Mechanics*, 333 :375–402, 1997.

[14] Ruben Rathnasingham. System identification and active control of a turbulent boundary layer. Technical report, Aerospace Computational Design Lab, Dept. of Aeronautics & Astronautics, Massachusetts Institute of Technology, 1997.

[15] Peter Schmid. Dynamic mode decomposition of numerical and experimental data. *Journal of Fluid Mechanics*, 656 :5–28, 8 2010.

[16] R. D. Wallace and B. J. McKeon. Laminar separation bubble manipulation with dynamic roughness. *6th AIAA Flow Control Conference, New Orleans, Louisiana*, (2012-2680), June 2012.

[17] DR Williams, C Rowley, T Colonius, R Murray, D MacMartin, D Fabris, and J Albertson. Model-based control of cavity oscillations part i : Experiments. *AIAA paper*, 971 :2002, 2002.

[18] Serhiy Yarusevych, Pierre E Sullivan, and John G Kawall. Coherent structures in an airfoil boundary layer and wake at low reynolds numbers. *Physics of Fluids*, 18 :044101, 2006.

Chapter 4

Data-assimilation of mean flows

Contents

4.1 Introduction

Data-assimilation is a numerical technique for the identification of model-parameters from observed measurements. It can be used for the interpolatory or extrapolatory recovery of unobserved physical quantities.

Data-assimilation was first developed for meteorological applications to reconstruct and predict time-evolving atmospheric flows and weather patterns, from measurements which were dispersed over the entire globe. More recently, data-assimilation has been employed in many other research domains, for example in structural and fluid dynamics (see Avril *et al.*, 2008; Apte *et al.*, 2010; Tissot *et al.*, 2011; Bukshtynov *et al.*, 2011).

Underlying any data-assimilation effort is a physically motivated model postulated by the user, to which the observed data will be optimally matched. For this reason, the cost of data-assimilation not only involves the simulation of the model, but also the additional cost involved in the optimization procedure. Data-assimilation thus exceeds numerical simulation in computational cost and effort. In particular, the time-resolved assimilation of high-Reynolds number time-varying problems is often beyond the capabilities of today's computer resources; nonetheless, research in this area is very active. For example, Daescu & Navon (2007) address the high cost of time-resolved data-assimilation by using reduced-order physics-based models during the optimization step, yielding an affordable assimilation technique. Alternatively, the computational cost associated with time-varying problems can also be diminished by concentrating on mean quantities and averaged models. Following this concept, a data-assimilation algorithm for mean-velocity measurements is

developed in this chapter where the parametric model is taken as the Reynolds-Averaged Navier-Stokes (RANS) equations, and the processed data-set is based on mean-velocities only. Parametrization of the RANS equations is accomplished by assuming an unknown Reynolds stress tensor. In this particular case, no additional assumptions related to closure, *e.g.* a Boussinesq hypothesis, $k-\varepsilon$ or other turbulence models, are needed. Therefore, besides being mainly used for reconstructive purposes, data-assimilation of mean-velocity measurements can also be performed to extract turbulent statistics without postulating any closure assumptions.

As the output of data-assimilation is a model that optimally fits a given data-set, it can also be applied to control design (passive or active) where it provides the underlying plant model; even though this appears to be an interesting application of data-assimilation, this aspect will not be pursued within the scope of this thesis.

Data-assimilation algorithms have recently produced impressive results in a wide range of applications; however, it seems rather difficult to *a priori* estimate the performance of a specific algorithm, owing to the sensitivity to model details and data inaccuracies, as well as to the non-linear nature of the optimization problem. For this reason, we simply demonstrate the efficiency of our mean-velocity assimilation on three different examples: an experimental turbulent pipe-flow, a numerical simulation of flow around a cylinder, and an experimental flow over an idealized airfoil.

The first example (section 4.2) presents the assimilation of mean-velocity measurements taken from a turbulent-pipe flow at a Reynolds number of about $Re = 37000$. At such Reynolds numbers, the probe size limits the minimal distance from the wall at which measurements can be taken. The extrapolatory property of the assimilation procedure is thus particularly useful, as the mean velocity profile can be reconstructed between the last measurement point and the wall.

The experimental measurements have been performed by Mckeon *et al.* (2004) at the Superpipe facility of the Princeton Gas Dynamics Laboratory. The mean streamwise velocity has been measured at 57 locations in the radial direction. Using only 15 of these data-measurements as an input to the data-assimilation algorithm, the entire mean-flow profile is reconstructed (see figure 4.1). Also included in this figure is the relative error between the reconstructed flow and the 57 true measurements of the mean-velocity profile. As can be seen, the relative error is relatively high far from the 15 data-measurements taken for the reconstruction but rather low near these points. The result of this 1D assimilation problem is not satisfying in itself, but it gave useful information about the behavior of such an adjoint-based optimization problem. An estimation of the Reynolds number and pressure drop have been obtained from the data-assimilation procedure; the values ($Re = 36235$, $\Delta p = 4.72 Pa.m^{-1}$) are not too far from a classical Spalding profiles estimation ($Re = 37155$, $\Delta p = 6.87 Pa.m^{-1}$).

Section 4.3 focuses on a numerical simulation of flow around a cylinder at a Reynolds number of $Re = 150$. Different input data-sets are processed to reconstruct the mean flow field while demonstrating the capability of interpolation, extrapolation and variable reconstruction during the assimilation process. Among these options, figure 4.2 illustrates an example of interpolatory and state-variable

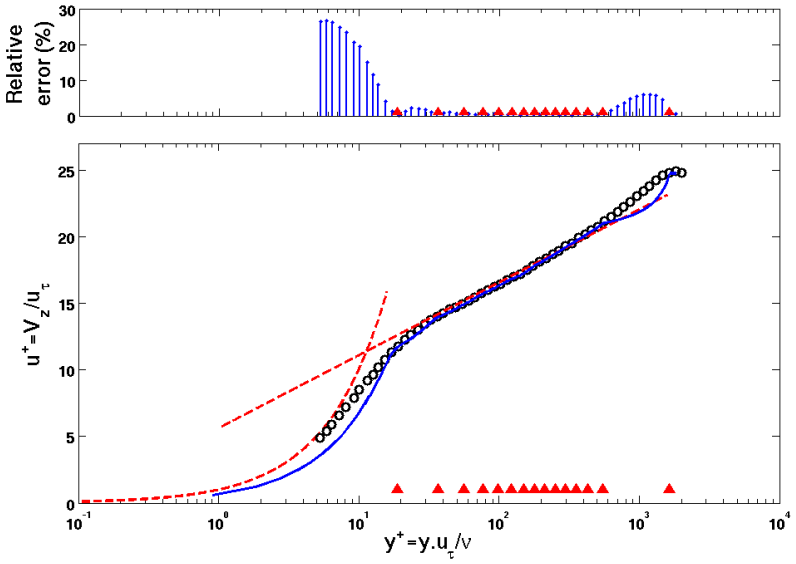

Figure 4.1: Mean velocity versus wall distance (in inner scales). Black circles, measurements ; blue line, reconstructed velocity field ; red dashed line, asymptotic solutions for the viscous and log layers. The error between the reconstructed and measured mean velocities is shown in the upper sub-plot, quantified by percentage of the measured velocity.

reconstruction based on velocity magnitude measurements. First, the full flow field is computed using a direct numerical simulation of the two-dimensional Navier-Stokes equations (top sub-figures), from which the velocity magnitude is extracted (middle sub-figure). This latter magnitude is then used as input for the assimilation procedure based on a two-dimensional RANS model resulting in the reconstructed velocity flow fields shown in the bottom sub-figures. This example demonstrates the successful recovery of full mean flow information on a fine grid from magnitude data sampled on a coarse grid.

Even if the velocity magnitude measurements are artificially polluted by white noise, the individual velocity components could be reconstructed with sufficient accuracy. This fact proves encouraging for an application of data-assimilation techniques to experimentally measured and/or more complex mean flows.

The idealized airfoil is identical to the one described in chapter 3, but a two-camera PIV measurement system has been used to extract flow-field measurements. Physically, two competing instability mechanisms are present in the flow: the convectively unstable shear layer bounding the recirculation bubble, and the absolutely unstable Von Karman vortex-street forming at the trailing edge of the profile. The objective of the assimilation procedure is to reconstruct the entire flow field using only 20 measurement locations, for which the streamwise and normal velocity components are recorded.

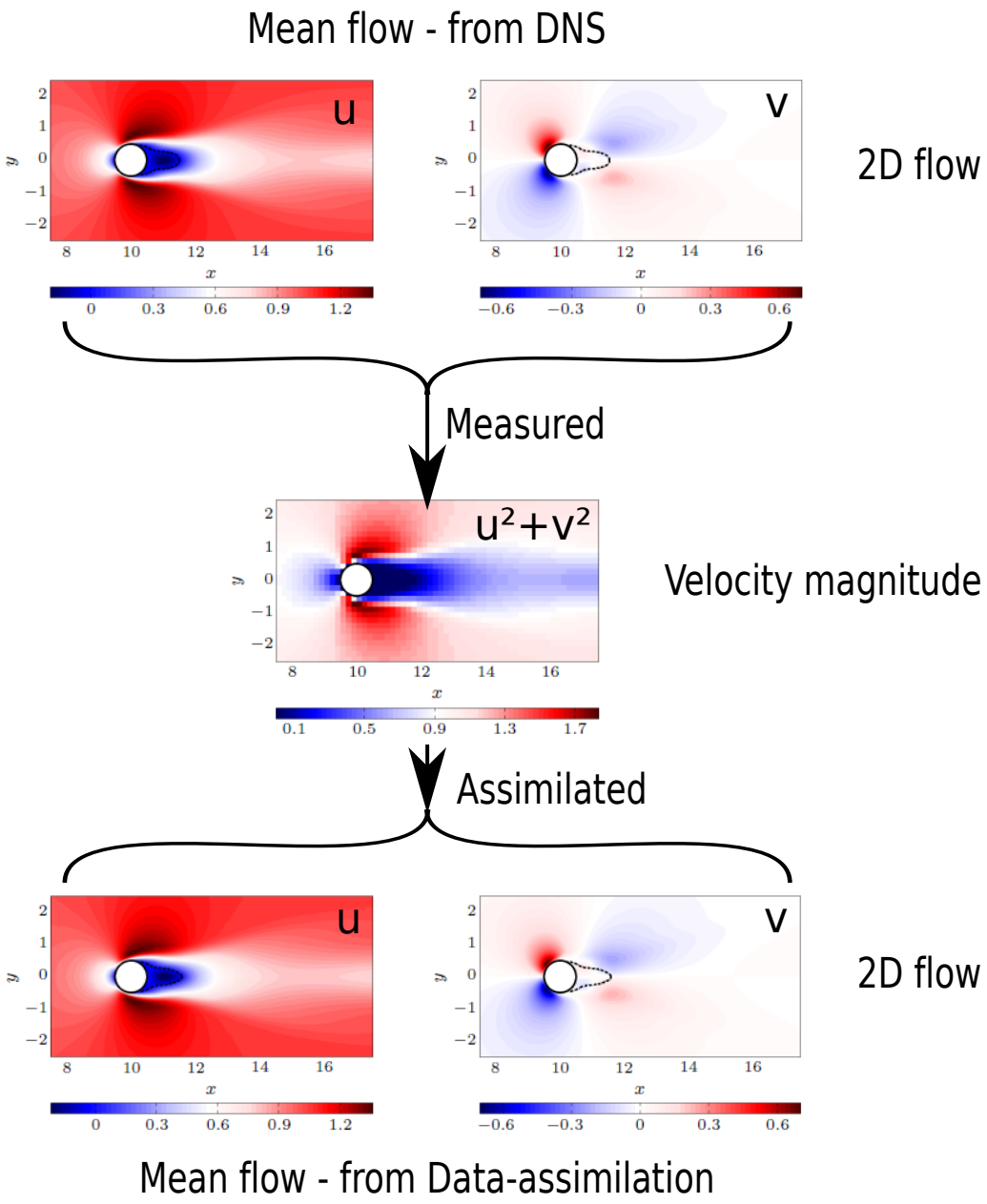

Figure 4.2: Mean velocity reconstruction by data-assimilation of velocity magnitude measurements. Top: initial mean flow from a direct numerical simulation, (left) streamwise velocity component, (right) normal velocity component; Middle: velocity magnitude on a coarsened grid, taken as the input to the assimilation algorithm; Bottom: reconstructed flow fields, (left) streamwise velocity component, (right) normal velocity component.

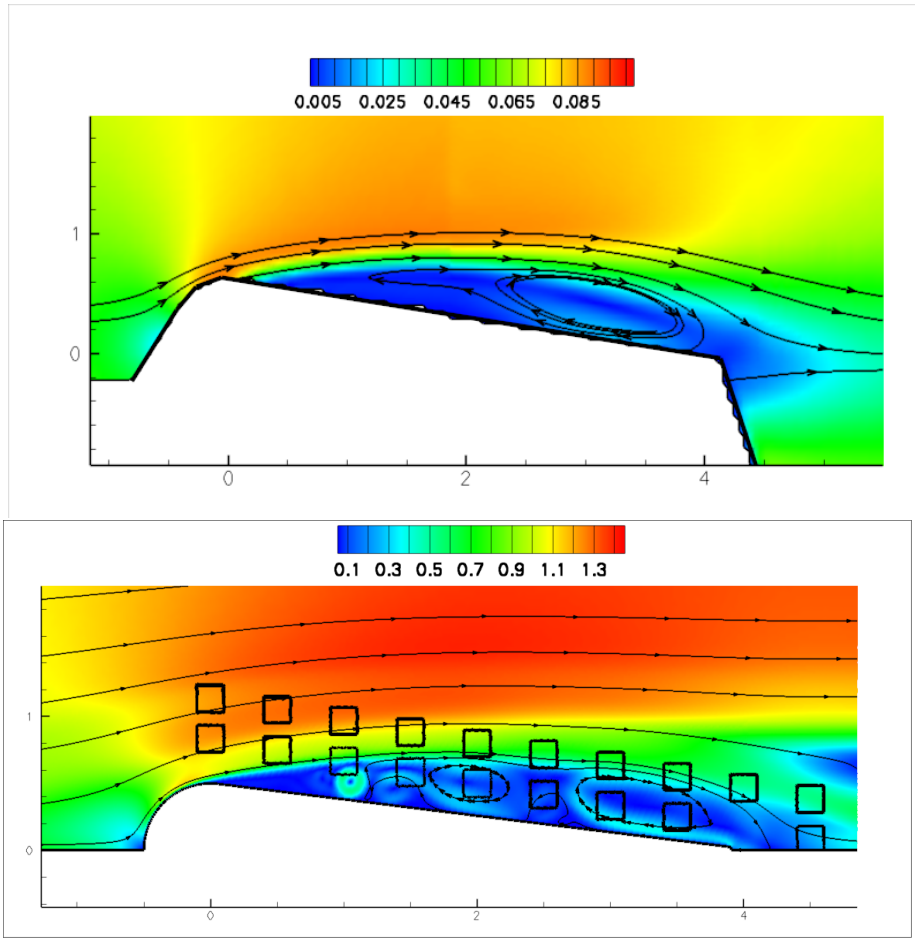

Figure 4.3: Top: mean velocity field from averaging time-resolved PIV measurements, visualized by color contours of the velocity magnitude and streamlines; Bottom: reconstructed flow field using data-assimilation, visualized as above. The black squares indicate the measurement locations that serve as input to the data-assimilation algorithm.

Figure 4.3 shows, on top, the mean velocity determined from averaging the time-resolved PIV measurements (color-contours of velocity magnitude and streamlines). The lower figure displays the reconstructed mean-velocity field from our assimilation procedure. The 20 measurement locations which act as input to the assimilation are shown in black squares. Even though the details of the reconstructed flow confined to the interior of the separation bubble do not agree with the true averaged measurements, the remaining flow features are well-captured, both qualitatively and quantitatively.

These three examples are probing the performance but also the limitations of data-assimilation techniques for mean-velocity recovery from under-sampled data using an underlying RANS model. More details for each of these cases will be presented in what follows.

4.2 Article : Data-assimilation for mean flow and shear stress reconstruction

Submitted to Physics of Fluids

Data-assimilation for mean-flow and shear-stress reconstruction

Nicolas Dovetta*
LadHyX, Ecole Polytechnique, F-91128 Palaiseau, France

Beverley J. McKeon†
GALCIT, California Institute of Technology, Pasadena, CA 91125, U.S.A.

Dimitry P. G. Foures‡
DAMTP, University of Cambridge, Cambridge, CA1 2AB, U.K.

Peter J. Schmid§
Dept. of Mathematics, Imperial College London, London SW7 2AZ, United Kingdom

Denis Sipp¶
DAFE-ONERA, 91170 Meudon, France

(Dated: April 24, 2014)

Experimental measurements can be thought of as low-order representations of a given flow. Data-assimilation allows the optimal reconstruction of full flow fields or of unmeasured and/or unobservable quantities by that complying with a model of the underlying physics. An assimilation technique that reconstructs mean-flow quantities from a few measurements of a turbulent flow is presented. The Reynolds stress tensor is used as an adjustable parameter of the Reynolds-Averaged Navier-Stokes equations (RANS), in order to match the solution to the measured velocity values. Using this procedure, the mean flow is fully reconstructed and the Reynolds stress tensor is identified. A pipe flow at a Reynolds number of $Re = 37155$ (measurements taken from [10]) is considered. The mean-velocity measurements in combination with the RANS equation allow the reconstruction of the turbulent moments and other unmeasured quantities from only a few measurement points; they compare favorably with the full profile. From this reconstruction the wall shear stress, a quantity that is difficult to determine experimentally, can be calculate without resorting to common semi-empirical velocity profiles, such as given by *e.g.* Spalding[15] or Musker[14].

* dovetta@ladhyx.polytechnique.fr
† mckeon@caltech.edu
‡ foures@damtp.cam.ac.uk
§ peter.schmid@imperial.ac.uk
¶ sipp@onera.fr

I. INTRODUCTION

In this article it is shown how a mean-velocity profile can be optimally reconstructed from a rather limited number of mean-velocity measurements from a turbulent boundary layer. Based on the Reynolds-Averaged Navier-Stokes equations, an optimization technique is presented that uses the few experimental mean-flow measurements to provide a full profile that allows the evaluation of the mean velocity across the boundary layer and, more importantly, close to the wall where precise measurements are difficult or prohibitive to attain.

Data-assimilation is the chosen approach to solve this reconstruction problem. In general, it refers to a family of techniques that use observations, a model and a fitting criterion to build what is commonly referred to as an assimilated or fitted model. Data-assimilation has its roots in meteorology where predicting the future evolution of the atmosphere's characteristics has to take into account the scattered weather data from around the world. Within this context, two types of estimation problems may be distinguished [9]: (i) estimation of the state variables (*e.g.* atmospheric pressure, temperature, velocity) at a given time using a spatial distribution of measurements available at that time (referred to as off-line or fixed-sample estimation), or (ii) estimation of the future state-vector trajectory corrected with the available data (known as online, recursive or sequential estimation). The mean-flow reconstruction technique from turbulent measurements, treated in this article, falls into the first category, as the temporal dimension is removed by averaging in time. Data-assimilation technique for off-line state estimation can either rely solely on past measurements and neglect explicit physical constraints, or take into account a specified physical model under a weak or strong formulation. Among the statistical approaches for noisy data, the Wiener-filtering methods are most popular and widely used, especially as part of algorithms such as the optimal interpolation (OI) method or the Kriging technique, well known in the atmospheric flow-prediction community [6, 8]. In fluid mechanics, methods approximately related to data-assimilation have been used to reconstruct gaps in particle image velocimetry (PIV) measurements [4] or to improve the standard PIV algorithm [11].

In our work, the Reynolds-Averaged Navier-Stokes (RANS) equations are enforced as a strong constraint during the assimilation process. This means that the estimated states (mean velocity and turbulent moments) will be solutions of the RANS equations. When using the strong-constraint form, the underlying model has to be flexible or compliant to be able to fit the data. The compliance of a model refers to a set of selected parameters that are adjustable in the model. Choices of parameters are, for example, an initial or inflow condition as in [1, 7, 12] or a material property as in [2, 5]. In our application, a compound quantity involving the unknown Reynolds stress tensor and the pressure drop is taken as the compliance parameter; the state is the mean-velocity field. Data-assimilation problems based on strong constraints can be recast into a variational formulation [3] which then allows an iterative solution following a gradient-based optimization method. In the end, a distance measure between the data and the model-estimated mean-velocity profile is minimized, which results not only in the recovered profile but also in the associated values of the compliance parameters.

II. MOTIVATION

Two principal motivations for the current work shall be highlighted. The first is concerned with the reconstruction of a turbulent boundary layer profile from limited measurements with no accessory assumptions on the behavior of different layers. Indeed, wall-shear estimation is often realized using semi-empirical profiles (such as, *e.g.* Spalding or Musker profiles). With the data-assimilation approach, only the (one-dimensional) Reynolds-Averaged Navier-Stokes equations are postulated and enforced. No further empirical input is necessary. An additional motivation is the identification of turbulent mean quantities and the improvement of mean PIV-measurements in two and three spatial dimensions; this present article is a first step in this direction.

III. ASSIMILATION PROCEDURE

Three components are required for an assimilation procedure: an underlying model, compliance parameters and measured data. In this work, we use the Reynolds-Averaged Navier-Stokes equations as a model, the Reynolds shear stress, pressure drop and Reynolds number as compliance parameters, and mean-velocity measurements from the experiment as input data. The goal then is to find the values of the compliance parameters such that the recovered mean-velocity profile matches the measured values.

A. Model equation

The model equation in our case is the axial (z) momentum part of the one-dimensional Reynolds-Averaged Navier-Stokes (RANS) equations in radial coordinates under the assumption of a fully developed turbulent pipe flow. It reads

$$\frac{\nu}{r}\frac{\partial}{\partial r}\left(r\frac{\partial V_z}{\partial r}\right) - \frac{1}{r}\frac{\partial\left(r\overline{V_r'V_z'}\right)}{\partial r} - \frac{\partial p}{\partial z} = 0 \tag{1}$$

where ν is the kinematic viscosity of the fluid, V_z stands for the axial mean velocity, taken as a function of the radius r, $\partial p/\partial z$ represents the constant axial pressure drop and $\overline{V_r'V_z'}$ is the Reynolds stress component that affects the axial momentum equation (again, taken as a function of the radius only). This equation establishes a link between the mean velocity and both the turbulent Reynolds stress and the pressure drop. The boundary conditions are $V_z = 0$ and $\overline{V_r'V_z'} = 0$ at the wall ($r = R$), $\partial V_z/\partial r = 0$ and $\overline{V_r'V_z'} = 0$ on the pipe's centerline ($r = 0$). Integrating these equations through the pipe, we obtain the following force-balance equation:

$$\pi R^2\frac{\partial p}{\partial z} = -2\pi R\tau_w \tag{2}$$

where $\tau_w = -\nu\left.\frac{\partial V}{\partial r}\right|_{r=R}$ is the wall-shear stress (the minus sign has been added to make this quantity positive).

B. Type of measurements

Measurements of the mean velocity are taken from experiments conducted in the Princeton/ONR Superpipe facility, see [10], a facility capable of investigating fully developed turbulent pipe flow over a wide range of Reynolds numbers. The pipe has an internal diameter ($2R$) of about 13 centimeters, an aspect ratio of $L/(2R) = 200$ and a wall roughness of less than 0.15 millimeters. Mean velocities are measured with a Pitot tube at 57 different wall-normal locations. More detailed information about the experiment can be found in reference [10] and on the Gas Dynamics Laboratory website [**?**]. The kinematic viscosity was accurately evaluated to be: $\nu = 1.8487\times10^{-5}$???. For the data-assimilation procedure, only 15 measurements (of the 57 available wall-normal locations) will be considered, in order to validate the accuracy of the assimilation technique.

To formulate the optimization problem let $V_z^{mes}(r_i)|_{i\in[0:N]}$ denote the set of measured mean velocities. Here we assume that we have a measurement at the centerline of the channel ($r_0 = 0$, $V_z^{mes}(r_0) > 0$) and that $r_N = R$, which induces that $V_z^{mes}(r_N) = 0$ (no-slip condition).

Analogously, we define a set of computed mean velocities at the same radial locations $V_z(r_i)|_{i\in[0:N]}$. The goal of the data-assimilation algorithm is then to find the pressure drop and Reynolds stresses such that $V_z(r_i) = V_z^{mes}(r_i)$ for all indices $i \in [0 : N]$. Thus, a cost functional to minimize can be defined as the 2-norm of the difference between measured and computed sets of mean velocities according to

$$J(V_z) = \sum_{i=0}^{N}\left[V_z(r_i) - V_z^{mes}(r_i)\right]^2 r_i. \tag{3}$$

Minimization of this cost functional while respecting the underlying model leads to a constrained optimization problem.

C. Model compliance parameter

As mentioned above, the constant pressure drop and the radially dependent Reynolds stress component $\overline{V_r'V_z'}$ are taken as unknowns in the optimization problem. Based on the model equation (1), the unknown parameters and variables can be regrouped into one variable, a composite function of the radius $g(r)$ satisfying:

$$\frac{1}{r}\frac{\partial}{\partial r}\left(r\frac{\partial V_z}{\partial r}\right) = \frac{1}{r}\frac{\partial}{\partial r}\left[rg(r)\right]. \tag{4}$$

The following boundary condition $V_z(r = 0) = V_z(r_0)$ has to be applied to compute V_z from g. Using $g(r_0) = 0$ (symmetry condition), we obtain:

$$\frac{\partial V_z}{\partial r} = g(r), \tag{5}$$

so that: $V_z(r) - V_z(r_0) = \int_{r_0}^{R} g(r')dr'$.

Once g and V_z have been identified, we may obtain a value for the pressure gradient and the Reynolds shear-stress:

$$\frac{\partial p}{\partial z} = \frac{2\nu g(R)}{R} \tag{6}$$

$$\overline{V_r' V_z'} = \nu \left[g(r) - \frac{r}{R} g(R) \right]. \tag{7}$$

The Reynolds number may then be computed as $Re = V_m R/\nu$, where $V_m = 2\int_0^R r' V dr'/R^2$ is the actual mean mass-flow rate. The wall shear-stress τ_w may finally be obtained from Eq. (2), the friction velocity from $u_\tau = \sqrt{\tau_w}$ and the friction length-scale from $\delta^+ = \nu/u_\tau$.

D. Optimization

The objective of the optimization step is to find a scalar function g, such that the solution of (5) minimizes the cost functional J defined in (3). This constrained optimization problem is easily transformed into an unconstrained problem using an augmented Lagrangian formulation. We define

$$\mathcal{L} = J(V_z) - \int_0^R \left[\frac{\partial V_z}{\partial r} - g(r') \right] u^\dagger(r')\, r' dr' \tag{8}$$

which introduces $u^\dagger$ as the solution to the adjoint one-dimensional governing equation. The minimization of this augmented Lagrangian $\mathcal{L}$ will ensure the minimization of J and the enforcement of the RANS equation.

An iterative algorithm can be derived by taking the first variations of the Lagrangian functional $\mathcal{L}$ with respect to all involved variables and setting these first variations to zero. The first variation with respect to $u^\dagger$ recovers the governing equation (5), while the first variation with respect to V_z yields an adjoint RANS-equation for the adjoint variable $u^\dagger$ which reads

$$\frac{1}{r}\frac{\partial}{\partial r}\left[r u^\dagger(r) \right] = -\sum_{i=0}^{N} 2\left[V_z(r) - V_z^{mes}(r_i) \right] \delta(r - r_i). \tag{9}$$

This yields:

$$u^\dagger(r) = -r^{-1} \sum_{r_i \le r} 2\left[V_z(r_i) - V_z^{mes}(r_i) \right] r_i, \tag{10}$$

Note that any mismatch between the assimilated profile and the true measurements acts as driving term in the adjoint term. Finally, the first variation with respect to the function g results in an optimality condition, expressed as a gradient of the cost functional with respect to g. We obtain

$$\nabla_g J = u^\dagger \tag{11}$$

which can be used in any standard gradient-based optimization algorithm to iteratively find the minimum of J.

Using a steepest-gradient descent method, the final solution g is a sum of a series of gradients u^{dag}. Hence, since $u^\dagger(0) = 0$ and $u^\dagger(R) \neq 0$, we can see that: $g(0) = 0$, which is consistent with the assumptions, and $g(R) \neq 0$, which ensures $\partial p/\partial z \neq 0$.

E. Results

Before presenting the results of the data-assimilation process, we introduce the wall-normal coordinate y^+ in inner units defined as $y^+ = (R - r)/\delta^+$, the axial mean velocity scaled by the friction velocity $V_z^+ = V_z/u_\tau$, and by the mean velocity averaged over the pipe radius $V_z^* = V_z/V_m$, the Reynolds shear-stress scaled by the friction velocity $\overline{V_r' V_z'}^+ = \overline{V_r' V_z'}/u_\tau^2$.

Figure 1 displays the mean velocity recovered from a limited number of data points (indicated by red symbols) using the data-assimilation algorithm. The full mean-velocity profile is successfully reconstructed, with satisfactory accuracy at radial locations between the included data-points and in the near-wall region where measurements were unobtainable. These findings are further corroborated in figure 2 which presents the recovered mean-velocity profile (in

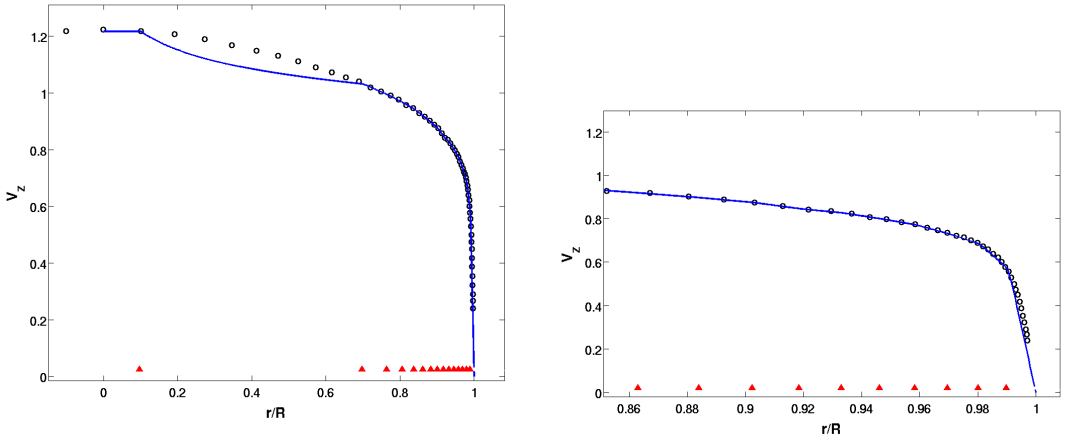

FIG. 1: Mean-velocity profile V_z versus the normalized radius r/R. Black symbols indicate true measurements, while the blue line displays the reconstructed mean-velocity profile using data-assimilation of a restricted set of measurements. The radii where velocity measurements entered the data-assimilation algorithm are shown as the red circles. (Left) mean-velocity profile over the entire pipe radius, (right) magnified region close to the pipe wall.

blue) in inner units and compares it to well-known asymptotic solutions for the viscous sublayer and the logarithmic layer. Good agreement is observed, even though only 15 experimental values have been used in the reconstruction procedure. Quantitatively, the relative error between the true measurements and the values from the data-assimilated mean-velocity profile never exceeds 0.5%. Again, the recovered mean-velocity profile gives accurate estimates for the near-wall region, extrapolating the measurements from the outer region. Finally, figure 3 shows the recovered Reynolds stress component $\overline{V_r' V_z'}^+$ versus the outer scale r/R and the inner scale y^+. Both the magnitude and shape of this cross-moment are comparable to the results found in direct numerical simulations [13]. As mentioned above, the data-assimilation procedure also produces the Reynolds number and the axial pressure drop. In our case, we recover a Reynolds number of $Re = 36235$ and an axial pressure drop of 4.72 $Pa\ m^{-1}$. These values should be compared to the values based on a semi-empirical Spalding profile, namely, $Re = 37155$ and 6.87 $Pa\ m^{-1}$.

As it can be observed the reconstruction lacks of smoothness, the optimisation is recovering a solution that satisfies the constrains (governing equation and matches the data). The solution plotted, as sharp as it is, does follow all the constraints that have been the input of the optimization problem. The formulation of the problem does not give any reason for such non-smooth (and presumably not physical) solution to be avoided. In order to obtain a solution of our optimization problem that is physically more relevant additional constraints have to be implemented. Such constraint could have many theoretical origin, such as the principle of total variation diminishing applied to the second derivative. The system may also be constraint by additional measurements as a total debit value which will force in every point instead of the local measurement data that have been applied here.

IV. CONCLUDING REMARKS

This article introduces a data-assimilation technique based on a variational formulation to reconstruct a turbulent mean-velocity profile from selected measurement values that complies with the one-dimensional Reynolds-Averaged Navier-Stokes equations for the mean flow. The Reynolds shear-stress, the axial pressure drop and the Reynolds number are used as parameters to attain a best fit to the measurements. The recovered mean-flow profile shows resonable agreement with results from numerical simulations and asymptotic results. The relative error is contained to small values around the measurement point but can reach over 30

Even though, data-assimilation is computationally more costly than commonly applied models (such as the Spalding profile), it does not rely on semi-empirical assumptions but rather enforces the full equations governing the mean velocity profile. It thus offers a potential alternative to recovering near-wall turbulent mean quantities, such alternative would be useable once more investigation is performed in order to obtain a smoother and more physical solution of

6

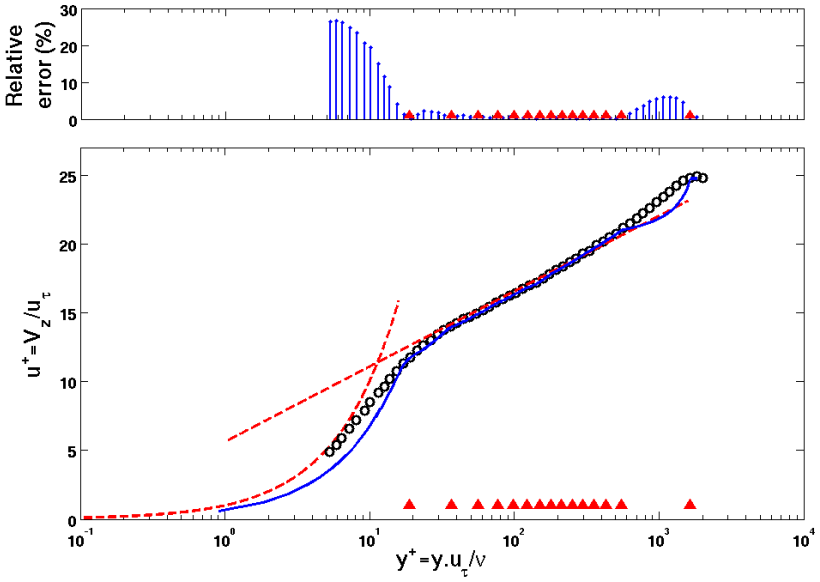

FIG. 2: Mean-velocity profile versus distance from the wall (in inner scales). Black symbols indicate true measurements. The blue line shows the reconstructed mean-velocity profile. The red dashed lines are asymptotic solutions for the viscous sublayer and the logarithmic layer, respectively. The relative reconstruction error is shown in the upper graph.

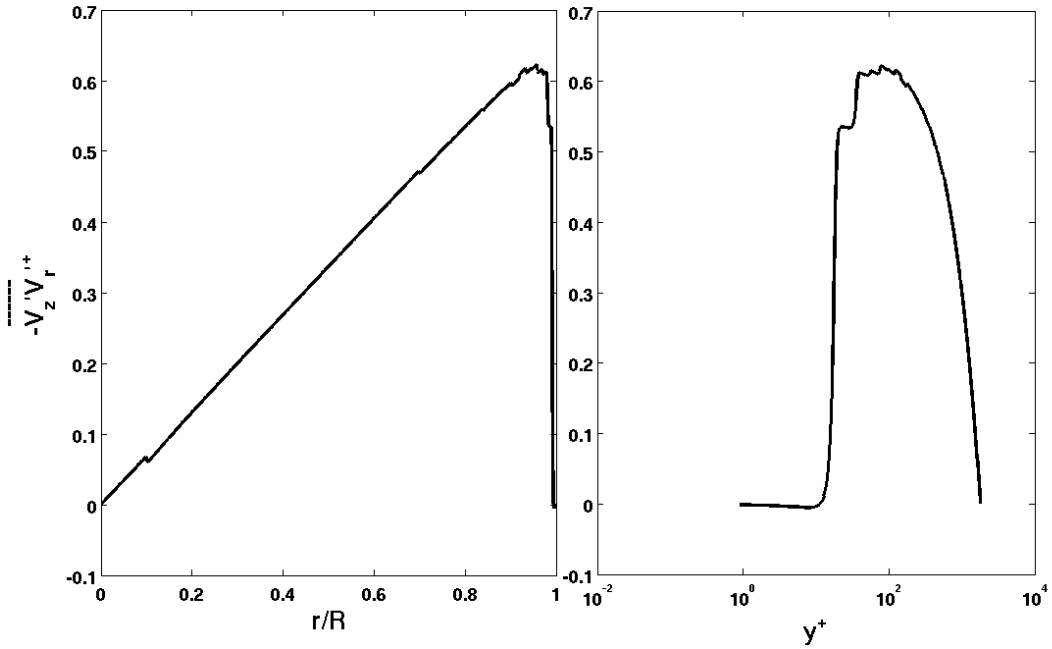

FIG. 3: Shear stress (normalized with the velocity scale u_τ) as a function of : the normalized radius (outer scale, left plot); the distance from the wall (inner scale, right plot).

the problem.

[1] Apte, A., Auroux, D., Ramaswamy, M. (2010) Variational data-assimilation for discrete Burgers equation. *U. Elec. J. Diff. Equ.*, **19**, 15–30.
[2] Avril, S., Bonnet, M., Bretelle, A.-S., Grédiac, M., Hild, F., Ienny, P., Latourte, F., Lemosse, D., Pagano, S., Pagnacco, E., Pierron, F. (2008) Overview of identification methods of mechanical parameters based on full-field measurements. *Exp. Mech.*, **48**, 381–402.
[3] Bardos, C., Pironneau, O. (2005) Data assimilation for conservation laws. *Meth. Appl. Anal.* **12**, 103–134.
[4] Bui-Thanh, T., Damodaran, M., Willcox, K.E. (2004) Aerodynamic data reconstruction and inverse design using proper orthogonal decomposition. *AIAA J.* **42**, 1505–1516.
[5] Bukshtynov, V., Volkov, O., Protas, B. (2011) On optimal reconstruction of constitutive relations. *Physica D* **240**, 1228–1244.
[6] Ghil, M., Malanotte-Rizzoli, P. (1991) Data assimilation in meteorology and oceanography. *Advances in Geophysics.*
[7] Gronskis, A., Heitz, D., Mémin, E. (2013) Inflow and initial conditions for direct numerical simulation based on adjoint data assimilation. *J. Comp. Phys.* **242**, 480–497.
[8] Kalnay, E. (2002) Atmospheric Modeling, Data Assimilation and Predictability. *Cambridge University Press.*
[9] Lewis, J.M., Lakshmivarahan, S., Dhall, S. (2006) Dynamic Data Assimilation: A Least Squares Approach. *Encyclopedia of Mathematics and Its Application 104, Cambridge University Press*, **13**.
[10] McKeon, B.J., Li, J.D., Jiang, W., Morrison, J.F., Smits, A.J. (2004) Further observations on the mean velocity distribution in fully developed pipe flow. *J. Fluid Mech.* **501**, 135–147.
[11] Ruhnau, P., Stahl, A., Schnörr, C. (2006) On-line variational estimation of dynamical fluid flows with physics-based spatio-temporal regularization. *Pattern Recognition*, **4174**, 444–454.
[12] Tissot, G., Cordier, L., Noack, B.R. (2011) Résolution d'un problème d'assimilation variationnelle 4D-VAR par des modèles réduits POD adaptatifs., *AFM.*
[13] Wu, X., Moin, P. (2008) A direct numerical simulation study on the mean velocity characteristics in turbulent pipe flow. *J. Fluid Mech.* **608**, 81–112.
[14] Musker, A.J. (1979) Explicit expression for the smooth wall velocity distribution in a turbulent boundary layer. *AIAA J.* **17**, 655–657.
[15] Spalding, D.B. (1961) A simple formula for the law of the wall. *J. Appl. Mech. Trans. ASME Ser. E* **83**, 455.
[] `http://www.princeton.edu/mae/people/faculty/smits/homepage/data-1/superpipe-data/mckeon/`

4.3 Article : A data-assimilation method for Reynolds-Averaged Navier-Stokes-driven mean flow reconstruction

Under consideration for publication in J. Fluid Mech. 1

A data-assimilation method for Reynolds-Averaged Navier-Stokes-driven mean flow reconstruction

Dimitry P.G. Foures[1], Nicolas Dovetta[2], Denis Sipp[3] and Peter J. Schmid[4]

[1]DAMTP, Centre for Mathematical Sciences, University of Cambridge, Cambridge CB3 0WA, United Kingdom

[2]LadHyX, Ecole Polytechnique, 91128 Palaiseau, France

[3]ONERA-DAFE, 8 rue des Vertugadins, 92190 Meudon, France

[4]Department of Mathematics, Imperial College London, London SW7 2AZ, United Kingdom

(Received 1 May 2014; revised ?; accepted ?. - To be entered by editorial office)

We present a data-assimilation technique based on a variational formulation and a Lagrange multipliers approach to enforce the Navier-Stokes equations. A general operator (referred to as the measure operator) is defined in order to mathematically describe an experimental measure. The presented method is applied to the case of mean flow measurements. Such a flow can be described by the Reynolds-Averaged Navier-Stokes (RANS) equations, which can be formulated as the classical Navier-Stokes equations driven by a forcing term involving the Reynolds stresses. The stress term is an unknown of the equations and is thus chosen as the control parameter in our study. The data-assimilation algorithm is derived to minimize the error between a mean flow measurement and the measure performed on a numerical solution of the steady, forced Navier-Stokes equations; the optimal forcing is found, when this error is minimal. We demonstrate the developed data-assimilation framework on a test case: the two-dimensional flow around an infinite cylinder at a Reynolds number of $Re = 150$. The mean flow is computed by time-averaging instantaneous flow fields from a direct numerical simulation. We then perform several 'measures' on this mean flow and apply the data-assimilation method to reconstruct the full mean flow field. Spatial interpolation, extrapolation, state vector reconstruction and noise filtering are considered independently. The efficacy of the developed identification algorithm is quantified for each of these cases and compared to more traditional methods when possible. We also analyze the identified forcing in terms of unsteadiness characterization, present a way to recover the second-order statistical moments of the fluctuating velocities, and finally explore the possibility of pressure reconstruction from velocity measurements.

1. Introduction

In a large variety of experimental scientific domains where measurements are performed, a major challenge has to be faced: no matter the type of data acquisition, the measured quantities are only a very sparse representation of the real, and therefore inaccessible, field. This sparsity can manifest itself in several forms depending on the specific circumstances. For example, in fluid mechanics, measurements are often under-resolved in time or space, or only contain partial information about the total state. The measured field can be thought of as a low-order representation of the real field. Moreover, the measured fields are commonly contaminated by noise and thus deviate from the true

values. Techniques that aim at a full reconstruction of the state vector from available (limited) data are referred to as inverse methods. The data-assimilation approach took its roots in the domain of weather forecasting where predicting the future evolution of both atmospheric and oceanic flows is based on the space-time extrapolation of unequally distributed data of different types measured at weather stations all around the world.

Several types of estimation problems can be distinguished. For example, the full state (for instance, pressure, velocity, temperature, etc.) can be estimated at a fixed time everywhere in space, or the future state-vector trajectory can also be predicted. Mathematically, both of these cases fall into the same category of inverse problems, where full information is retrieved from low-order, limited measurements. Many different methods have been developed to achieve accurate data reconstruction, ranging from simple interpolation techniques to more sophisticated approaches which take advantage of the underlying governing equations of the system. The formulation of such a problem using a variational formulation has been thoroughly studied in the meteorological community (Le Dimet & Talagrand (1986), Courtier (1997), Mohammadi & Pironneau (2004)). A review of various data-assimilation techniques used in meteorology is given in Ghil & Malanotte-Rizzoli (1991). Recently, the interest in data-assimilation has reached fluid experimentalists, who wish to extract a maximum amount of information from their measurements. This method can therefore be applied to improve the quality of a particle image velocimetry (PIV) or magnetic resonance imaging (MRI) acquisition. This includes spatial refinement, extension of the measured fields beyond their domain of acquisition, and the reconstruction of unmeasured flow field quantities from measured ones. In this context, it is worth mentioning the 'gappy POD' method proposed by Everson & Sirovich (1995), based on incomplete proper orthogonal decomposition, which has been used successfully to reconstruct missing PIV snapshots (see Gunes *et al.* (2006)).

This paper focuses on data-assimilation using variational methods and the enforcement of the governing equations with Lagrange multipliers (or adjoint variables). This approach is widely used in the flow optimization community for finding optimal perturbations, forcing or control strategies, to cite but a few applications (Hill (1995), Luchini & Bottaro (2001), Gunzburger (2000), Schmid (2007)). The adjoint variables can be interpreted as sensitivities and therefore yield valuable information on the impact of any kind of changes in the constraints that apply to the system. A variable then has to be chosen as a design parameter (or control parameter) which will be optimised in order to identify an extremum of a cost functional measuring the deviation from the simulated state vector to the dataset of measurements. The control parameters can be of various kind, e.g., an initial condition (Lundvall *et al.* (2006)), a physical parameter, or a material characteristic (Avril *et al.* (2008)). The outcome of such data-assimilation techniques is twofold: both the state and the design parameter are identified optimally, as the error between the model-based solution and the true measurements reaches a minimum. Beyond reconstructing the state vector, the application of such a methodology leads to an improvement of the model through the identification of the optimal control variable.

Variational techniques for fluid flow estimation from image sequences have been introduced recently to consistently combine image measurements with constraints expressing that the fluid behaves as a continuum material (Heitz *et al.* (2010)). The objective is to add physical constraints to the measurements (here snapshots of optical intensity) to improve the quality of the flow reconstruction in terms of velocity components. Classical PIV algorithms rely on correlation techniques to extract the velocity fields. More physical constraints have already been considered: optical flow model (Ruhnau *et al.* (2005)), Stokes equations (Ruhnau & Schnorr (2007)) and even time-dependent vorticity transport equations (Ruhnau *et al.* (2007)).

In the present paper, contrary to these authors, we directly consider snapshots with velocity components (for example obtained with a PIV technique). Also, we do not aim at reconstructing a series of flow snapshots obtained at successive times but rather the time-average of these snapshots – the mean-flow –, and their second order statistics – the Reynolds stresses. For this, we will use as a regularization the full Reynolds-Averaged-Navier-Stokes (RANS) equations. It is important to note that this choice of regularization operator (or kernel) is not unique. However, we choose the RANS equations as we believe they describe the physics of the problem accurately. The computational cost should therefore remain reasonable, even in three-dimensional configurations, since only steady-state solutions of the RANS equations and adjoint solutions, which do not involve time, need to be evaluated numerically. The approach employed in this paper can be applied to any unsteady (not necessarily turbulent) flow. Such a flow can, in a first instance, be described by its first statistical moment, the mean-flow. Even if the original flow can only be fully understood using both the mean and the unsteady components, we can gain some information about the flow by replacing the full unsteady terms by the second-order momentum, i.e. the Reynolds stress tensor. The goal of the present study is to investigate the possibilities of state-vector reconstruction from sparse mean flow measurements. We presume that the mean (or time-averaged) flow satisfies the RANS equations. In this set of equations, the Reynolds stress tensor appears as an additional unknown, and its definition in terms of the mean quantities is known as the closure problem. However, in our case, this unknown is chosen as a design variable (sometimes referred to as the control parameter) in an optimization process and will be considered as an unknown forcing term in the standard, steady Navier-Stokes equations. We thus identify the full mean flow from sparse data measurements (taken from a direct numerical simulation), together with the corresponding optimal forcing, that ensures the averaged flow to be a solution of the RANS equations.

This article presents the mathematical framework of variational data-assimilation and applies it to the specific case of time-averaged quantities of unsteady flows. We present, in § 2, the governing equations of the problem as well as the theory for the data-assimilation procedure. Once the optimization algorithm has been derived, we define the test case in § 3. The geometry is presented as well as the base and mean flows around a cylinder at a Reynolds number of $Re = 150$. We then present, in § 4, the results in terms of interpolation and extrapolation of data measurements. In the same section, a more realistic case is considered where the magnitude of the velocity field is measured and the full state vector is retrieved. The ability of the developed optimization algorithm to filter out measurement noise is also investigated. The identified forcing is used in order to characterize the unsteadiness of the flow in section § 5. We lastly stress the versatility as well as the many possible improvements of the presented method in § 6 and draw our conclusions.

2. Data-assimilation of flow measurements

The presented technique aims at finding a solution of a parameterized model equation, that optimally matches the data-measurements. The section starts by introducing the considered model and the type of measure performed. The optimization procedure is then developed in a further section. Finally, uniqueness and other properties of the optimal solution will be briefly discussed.

2.1. *Mean flow considerations*

Any unsteady (laminar or turbulent) flow can be described following the Reynolds decomposition, where the total flow $(u, v, w, p)^\top$ is taken as a sum of a steady term $(\overline{u}, \overline{v}, \overline{w}, \overline{p})^\top$

(the time-average) and an unsteady term $(u', v', w', p')^\top$ (the fluctuations around the mean); the $\overline{\cdot}$ operation denotes the average in time. Any fluctuation term q' naturally satisfies the property $\overline{q'} = 0$, and we furthermore have $\partial_t \overline{q} = 0$. By time-averaging the Navier-Stokes equations for the total flow, we obtain the so-called steady RANS equations, which read

$$\overline{\mathbf{u}} \cdot \nabla \overline{\mathbf{u}} + \nabla \overline{p} - Re^{-1} \nabla^2 \overline{\mathbf{u}} = \mathbf{f}^*, \tag{2.1a}$$

$$\nabla \cdot \overline{\mathbf{u}} = 0. \tag{2.1b}$$

In the case of the RANS equations, the forcing term can be expressed as

$$\mathbf{f}^* = -\nabla \cdot \mathbf{R}, \text{ with } R_{ij} = \overline{\mathbf{u}_i' \mathbf{u}_j'}. \tag{2.2}$$

with $\mathbf{R}$ being the Reynolds stress tensor, which represents the flow unsteadiness.

By using the incompressibility condition $\partial_i \mathbf{u}_i' = 0$, we can write $f_i^* = \overline{\mathbf{u}_j' \partial_j \mathbf{u}_i'}$. This expression shows that the forcing has to vanish $\mathbf{f}^* = 0$ on solid walls, where no-slip boundary conditions apply. Also, we notice that $\nabla \cdot \mathbf{f}^* \neq 0$ in the bulk of the flow.

A challenge in turbulence research (and, more generally, in any investigation of unsteady flow behaviour) is to model this second-order moment of the velocity field by linking it to the mean flow. This issue is often referred to as the closure problem. This tensor, however, does not *explicitly* depend on the mean flow, and $-\nabla \cdot \mathbf{R}$ can therefore be considered as an independent volumetric forcing term $\mathbf{f}^*$ applied to the standard, steady Navier-Stokes equations, as written in (2.1). This forcing term will be considered as a design variable in the following optimization procedure.

2.2. *Data-assimilation and error measure*

The starting point of our reconstruction algorithm is the measured quantity which will be later on referred to as the target field and denoted $\overline{\mathbf{m}}$. Motivated by PIV/MRI flow reconstruction, we choose not to consider measurements of the pressure field and only focus on field reconstruction based on velocity-only measurements. The measured field is obtained by the application of a low-rank projection operator $\mathcal{M}\colon V \to M$ which maps the velocity vectorial field onto a finite-dimensional vector. We denote by V the space of vectorial fields and by M the measure space. This mapping, or measure, can be expressed as

$$\overline{\mathbf{m}} = \mathcal{M}\left(\overline{\mathbf{u}}\right), \tag{2.3}$$

where $\overline{\mathbf{u}} = (\overline{u}, \overline{v}, \overline{w})^\top$ is the mean-velocity vector. This operator $\mathcal{M}$ defines the type of data acquisition performed. This measure corresponds to a discrete, low-order representation of the real solution $\overline{\mathbf{u}}$. The operator $\mathcal{M}$ also defines the type of quantity observed, and accounts for the spatial quality and location of the measure.

We consider a flow field $(\tilde{u}, \tilde{v}, \tilde{w}, \tilde{p})^\top$ to be a solution of the steady, forced Navier-Stokes equations, without any assumption on the forcing term $\mathbf{f}$,

$$\tilde{\mathbf{u}} \cdot \nabla \tilde{\mathbf{u}} + \nabla \tilde{p} - Re^{-1} \nabla^2 \tilde{\mathbf{u}} = \mathbf{f}, \tag{2.4a}$$

$$\nabla \cdot \tilde{\mathbf{u}} = 0. \tag{2.4b}$$

This system of equations is completed by homogeneous Dirichlet boundary conditions on solid walls, non-homogeneous Dirichlet boundary conditions for the inflow and appropriate outflow boundary conditions. These boundary conditions will be stated more explicitly when we define the geometry of the example chosen to demonstrate the method. By tuning the forcing term $\mathbf{f}$ appropriately, we seek the flow $(\tilde{\mathbf{u}}, \tilde{p})^\top$ that will best match

the measurements $\overline{\mathbf{m}}$. The solution of (2.4) with $\mathbf{f} = 0$ will be classically referred to as the base-flow solution.

The true mean flow is assumed to satisfy equations (2.1), with $\mathbf{f}^*$ as the true forcing (which is directly derived from the true Reynolds stress tensor). The goal is to find the optimal forcing $\mathbf{f}_{opt}$ such that the corresponding velocity field $\tilde{\mathbf{u}}_{opt}$ is compatible with the measured quantity $\overline{\mathbf{m}}$. To find this optimal forcing, we have to define the distance (error) between the observed quantity $\overline{\mathbf{m}}$ and the corresponding measure $\tilde{\mathbf{m}}$ of the reconstructed field $\mathcal{M}(\tilde{\mathbf{u}})$. The error is thus defined as

$$\mathcal{E}(\tilde{\mathbf{u}}) = \frac{1}{2}\|\overline{\mathbf{m}} - \mathcal{M}(\tilde{\mathbf{u}})\|_M{}^2 = \frac{1}{2}\|\Delta\mathbf{m}\|_M{}^2 = \frac{1}{2}\langle\Delta\mathbf{m}, \Delta\mathbf{m}\rangle_M, \tag{2.5}$$

where $\|\cdot\|_M$ is the norm associated with the scalar product $\langle\cdot,\cdot\rangle_M$ which acts on the measure space. Moreover, we implicitly defined in this expression $\Delta\mathbf{m}$ as the error field between the real and simulated measure evaluated at each measurement location. The goal is to reduce the error functional $\mathcal{E}$ as much as possible by adjusting the forcing $\mathbf{f}$, until a minimum value is reached, at which the optimal forcing $\mathbf{f}_{opt}$ emerges.

In this article, the reference velocity field $\overline{\mathbf{u}}$ and the measurements are obtained by direct numerical simulations, thus allowing us to consider the full velocity error field:

$$\Delta\mathbf{u} = \overline{\mathbf{u}} - \tilde{\mathbf{u}}. \tag{2.6}$$

The field $\Delta\mathbf{u}$ is a vector field. In a real experimental situation, such an error field cannot be evaluated since the flow $\overline{\mathbf{u}}$ is by definition not accessible. By minimising the error on the measure $\mathcal{E}$, we expect to also decrease the norm of the true error $\Delta\mathbf{u}$ and thus reconstruct the field $\overline{\mathbf{u}}$.

Note finally that the problem of identifying the optimal forcing $\mathbf{f}_{opt}$ is not yet a well-posed problem; in fact, inspection of equation (2.4) shows that infinitely many solutions exist at this stage. More specifically, starting with a forcing term $\mathbf{f}$, a modified forcing $\mathbf{f}' = \mathbf{f} + \nabla\phi$ will lead to the same solution $\tilde{\mathbf{u}}$ with the appropriate modification in the pressure term ($\tilde{p}' = \tilde{p} + \phi$), ensuring the incompressibility of the velocity field. In compact form, we can write

$$\tilde{\mathbf{u}}(\mathbf{f}, \tilde{p}) = \tilde{\mathbf{u}}(\mathbf{f} + \nabla\phi, \tilde{p} + \phi). \tag{2.7}$$

In the next section, we will add constraints on $\mathbf{f}$ so as to define properly the minimization problem.

2.3. *Comments on the choice of the reconstruction operator*

In the previous section, we chose the forced Navier-Stokes equations (as presented in (2.4)) as the underlying governing equations for the data-assimilation procedure. However, it is legitimate to ask whether another, simpler kernel (modeling equation) could be used in order to reconstruct the field. An obvious simplification would be to consider the following Stokes operator:

$$\nabla\tilde{p} - Re^{-1}\nabla^2\tilde{\mathbf{u}} = \mathbf{g}, \tag{2.8a}$$

$$\nabla\cdot\tilde{\mathbf{u}} = 0. \tag{2.8b}$$

If such a model was to be chosen, the identified forcing $\mathbf{g}_{opt}$ would contain all nonlinear properties of the reconstructed flow. Indeed, if the same minimum of the error functional $\mathcal{E}$ is reached using both methods (Navier-Stokes and Stokes), we can write:

$$\mathbf{g}_{opt} = \mathbf{f}_{opt} - \mathbf{u}_{opt}\cdot\nabla\mathbf{u}_{opt}. \tag{2.9}$$

It thus seems possible to obtain the same solution with the simpler Stokes kernel. Yet, we verified that the optimization procedure is not well-posed in such a case and that the

descent algorithm has difficulties decreasing the objective functional despite numerous iterations (we found that $\mathcal{E}$ decreased by a more order of magnitude using 6000 iterations with the Stokes kernel while a decrease by seven orders of magnitude using 2000 iterations was achieved with the Navier-Stokes kernel, see Fig. 3 below). We conclude that the optimization space corresponding to $\mathbf{f}$ appears to be more convex than the optimization space of $\mathbf{g}$. Hence, based on our experiment, for the descent algorithm to be efficient, it is advantageous to treat the convective phenomena by the Navier-Stokes kernel while having the optimization procedure search for the Reynolds stress term $\mathbf{f}$.

We conclude that choosing a kernel for the optimization procedure that accurately captures the underlying physics leads to a well-posed optimization problem.

2.4. *Variational formulation*

An optimal forcing $\mathbf{f}$ is sought such that the error $\mathcal{E}$ reaches a minimum. The chosen functional, however, does not explicitly depend on $\mathbf{f}$; rather, the dependence on $\mathbf{f}$ arises implicitly as $\tilde{\mathbf{u}}$ is a solution of (2.4). Therefore, in order to account for this constraint in the optimization, we have to define an augmented functional which not only measures the error $\mathcal{E}$ but also ensures that the flow equations are satisfied. This new functional is called the Lagrangian functional $\mathcal{L}$ and can be formulated as

$$\mathcal{L}(\mathbf{f},\tilde{\mathbf{u}},\tilde{p},\tilde{\mathbf{u}}^\dagger,\tilde{p}^\dagger)=\mathcal{E}\left(\tilde{\mathbf{u}}\right)-\left\langle\tilde{\mathbf{u}}^\dagger,\tilde{\mathbf{u}}\cdot\nabla\tilde{\mathbf{u}}+\nabla\tilde{p}-Re^{-1}\nabla^2\tilde{\mathbf{u}}-\mathbf{f}\right\rangle-\left\langle\tilde{p}^\dagger,\nabla\cdot\tilde{\mathbf{u}}\right\rangle, \tag{2.10}$$

where $\langle\cdot,\cdot\rangle$ represents the spatial scalar product

$$\langle\mathbf{a},\mathbf{b}\rangle=\int_\Omega\mathbf{a}\cdot\mathbf{b}\,\mathrm{d}\Omega, \tag{2.11}$$

with $\mathbf{a}$ and $\mathbf{b}$ denoting arbitrary (possibly vectorial) functions of space. To this scalar product is associated the L^2-norm defined as:

$$\|\mathbf{c}\|_2=\sqrt{\langle\mathbf{c},\mathbf{c}\rangle}, \tag{2.12}$$

with $\mathbf{c}$ denoting again an arbitrary function of space. Now that we have embedded the constraint in the Lagrangian functional, the forcing appears explicitly in the functional to optimise. However, unconstraining the problem comes at the expense of introducing new (*a priori* unknown) variables, the adjoint state variables $(\tilde{u}^\dagger,\tilde{v}^\dagger,\tilde{w}^\dagger,\tilde{p}^\dagger)^\top$ which are the Lagrange multipliers enforcing the incompressible Navier-Stokes equations.

We are looking for a minimum of the cost functional, which means that all the partial functional derivatives of $\mathcal{L}$ have to vanish. We notice that enforcing a vanishing first variation with respect to adjoint variables is equivalent to the constraint (2.4). Enforcing the variation with respect to direct variables to be zero yields the adjoint Navier-Stokes equations

$$-\tilde{\mathbf{u}}\cdot\nabla\tilde{\mathbf{u}}^\dagger+\tilde{\mathbf{u}}^\dagger\cdot\nabla\tilde{\mathbf{u}}^\top-\nabla\tilde{p}^\dagger-Re^{-1}\nabla^2\tilde{\mathbf{u}}^\dagger=\frac{\delta\mathcal{E}}{\delta\tilde{\mathbf{u}}}, \tag{2.13}$$

$$\nabla\cdot\tilde{\mathbf{u}}^\dagger=0. \tag{2.14}$$

together with an appropriate set of boundary conditions, stemming from the vanishing of the boundary terms in the functional derivative. Again, the boundary conditions will be detailed later, when the definition of the test-case geometry is presented.

We observe that the adjoint equations are forced by the functional derivative of the error functional $\mathcal{E}$ with respect to $\tilde{\mathbf{u}}$. The forcing will therefore depend on the type of the selected physical measure $\mathcal{M}$, as well as the associated scalar product used to define the error. We can derive the formal expression for the forcing by using the definition of the adjoint of an operator with respect to a scalar product. For example, for any $\mathbf{v}\in V$ (V

being the space of the velocity vectors), $\mathbf{n} \in M$ (M being the space of the measure) and any operator $\mathcal{N}\colon V \to M$ we can write

$$\langle \mathcal{N}(\mathbf{v}), \mathbf{n} \rangle_M = \left\langle \mathbf{v}, \mathcal{N}^\dagger(\mathbf{n}) \right\rangle, \tag{2.15}$$

where the scalar product on the right-hand side is a scalar product on the space of velocity fields V, and $\mathcal{N}^\dagger\colon M \to V$ stands for the adjoint operator of $\mathcal{N}$ with respect to these scalar products. With this property, we can derive the following expression for the forcing term in the adjoint equation

$$\frac{\delta \mathcal{E}}{\delta \tilde{\mathbf{u}}} = -\frac{\delta \mathcal{M}^\dagger}{\delta \tilde{\mathbf{u}}} \Delta \mathbf{m}. \tag{2.16}$$

At this stage, the operator $\frac{\delta \mathcal{M}^\dagger}{\delta \tilde{\mathbf{u}}}$ has yet to be defined; the dependence of the forcing term on the error $\Delta\mathbf{m}$ is nonetheless evident: the adjoint momentum equation is linearly forced by the error measure $\Delta\mathbf{m}$.

The derivation of the gradient with respect to the forcing $\mathbf{f}$ is straightforward. By noticing that the partial derivative of $\mathcal{L}$ with respect to $\mathbf{f}$ is indeed the total derivative of $\mathcal{E}$, the gradient of the error functional with respect to the forcing can be expressed as

$$\nabla_{\mathbf{f}} \mathcal{E} = \tilde{\mathbf{u}}^\dagger, \tag{2.17}$$

where $\mathbf{u}^\dagger$ is solution of (2.13) with appropriate boundary conditions and $\mathbf{u}$ is solution of (2.4) with the specified boundary conditions and the considered $\mathbf{f}$.

With the gradient of the error with respect to the forcing known, we need to employ a descent algorithm to minimise the error and identify both the optimal forcing $\mathbf{f}_{opt}$ and the associated recovered field $\tilde{\mathbf{u}}_{opt}$. We will use a conjugate-gradient descent method along with a line-search algorithm. We also need to choose an initial guess $\mathbf{f}_g$ in order to start the optimization procedure. We decide to start from a forcing $\mathbf{f}_g$ that is divergence-free ($\nabla \cdot \mathbf{f}_g = 0$) and zero at the no-slip walls ($\mathbf{f}_g = 0$). For example, $\mathbf{f}_g = 0$ verifies these conditions.

In the following, we will denote $\mathbf{f}_{opt}$ as the solution that is obtained at the end of the minimization process. It is worth noting that, using a gradient-based approach, this forcing can be expressed as a linear combination of gradients (evaluated at different locations in the optimization space). Therefore, the identified forcing will naturally satisfy $\nabla \cdot \mathbf{f}_{opt} = 0$ and $\mathbf{f}_{opt} = 0$ on solid boundaries (because $\tilde{\mathbf{u}}^\dagger$ and the initial guess $\mathbf{f}_g$ satisfy these conditions). Therefore, the use of the present iterative gradient-based method combined with the above mentioned choice of the initial condition implicitly imposes additional constraints on the choice of the forcing $\mathbf{f}$ that minimizes the cost-functionnal $\mathcal{E}$. Uniqueness of the resulting solution $\mathbf{f}_{opt}$ and its relation to the true forcing $\mathbf{f}^*$ will be discussed in section 2.6. Finally, the flow-field $(\tilde{\mathbf{u}}_{opt}, \tilde{p}_{opt})$ will refer in the following to the solution of equation (2.4) with the forcing $\mathbf{f}_{opt}$.

2.5. *Type of measure*

As detailed in the previous section, the error functional $\mathcal{E}$ is entirely defined by the operator $\mathcal{M}$ which is at the heart of the data-assimilation technique. Here, we will consider operators that can be decomposed into two operators $\mathcal{P}$ and $\mathcal{Q}$, respectively describing the projection from the true solution (having an infinite number of degrees of freedom, space V) to a low-rank representation of the field, i.e., the sampled data points (with, in practice, a finite number of degrees of freedom, space M), and the projection from the vector of velocities to whatever quantity is indeed observed. According to this definition, we can write

$$\mathcal{M}(\mathbf{u}) = \mathcal{P}(\mathcal{Q}(\mathbf{u})). \tag{2.18}$$

The simplest operator $\mathcal{Q}$ one can imagine is the identity, indicating that the measure is performed on all the components of the velocity field, such as for PIV measurements. However, many other measures are possible, for example observation of a single component of the velocity field. In this case, we would have $\mathcal{Q}(\mathbf{u}) = u$ which would be a scalar field containing the streamwise velocity only. In any case, for vectorial or scalar measured quantities alike, we will use

$$\mathcal{Q}(\mathbf{u}) = \mathbf{q}. \tag{2.19}$$

At this stage, the vector $\mathbf{q}$ still belongs to an infinite-dimensional space. The operator $\mathcal{P}$, acting on $\mathbf{q}$, describes the 'geometrical' features of the measure. This operator is responsible for the discretisation of the continuous field $\mathbf{q}$ onto a finite-dimensional vector containing all the data points; the projection operator $\mathcal{P}$ defines the spatial sampling quality and the spatial extent of the measure. The measure can, for instance, be the evaluation of $\mathbf{q}$ at a finite number N of locations in the domain

$$[\mathcal{P}(\mathbf{q})]_i = \mathbf{q}(\mathbf{x}_i) = \int_\Omega \mathbf{q}(\mathbf{x})\delta(\mathbf{x}-\mathbf{x}_i)\ \mathrm{d}\Omega, \tag{2.20}$$

where $\delta(\mathbf{x}_i)$ is the delta function centred on the coordinate points $\mathbf{x}_i = (x_i, y_i, z_i)^\top$.

However, a more general type of measure would be a weighted, local average of the real field over small elements of the domain Ω_i such as

$$[\mathcal{P}(\mathbf{q})]_i = \int_\Omega \mathbf{q}(\mathbf{x})b_i(\mathbf{x})\ \mathrm{d}\Omega, \tag{2.21}$$

where b_i is the weight function associated with element Ω_i. The before-mentioned case with point-wise measure would correspond to $b_i = \delta(\mathbf{x}_i)$. An average over each measurement cell Ω_i can be described by the weight function $b_i(\mathbf{x}) = H(\Omega_i)$, where $H(\Omega_i)$ is equal to $1/V_{\Omega_i}$ (V_{Ω_i} being the volume of the element Ω_i, $V_{\Omega_i} = \int_{\Omega_i} \mathrm{d}\Omega_i$) for $\mathbf{x} \in \Omega_i$ and zero everywhere else. At this point, we decide to stay as general as possible by not specifying the basis functions b_i. The measurement mesh, and therefore the projection operator $\mathcal{P}$ is entirely defined by the basis functions $(b_i)_{i\in[\![1,N]\!]}$.

In the case of a discrete measure operator $\mathcal{P}$, the space M is a finite-dimensional space. In this case, the scalar product on the space M will be defined as the classical vectorial dot product (the sum of the component-wise products). According to the previous definition, and using the usual vectorial scalar product for $\langle\cdot,\cdot\rangle_M$, we can express the error defined in (2.5) as

$$\mathcal{E}(\tilde{\mathbf{u}}(\mathbf{f})) = \frac{1}{2}\sum_{i=0}^{N} {\Delta m_i}^2, \quad \text{with} \quad \Delta m_i = \overline{m}_i - \int_\Omega \mathbf{q}b_i\ \mathrm{d}\Omega, \tag{2.22}$$

and then compute its derivative as

$$\left\langle \frac{\delta\mathcal{E}}{\delta\tilde{\mathbf{u}}}, \delta\tilde{\mathbf{u}} \right\rangle = -\sum_{i=0}^{N} \Delta m_i \int_\Omega \frac{\delta\mathcal{Q}}{\delta\tilde{\mathbf{u}}}\delta\tilde{\mathbf{u}}b_i\ \mathrm{d}\Omega. \tag{2.23}$$

After rearranging the integral and the sum, we find

$$\frac{\delta\mathcal{E}}{\delta\tilde{\mathbf{u}}} = -\sum_{i=0}^{N} \frac{\delta\mathcal{Q}}{\delta\tilde{\mathbf{u}}}b_i\Delta m_i. \tag{2.24}$$

This expression is in the space of velocities V and corresponds to the forcing term in the adjoint equations; it is proportional to the error made at each measure location (over the domain Ω_i in the case of averaged measures). If the point-wise measurement had been

used instead, we would have a sum of Dirac distributions centred on each measurement point. We see that the averaged evaluation (2.21) is more regular than the discrete one because the field $\frac{\delta\mathcal{E}}{\delta\tilde{\mathbf{u}}}$ is piecewise continuous. Moreover it is mathematically closer to a real physical measure.

Moreover, from equations (2.16) and (2.24), we identify

$$\frac{\delta\mathcal{M}}{\delta\tilde{\mathbf{u}}}^{\dagger}\Delta\mathbf{m} = \sum_{i=0}^{N}\frac{\delta\mathcal{Q}}{\delta\tilde{\mathbf{u}}}b_i\Delta m_i. \tag{2.25}$$

2.6. *Relation between* $\mathbf{f}_{opt}$ *and* $\mathbf{f}^*$

The link between the optimal solution $\mathbf{f}_{opt}$ with the true forcing $\mathbf{f}^*$ is an important issue to be discussed. We start by recalling that on the one hand we have $\nabla\cdot\mathbf{f}_{opt} = 0$ with $\mathbf{f}_{opt} = 0$ on solid-wall boundaries (see section 2.4), while on the other hand we have $\nabla\cdot\mathbf{f}^* \neq 0$ with $\mathbf{f}^* = 0$ on the walls (see section 2.1). It is therefore tempting to compare $\mathbf{f}_{opt}$ to the divergence-free part of $\mathbf{f}^*$ and discuss their relation.

The real forcing $\mathbf{f}^*$ (as expressed in (2.2)) can be decomposed into:

$$\mathbf{f}^* = \mathbf{f}^*_s + \nabla\phi, \tag{2.26}$$

where $\mathbf{f}^*_s$ is a divergence-free part of $\mathbf{f}^*$ and $\nabla\phi$ a potential component. By taking the divergence of this equation and setting $\nabla\cdot\mathbf{f}^*_s = 0$, we find:

$$\nabla\cdot\mathbf{f}^* = \nabla^2\phi. \tag{2.27}$$

In order to uniquely define the above decomposition, boundary conditions have to be chosen for ϕ on the solid walls. In order for $\mathbf{f}^*_s$ to be closest to the identified forcing $\mathbf{f}_{opt}$, we would like to set $\nabla\phi = 0$ at the no-slip walls. Yet, for a Poisson equation, we cannot prescribe simultaneously the tangential and normal components of $\nabla\phi$ to be zero on the no-slip walls and it is only possible to impose the normal component to zero:

$$\partial_n\phi = \nabla\phi\cdot\mathbf{n} = 0, \tag{2.28}$$

with $\mathbf{n}$ as the outward normal to the domain. Solving equation (2.27) with this homogeneous Neumann condition then allows us to find ϕ and therefore to fully identify the projected forcing $\mathbf{f}^*_s$ from equation (2.26). The normal (with respect to the no-slip boundary) component of $\mathbf{f}^*_s$ therefore vanishes on the no-slip walls, but its tangential component does not. Hence, the divergence-free part of $\mathbf{f}^*$, i.e. $\mathbf{f}^*_s$, is not expected to be exactly equal to $\mathbf{f}_{opt}$, since on the no-slip walls their tangential component is not equal. Yet, we will see below (see section 4.1 in the case of full-state information identification), that these fields are nearly identical in the whole space except in the vicinity of the solid walls. Also, we will check that the iterative process converges toward a very small value of $\mathcal{E}(\tilde{\mathbf{u}}_{opt})$.

The reconstructed pressure will also be different from the real pressure $\overline{p}$. In fact, since $\mathbf{f}_{opt} \simeq \mathbf{f}^* - \nabla\phi$, it is seen that

$$\tilde{p}_{opt} \simeq \overline{p} - \phi, \tag{2.29}$$

where $\tilde{p}_{opt}$ is the pressure recovered by our algorithm and $\overline{p}$ is the true pressure as defined in equations (2.1). The reconstructed pressure $\tilde{p}_{opt}$ is therefore an augmented pressure which includes the potential part of the forcing ϕ. We will discuss the possibilities of pressure reconstruction in section 5.3.

It may appear striking to the reader to look for an optimal solution $\mathbf{f}_{opt}$ in a space which, by definition, does not contain the true forcing $\mathbf{f}^*$. However, in the case of a kernel based on incompressible equations, the sole knowledge of velocity measurements

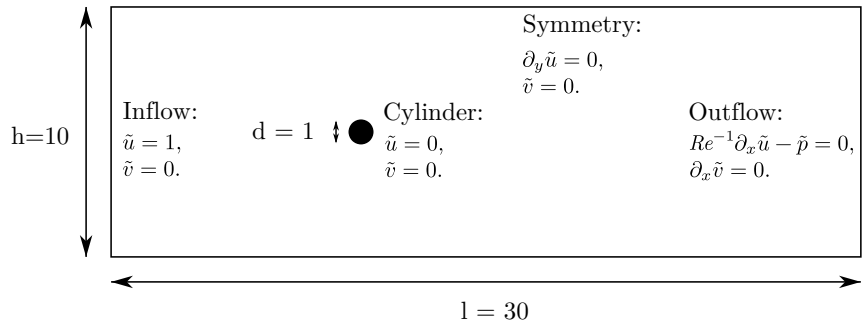

FIGURE 1. Sketch of the geometry of two-dimensional flow around an infinite cylinder. The full computational domain, the characteristic lengths and the applied boundary conditions are shown. The cylinder's diameter, the height and length of the domain d, h and l are given in nondimensional units.

automatically induces that the gradient of the error $\mathcal{E}$ with respect to the forcing $\mathbf{f}$ is divergence-free. Therefore, an optimization procedure based on a gradient with an incompressibility constraint can only find an optimal solution in the space of the divergence-free functions.

In order to obtain some gradient information in a wider space (containing non divergence-free functions), we can, along with velocity data, consider pressure measurements as input variables to the data-assimilation algorithm. In that case, the adjoint field is no longer incompressible, since the cost functional now depends also on $\tilde{p}$; we then have

$$\nabla \cdot \tilde{\mathbf{u}}^\dagger = -\frac{\delta \mathcal{E}}{\delta \tilde{p}}. \tag{2.30}$$

The gradient $\nabla_{\mathbf{f}} \mathcal{E}$ (see equation (2.17)) and consequently the identified forcing are no longer divergence-free, and therefore matching both the solenoidal and irrotational components of the forcing becomes possible.

In this study, we restrict ourselves to a target field exclusively composed of velocity variables, as it is of both experimental and theoretical interest.

3. Flow around a cylinder

We apply the data-assimilation method described above to a simple test case: the two-dimensional flow around an infinite circular cylinder. Even though the theory was presented for a general three-dimensional flow, it applies straightforwardly to a two-dimensional case. The geometry, as well as the corresponding boundary conditions are presented in figure 1. We restate the boundary conditions of the direct system (2.4) for clarity:

$$\begin{array}{ll} \tilde{u} = 1,\ \tilde{v} = 0 & \text{at the inlet,} \\ \tilde{u} = 0,\ \tilde{v} = 0 & \text{on the cylinder's surface,} \\ \partial_y \tilde{u} = 0,\ \tilde{v} = 0 & \text{on symmetry boundaries,} \\ Re^{-1}\partial_x \tilde{u} - \tilde{p} = 0,\ \partial_x \tilde{v} = 0 & \text{at the outlet.} \end{array} \tag{3.1}$$

The boundary conditions of the adjoint system (2.13) are obtained via the integration-by-parts step as explained in 2.4. These conditions read:

$$\begin{array}{ll} \tilde{u}^\dagger = 0,\ \tilde{v}^\dagger = 0 & \text{at the inlet,} \\ \tilde{u}^\dagger = 0,\ \tilde{v}^\dagger = 0 & \text{on the cylinder's surface,} \\ \partial_y \tilde{u} = 0,\ \tilde{v} = 0 & \text{on symmetry boundaries,} \\ Re^{-1}\partial_x \tilde{u}^\dagger + \tilde{p}^\dagger = -\tilde{u}\tilde{u}^\dagger,\ Re^{-1}\partial_x \tilde{v}^\dagger = -\tilde{u}\tilde{v}^\dagger & \text{at the outlet.} \end{array} \tag{3.2}$$

This flow has been shown (see Jackson (1987)) to undergo a first transition (more precisely, a supercritical Hopf bifurcation) at a critical Reynolds number of $Re_c \simeq 46$, above which the base flow (solution of the system (2.4) with $\mathbf{f} = 0$) is no longer stable. Beyond this threshold, the flow becomes time periodic, and vortices are shed from the back of the cylinder. After this transition, we can define any mean quantity by averaging its instantaneous value over a finite number of periods in. By doing so, we can compute the mean-velocity field $\overline{\mathbf{u}}$ as well the different components of the Reynolds stress tensor $\overline{\mathbf{u}_i'\mathbf{u}_j'}$, defined in (2.2).

As we mentioned earlier, the optimization method employed in the remainder of this article requires the definition of an initial guess $\mathbf{f}_g$ for the forcing. We choose $\mathbf{f}_g = 0$, which means that the first computed flow $\tilde{\mathbf{u}}$ is the base flow $\mathbf{u}_b$.

For our simulations, we choose a Reynolds number of $Re = 150$ and compute the base flow $\mathbf{u}_b$ (using a classical Newton method), the mean flow $\overline{\mathbf{u}}$ (using time-averaging) and the various components of the Reynolds stress tensor. These fields are computed with high accuracy using a finite element method, using FreeFem++ software (see www.freefem.org), on a mesh of $N \simeq 1.7 \times 10^5$ degrees of freedom. The base flow is represented in figures 2(a),(b); the mean flow is displayed in figures 2(c),(d) and finally the initial error is plotted in figures 2(e),(f).

4. Navier-Stokes-driven field reconstruction

To validate the presented data-assimilation method, several measure operators $\mathcal{M}$ are considered, each of them chosen to demonstrate the efficacy of the method in various reconstruction scenarios. In the two following sections the considered measure is the full velocity vector and the error on both components of the velocity is estimated. Spatial interpolation and extrapolation are investigated. In a further section, we consider a more challenging and realistic case where only the velocity magnitude is measured, on a relatively coarse mesh. We demonstrate the ability of the method to not only reconstruct the measured quantity but also to identify the full velocity vector. The robustness of the identification algorithm when the measure is corrupted by noise is also assessed.

4.1. *Full-state information identification*

As a starting point, we will choose the operator $\mathcal{M}$ to be the identity operator on V, such that the assimilated field is the full, continuous velocity field (in practice, it is a discrete field, evaluated on the finite-element grid). In this case, we choose $\langle\cdot,\cdot\rangle_M \equiv \langle\cdot,\cdot\rangle$ and $\|\cdot\|_M \equiv \|\cdot\|_2$. We present the convergence curves for the case $\mathcal{M} = \mathcal{I}$ for both the cost functional $\mathcal{E}$ and the norm of the gradient $\nabla_{\mathbf{f}}\mathcal{E}$ in figure 3. It is seen that both quantities decrease by several orders of magnitude, indicating that the error $\mathcal{E}$ becomes extremely weak in the case of full-state information identification.

We plot in figures 4(a) and (b) both components of the true forcing $\mathbf{f}^*$ (computed via a direct numerical simulation) and in figures 4(e) and (f) those related to the identified forcing $\mathbf{f}_{opt}$. There exists a strong correlation for the streamwise component, but no similarity can be found for the cross-stream component. This was expected because the identification algorithm yields a forcing $\mathbf{f}_{opt}$ which is divergence-free while $\mathbf{f}^*$ is not. The divergence-free component of the latter forcing, $\mathbf{f}_s^*$, is computed following the procedure explained in section 2.6 and we plot the results in figures 4(c) and (d). We can see that the identified forcing $\mathbf{f}_{opt}$ is indeed matching the projected forcing $\mathbf{f}_s^*$. However, some discrepancies appear on the cylinder's surface, which are due to the different tangential values of these two fields on the cylinder surface.

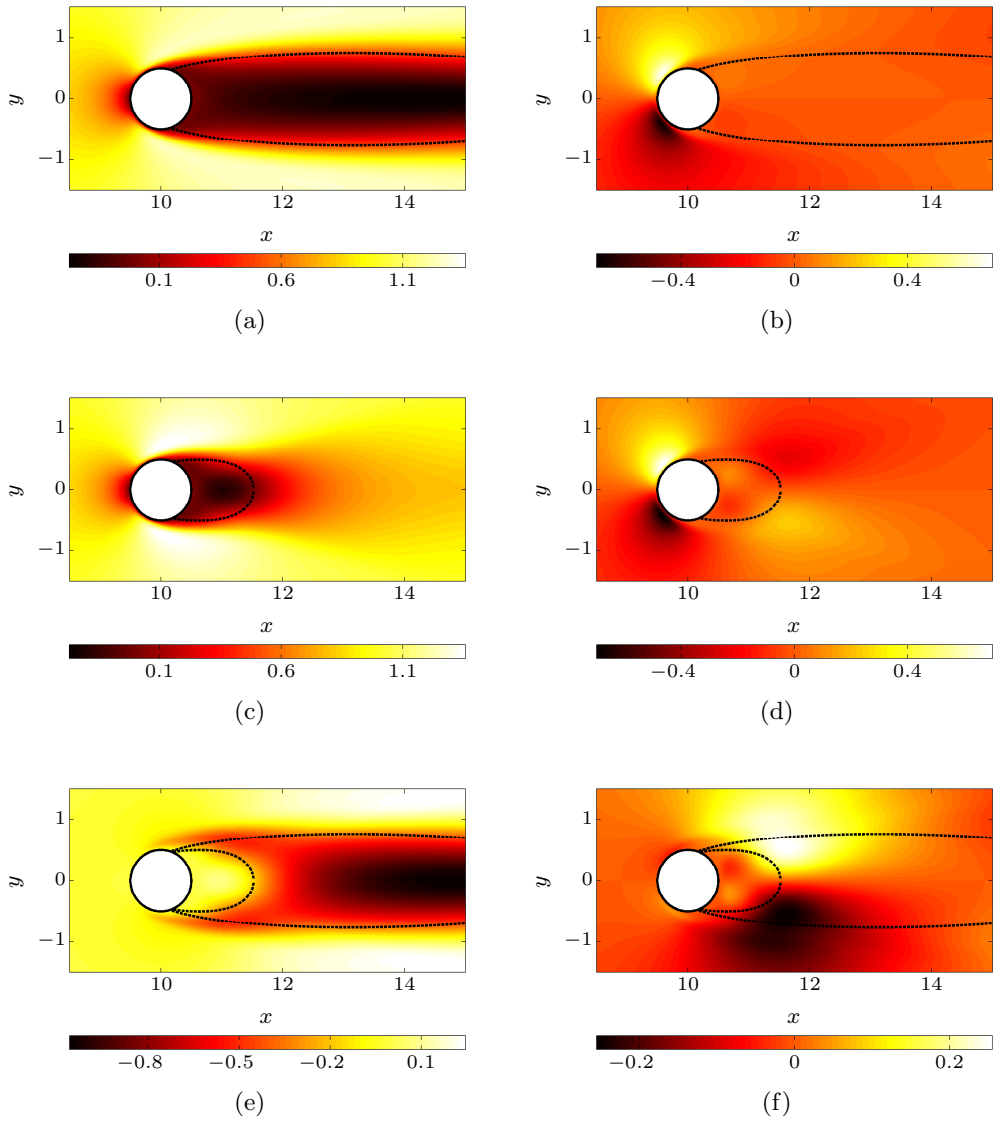

FIGURE 2. Flow around an infinite cylinder at $Re = 150$. (a) and (b): Base flow $\mathbf{u}_b$, (c) and (d) time-averaged flow $\overline{\mathbf{u}}$; (e) and (f): Difference (evaluated on both components) $\Delta\mathbf{u}$, measuring the error committed when approximating the mean flow by the base flow. The left column represents the x-component of the corresponding vector field, while the right column displays the y-component. The dashed-lines refer for each vector-field to the extent of the recirculation bubble. In figures (e) and (f), the dashed lines of figures (a), (b), (c), (d) have been reproduced for comparison.

Differences between $\mathbf{f}_{opt}$ and the projection of $\mathbf{f}^*$ over the space of divergence-free fields are best analysed by comparing the curl of these two fields, since the curl of a potential field is zero. We can observe in figures 4(g) and (h) that the z-component of these fields is nearly the same everywhere except in the vicinity of the cylinder boundary. We therefore have $\mathbf{f}_{opt} = \mathbf{f}_s^*$ almost everywhere, which validates our optimization procedure.

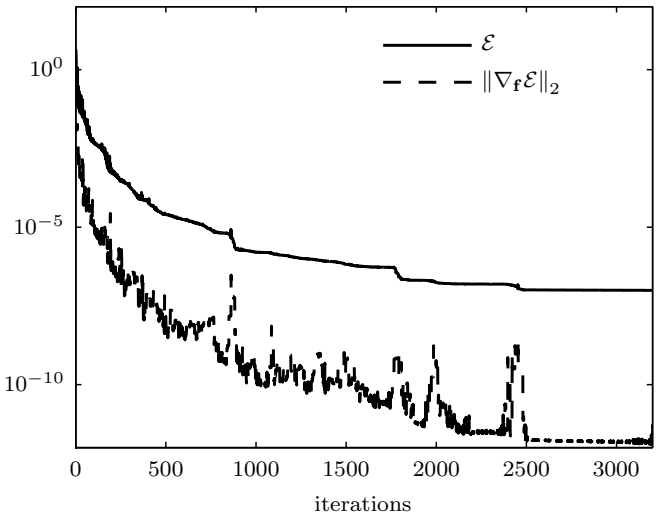

FIGURE 3. Convergence curves for full-identification case ($\mathcal{M} = \mathcal{I}$). The solid line represents $\mathcal{E}$, and the dashed line represents $\|\nabla_{\mathbf{f}}\mathcal{E}\|_2$.

4.2. *Partial-state information identification*

In the case of a partial-state information identification, we still minimise $\mathcal{E}$ as defined in (2.5), expecting that this minimization results in a decrease of the real error $\boldsymbol{\Delta}\mathbf{u}$ (see equation (2.6)). We therefore need to decide how to measure the real error $\boldsymbol{\Delta}\mathbf{u}$. We choose to use two norms: the L^2-norm (normalised by $\sqrt{V_\Omega}$ to remove any dependence on the chosen area of integration) and the L^∞-norm. The first will give information about the average error while the second will yield the error at the worst reconstructed location. We therefore define the following residuals (measuring the real errors):

$$\begin{aligned} r_2 &= \frac{1}{\sqrt{V_\Omega}}\left\|\boldsymbol{\Delta}\mathbf{u}\right\|_2 = \sqrt{\frac{1}{V_\Omega}\int_\Omega \left|\boldsymbol{\Delta}\mathbf{u}\right|^2 \,\mathrm{d}\Omega}, \\ r_\infty &= \left\|\boldsymbol{\Delta}\mathbf{u}\right\|_\infty = \lim_{p\to+\infty}\left(\int_\Omega \left|\boldsymbol{\Delta}\mathbf{u}\right|^p \,\mathrm{d}\Omega\right)^{1/p}. \end{aligned} \tag{4.1}$$

4.2.1. *Interpolation*

Interpolation consists of reconstructing the field in-between the available, measured data points. In what follows, the measure (as defined in (2.21)) is an average over each element of a rectangular mesh (called measurement mesh) and is reconstructed on the computational mesh which has a very high resolution. Here, $\mathcal{Q}$ is the identity operator, i.e., the two components of the velocity vector are measured:

$$\mathcal{Q}\left(\tilde{\mathbf{u}}\right) = \tilde{\mathbf{u}}. \tag{4.2}$$

In order to characterise the efficacy of the field reconstruction method, the discretisation projection operator $\mathcal{P}$ defined in (2.21) is considered, with the b_i being the basis functions of a mesh composed of squares paving the whole computational domain. The different measurement meshes have different line-density (density per unit length) of points $n \in [2, 20]$. For instance, the case $n = 2$ corresponds to 60×20 measurements meshes. An integrated measure is performed on each of the elements composing the measurement mesh, according to the expression (2.21). The identification algorithm is

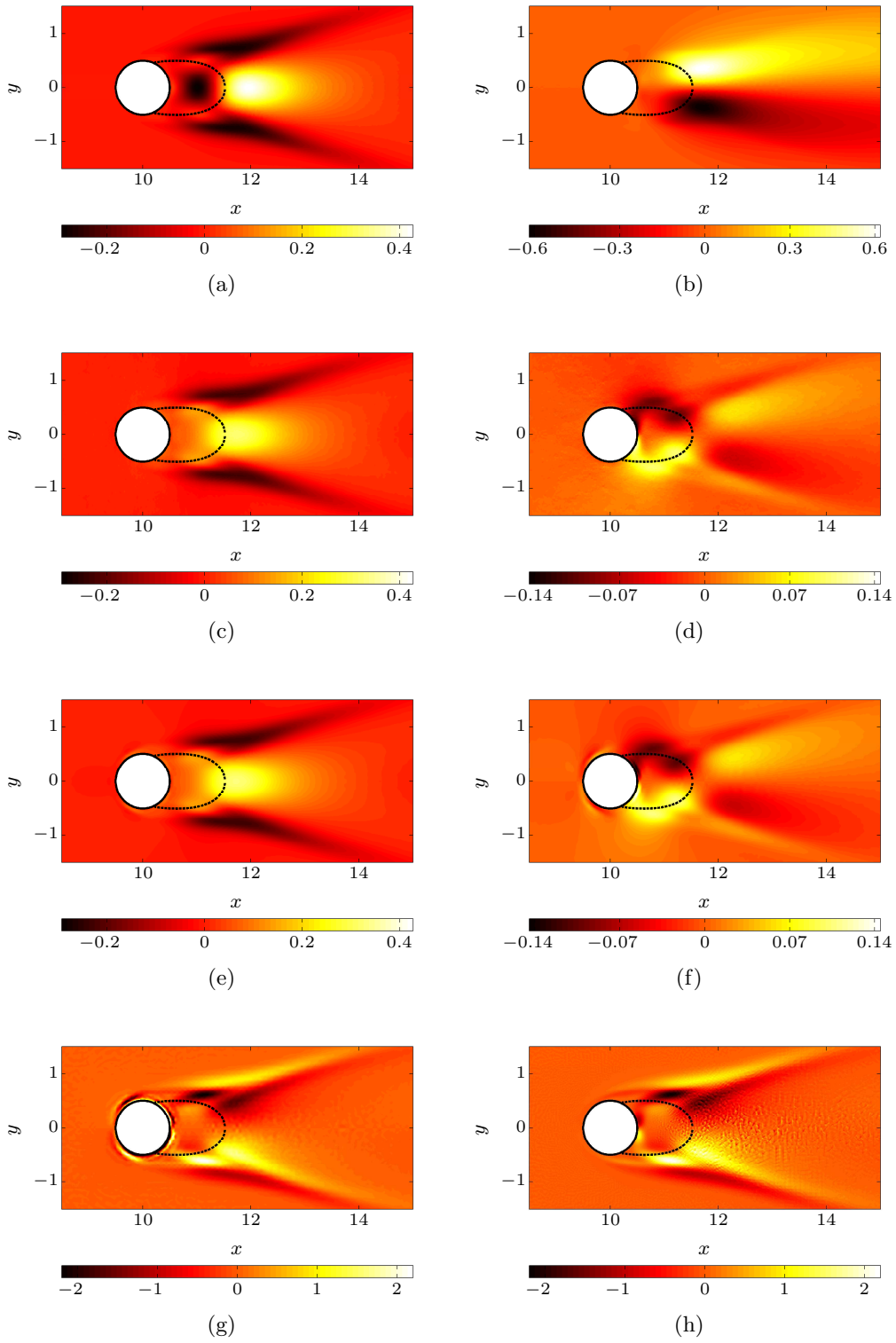

FIGURE 4. Averaged forcing term $\mathbf{f}^*$ displaying the x and y components, respectively, in figures (a) and (b). Projected forcing $\mathbf{f}_s^*$ (see 2.6 for its definition) for both components, in figures (c) and (d). Optimally identified forcing $\mathbf{f}_{opt}$ for both components, in figures (e) and (f). Note that the colour scales are identical for all streamwise components, but vary for the cross-stream components. Figures (d) and (f) have however the same colour scale to allow comparison. Figures (g) and (h) respectively represent the z-component of $\nabla \times \mathbf{f}^*$ and $\nabla \times \mathbf{f}_{opt}$. The difference is mainly located close to the cylinder's surface. The dashed-lines refer for each vector-field to the extent of the recirculation bubble.

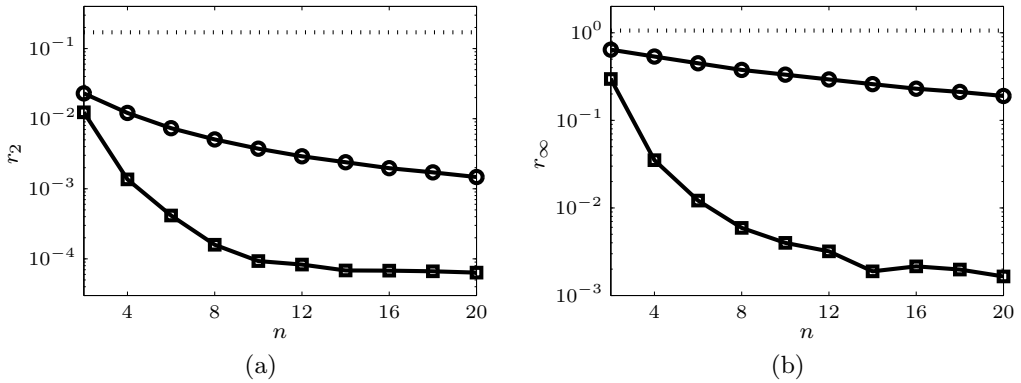

FIGURE 5. Results for the interpolation case. The norm of the error is plotted against the line-density of nodes n. Circle symbols represent the spline interpolation case (naïve approach) and square symbols represent the data-assimilation results. The error of approximating the mean flow by the base flow is represented with a dashed line. For $n \simeq 10$, the reconstruction of the field is efficient and a further increase of resolution yields only little improvement. (a) r_2 error, (b) r_∞ error as defined in (4.1).

applied to all the above measurement meshes and, for each optimum found, the errors r_2 and r_∞ as defined in (4.1) are plotted against the line-density of points n in figure 5.

First, it is encouraging that even for the worst case considered ($n = 2$), the reconstructed mean flow corresponds to a relatively low error. The measure $\mathcal{M}(\overline{\mathbf{u}})$ performed in a particularly under-resolved case ($n = 2$) as well as the corresponding reconstructed field $\tilde{\mathbf{u}}_{opt}$ and error $\boldsymbol{\Delta}\mathbf{u}$ are plotted in figure 6. From this figure, we can confirm that the data-assimilation algorithm successfully identifies the mean field. Indeed, for this extremely coarse case, the L^2 error is $r_2 = 0.012$, which is very small considering the amount of information initially given. However, the maximum error is $r_\infty = 0.297$. We have found an average error of 1.2%, and of 29.7% at the worst reconstructed location. Both these errors are relative to the unit inflow velocity. We see in figure 6(e) and 6(f) that the error is mainly located in the near-wake of the cylinder. The worst-reconstructed area corresponds to the end of the recirculation bubble whose reattachment point location does not exactly match the real one (extracted from the mean flow $\overline{\mathbf{u}}$); its length is underestimated by the identification algorithm. For more accurate measures (increasing n), the error decreases: the more information is available initially, the more accurately the field is reconstructed. For the finest meshes, we can reduce the errors to 6.36 10^{-3}% in L^2-norm and 0.17% in L^∞-norm.

Spline interpolation is a non-physical, but common way to obtain highly refined fields from measurements on a coarse grid. To assess the improved quality of data-assimilation interpolation, figure 5 also presents the interpolation error for a classical spline interpolation reconstruction. We notice that this simple interpolation technique is producing better results than a base-flow approximation, but is far from being as accurate as the presented algorithm. The data-assimilation method always outperforms spline interpolation and can lead to more accurate results by two orders of magnitude.

4.2.2. *Extrapolation*

In this section, the operator defining the measured quantity is still the identity ($\mathcal{Q} = \mathcal{I}$), i.e., the full velocity vector is assimilated on a given measurement mesh. However, the projection operator $\mathcal{P}$ is now designed to investigate the extrapolation capabilities of the method. The used mesh is the finer one from the previous section (the line-density

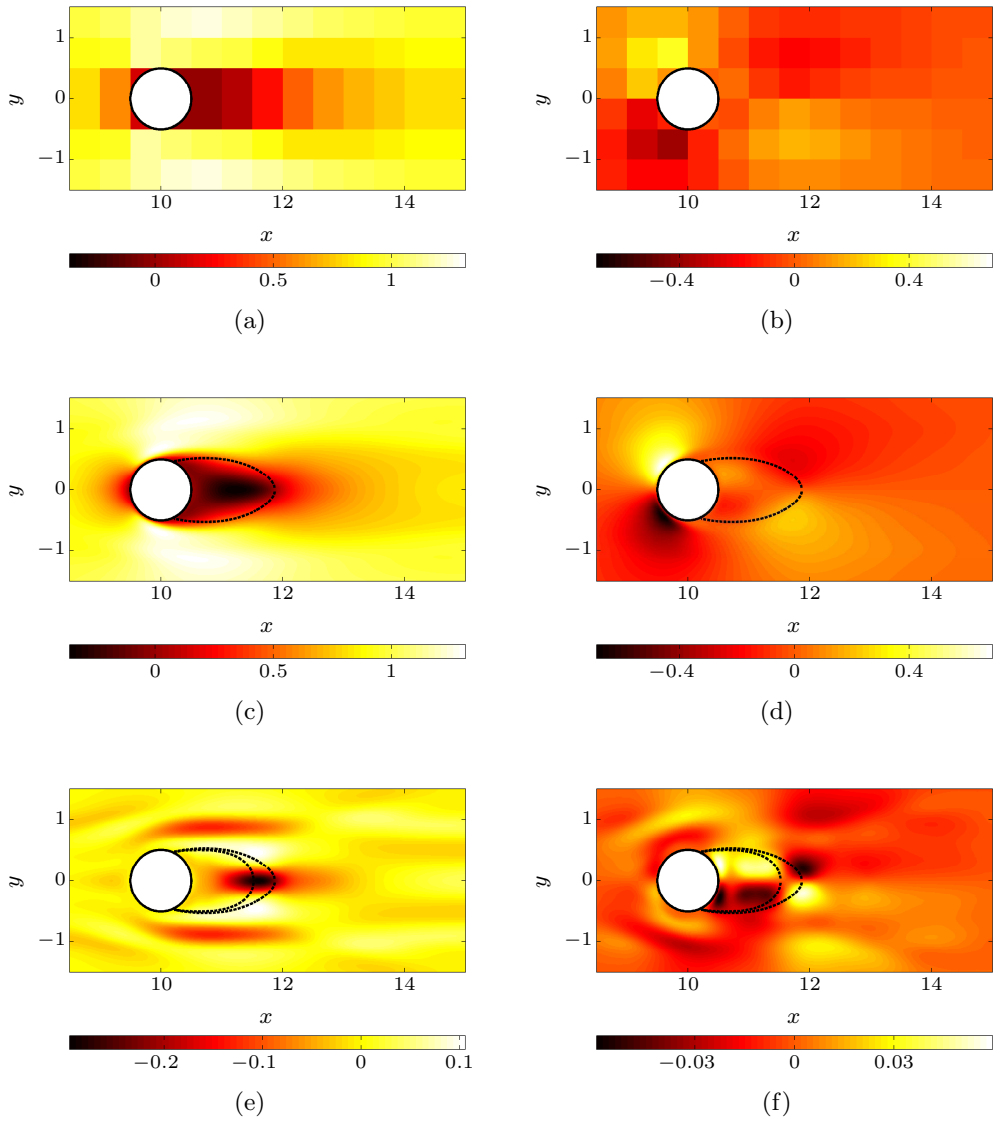

FIGURE 6. Measures of the two velocity components: (a) $\mathcal{M}(\overline{u})$, (b) $\mathcal{M}(\overline{v})$. The measurement corresponds to a rectangular mesh of line-density of points $n = 2$, and the measurement window is the full flow field. Reconstructed fields: (c) $\tilde{u}$, (d) $\tilde{v}$. Error fields: (e) Δu and (f) Δv. The dashed-lines in figures (c) and (d) refer to the extent of the recirculation bubble of the reconstructed field. In figures (e) and (f), these dashed lines have been reproduced along with those of the true mean-flow.

of points is $n = 20$), but locations, where measurements are performed, are limited in space. More precisely, the assimilation (or identification) window has the height of the computational domain but varies in length. For a given abscissa x_0, we consider two different identification windows: the first starting at $x = 5$ and ending at $x = x_0$, and the second starting at $x = x_0$ and ending at $x = 25$. The two identification windows are thus $W_1 = [5, x_0]$ and $W_2 = [x_0, 25]$.

The results are presented in figure 7. The first series of simulations for the identification window $W_1 = [5, x_0]$ shows that the error is decreasing with the length of the

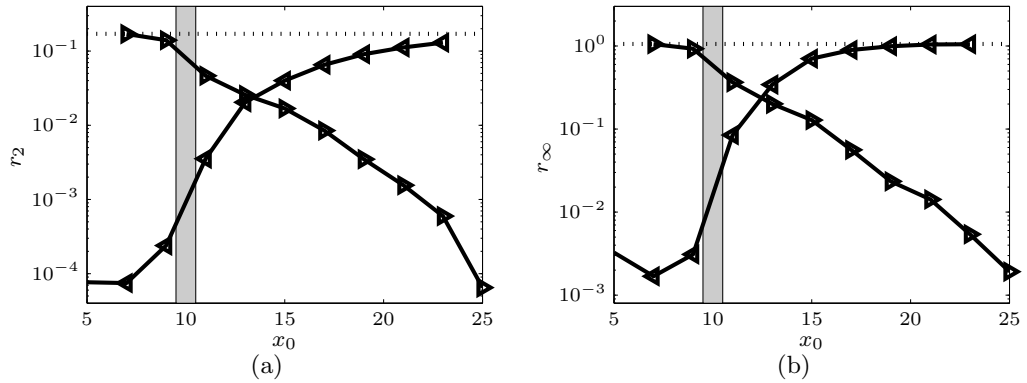

FIGURE 7. Results for the extrapolation case. The error $\|\Delta\mathbf{u}\|$ is plotted against the streamwise coordinate x_0 defining the extent of the identification window. Right oriented triangles are associated with the measurement window $W_1 = [5, x_0]$, while the left oriented triangles correspond to the identification window $W_2 = [x_0, 25]$. The error of approximating the mean flow by the base flow is represented by a dashed line. (a) r_2 error, (b) r_∞ error as defined in (4.1). The grey rectangle represents the location of the cylinder.

identification window. The algorithm starts to produce accurate results as soon as the zone around the cylinder is included in the assimilation window (from $x_0 = 11$). In particular, if the data-assimilated does not contain any measures where the mean flow and base flow are different (unsteady zones), the identification will not be able to match the mean flow, since hardly any information is provided. However, as soon as some unsteady zones are assimilated, the algorithm is able to reconstruct not only the identified zone, but the full flow field. This demonstrates that extrapolation is a true capability of the presented data-assimilation method. The second series of simulations corresponds to the identification window $W_2 = [x_0, 25]$. In this case, even for small identification windows (starting from $x_0 = 23$), the mean and base flows are different in the considered zone. Therefore, the extrapolation is relatively effective, even with little information, as we can see by considering the L^2-norm plot of the error (figure 7(a)). However, the L^∞ residual r_∞ remains rather large (see figure 7(b)).

The results of the extrapolation for the identification window $W_2 = [13, 25]$ (corresponding to $x_0 = 13$) are presented in figure 8. We can see that only limited information is available downstream of the cylinder; in particular, the location of the reattachment point of the recirculation bubble is outside the identification window. Despite this lack of information, the reconstructed field $\tilde{\mathbf{u}}$ is very similar to the mean flow $\overline{\mathbf{u}}$. However, some non-negligible errors in the reconstruction appear immediately upstream of the identification window (nearly no error can be found within the identification window). Interestingly, the incoming flow field has been modified from a uniform flow to a y-dependent flow field (the uniform inflow boundary condition is still satisfied further upstream), as we can see in figure 8(c), illustrating that several types of solutions can be found depending on the quality of the measure. In fact, it is likely that the cost functional is multimodal (several local minima may exist), associated with different flow fields, one of which is the physical solution of the problem. There is however no guarantee, as demonstrated here, to find this physical solution. Nevertheless, even if the mean flow is not exactly matched, the reconstructed field yields far more information about the nature of the flow than is contained in the initial information we measured.

The results of the extrapolation procedure indicate that the field is best reconstructed as long as the recirculation bubble is part of the measurement window. This finding is

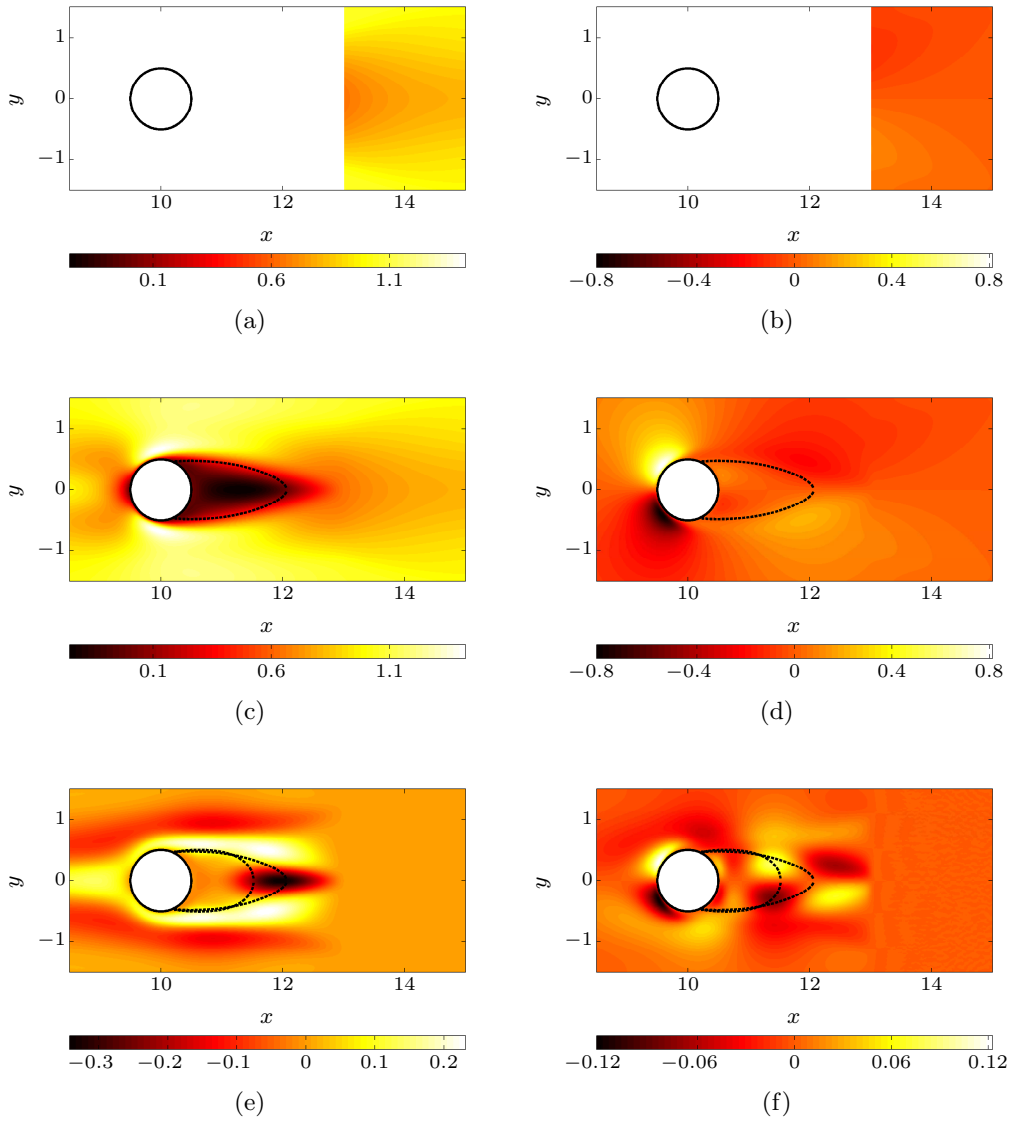

FIGURE 8. Measures of the two velocity components: (a) $\mathcal{M}(\overline{u})$, (b) $\mathcal{M}(\overline{v})$. The measurement corresponds to a rectangular mesh of line-density of points $n = 20$ and the measurement window is $W_2 = [13, 25]$ ($x_0 = 13$). Reconstructed fields: (c) $\tilde{u}$, (d) $\tilde{v}$. Error fields: (e) Δu and (f) Δv. The dashed-lines in figures (c) and (d) refer to the extent of the recirculation bubble of the reconstructed field. In figures (e) and (f), these dashed lines have been reproduced along with those of the true mean-flow.

reminiscent of the results by Marquet *et al.* (2008) and Pralits *et al.* (2010) who showed that the recirculation bubble is the most sensitive region regarding the overall dynamics of the flow field.

4.2.3. *State vector reconstruction*

In order to approach real cases for which this method is likely to be employed, we proceed from the full two-component velocity matching to a scalar-field matching based on the velocity magnitude. The operator defining the measured quantity is therefore

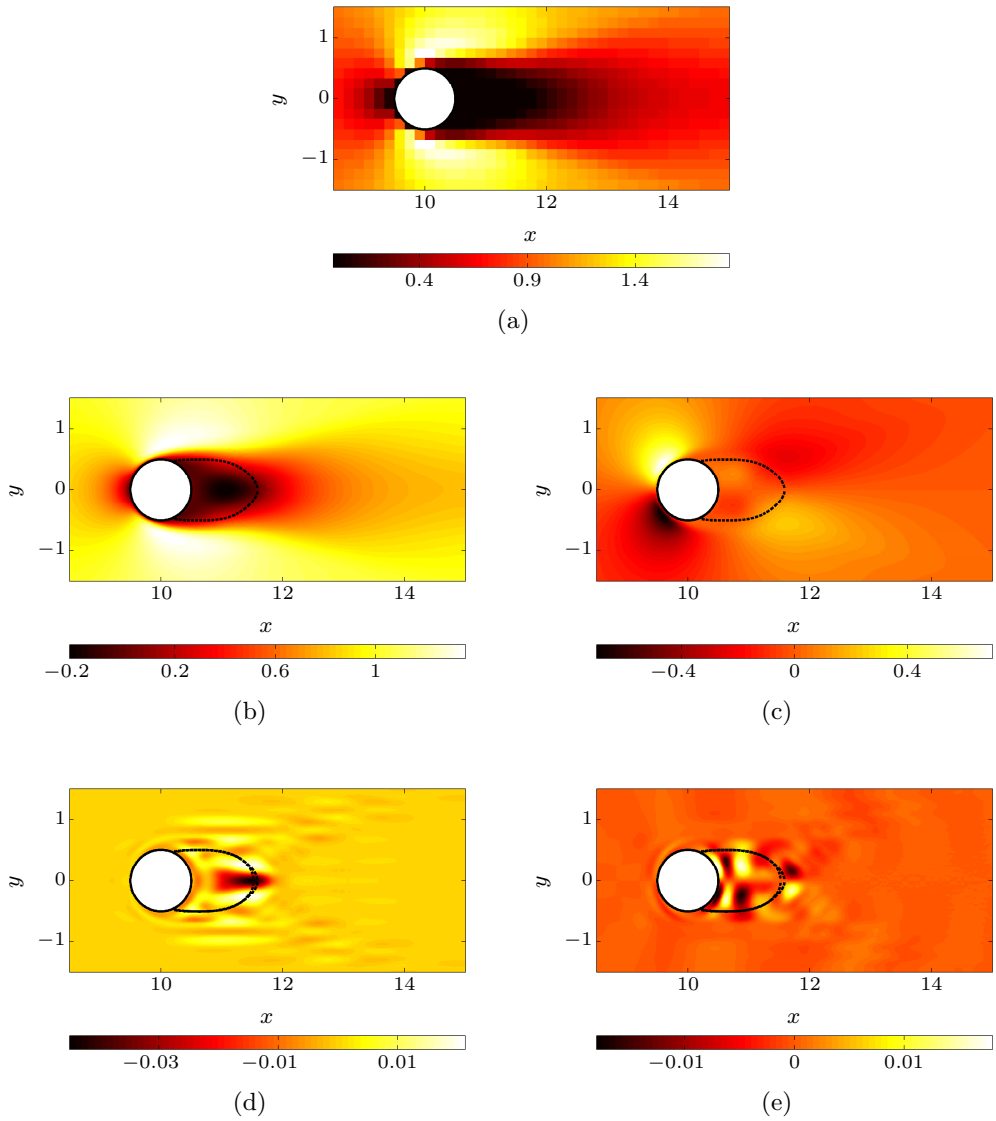

FIGURE 9. (a): Velocity magnitude measures on a mesh corresponding to $n = 6$. (b) and (c): Reconstructed field $\mathbf{u}_{opt}$. (d) and (e): Two components of the error $\Delta\mathbf{u}$. The dashed-lines in figures (b) and (c) represent the extent of the recirculation bubble for the reconstructed field. In figures (d) and (e), these lines have been reproduced along with those of the true recirculation bubble.

$$\mathcal{Q}(\mathbf{u}) = \frac{1}{2}\left|\mathbf{u}\right|^2 = \frac{1}{2}\left(u^2 + v^2\right), \tag{4.3}$$

The projection operator $\mathcal{P}$ is chosen such that the measure domain is the entire domain and the line-density of points of the measures is $n = 6$. The measured field $\tilde{\mathbf{m}}$ is plotted in figure 9(a). The reconstructed field from data-assimilation of the measurements is presented in figures 9(b) and (c).

We observe that even though only velocity magnitude on a rather coarse mesh has been used as an input to our data-assimilation algorithm, it is possible to retrieve a

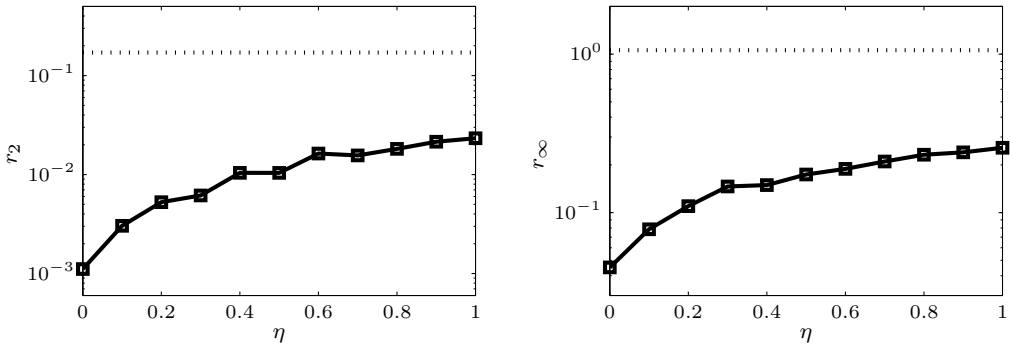

FIGURE 10. Results for the noise reduction case. The error (measured relative to the base flow error) $\|\Delta\mathbf{u}\|$ is plotted (square symbols) against the noise strength η in the measured signal. The error made by approximating the mean flow by the base flow is represented with a dashed line. (a) r_2 error, (b) r_∞ error as defined in (4.1).

good approximation of the full component-wise mean-velocity field. Both the streamwise and normal velocity components have been recovered accurately, with a small error concentrated around the recirculation zone in the near-wake of the cylinder.

4.3. *Noise reduction*

Experimental measurements are often contaminated by noise, and for an application of data-assimilation to experimental data the ability of the technique to deal with measurement noise must be studied. We consider the same measure operator $\mathcal{M}$ as presented in the previous section: velocity magnitude measured on a mesh of line-density $n = 6$. We thus have $\mathbf{m}^* = \mathcal{M}(\overline{\mathbf{u}})$ where the star indicates a noiseless quantity. We add to this measure a noise component

$$\overline{\mathbf{m}} = \mathbf{m}^* + \eta\xi, \tag{4.4}$$

with ξ a random N-dimensional vector and η a real number controlling the amplitude of the added noise. The vector ξ is constructed with a uniform distribution chosen such that $|\xi_i| < \sqrt{\|\mathbf{m}^*\|_M{}^2/N}$. The level of noise is governed by the real number η; for example, $\eta = 0.1$ corresponds to a noise-to-signal ratio of 10%, while for $\eta = 1$ we have a 100% noise-to-signal ratio. These ratios depend on the norm used to define the noise, in our case, the L^2-norm. We present in figure 10 the results of data-assimilation as a function of the noise level η. The error is, as expected, an increasing function of the noise level. The algorithm however captures the flow features very well, even for large noise amplitudes. The measure, the reconstructed field and the error are plotted in figure 11 for $\eta = 1$. The identified field $\tilde{\mathbf{u}}$ is also relatively noisy, but the flow has been remarkably reconstructed from a low-resolution, scalar and noisy measure. Moreover, the recirculation bubble is accurately reconstructed, together with the main features of the flow.

The evolution, during the iterative process, of both the cost functional $\mathcal{E}$ and the real L^2 residual r_2 for the two cases, $\eta = 0$ (no noise) and $\eta = 1$ (noise level of 100%), are plotted in figure 12. We can see that for both cases, the cost functional $\mathcal{E}$ decreases monotonically (due to the gradient descent), but reaches an asymptote at a higher value for the noisy case, confirming that it is not possible to match the measurement noise with a solution of the Navier-Stokes equations. The Navier-Stokes operator thus acts as a filter and cannot provide a fit matching the noise-corrupted measurement. Analyzing

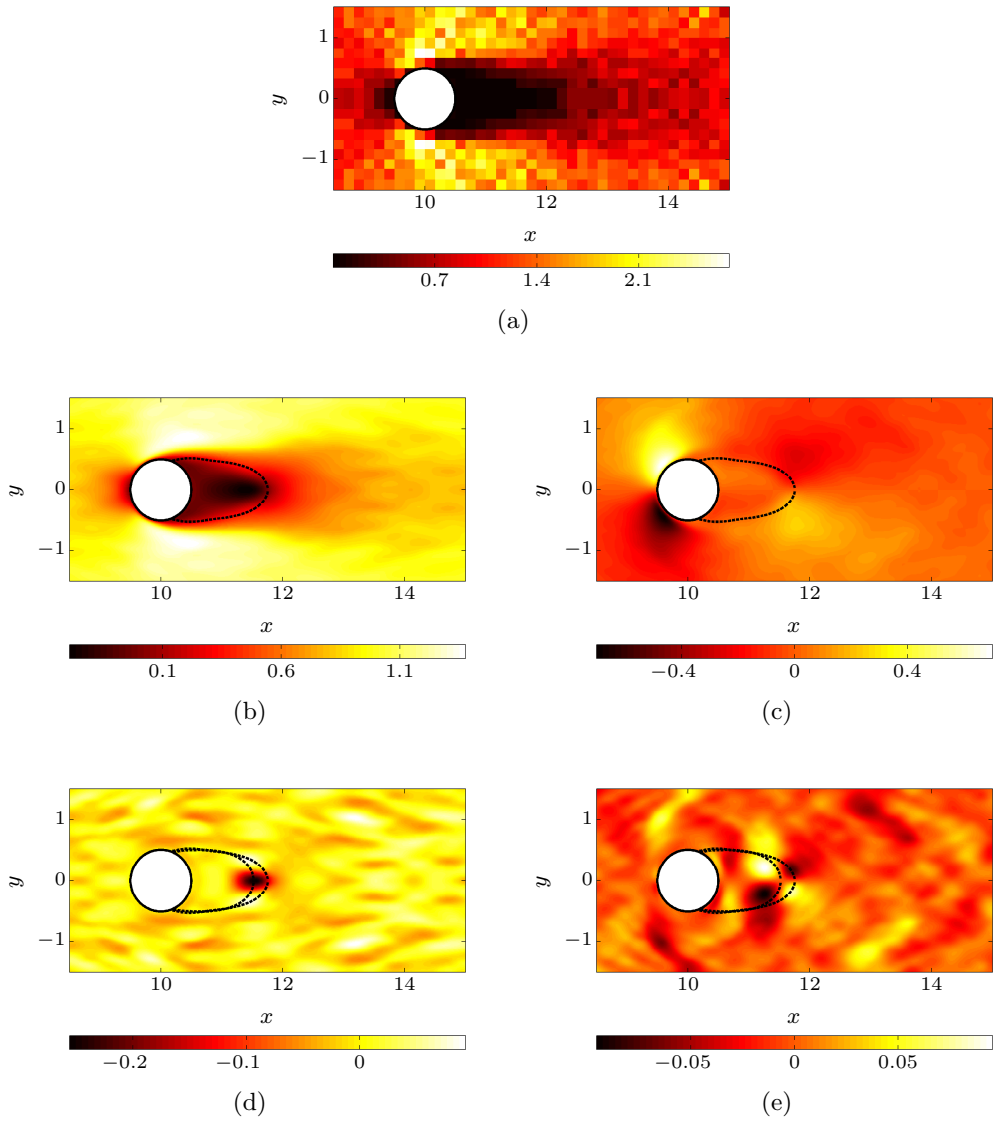

FIGURE 11. (a): Velocity magnitude measures on a mesh corresponding to $n = 6$. The noise level has been set to $\eta = 1$, i.e., we have a 100% noise-to-signal ratio according to our definition. (b) and (c): Reconstructed field $\mathbf{u}_{opt}$. (d) and (e): Two components of the error $\Delta\mathbf{u}$. The dashed-lines in figures (b) and (c) refer to the extent of the recirculation bubble of the reconstructed field. In figures (d) and (e), these dashed lines have been reproduced along with those of the true mean-flow.

the evolution of r_2, we see that in the noiseless case the real error monotonically decreases, while it starts to decrease and then increases again, after approximately 200 iterations, for the noisy measurements case. This means that after the turning point, the algorithm tries to match the measurement noise, which drives the solution away from the physical solution $\overline{\mathbf{u}}$. In a real situation, this convergence curve is not accessible, and we therefore cannot terminate the iterative identification when the error is lowest. It is however useful to evaluate when to stop the reconstruction based on a comparison between the norm of the gradient of the cost functional and an estimation of the measurement noise level.

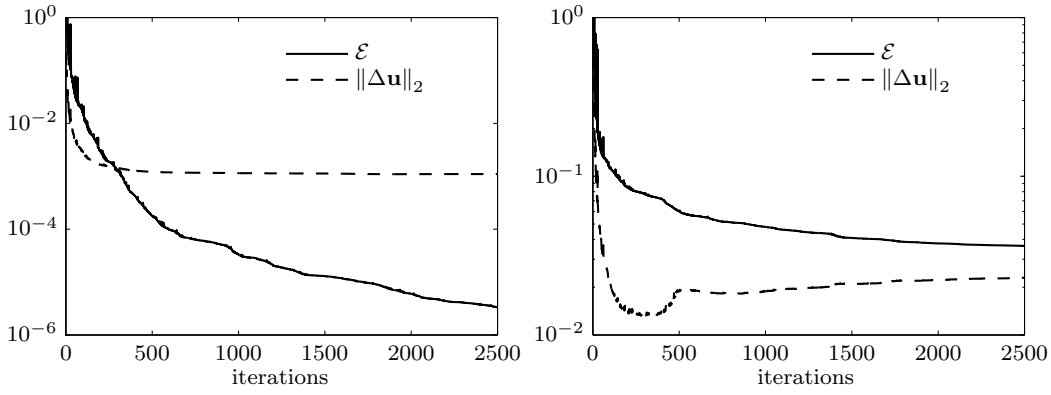

FIGURE 12. (a) Convergence curves for the noiseless case ($\eta = 0$) and (b) for the noisiest case ($\eta = 1$). We notice that for the case without noise, both the cost functional $\mathcal{E}$ and the real residual r_2 are monotonically decreasing. For the noisy case, however, even though $\mathcal{E}$ decreases as a result of the optimization, around the 200th iteration, the real residual r_2 starts to increase again, signifying that from this point forward the optimization actually leads to a deterioration of the identified optimal mean flow $\tilde{\mathbf{u}}$.

5. Additional flow reconstruction

5.1. *Drag evaluation*

Another way to assess the quality of the reconstructed fields is to compare the cylinder drag of the mean field with the drag of the reconstructed field. The drag coefficient C_D induced by a field $(\mathbf{u}, p)^\top$ on the cylinder is defined as

$$C_D = \underbrace{2\int_{\mathcal{C}} Re^{-1}\left(\nabla\mathbf{u} + \nabla\mathbf{u}^\top\right)\mathbf{n}\cdot\mathbf{e}_x \ \mathrm{d}l}_{C_V} + \underbrace{2\int_{\mathcal{C}} -p\mathbf{n}\cdot\mathbf{e}_x \ \mathrm{d}l}_{C_P}, \tag{5.1}$$

where $\mathcal{C}$ represents the cylinder's surface and $\mathrm{d}l$ the integration element along this contour. The factors 2 stem from the normalization by the dynamic pressure $\frac{1}{2}\rho U^2$, which simplifies to $\frac{1}{2}$ in the non-dimensional variables. As seen in equation (5.1), we can divide the drag force into two components: the viscous drag C_V and the pressure drag (or form drag) C_P. We expect the C_V-component to be accurately predicted (as it only depends on the velocity vector which is properly reconstructed), and the C_P-component to exhibit a more appreciable mismatch (as the true pressure field $\bar{p}$ is only recovered up to a scalar field ϕ linked to the potential part of the Reynolds stress term, as explained in (2.29)).

We display in table 1 the different drag coefficients obtained for the true mean flow $(\bar{\mathbf{u}}, \bar{p})^\top$ and for several reconstruction scenarios. We notice that, as expected, the viscous drag is accurately predicted whereas the relative error on the pressure drag is always greater than 10%. Note that for larger Reynolds numbers, the viscous drag is expected to decrease and, therefore, the relative total error to increase.

5.2. *Unsteadiness characterization*

In the previous sections, we have exploited the reconstruction abilities of the data-assimilation technique by analyzing the reconstructed state vector for several cases of interest. In this section, we explore the possibilities of unsteadiness characterization offered by the identified forcing $\mathbf{f}_{opt}$ in the case of full-state information identification, where the global optimal has been reached.

	Viscous drag (C_V)	Pressure drag (C_P)	Total drag (C_D)
Mean flow	0.30 (-)	1.13 (-)	1.43 (-)
Base flow	0.25 (18.3%)	0.86 (23.3%)	1.11 (22.3%)
Full state identification	0.30 (1.3%)	1.00 (11.0%)	1.30 (9.0%)
Interpolation ($n = 2$)	0.29 (3.7%)	0.95 (15.7%)	1.24 (13.1%)
Extrapolation ($x_0 = 13$)	0.30 (2.2%)	0.98 (12.6%)	1.28 (10.4%)
Velocity magnitude ($\eta = 0$)	0.30 (2.9%)	1.00 (11.2%)	1.30 (9.4%)
Velocity magnitude ($\eta = 1$)	0.29 (5.4%)	1.00 (10.7%)	1.29 (9.6%)

TABLE 1. Drag coefficients for the mean flow obtained through DNS simulation, for the base flow, for the full-state identification and for several reconstruction scenarios corresponding to the cases displayed in figures 6, 8, 9 and 11. The relative error with respect to the mean flow is displayed in parentheses for each case.

As covered in section 2.6, the algorithm only identifies the solenoidal part of the true forcing $\mathbf{f}^* = -\nabla \cdot \mathbf{R}$. However, it is the full Reynolds stress tensor $\mathbf{R}$, rather than the components of its divergence, that would be most valuable. In a two-dimensional setting, this tensor can be expressed as

$$\mathbf{R} = \begin{pmatrix} \alpha & \beta \\ \beta & -\alpha \end{pmatrix} + k\mathbf{I}, \tag{5.2}$$

with $\alpha = \frac{1}{2}\left(\overline{u'^2} - \overline{v'^2}\right)$, $\beta = \overline{u'v'}$ and $k = \frac{1}{2}\left(\overline{u'^2} + \overline{v'^2}\right)$ denoting the fluctuating kinetic energy. These quantities vanish on the cylinder's surface due to the no-slip boundary condition.

It should then be possible to optimally reconstruct a tensor of this particular structure from the identified forcing $\mathbf{f}_{opt}$. As we explained in section 2.6, the forcing $\mathbf{f}^*$ can be decomposed into a solenoidal part and a potential component as $\mathbf{f}^* = \mathbf{f}_s^* + \nabla\phi$. Furthermore, we also have $\mathbf{f}_s^* \simeq \mathbf{f}_{opt}$ (strict equality is not true because of the boundary condition issue discussed in 2.6). In summary, we have:

$$\mathbf{f}^* = -\begin{pmatrix} \partial_x\alpha + \partial_y\beta \\ \partial_x\beta - \partial_y\alpha \end{pmatrix} - \nabla k \tag{5.3a}$$

$$\simeq \mathbf{f}_{opt} + \nabla\phi \tag{5.3b}$$

Then taking the curl of this expression, the gradient terms drop and we are left with one equation relating α, β and the the identified forcing $\mathbf{f}_{opt}$. Such an identification, however, is under-constrained as we have only one equation for two unknowns. If we further assume that $-\nabla k \simeq \nabla\phi$ (see next section for justification in the cylinder case), we obtain:

$$-\begin{pmatrix} \partial_x\alpha & \partial_y\beta \\ \partial_x\beta & -\partial_y\alpha \end{pmatrix} = \mathbf{f}_{opt}. \tag{5.4}$$

This yields two equations for two unknowns, along with the boundary conditions $\alpha = 0$ and $\beta = 0$ on the boundaries. Yet, recalling that the optimal forcing is divergence-free ($\nabla \cdot \mathbf{f}_{opt} = 0$), we obtain a constraint on α and β, which is non-physical so that the identified α and β obtained by solving (5.4) will, in general, not match their experimental values. Instead, we propose a weaker constraint to relate the left and right-hand-sides of equation (5.4). We decide in the following to minimise the cost functional

$$\mathcal{I}(\alpha, \beta) = \int_\Omega \left((-\partial_x\alpha - \partial_y\beta - f_x)^2 + (-\partial_x\beta + \partial_y\alpha - f_y)^2 \right) \mathrm{d}\Omega, \tag{5.5}$$

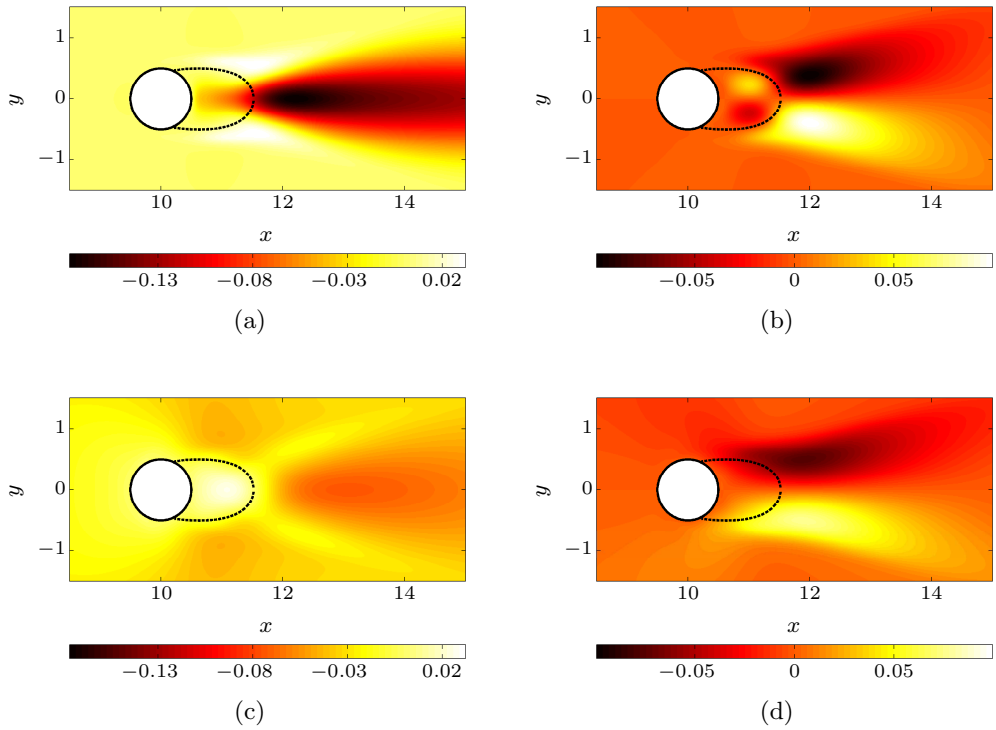

FIGURE 13. (a) α and (b) β (respectively, left and right column) of the real reduced Reynolds stress tensor , and reconstructed tensor components (c) α_{opt} and (d) β_{opt}. The dashed-lines indicate the extent of the recirculation bubble of the true mean-flow.

where $\mathbf{f}_{opt} = (f_x, f_y)$. This minimization problem is solved by setting the gradient of this cost functional to zero. This leads to the two independent equations

$$\nabla^2 \alpha = -\partial_x f_x + \partial_y f_y, \tag{5.6}$$

$$\nabla^2 \beta = -\partial_y f_x - \partial_x f_y, \tag{5.7}$$

which have to be solved subject to the boundary conditions stated above. The results are presented in figure 13.

We see in this figure that the reconstruction of the coefficients which characterise the unsteadiness of the flow fails for α but yields relatively good results for β.

5.3. *Pressure reconstruction*

The component of the reconstructed field that we have not yet analysed, is the pressure $\tilde{p}_{opt}$. We know that the optimally identified pressure $\tilde{p}_{opt}$ is the difference between the real mean-pressure $\overline{p}$ and the potential ϕ (see equation (2.29)). It is interesting to compare the reconstructed pressure field $\tilde{p}_{opt}$ to the base-flow pressure p_b (for sake of comparison), to the real mean-pressure $\overline{p}$ and to the total pressure $p_T = \overline{p} + k$ (sum of the real mean-pressure and the fluctuating kinetic energy k). This is achieved in figure 14.

Analysing the base-flow pressure p_b and the real mean-pressure $\overline{p}$, we notice that the pressure drop is centred on the respective recirculation bubbles. However, the real mean-pressure also displays a constant pressure drop in the wake of the cylinder. If we consider the total pressure p_T, we can see that this wake effect disappears, and the pressure drop appears to be mainly located within the recirculation bubble. When compared to the reconstructed pressure $\tilde{p}_{opt}$, we can see that the two pressure fields p_T and $\tilde{p}_{opt}$ are very

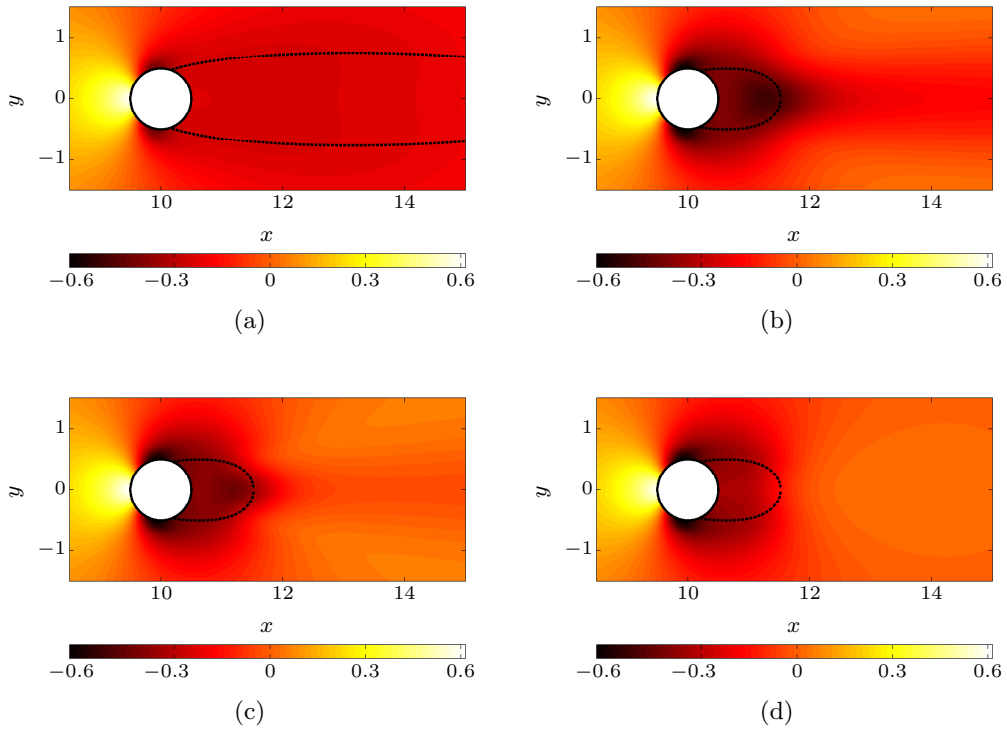

FIGURE 14. (a) Base-flow pressure p_b, (b) mean flow pressure $\overline{p}$, (c) total pressure $p_T = \overline{p}+k$, (d) reconstructed pressure $\tilde{p}_{opt}$. The dashed-lines indicate the extent of the recirculation bubbles, (a) in the case of the base-flow, (b,c,d) in the case of the true mean-flow.

similar, even though the reconstructed pressure is slightly overestimated near the end of the recirculation bubble, around the stagnation point. The difference between these two pressure fields is weak, so that $-k \simeq \phi$, therefore justifying the assumption $-\nabla k \simeq \nabla\phi$ of the previous section. It is remarkable that the pressure reconstructed from velocity measurements only $\tilde{p}_{opt}$, is rather close to the total pressure p_T, and also not that far from the real pressure $\overline{p}$. In order to improve the identification of the real mean-pressure field, it is mandatory to incorporate pressure measurements within the data-assimilation algorithm. This is briefly discussed below.

6. Concluding remarks and extensions

Despite recent progress in experimental measuring techniques, many data from experiments are still limited in terms of resolution, in terms of access to specific regions of interest, and in terms of quantities that can be measured reliably. We have developed and introduced a data-assimilation technique for the recovery of mean flow fields that are solutions of the Reynolds-Averaged Navier-Stokes (RANS) equations and match the available data-points. The algorithm, based on an iterative, direct-adjoint optimization approach, has been validated on two-dimensional flow past a circular cylinder at a supercritical Reynolds number ($Re = 150$). The method has been used in an interpolatory mode (recovering mean-velocity fields from much coarser measurements), in an extrapolatory mode (extending the mean-velocity field into domains where no measurements have been taken), and in a state-vector reconstruction mode (determining mean-velocity components from measurements of only the magnitude). In all cases, we have observed a

satisfactory recovery of the mean-velocity field that proves substantially more accurate than more naïve approaches based on higher-order interpolation that disregard physical constraints on the mean fields. Moreover, the influence of noise in the input data fields has been assessed, and the method has been found to be robust, even in the face of a noise-to-signal ratio of 100%.

Together with the assimilated mean-velocity field, we also obtain the forcing vector field that renders the error between the available measurements and the recovered mean-velocity field minimal. From this forcing, information about the unsteadiness and the pressure field can be extracted. However, this information is limited to the solenoidal part of the Reynolds stress tensor and the non-kinetic part of the pressure. Despite this limitations, it has to be kept in mind that only steady (averaged) information has entered the data-assimilation algorithm. Yet, we were able to gain insight — albeit partial and incomplete — on the second-order moments of the unsteady flow. This is quite remarkable, given the limited input information.

Various extensions and variations of the presented algorithms are conceivable. For large Reynolds number applications, the current numerical technique can be adapted to aid in the solving of equation (2.4) (which can be challenging for large Reynolds numbers when using Newton's iteration method). Due to the averaging, we know that the mean flow will be similar to a base flow at a lower Reynolds number. We therefore propose to artificially decrease the Reynolds number in equation (2.4). Ideally one would choose the Reynolds number yielding a base flow as close as possible to the measured mean flow. We therefore have $Re = Re^* - \Delta Re$ with Re^* as the real flow Reynolds number and ΔRe ($0 < \Delta Re < Re^*$) as the adjustment performed. We can start with a zero initial guess ($\mathbf{f}_g = 0$) and identify the optimal forcing $\mathbf{f}_{opt}$. The identified total forcing (for the Navier-Stokes equation with the given Reynolds number Re^*) takes the form $\mathbf{f}^*_{opt} = \mathbf{f}_{opt} + \frac{\Delta Re}{Re Re^*}\nabla^2\tilde{\mathbf{u}}_{opt}$, where we have added the contribution due to the artificial decrease of Reynolds number. We notice that this method does not violate the divergence-free forcing condition. This technique can be thought of as a preconditioning method allowing to bypass the problem of solving the Navier-Stokes equations for high Reynolds numbers. It can also be interpreted as a preconditioning step for the optimization. The initial guess $\mathbf{f_g}$ could also be obtained by a RANS model (based, for example, on an eddy-viscosity closures or more elaborate Reynolds stress models). Indeed, by so proceeding we avoid the costly (and probably ill-posed) computation of a high Reynolds-number base flow. Moreover, it is also possible to compare the Reynolds stresses issued from the turbulence model with those of the optimal solution compatible with the experimental observations. This approach would be interesting and useful in assessing the performance of turbulence closures in more complex flow configurations.

The cost functional, i.e., the error between measured and the model-predicted data can be augmented by a weight function which directs more emphasis towards regions that are of more relevant. For example, shear layers or regions close to walls can be singled out as more important and as having a larger contribution to the cost functional. Also, pressure measurements could be considered, leading to a more well-posed optimization problem as explained in section 2.6. Some of these extensions will be pursued in a future study. In its current form, the data-assimilation method is a very valuable tool for the experimentalist to recover more information about the flow than is directly measurable. In this sense, it takes the measured data beyond their intrinsic information content and extends the scope of current measurement capabilities.

REFERENCES

Avril, S., Bonnet, M., Bretelle, A.-S., Grédiac, M., Hild, F., Ienny, P., Latourte, Félix, Lemosse, D., Pagano, S., Pagnacco, E. & Pierron, F. 2008 Overview of identification methods of mechanical parameters based on full-field measurements. *Experimental Mechanics* **48** (4), 381–402.

Courtier, P. 1997 Dual formulation of four-dimensional variational assimilation. *Quarterly Journal of the Royal Meteorological Society* **123** (544), 2449–2461.

Everson, R. & Sirovich, L. 1995 Karhunen–loeve procedure for gappy data. *JOSA A* **12** (8), 1657–1664.

Ghil, M. & Malanotte-Rizzoli, P. 1991 Data assimilation in meteorology and oceanography. *Adv. Geophys* **33**, 141–266.

Gunes, H., Sirisup, S. & Karniadakis, G.E. 2006 Gappy data: To krig or not to krig? *Journal of Computational Physics* **212** (1), 358–382.

Gunzburger, M.D. 2000 Adjoint equation-based methods for control problems in incompressible, viscous flows. *Flow, Turbulence and Combustion* **65** (3-4), 249–272.

Heitz, D., Mémin, E. & Schnorr, C. 2010 Variationnal fluid flow measurements from image sequences: synopsis and perspectives. *Experiments in Fluids* **48** (3), 369–393.

Hill, D.C. 1995 Adjoint systems and their role in the receptivity problem for boundary layers. *Journal of Fluid Mechanics* **292**, 183–204.

Jackson, C.P. 1987 A finite-element study of the onset of vortex shedding in flow past variously shaped bodies. *Journal of Fluid Mechanics* **182** (1), 23–45.

Le Dimet, F.-X. & Talagrand, O. 1986 Variational algorithms for analysis and assimilation of meteorological observations: theoretical aspects. *Tellus* **38A**, 97–110.

Luchini, P. & Bottaro, A. 2001 Linear stability and receptivity analyses of the stokes layer produced by an impulsively started plate. *Physics of Fluids* **13**, 1668.

Lundvall, J., Kozlov, V. & Weinerfelt, P. 2006 Iterative methods for data assimilation for burgers's equation. *Journal of inverse and ill-posed problems* **14** (5), 505–535.

Marquet, O., Sipp, D., Chomaz, J-M. & Jacquin, L. 2008 Amplifier and resonator dynamics of a low-reynolds-number recirculation bubble in a global framework. *Journal of Fluid Mechanics* **605**, 429–443.

Mohammadi, B. & Pironneau, O. 2004 Shape optimization in fluid mechanics. *Annual Review of Fluid Mechanics* **36**, 255–279.

Pralits, J., Brandt, L. & Giannetti, F. 2010 Instability and sensitivity of the flow around a rotating circular cylinder. *Journal of Fluid Mechanics* **650**, 513.

Ruhnau, P., Kohlberger, T., Nobach, H. & Schnorr, C. 2005 Variationnal optical flow estimation for particle image velocimetry. *Experiments in Fluids* **38**, 21–32.

Ruhnau, P. & Schnorr, C. 2007 Optical stokes flow estimation: An imaging-based control approach. *Experiments in Fluids* **42**, 61–78.

Ruhnau, P., Stahl, A. & Schnorr, C. 2007 Variational estimation of experimental fluid flows with physics-based spatio-temporal regularization. *Measurement Science and Technology* **18**, 755–763.

Schmid, P.J. 2007 Nonmodal stability theory. *Annual Review of Fluid Mechanics* **39**, 129–162.

4.4 Article : Data-assimilation of a 2D PIV measurement over an idealized airfoil

Under consideration for publication in J. Fluid Mech. 1

Data-assimilation of mean-velocity from 2D-PIV measurements of flow over an idealized airfoil

NICOLAS DOVETTA[1]†, DIMITRY P. G. FOURES[2], BEVERLEY J. McKEON[3], PETER J. SCHMID[4] AND DENIS SIPP[5]

[1]LadHyX, Ecole Polytechnique, F-91128 Palaiseau, France
[2]DAMTP, University of Cambridge, Cambridge CB3 0WA, United Kingdom
[3]GALCIT, California Institute of Technology, Pasadena, CA 91125, U.S.A.
[4]Dept. of Mathematics, Imperial College London, London SW7 2AZ, United Kingdom
[5]ONERA-DAFE, Rue des Vertugadins, F-99999 Meudon, France

(Received ? ; revised ?; accepted ?. - To be entered by editorial office)

Measurements taken from experiments or from numerical simulations can often be thought of as spatially undersampled representations of a high-dimensional flow field. Data-assimilation is a methodology that recovers non-measured components of the high-dimensional flow field by matching a parameterized model to the measured data. Flow around an idealized airfoil at a Reynolds number of $Re = 12500$ is measured using time-resolved particle image velocimetry (TR-PIV). Subsequent averaging over a sequence of snapshots produces the mean velocity field and allows the computation of the fluctuations about it. The mean flow is then sampled at a limited number of points in the flow domain, and the Reynolds-Averaged Navier-Stokes (RANS) equations are used, together with a data-assimilation strategy, to recover the mean flow in the entire domain from these limited data points. The recovered and measured mean flows are compared to assess the potential and effectiveness of data-assimilation techniques in providing pertinent flow-field information from restricted measurements.

1. Introduction

Available information about a flow field is often limited to spatial regions of the flow domain or to specific measurable quantities. This is particularly true in experiments where access to wall-regions is often constrained by the size of the probe or where certain quantities can only be measured with great difficulty or not at all. Nevertheless, flow information from the wall-region, beyond what is accessible through direct measurement, is often desirable when comparisons of experimental results with models or computations are made. Data-assimilation is a technique that aims at reconstructing flow information from a limited number of input data. In its most general form, it optimally fits a prescribed model equation to the observed data, which then allows the evaluation of the flow field, via the model, at spatial locations off the original data set and the computation of composite or derived field quantities.

Data-assimilation originated and took its roots in weather forecasting, where a predictive model for the temporal evolution of the atmospheric flow had to account for unequally distributed weather data from around the world. From applications in this

† Email address for correspondence: nicolas.dovetta@ladhyx.polytechnique.fr

field, two types of estimation problems can be distinguished (see Lewis *et al.* 2006). In the first type, state variables such as, e.g., the velocity field, temperature or atmospheric pressure, are estimated at a given time using available, but incomplete, measurements at this same time; this type is referred to as off-line or fixed-sample estimation. The second type is concerned with an estimation of the future state-vector trajectory, while constantly correcting with data as they become available; this type is known as on-line, recursive or sequential estimation. We will concentrate on the first, off-line type: the recovery of time-averaged (and thus time-independent) flow information from limited data.

Data-assimilation techniques for off-line state estimation make use of either a history of measurements (without any constraints given by a physical model), or take into account a physical model using a weak or strong formulation. When accounting for noisy data, statistical approaches are taken, and the most widely used techniques are based on Wiener filtering, such as the optimal interpolation (OI) method or the Kriging algorithm. Many examples can be found in the atmospheric flow-prediction literature (see Ghil & Malanotte-Rizzoli 1991; Kalnay 2002). Within the fluid mechanics community, data-assimilation is a far less common tool. Related techniques have been used to repair gappy data-sequences in PIV-measurements (see Bui-Thanh *et al.* 2004); however, the full potential of gaining flow information from limited data, while respecting an underlying model, has not yet been realized or explored.

In this article, we use data-assimilation techniques to extract a mean-flow field and information about the turbulent shear stress from a limited number of mean-velocity values. As our underlying model, we postulate the Reynolds-Averaged Navier-Stokes (RANS) equations and enforce this model as a strong constraint. Consequently, the estimated state is a solution of the RANS equations. In general, strong constraints require a parameterized (tunable) model in order to fit the data; the set of parameters, also referred to as the model compliance, could, for example, be an initial condition, as in Apte *et al.* (2010) or Tissot *et al.* (2011), or a material property, as in Avril *et al.* (2008) or Bukshtynov *et al.* (2011). In our case, the model compliance is a part of the unknown Reynolds stress tensor, while the state is the mean-velocity field (see Foures *et al.* 2013). Data-assimilation problems with strong constraints are most conveniently formulated as a variational problem, leading to an iterative optimization scheme.

The mathematical background and algorithmic details of the RANS-based data-assimilation technique has been developed in Foures *et al.* (2013), where "measurements" were taken from a two-dimensional direct numerical simulation of flow around a cylinder at a supercritical Reynolds number of $Re = 150$. In a subsequent study Dovetta *et al.* (2013), the measurement data came from an experimental turbulent pipe flow at a Reynolds number of $Re = 39000$ and matched to a one-dimensional RANS equation. This latter case resulted in a *linear* optimization problem, and the wall-shear stress, pressure drop and Reynolds number could be accurately recovered from a few mean-flow measurements, without resorting to semi-empirical models. In this present case, the reconstruction of a two-dimensional mean-flow field, together with the matching Reynolds shear stress, is attempted. Additional difficulties arise from the *nonlinear* nature of the optimization problem and, more importantly, from uncertainties in the processed data, which require modifications of the original algorithm. In this respect, the present configuration represents most realistic operating conditions, commonly encountered in experiments at high Reynolds numbers. In particular, we will address the challenges of the algorithm, the fidelity of the recovered field and the correlation between errors in the input data and output fields. Despite imperfections in the assimilated flow field, the proposed technique is nonetheless able to furnish qualitative and approximate information on first-order and

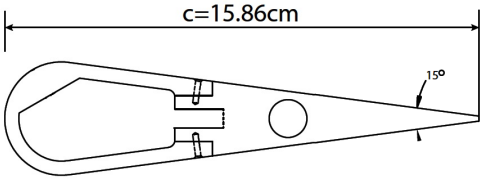

FIGURE 1. Cross-sectional sketch of the idealized airfoil profile (from Gonzalez *et al.* (2010)).

second-order turbulence statistics from a relative small number of mean-flow measurements.

2. Experimental set-up

Experiments have been performed on an idealized airfoil (shown in figure 1) with a chord-length of 15.86 cm, a width of 3.43 cm and a spanwise extent of 50.8 cm. The airfoil is symmetrical and consists of a cylindrical leading edge followed by two plane surfaces connecting at the trailing edge. At a zero angle of attack and a chord-based Reynolds number of $Re_c = 12500$, the flow separates at the transition point between the cylinder and the plane surfaces and forms recirculation bubbles on both sides (see Wallace & McKeon 2012). The flow is above the critical Reynolds number for the onset of von-Karman vortex shedding ($Re_c \approx 2000$); in addition, the shear layers forming around the separation bubbles are convectively unstable, giving rise to the formation of Kelvin-Helmholtz vortices. These two instabilities ensure a dynamics that is reminiscent of the behavior of separated flows at far higher Reynolds numbers (see Prasad & Williamson 1997) — a fact that makes this configuration an attractive choice for studying unsteady flow dynamics on aerodynamic geometries.

Experiments have been performed in a free-surface water facility (see Norman & McKeon (2008); Wallace & McKeon (2012)). The test section measured 1.6 m in length, 0.46 m in width and 0.5 m in depth. The flow is conditioned by a perforated plate, a honey-comb mesh, three turbulence-reducing screens and a 4-to-1 fifth-order-polynomial contraction (see Gharib 1983). The free-stream velocity is 7.4 cm/s and the water temperature is 23°C, which results in a chord-based Reynolds number of $Re_c = 12500$.

A LaVision time-resolved 2D-PIV setup is used, with two Photron Fastcam APX-RS high-speed cameras with Nikon lenses of 50 mm focal length and 1:1.2 aperture. The cameras are synchronized with a high-speed controller; at a framerate of 83 Hz, their resolution is 1024×1024 pixels; they are calibrated at 5.25 px/mm. The camera's frequency is chosen to guarantee a particle displacement between 5 and 7 pixels between any two consecutive snapshots. The seeding particles are hollow glass spheres (reference 110P8 with an average diameter of 11.7 μm and a specific gravity of 1.1), and the seeding density is about 0.1 particles per square pixels. The particles are illuminated by a 2 mm-thick laser sheet provided by a Photonics DM20-527 solid-state laser. In an effort to avoid large uncertainty near the illuminated profile due to surface reflection, the image-intensity is calibrated using white-image subtraction (normalization of the image intensity using the average light distribution) and background-image subtraction. The white and background images are taken before each run and averaged over 100 snapshots. The camera view covers the flow from 3 cm upstream of the leading edge to 12 cm downstream of the trailing edge with a 30% overlap (see figure 2 for a sketch) in order to include a large area of mean-flow and fluctuation measurements. Finally, 20480 instantaneous flow fields are taken per position over 10 runs (2048 snapshots per run, limited by the camera

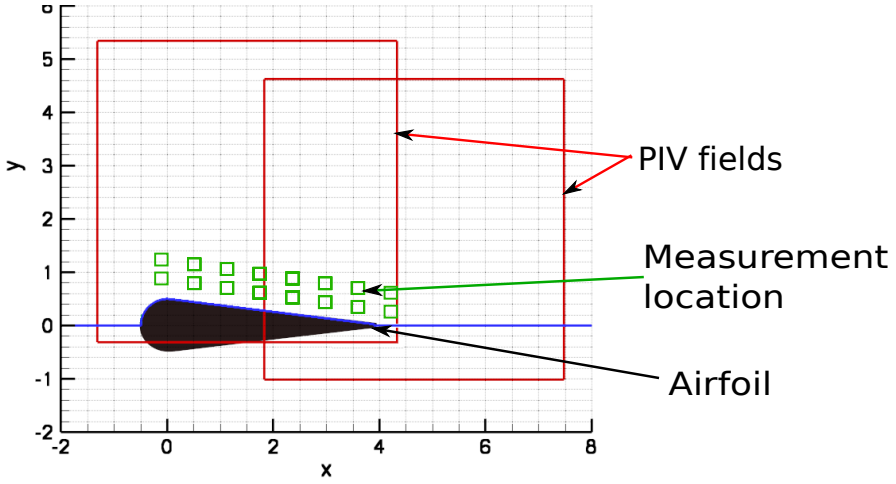

FIGURE 2. Experimental setup of the flow around an idealized airfoil, showing the spatial coverage of the flow by the cameras. The measurements taken from the flow and used in the data-assimilation are indicated by green square symbols.

memory), which represents approximately 115 times the chord-based convection timescale.

The computation of velocity vectors is performed using Davis software. A cross-correlation technique is applied to each sequential image with a window-size reduced from 32×32 px^2 to 16×16 px^2 over three passes (with 50% overlap and a 2:1 elliptic weight). Lastly, the data are post-processed, single missing vectors are interpolated, and the final field is filtered with a 3×3 smoother. This results in a total of 15067 two-dimensional velocity vectors per instantaneous flow field, once masked areas have been deleted. The averaged mean flow from the PIV-snapshots is shown in figure 3.

To evaluate the data-assimilation procedure, a data-set that contains 20 measurement points (see figure 2) is extracted and used as input to our assimilation algorithm. The full mean-velocity field is used as a reference to assess the quality of the mean-field reconstruction. In addition, the Reynolds stresses are derived from variations about the mean-velocity field and compared to the identified Reynolds stresses.

3. Basic elements for data-assimilation

Only an abridged exposition of the data-assimilation procedure, as deemed necessary for the subsequent recovery of the mean-velocity field from experimental PIV-measurements, will be presented below. For a more general, theoretical framework, the reader is referred to Foures *et al.* (2013). In essence, three ingredients are needed for a strongly-constrained data-assimilation: a data-set, a compliance model, and a fitting criterion. This section provides details on these three components, while the following section will describe the numerical particulars and the optimization procedure.

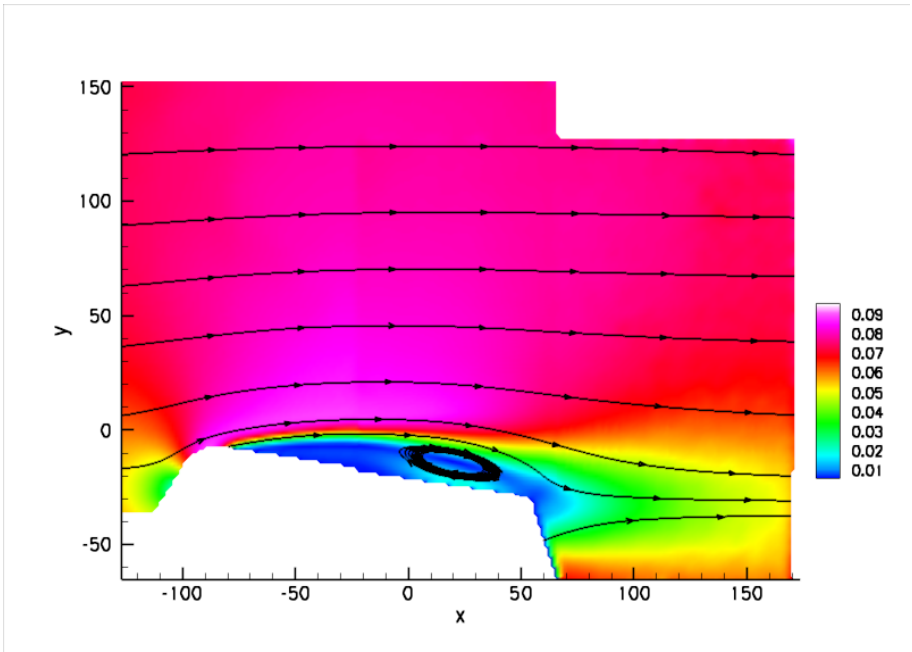

FIGURE 3. Mean-velocity field from averaging time-resolved PIV measurements, visualized by color contours of the velocity magnitude and by streamlines.

3.1. *Model*

The measured mean flow is assumed to comply with the incompressible, two-dimensional Reynolds Averaged Navier-Stokes (RANS) equations, given as

$$\begin{aligned} \overline{\mathbf{u}} \cdot \nabla \overline{\mathbf{u}} + \nabla \overline{p} - \frac{1}{Re} \nabla^2 \overline{\mathbf{u}} &= \nabla \cdot \mathbf{R}, \\ \nabla \cdot \overline{\mathbf{u}} &= 0. \end{aligned} \tag{3.1}$$

The mean velocity is denoted by $\overline{\mathbf{u}}$, the mean pressure by $\overline{p}$. The 2×2 Reynolds stress tensor $\mathbf{R}$ is defined in a standard manner as

$$\mathbf{R} = -\begin{pmatrix} \overline{u'^2} & \overline{u'v'} \\ \overline{u'v'} & \overline{v'^2} \end{pmatrix}, \tag{3.2}$$

with u' and v', respectively, representing the fluctuating component of the streamwise and wall-normal velocities. The divergence of the Reynolds stress tensor is taken as a tunable parameter in the data-assimilation procedure and thus represents our model compliance. It is expressed in terms of a vector-valued forcing term $\nabla \cdot \mathbf{R} = \mathbf{f}$.

The unknown pressure is not part of the model compliance and thus cannot be recovered by data-assimilation of the mean-velocity field. This is apparent from (3.1) which shows that the part of $\mathbf{f}$ that can be expressed as the gradient of a scalar potential is indistinguishable from the unknown pressure gradient. Mathematically, the forcing term $\mathbf{f}$ can be split according to

$$\mathbf{f} = \underbrace{\nabla \phi}_{\mathbf{f}_i} + \underbrace{\nabla \times \psi}_{\mathbf{f}_s}, \tag{3.3}$$

where $\mathbf{f}_i$ and $\mathbf{f}_s$, respectively, represent the irrotational and solenoidal part of $\mathbf{f}$. This

decomposition is unique with $\mathbf{f}_s \cdot \mathbf{n} = 0$. The model (3.1) can now be recast as follows

$$\begin{aligned} \overline{\mathbf{u}} \cdot \nabla \overline{\mathbf{u}} + \nabla \overline{p}' - \frac{1}{Re} \nabla^2 \overline{\mathbf{u}} &= \mathbf{f}_s, \\ \nabla \cdot \overline{\mathbf{u}} &= 0, \end{aligned} \tag{3.4}$$

with $\overline{p}' = \overline{p} + \phi$. This final form of the model is composed of the forced RANS equations (3.4), with the model compliance parameter $\mathbf{f}_s$, and will serve as the underlying model of our assimilation procedure.

3.2. *Data set*

Figure 2 shows the locations in the flow field where measurements are taken for the data-assimilation. Each green square symbol represents an area over which the mean velocity is spatially averaged. The resulting values are then taken as input to the assimilation algorithm. To enable a comparison between this data-set and the velocity field recovered from our model, this velocity averaging is formulated as a scalar product. We take as Ω_i the area of the i-th square over which the velocity measurements are averaged. The scalar mask b_i, defined as $b_i = 1$ on Ω_i and $b_i = 0$ elsewhere, then allows the expression of the i-th measurement $\mathbf{m}_i$ as

$$\mathbf{m}_i \simeq \frac{\displaystyle\int_\Omega b_i \overline{\mathbf{u}}_{true} \, \mathrm{d}\Omega}{\displaystyle\int_\Omega b_i \, \mathrm{d}\Omega} \tag{3.5}$$

with $\mathbf{m}_i$ representing the two-component measurement vector (with the streamwise and normal mean-velocity) associated with square Ω_i. In the above expression, Ω stands for the entire domain, and $\overline{\mathbf{u}}_{true}$ is the measured mean-velocity. From (3.5), we define $\mathbf{m} = (\mathbf{m}_i)_{i \in (1..N)}$ with N the number of measurements, together with the corresponding mapping M,

$$\mathbf{m} = \mathsf{M}\left(\overline{\mathbf{u}}_{true}\right). \tag{3.6}$$

This final expression represents a mathematical formulation of the measurement process and allows a compact formulation of the fitting criterion, defined in the next section.

3.3. *Fitting criterion*

The fitting criterion is a scalar function that quantifies the distance between predicted $\mathsf{M}\left(\overline{\mathbf{u}}(\mathbf{f}_s)\right)$ and measured $\mathbf{m}$ mean-velocity. Defining $\mathbf{e}_m$ as the difference between the two quantities, we can write

$$\mathbf{e}_m = \mathbf{m} - \mathsf{M}\left(\overline{\mathbf{u}}(\mathbf{f}_s)\right). \tag{3.7}$$

For our computations, the fitting criterion is taken as the Euclidean norm of $\mathbf{e}_m$, i.e.,

$$\mathsf{E}\left(\overline{\mathbf{u}}(\mathbf{f}_s), \mathbf{m}\right) = \frac{1}{2} \|\mathbf{e}_m\|_2^2. \tag{3.8}$$

An L_2-norm has been chosen here, but another type of norm or an entirely different fitting criterion can be readily adopted for the data-assimilation problem. The fitting criterion above serves as the objective functional of a variational formulation, presented in the next section. This formulation then yields an iterative optimization scheme that will render the fitting criterion minimal and ensure an optimal match of the model-predicted and measured data.

4. Optimization and data-assimilation

The minimization of the fitting criterion subject to the constraint given by the model leads to an optimization problem that is best formulated variationally. Below we give an outline of the optimization steps. Again, additional details and generalizations can be found in Foures *et al.* (2013).

4.1. *Problem formulation and optimization algorithm*

The assimilation problem consists of finding the mean velocity and model compliance, i.e., $(\overline{\mathbf{u}}, \mathbf{f}_s)$, that satisfy the model equation (3.4) and minimize the fitting criterion (3.8). This constitutes a nonlinear optimization problem, since the fitting criterion does not depend linearly on the forcing term. We choose a variational approach, yielding a direct-adjoint optimization algorithm, to solve this problem. An augmented Lagrangian has to be formulation, consisting of the objective functional (our fitting criterion) and the constraints (our model equations) which are enforced in a weak form by Lagrange multipliers or adjoint variables. We have

$$\mathcal{L}(\mathbf{f}_s, \overline{\mathbf{u}}, \mathbf{u}^\dagger, p', p^\dagger) = \mathsf{E}\left(\overline{\mathbf{u}}\right) - \left\langle \mathbf{u}^\dagger, \overline{\mathbf{u}} \cdot \nabla \overline{\mathbf{u}} + \nabla p' - \frac{1}{Re}\nabla^2 \overline{\mathbf{u}} - \mathbf{f}_s \right\rangle - \left\langle p^\dagger, \nabla \cdot \overline{\mathbf{u}} \right\rangle . \quad (4.1)$$

The scalar product, denotes by $\langle ., . \rangle$, is associated with the Euclidian norm for vector and scalar fields on the domain Ω. The Lagrange multipliers, or adjoint variables, are denoted by $(\mathbf{u}^\dagger, p^\dagger)$ and have been introduced to enforce the model equations. The augmented Lagrangian (4.1) can be expanded using first variations with respect to all independent variables (direct and adjoint), leading to three sets of equations: the direct equations (3.4), the adjoint equations (4.2) and the optimality condition providing the steepest descent direction, equation (4.3). We have

$$\begin{aligned} -\overline{\mathbf{u}} \cdot \nabla \mathbf{u}^\dagger + \mathbf{u}^\dagger \cdot \nabla \overline{\mathbf{u}}^\top - \nabla p^\dagger - \frac{1}{Re}\nabla^2 \mathbf{u}^\dagger &= \frac{\delta \mathsf{E}}{\delta \overline{\mathbf{u}}}, \\ \nabla \cdot \mathbf{u}^\dagger &= 0, \end{aligned} \quad (4.2)$$

and

$$\nabla_{\mathbf{f}_s} \mathsf{E} = \mathbf{u}^\dagger. \quad (4.3)$$

From these three sets of equations, a direct-adjoint optimization scheme can be devised for the iterative solution of the nonlinear assimilation problem. The procedural steps can be summarized as follows:

---

1. Take an initial guess for $\mathbf{f}_s$ (e.g., $\mathbf{f}_s = 0$)
2. Solve direct equations (3.4) to obtain $\overline{\mathbf{u}}(\mathbf{f}_s)$
3. Evaluate the fitting criterion E using (3.8)
4. While E exceeds a user-specified threshold
   4.1. Solve the adjoint equations (4.2) to obtain $\mathbf{u}^\dagger$
   4.2. Find the steepest-descent direction using (4.3)
   4.3. Use a line search along the steepest-descent direction evaluating the direct equations (3.4)
   4.4. Compute the optimal E using (3.8)
5. End

The right-hand side of the momentum part of the adjoint equation (4.2) needs further explanation. The first variation of the fitting criterion E with respect to $\overline{\mathbf{u}}$ can be derived,

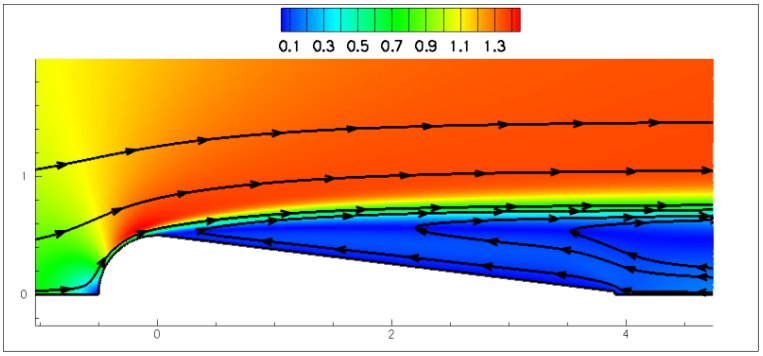

FIGURE 4. Base flow for $Re_c = 12500$ from the solution of the RANS equations with $\mathbf{f}_s = 0$. The color contours display the velocity magnitude; streamlines are indicates as black lines. This flow field acts as the starting point of the iterative data-assimilation algorithm.

starting from its definition (3.8), as

$$\left\langle \frac{\delta \mathsf{E}}{\delta \overline{\mathbf{u}}}, \delta \overline{\mathbf{u}} \right\rangle = \sum_{i=0}^{N} \mathbf{e}_{m_i} \frac{\displaystyle\int_\Omega b_i \delta \overline{\mathbf{u}} \, \mathrm{d}\Omega}{\displaystyle\int_\Omega b_i \, \mathrm{d}\Omega}. \tag{4.4}$$

After rearranging the integral and the sum, we obtain (invoking the Lax-Milgram theorem)

$$\frac{\delta \mathsf{E}}{\delta \overline{\mathbf{u}}} = \sum_{i=0}^{N} \frac{\mathbf{e}_{m_i} b_i}{\displaystyle\int_\Omega b_i \, \mathrm{d}\Omega}. \tag{4.5}$$

This final expression (4.5) is used in lieu of the driving term in the momentum part of the adjoint equation (4.2).

4.2. *Numerical details*

The differential equations in the direct-adjoint optimization algorithm are solved numerically on a two-dimensional finite-element, triangular mesh using a P_2-basis for the velocity and a P_1-basis for the pressure. The resulting discretized system has approximately $2 \cdot 10^6$ degrees of freedom. The base flow, i.e., the solution of (3.4) for $\mathbf{f}_s = 0$, at a chord Reynolds number of $Re_c = 12500$ is computed using a Newton-Raphson algorithm; it is used as the initial guess in our data-assimilation algorithm and shown in figure 4. The computations have been non-dimensionalized, yielding a unit input velocity and a unit cylindrical diameter of the idealized airfoil. All subsequent comparisons with the experimental data will be performed with this non-dimensionalization.

5. Results

5.1. *Mean-flow*

The data-assimilation algorithm is applied to flow around the idealized airfoil. The input to the algorithm is composed of the mean velocity value at twenty selected locations, represented by square symbols in figures 6 and 2. The goal of the assimilation procedure is to reconstruct the full mean-velocity field as well as the solenoidal part of the divergence of the Reynolds stress tensor. The algorithm is initialized by $\mathbf{f}_s = 0$, which yields to the the base flow solution shown in figure 4. The iterative optimization scheme terminates

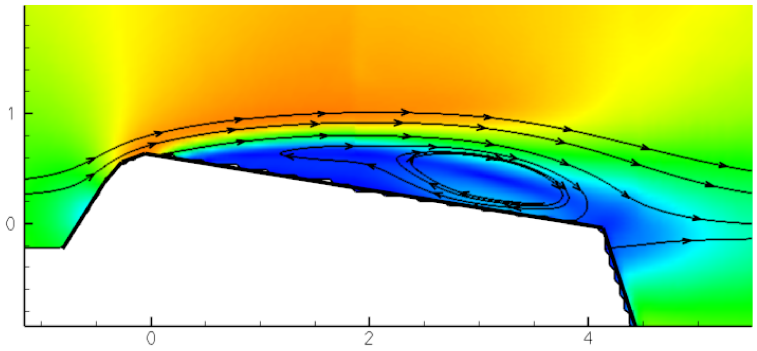

FIGURE 5. Mean velocity field from averaging the flow fields from TR-PIV measurements. The color contours visualize the velocity magnitude; streamlines are shown as black lines.

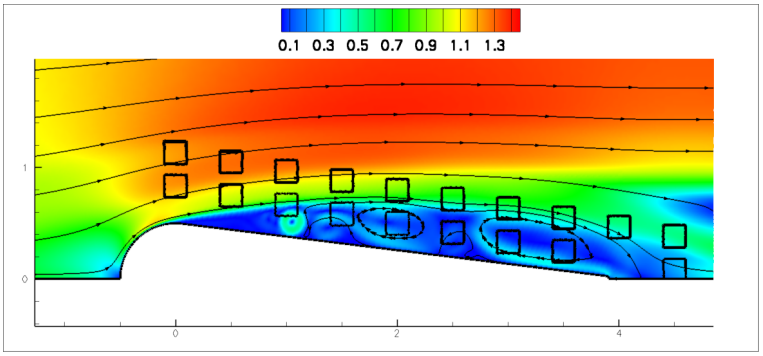

FIGURE 6. Assimilated mean-flow field from a limited number of locally-averaged measurements, i.e., solution of the RANS equation with optimal forcing. The modeled flow is matching the experimental data, with the fitting criterion at 1% of its initial value. The color contours visualize the velocity magnitude; streamlines are shown as black lines.

when the fitting criterion is reduced to one percent of its initial value. The mean velocity recovered in the process is depicted in figure 6 and can be compared to the mean velocity measured in the entire domain (see figure 5). The discrepancy between the first guess (the base flow in figure 4) and the true mean flow (figure 5) is quite perceptible: the shear layer thickness is half the size of the true shear layer, and the separation bubble of the base flow is still expanding while the measured recirculation bubble closes near the trailing edge.

Once the selected mean-velocity data-measurements have been assimilated by the RANS model (see figure 6), the recovered shear layer thickness is more representative of the true shear layer thickness, and the extent and shape of the recirculation bubble are accurately estimated by the assimilated mean flow. Moreover, the recovered flow field does not show strong variations and is qualitatively consistent with the true mean flow between two neighboring measurement locations, thus confirming a satisfactory interpolatory capability of the assimilation algorithm. A similar statement can be made about the extrapolatory ability, by observing the flow field away from the selected measurement points.

5.2. *Forcing*

Besides the recovered mean-velocity field, the data-assimilation also produces the forcing vector necessary to match solutions of the model to the selected measured data. As argued

earlier, the identified forcing approximates the solenoidal part of the divergence of the Reynolds stress tensor. The quality of the assimilation results can be assessed by a direct comparison of the rotational, out-of-plane component of the Reynolds stress tensor for the original PIV fields and the assimilated forcing vector field. The results are plotted in figure 7. This comparison is less straightforward than the comparison of the mean-velocity fields, since the computation of the rotational component of the Reynolds stress tensor divergence from TR-PIV fields poses challenges. The convergence of higher statistical moments is slower than the convergence to mean values; and with our estimate of the relative variance error during the computation of the mean fields between 0.1% and 10% (see appendix for details), the relative error in computing the Reynolds stress tensor is at least of the same order. Even assuming the lower error bound for our estimate, the Reynolds stress tensor has to be spatially differentiated twice, an operation that requires pre-filtering steps (in our case, two successive iterations of a Laplace smoother; see Pletcher *et al.* (2012)). When evaluating the Reynolds stress tensor divergence and comparing its rotational part to the optimal forcing vector, these difficulties have be kept in mind.

The out-of-plane component of the rotational part of the Reynolds stress divergence is plotted in figure 7(a). We observe structures of rather constant value and alternating sign that are elongated in the streamwise direction; these structures are formed near the separation point and appear to be following the mean-flow streamlines. This general shape is expected since the Reynolds stress tensor is quite small in the free-stream, but more significant in regions of stronger fluctuations (caused by shear-layer instabilities and von-Karman vortex shedding).

The reconstructed rotational part of the forcing is plotted in figure 7(b). Similar to the previous plot, longitudinal structures can be observed which arise near the separation point of the airfoil. As a consequence of the direct-adjoint optimization, the reconstructed forcing is assumed accurate in regions of the flow where the flow is particularly sensitive to small changes. In our case, the region near the separation zone is one of the most sensitive areas in the flow, which has also been demonstrated experimentally by Wallace & McKeon (2012). This observation explains the large magnitude of the rotational part of the forcing between the leading edge and the half-chord of the airfoil. Finally, in order to satisfy the fitting criterion the algorithm constructs a forcing term with localized values near the measurements squares. This is particularly noticeable near the trailing edge where distinct features appear just before the averaging area of some measurement locations. Nevertheless, the reconstruction of the rotational of the divergence of the Reynolds stress tensor is satisfactory.

6. Limitations and extensions

Figure 6 shows non-physical structures near the upstream part of the recirculation bubble. These structures can be attributed either to measurement uncertainties or to three-dimensional effects that are not accounted for in the present approach. Since the forcing in the optimization scheme promotes the model to match either corrupted data or a flow that is not truly solenoidal (or both), the appearance of non-physical structures should not come as too much of a surprise.

6.1. *Measurement uncertainties*

In appendix A, we give a detailed discussion of various sources of uncertainty, locate their peaks and estimate their impact on the recovered field. The total error is a function of the mean shear, the velocity magnitude and the amplitude of the velocity fluctuations.

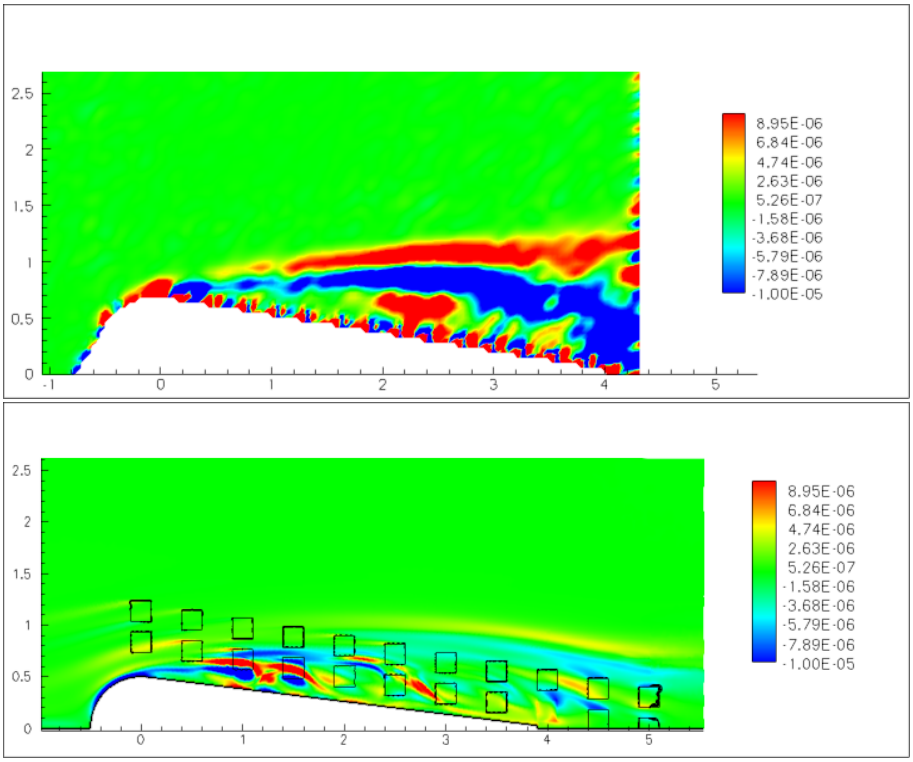

FIGURE 7. Out-of-plane component of the rotational part of the divergence of the Reynolds stress tensor over the airfoil. Top, values derived from time-resolved PIV flow fields; bottom, field identified during the assimilation procedure. Measurement locations are shown as black squares.

Figures 8 and 9 show the relative and absolute measurement error estimated using the expressions from the appendix. The relative error is rather small throughout the far-field (less than 5%), but quite significant in the recirculation bubble (more than 30%). The non-physical structures inside the recirculation zone that were recovered by the data-assimilation algorithm can certainly be ascribed to the substantial uncertainty of the mean velocity in this location.

A modification of the data-assimilation algorithm that accounts for data uncertainty suggests itself. Error bounds on the data may be incorporated into the fitting criterion. We define a general, real-valued function N that accounts for measurement uncertainty. We can then recast the fitting criterion as

$$\mathsf{E}\left(\overline{\mathbf{u}}(\mathbf{f}_s), \mathbf{m}\right) = \mathsf{N}\left(\mathbf{e}_m\right). \tag{6.1}$$

We assume that the total measurement error (from all known sources) can be bounded by $\mathbf{E}$. The derivative of N with respect to measurement discrepancies can be defined as follows,

$$\mathsf{N}'(\mathbf{x}) = \begin{cases} \mathbf{x} + \mathbf{E} & \text{for} \quad \mathbf{x} < -\mathbf{E} \\ \mathbf{0} & \text{for} \quad |\mathbf{x}| \leqslant \mathbf{E} \\ \mathbf{x} - \mathbf{E} & \text{for} \quad \mathbf{E} < \mathbf{x} \end{cases} \qquad \text{and} \qquad \mathsf{N}(0) = 0. \tag{6.2}$$

With this definition, the function N is constant for all measurement discrepancies $\mathbf{e}_m$ if $|\mathbf{e}_m| \leqslant \mathbf{E}$. As a consequence, the modified fitting criterion (6.1) will cause the algorithm to produce a solution that matches the measurements up to their uncertainties. Equa-

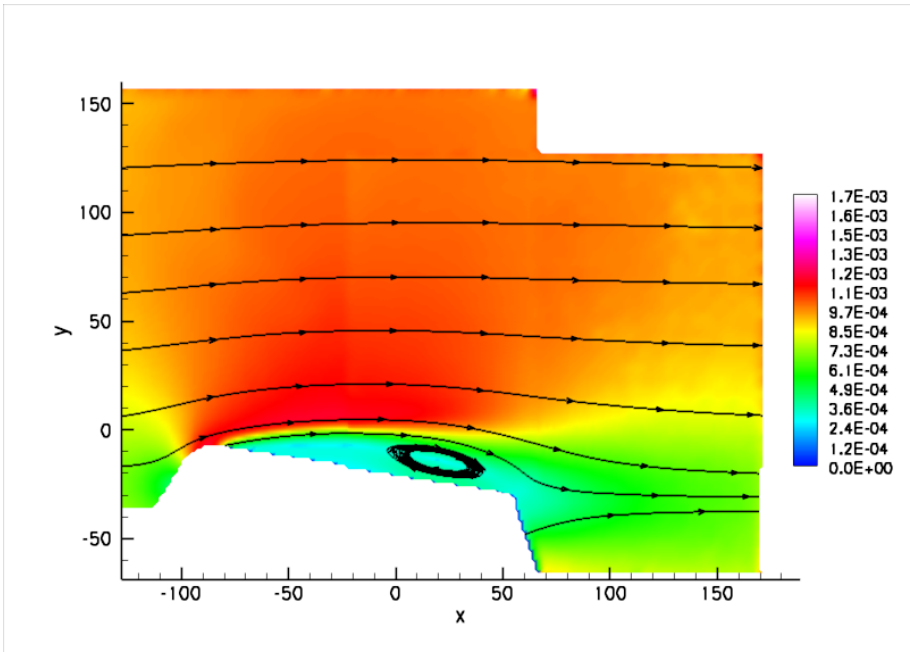

FIGURE 8. Color contours of the measurement error in m/s for flow around an idealized airfoil. For comparison, the freestream velocity is $7 \cdot 10^{-2}$ m/s. Streamlines are shown in black.

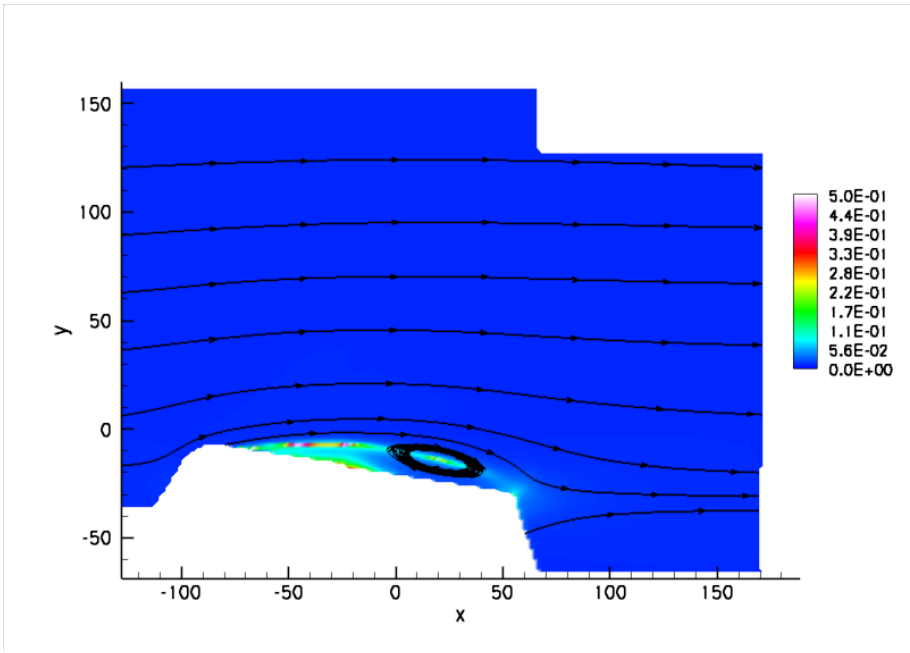

FIGURE 9. Color contours of the relative measurement error in percentage of the local velocity magnitude for flow around an idealized airfoil. Streamlines are shown in black.

tion (6.2) is a hard-bound approach to account for uncertainty in the data-assimilation. Alternatives include the implementation of a soft-bound expression for the fitting criterion or a standard Tikhonov regularization approch combined with weight functions proportional to error bounds (see Flemming 2011; Bukshtynov *et al.* 2011). The modified fitting criterion (6.1) impacts the optimization algorithm, and the expression (4.5) has to be slightly adjusted to allow uncertainty measures in the algorithm. We have

$$\frac{\delta \mathsf{E}}{\delta \overline{\mathbf{u}}} = \sum_{i=0}^{N} \frac{\mathsf{N}'(\mathbf{e}_{m_i}) b_i}{\int_\Omega b_i \, \mathrm{d}\Omega}. \tag{6.3}$$

Since N only appears as its derivative, it seems more suitable to define N by its derivative, as in equation (6.2). The above expression replaces the right-hand side of the momentum part of the adjoint equation (4.2) during the optimization procedure.

6.2. *Effects of three-dimensionality*

The nature of the experimental data motivated us to use the two-dimensional Navier-Stokes equations as the underlying model for data-assimilation. In our case, three-dimensional (out-of-plane) velocities are not captured in the measurements and the processed data. While this approximation seems justified in the freestream of our chosen configuration, the flow inside the recirculation region will certainly exhibit three-dimensional components in the mean flow. As a consequence, $\partial_x u + \partial_y v \neq 0$ and the enforcement of a two-dimensional solenoidal velocity field, represented by the right-most term in (4.1), is not strictly correct throughout the flow domain. Unphysical recovered flow fields inside the separation bubble may thus result.

As with measurement uncertainties, a modification to the algorithm can account for this potential source of incorrect mean-flow recovery. We may introduce an additional compliance parameter $d = -\partial_z w = \partial_x u + \partial_y v$ and replace the divergence-related term in (4.1) by $\langle p^\dagger, \nabla \cdot \bar{\mathbf{u}} - d \rangle$, which for genuinely two-dimensional flow ($d = 0$) reverts back to the previous augmented Lagrangian (4.1). Other non-zero three-dimensional mean-flow effects, contained in the momentum equation, will be compensated for by the driving term $\mathbf{f}_s$, as before.

7. Conclusions

Building on past successes of mean-flow recovery by data-assimilation applied to numerical simulations of flow around a cylinder at a Reynolds number of $Re = 150$ (see Foures *et al.* 2013) and applied to one-dimensional, experimental data from a turbulent pipe flow at a Reynolds number of $Re \approx 35000$ (see Dovetta *et al.* 2013), we have extended the assimilation algorithm and employed it to time-resolved PIV-data of flow over an idealized airfoil at a Reynolds number of $Re = 12500$. A nonlinear optimization scheme, using direct and adjoint information derived from the Reynolds-Averaged Navier-Stokes equations, iteratively matches the model-based mean-velocity field to a few selected measurement points. Even though only 20 data points have been used, the mean-velocity field is recovered in a satisfactory manner. Moreover, the rotational part of the Reynolds-stress tensor divergence is identified, which represents the driving term that gradually forces the modeled mean-flow field towards the selected data points.

Despite complex instability mechanisms present in the flow, the data-assimilation procedure is able to reconstruct, in a satisfactory manner, the mean-velocity field around the airfoil from only 20 data points. Moreover, the rotational part of the divergence of the Reynolds stress tensor is identified qualitatively. An application of this technique could

concern the recovery of mean-velocity fields from limited measurements, which could be accomplished by interpolation between measurement points (for a more highly resolved flow field) or by extrapolation beyond the measurement points (for extending the flow fields past the interrogation window). PIV measurements, as in this article, or any other velocity-measuring technology (*e.g.* Pitot-tubes or anemometry probes) can be used. The recovery of part of the Reynolds stress tensor can provide qualitative information about regions of the domain where turbulent fluid motion is most active.

The impact of measurement uncertainties and weak three-dimensionality on the reconstructed flow cannot be entirely neglected. A variation of the algorithm that accounts for error bounds in the processed data as well as for three-dimensional effects via an additional compliance parameter would ultimately result in more accurate estimates of the mean-velocity field and aid in the convergence behavior of the optimization algorithm. Any development in this direction would increase the robustness of the technique and open a wider range of applications for this data-assimilation procedure. Further work in this direction is left for a future effort.

Appendix A. Sources of measurement error

In this appendix we give estimates for the uncertainty from various sources in order to quantify the precision of data entering the assimilation algorithm; special attention will be directed to the recirculation bubble.

We begin by decomposing the uncertainties into different components, each associated with a particular aspect of the experimental setup, data acquisition or data-processing. In particular, we consider as sources of uncertainty: the calibration of the cameras ($\mathbf{E}_{\mathrm{calib}}$), the experimental set-up assumptions ($\mathbf{E}_{\mathrm{set-up}}$), the sequential-correlation computations of the PIV-velocity vectors ($\mathbf{E}_{\mathrm{PIV}}$), the mapping from the experimental to the numerical coordinate system ($\mathbf{E}_{\mathrm{map}}$) and, finally, the variance-error from the averaging procedure ($\mathbf{E}_{\mathrm{var}}$). The combined measurement error $\mathbf{E}$ is taken as the sum of these components, i.e.,

$$\mathbf{E} = \mathbf{E}_{\mathrm{set-up}} + \mathbf{E}_{\mathrm{calib}} + \mathbf{E}_{\mathrm{PIV}} + \mathbf{E}_{\mathrm{map}} + \mathbf{E}_{\mathrm{var}}. \tag{A 1}$$

Two notations are adopted: $\mathbf{E}$ denotes the relative error, while $\delta\mathbf{u}$ stands for the absolute error of the assimilated velocity $\mathbf{u}$; consequently,

$$\mathbf{E} = \frac{\delta\mathbf{u}}{\mathbf{u}} \tag{A 2}$$

expresses the link between relative and absolute error.

A.1. *Experimental set-up*

The extraction of velocity-vector fields using particle-image velocimetry (PIV) makes assumptions about several geometric characteristics. The laser sheet and the calibration plate are taken as parallel to the streamwise and spanwise coordinate directions.

With a laser sheet of 1 mm thickness and of about three airfoil chords in length, we expect an error in parallelism on the order of 20 minutes of arc. A non-aligned laser sheet poses a problem only if a significant amount of particles traverse from the illuminated to the shaded (or reverse, from the shaded to the illuminated) areas between two consecutive camera snapshots. Particles in our flow move up to 0.8 mm between two images (based on the free-stream velocity). Additionally, in the free-stream, about 99% of the particles are illuminated by the laser sheet during two successive snapshots. For the smallest correlation window (16×16 pixels), there are thus between 10 and 25 particles, resulting in a 10% to 25% probability for one particle to leave (or enter into) the illuminated region

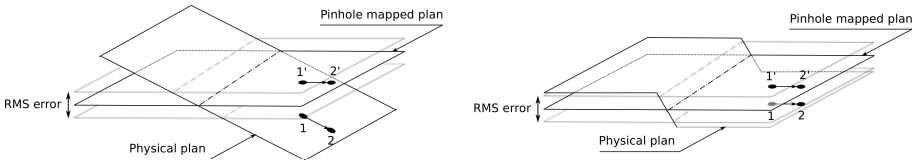

FIGURE 10. Example of velocity error due to calibration error. For the first snapshot the particle is in position 1, for the second snapshot the particle has moved to position 2 on the physical plane. The camera calibration suggests that the particle is in positions $1'$ and $2'$, respectively. The measured velocity is biased due to the angle between the two planes (left figure) and unbiased (right figure), even though the least-squares residual error is the same in both cases.

and to influence the sharpness of the correlation peak. This estimates show that errors stemming from the non-parallelism of the laser sheet are expected to be very small and generally negligible in view of other errors.

In contrast, the calibration plate may also be tilted by 20 minutes of arc with respect to the streamwise-spanwise plane. This angle uncertainty directly translates into a 0.01% measurement uncertainty. In general, a total error of about 0.01% in the measured velocity should be attributed to geometric factors in the experimental setup.

A.2. *Camera calibration*

Calibration of the cameras is performed by using a calibrating plate placed at the laser sheet location. This plate consists a grid of known dimensions which allows the extraction of a mapping between the camera-sensors' coordinate system and the physical domain. Typically, this mapping has a finite number of degrees of freedom (e.g., a pinhole model with eight parameters) and is computed using a least-squares fit. The non-zero RMS error, i.e., the residual of this fit, can be taken as the error committed during camera calibration. In our case, this error is between 0.45 and 0.5 pixels for both cameras, or 0.1 millimeters.

Thus, when the velocity is evaluated based on the position of the correlation peak, we must assume that the position of this peak is known, on average, up to half a pixel, causing a velocity error of $\delta\mathbf{u} = 6$ mm/s. However, this argument does not yield accurate estimates of the velocity errors due to camera calibration. In figure 10 different examples of estimating the physical plane are suggested; in these cases, it can be shown that the link between the residual and velocity error is given by the slope between the identified and physical plane. The least-squares residual error between the two planes is not sufficient to accurately estimate velocity uncertainty associated with calibration. For this reason, this component of the velocity error is omitted later.

A.3. *PIV correlation-peak position*

The bias error stemming from the PIV correlation computations is a source of error that can be readily estimated. Even though the displacement of the correlation peak can be induced by a variety of physical phenomena, for the sake of simplicity, we will considered only effects due to particle size and due to velocity variations within the interrogation window. The bias ϵ of the correlation peak (in pixels) can be explicitly expressed for the case of simple shear and under the assumption of a Gaussian correlation function. We introduce the dimension D_I of the interrogation window, the image magification M and the time interval Δt between two consecutive images. Particles are assumed to be identical of diameter d_τ (see Westerweel 1997, 2008). We then can state

$$\frac{\epsilon}{D_I} = \frac{1}{F_I(\mathbf{s}_D)} \left(\frac{d_\tau^2}{8D_I^2} + \frac{(M|\Delta u|\Delta t)^2}{12D_I^2} \right) \tag{A 3}$$

with $F_I(s_D)$ as the in-plane loss of correlation function, which depends on $\mathbf{s}_D$, the position of the correlation peak within the inter-rogation window; we have

$$F_I(\mathbf{s}_D) = \begin{cases} \left(1 - \dfrac{|s_x|}{D_I}\right)\left(1 - \dfrac{|s_y|}{D_I}\right) & \text{for } |s_x| < D_I,\ |s_y| < D_I, \\ 0 & \text{otherwise.} \end{cases} \tag{A 4}$$

The velocity bias error $\delta\mathbf{u}_{\mathrm{PIV}}$ due to PIV correlation peaks may be expressed in term of correlation peak displacement, leading to the quantification of the PIV-measurement error as

$$\delta\mathbf{u}_{\mathrm{PIV}} = \frac{\epsilon}{M\ \Delta t}. \tag{A 5}$$

This error varies spatially, since it depends on the velocity gradients.

A.4. *Coordinate-system bias*

The origin of either coordinate system is the center of the airfoil leading edge. The center of the airfoil is estimated in the calibrated plane using the background snapshot in which the airfoil is illuminated. The airfoil's position cannot be determined more precisely than a pixel (0.2 mm). This error will change the velocity at a given point, depending on the velocity gradient. Consequently, the associated error $\delta\mathbf{u}_{\mathrm{map}}$ is of the order of the velocity gradient $\|\nabla\mathbf{u}\|$ multiplied by the position error C_e. Mathematically, we have

$$\delta\mathbf{u}_{\mathrm{map}} \simeq \|\nabla\mathbf{u}\|C_e. \tag{A 6}$$

A.5. *Variance error during averaging*

The mean velocity is computed by taking the average over all measurement snapshots. Because of a limited number of snapshots, an error arises which can be estimated by considering the convergence of the mean quantities. If the convergence rate of the mean $\mathbf{u}$ is assumed to be similar to the mean of a random variable, the variance error of the mean may be simply estimated using the standard deviation of the velocity. We obtain

$$\mathrm{Var}(\mathbf{u}) = \mathrm{Var}\left(\frac{1}{N}\sum_{n=1}^{N}\mathbf{u} + \mathbf{u}'\right) = \frac{\sigma^2}{N}. \tag{A 7}$$

REFERENCES

Apte, A., Auroux, D. & Ramaswamy, M. 2010 Variational assimilation for Burgers equation. In *U. Elect. J. Diff. Equ. (AB Conf. Diff. Equ. and Comp. Sim.*, , vol. 19, pp. 15–30.

Avril, S., Bonnet, M., Bretelle, A.-S., Hild, F., Ienny, P., Latourte, F., Lemosse, D., Pagano, S., Pagnacco, E. & Pierron, F. 2008 Overview of identification methods of mechanical parameters based on full-field measurements. *Exp. Mech.* **48**, 381–402.

Bui-Thanh, T., Damodaran, M. & Willcox, K.E. 2004 Aerodynamic data reconstruction and inverse design using proper orthogonal decomposition. *AIAA J.* **42**, 1505–1516.

Bukshtynov, V., Volkov, O. & Protas, B. 2011 On optimal reconstruction of constitutive relations. *Physica D* **240** (16), 1228–1244.

Dovetta, N., McKeon, B.J., Foures, D.P.G., Schmid, P.J. & Sipp, D. 2013 Data-assimilation for mean flow and shear stress reconstruction in turbulent pipe flow. In *Congrès Français de Mécanique*.

Flemming, J. 2011 Generalized Tikhonov regularization: Basic theory and comprehensive results on convergence rates. PhD thesis, Techn. Univ. Chemnitz.

Foures, D.P.G., Dovetta, N., Sipp, D. & Schmid, P.J. 2013 A data-assimilation method for Reynolds-Averaged Navier-Stokes-driven mean-flow reconstruction. *J. Fluid Mech.* **x**, xxx–xxx, (submitted).

Gharib, M. 1983 The effect of flow oscillations on cavity drag, and a technique for their control. PhD thesis, California Institute of Technology.

Ghil, M. & Malanotte-Rizzoli, P. 1991 Data assimilation in meteorology and oceanography. In *Advances in Geophysics* (ed. B. Saltzmann), , vol. 33, pp. 141–266. Academic Press.

Gonzalez, C., Bruhat, J.-F., Wainfan, B. & McKeon, B.J. 2010 Control of laminar separation on an idealized airfoil using periodic dynamic roughness actuation. In *Gallery of Fluid Motion, Poster 26*.

Kalnay, E. 2002 *Atmospheric Modeling, Data Assimilation and Predictability*. Cambridge University Press.

Lewis, J.M., Lakshmivarahan, S. & Dhall, S. 2006 Dynamic data assimilation: A least squares approach. Encyclopedia of Mathematics and Its Application 104, vol 13, Cambridge University Press.

Norman, A. & McKeon, B.J. 2008 Effect of sting size on the wake of a sphere at subcritical Reynolds numbers. *38th Fluid Dynamics Conference and Exhibit* (2012-4183).

Pletcher, R.H., Anderson, D.A. & Tannehill, J.C. 2012 *Computational Fluid Mechanics and Heat Transfer*. CRC Press.

Prasad, A. & Williamson, C.H.K. 1997 The instability of the shear layer separating from a bluff body. *J. Fluid Mech.* **333**, 375–402.

Tissot, G., Cordier, L. & Noack, B.R. 2011 Résolution d'un problème d'assimilation variationnelle 4d-var par des modèles réduits pod adaptatifs. *AFM* Maison de la Mécanique, 39/41 rue Louis Blanc, 92400 Courbevoie, France(FR).

Wallace, R.D. & McKeon, B.J. 2012 Laminar separation bubble manipulation with dynamic roughness. *6th AIAA Flow Control Conference, New Orleans, Louisiana* (2012-2680).

Westerweel, J. 1997 Fundamentals of digital particle image velocimetry. *Meas. Sci. Technol.* **8**, 1379.

Westerweel, J. 2008 On velocity gradients in PIV interrogation. *Exp. Fluids* **44**, 831–842.

Chapter 5

Conclusions and outlook

Throughout this thesis two data-based techniques for the analysis and control of fluid systems have been studied, a system identification procedure that identifies model parameters from temporal input-output from data-sequences, and a data-assimilation algorithm which extracts physical quantities from measured data-set by matching the measurements to predictions from a prescribed model. Even if these two techniques are conceptually similar at some mathematical level, their results, field of application and level of maturity to address flow analysis and control problems are sufficiently different to warrant two different conclusions.

5.1 System identification

Chapter 2 demonstrated the capability of a data-based method to control shear flows that exhibit complex behavior. This has been accomplished using a feed-forward controller and a Multiple-Input Multiple-Output (MIMO) set-up. The design based on a finite impulse response formulation led to a simple, efficient and robust controller that successfully compensated perturbations in subcritical flow past a cylinder (modeled by the complex Ginzburg-Landau equation), and two-dimensional flow in a doubly obstructed channel. In the past, these types of flow control problems have been treated within the framework of linear quadratic Gaussian (LQG) control, a framework that does not account for the specific nature of convection dominated flows, but rather provides a generic solution that consequently suffers in robustness and efficiency. In contrast, the proposed identification and control design algorithms based on a finite impulse response (FIR) model are more appropriate for controlling convectively dominated flows, while still being significantly easier to implement, and equivalently optimal with respect to LQG.

The important contributions made through the extensive use of state-space formulations and LQG compensators, however, is not to be neglected as it establishes a performance standard to which data-based controllers have to be compared. Further work is needed to make connections between a large diversity of identification and control design algorithm from the general literature, and nature and needs of flow control conditions for each specific applications.

In Chapter 3, an experimental configuration of flow over an idealized airfoil at a Reynolds number of $Re = 12500$ is considered, with the intent of controlling the flow by a disturbance-rejection technique. To this end, controllability of the flow has first been established by demonstrating the decoupling of the noise amplifier from the oscillatory behavior. Despite this separation the linear identification step of the

full procedure failed to establish a correlation between upstream and downstream fluctuations in the shear layer. Without this connection, a proper model for the flow dynamics could not be found and therefore the control ultimately failed. This failure is attributed to the non-linear behavior of the flow as further investigations revealed that the estimation error from the upstream sensors was exceedingly large.More complex models that can accommodate non-linear behavior such as, non-linear auto-regressive models, or Hammerstein-Wiener models, should be considered instead of a finite impulse response before disturbance rejection control is again attempted for this flow.

As mentioned before, the data-quality plays an important role during the identification and control design step. Noise impacts not only the identified model parameters but also the controller robustness, stability and performance. To quantify this impact, an uncertainty propagation technique has been developed in the second part of chapter 2 which estimates the effect of measurement noise on the controller characteristics. Data uncertainties are propagated through the an ARMarkov/Least-Squares identification algorithm, after which they impact the stability margins of any given controller. This chapter also shows that quantifying model uncertainty is essential to quantifying *a priori* the performance of a controller. With this information, the model structure can be chosen to maximize the performance, robustness and stability of the controller even under the influence of corrupted data.

Further promising research directions include an analysis of the impact of data-uncertainty on the control design process. While in this thesis the uncertainty propagation has been limited to the identification step of the data-based controller design, it is desirable to also pursue uncertainty propagation through the control design process in order to determine which control algorithm is the most robust under the given data-uncertainty (see Appendix A for uncertainty propagation within realization algorithms and an LQG-controller).

Many sophisticated algorithms have been developed and presented in the general control literature to solve a large variety of guidance and control problems, but have not found their way into flow control applications. A first research direction that seems promising is the integration of control-relevant identification procedures already at the identification step (see Mäkilä *et al.*, 2001). For example, in chapter 2, the objective functional for the model identification has been based on a least-squares distance between the data-sequences and the model predictions. Control-relevant identification applied in this case would formulate an objective functional based on the final controller performance which is expected to lead to better controller performance. Furthermore, the cost functional is not the only parameter that can be optimized to increase the ultimate controller performance; the nature of the input sequence can also be optimized to not only decrease the model estimation error, but also to maximize the final control efficiency for the compensated problem.

In high-speed flow control experiments, the time needed to compute the control law is often a limiting factor, as it influences the delay of the controller response with respect to the time-evolving flow system. Reducing the cost of computing the control law is an important component in approaching real-time flow control

applications in high-speed flows. Judiciously simplified control laws, even stemming from complex identification schemes, together with recursive and on-line algorithms would constitute an interesting research direction for high-speed flow control.

5.2 Data-assimilation

Chapter 4 presents a framework for data-assimilation of mean flows. The technique makes use of the Reynolds-Averaged Navier-Stokes equations, together with localized mean-velocity measurements, to reconstruct a mean-velocity field for the entire domain and information about second-order turbulence statistics. Mathematically this problem leads to a non-linear optimization problem which can be solved by a direct-adjoint gradient-based method developed for this purpose. The quality of data-assimilation is difficult to estimate theoretically; this led us to apply the developed algorithm to three different test cases in order to demonstrate the performance and limitations of mean-velocity data-assimilation. The three cases are: a turbulent pipe flow, the flow around a cylinder, and the flow over an idealized airfoil.

For the turbulent pipe flow, the mean-velocity profile and the single associated shear-stress component are reconstructed from 15 mean-velocity measurements. The reconstructed shear stress shows the same spatial shape and amplitude as the one computed numerically by Wu & Moin (2008). The assimilation produces the Reynolds number and pressure drop in the pipe which compares favorably to results from matching a semi-empirical Spalding-profile to the full 57 measurements. The interpolation, extrapolation, and variable-reconstruction capabilities are demonstrated on this example.

The cylinder flow is more challenging due to its two-dimensional nature, which makes the numerical procedures, mostly coming from the optimization, more expensive. On the other hand, there is negligible uncertainty in the numerical data since geometry, domain and boundary conditions are exactly known. This two dimensional test case is intended to demonstrate the ability of the assimilation procedure to reconstruct a mean-velocity field from scattered measurements. As shown in the study, the quality of the reconstructed field is highly encouraging and thus suggests an application to two dimensional experimental data as a next step in complexity.

The last test case is the flow over an idealized airfoil at a Reynolds number of $Re = 12500$. This example contains many difficulties: the data are corrupted by measurement uncertainties, the boundary conditions are only approximately known, and due to the high Reynolds number computational costs for resolving all relevant scales are considerable. In light of these challenges, the results appear promising. An additional analysis of the origin of measurement uncertainty gives first indications on how to improve the data-assimilation process.

Despite its potential, data-assimilation of mean velocities from scattered measurements based on the RANS equations has not been applied to the best of our knowledge. Unlike data-assimilation of time-resolved data, which is prohibitively expensive, the recovery of mean-velocity fields from localized measurements may

be performed as a post-processing step, for example in parallel to other spectral or energy-based analysis of time-resolved PIV flow fields. RANS-based data-assimilation may give information that is valuable for the evaluation and quantification of turbulence statistics, as it does not rely on any additional empiricisms but is rather based on the equation governing the shape of the turbulent mean velocity. As has been shown in the last chapter, the Reynolds stress tensor is not fully reconstructed, but nevertheless second-order statistical moments can be recovered from a few first-moment (averaged) measurements.

An important issue of mean flow data-assimilation is the uniqueness of the computed solution. The problem by definition is highly overparametrized (*i.e.*, we have more parameters than constraints: for example the airfoil assimilation has $4 \cdot 10^4$ parameters for 42 constraints), which makes it highly unlikely to find a unique solution. Experimentally, we expect only one distribution of Reynolds stresses for a given mean flow. This contradictory situation encourages more investigations to construct data-assimilation formulations that are well-posed (*i.e.* only one unique solution of the assimilation problem).

Two approaches for improving well-posedness of the mean-velocity data-assimilation procedure seem promising: the regularization techniques that, for example, would penalize the norm of the forcing term or the norm of its spatial derivatives, and closure assumptions that would limit the size of the domain of admissible-forcing terms (i.e. reducing the overparametrization).

Regularization techniques are the most straightforward to implement, as by design a very small penalization is usually present in all optimization algorithm (for example convergence threshold for non-linear problems, or numerical Thikhonov penalization for linear least-squares minimization). Thus, modifying a data-assimilation algorithm in order to increase this penalization might be simply performed by increasing its corresponding built-in penalization. More generally, regularization may also be achieved at the objective functional level, where a specific constraint on the forcing term can be enforced. This way, different types of regularizations can be implemented such as, a penalization of the spatial derivative of the forcing or a penalization of its infinite norm. In all cases, the regularization approaches applied to compensate the overparametrization of data-assimilation are generally increasing the convexity of the optimization, and are thus leading to a well-posed problem. However, because the objective functional is changed to include penalization terms, the data-set and the ultimate-model predictions will certainly differ. More investigation on the insertion of regularization terms within mean-velocity data-assimilation algorithm would enable the user to choose a balance between well-posedness of the problem and the model fidelity to the data-set.

Closure assumptions tackle the overparametrization problem using physical hypotheses that reduce the number of degrees of freedom. Indeed, by imposing additional constraints on the model-parameters, the dimension of the admissible set of forcing is diminished. Unfortunately, the validity of the closure underlying assumptions impacts significantly the convergence of the corresponding assimilation procedure. For example an algorithm for mean-velocity data-set assimilation un-

der the Boussinesq closure hypothesis has been developed and applied, to both the cylinder and the idealized airfoil corresponding data-sets. The resulting models were not able to properly match the respective data-set, preventing any satisfactory data reconstruction from this algorithm. Despite the lack of convergence of Boussinesq-based mean-velocity assimilation, we believe that a significant amelioration of the well-posedness, without a prohibitive degradation of the convergence property, can be accomplished using more complex, and less constraining, closure hypotheses.

In order to be an attractive experimental post-processing tool, mean-velocity assimilation has to have the ability to cope with measurements corruption. It has been particularly revealed in chapter 4, where the mean-velocity measured in the recirculation bubble were significantly biased, leading to a reconstructed flow that presented non-physical structures. To increase the algorithm robustness towards data-uncertainty, a modification of the objective functional that includes measurement error-bounds was presented (often called epsilon-intensive loss function, see Azamathulla & Wu (2011)). This modified algorithm, once the measurement error-bounds has been estimated, could be applied to mean-velocity data-sets regardless of the measure-quality.

To conclude, an enhancement of the well-posedness and robustness of the data-assimilation algorithm would most likely lead to an attractive post-processing tool that extracts and reconstructs valuable information from any mean-velocity measurements.

Appendix A

Uncertainty propagation within the control design algorithm

Within the MPHC control-design framework Dovetta *et al.* (2013), the optimal control is found by minimizing a least-squares problem; consequently, a simple Taylor expansion of the least-squares linear optimization problem (presented chapter 2) may be used to assess the propagation of uncertainty through the entire control design procedure. However, if the control-design algorithm consists of the classical Linear Quadratic Regulator (LQR) framework, the optimal control law is found by the formulation of a state-space representation of the system and by the solution of its corresponding Riccati equation, in which case a separate uncertainty propagation framework has to be developed. First, this appendix briefly recalls the LQG control-design framework applied to a model that has been identified using the ARMarkov/Least-Squares identification procedure; a partial uncertainty propagation method is then developed.

A.1 LQG control-design procedure

From Markov parameters to a state space representation: ERA Originally proposed by Juang & Pappa (1985), the algorithm constructs state-space matrices from impulse-response coefficients (Markov parameters). It starts with the construction of Hankel matrices $\mathcal{H}(j)$ following

$$\mathcal{H}(j-1) = \begin{pmatrix} H_j & H_{j+p_1} & \cdots & H_{j+p_s} \\ H_{j+q_1} & H_{j+q_2} & \cdots & H_{j+p_s+q_1} \\ \vdots & \vdots & \ddots & \vdots \\ H_{j+q_r} & H_{j+q_r+p_1} & \cdots & H_{j+p_s+q_r} \end{pmatrix}, \tag{A.1}$$

where H_i is the i^{th} Markov parameter of the impulse response, and $(q_i)_{i\in[1,r]}$ and $(p_i)_{i\in[1,s]}$ are arbitrary sequences of integers. First, the Hankel matrix is decomposed in its singular vectors and singular values.

$$\mathcal{H}(0) = U^T \Sigma V, \tag{A.2}$$

with the matrices U and V containing the singular vectors of $\mathcal{H}(0)$, and Σ standing for the diagonal rectangular matrix with the singular values along its diagonal.

Subsequently, the matrices of the identified state-space representation for LTI systems $\{A_k, B_k, C_k, D_k\}$, after truncation of the lowest singular values in (A.2), can be written as

$$A_k = \Sigma_k^{-1/2} U_k \mathcal{H}(1) V_k^T \Sigma_k^{-1/2}, \tag{A.3}$$

$$B_k = \Sigma_k^{1/2} V_k E_{n_o}, \quad C_k = E_{n_i} U_k^T \Sigma_k^{1/2}, \quad D_k = H_1. \tag{A.4}$$

where E_{n_o} and E_{n_i} are rectangular identity matrices. The matrices A_k, B_k, C_k, and D_k form the state-space representation of the system whose impulse response is the sequence (H_i). Note that $(q_i)_{i\in[1,r]}$ and $(p_i)_{i\in[1,s]}$ are arbitrary sequences of increasing integers, often set to $q_i = p_i = i$, but different sequences can be taken in order to reduce the size of the Hankel matrices and the computational cost of the algorithm (e.g., in case of very long impulse responses).

From a state-space representation to optimal control design: LQG-control
LQG and LQR control-design algorithms may be found in Zhou *et al.* (1996). If the objective functional is as follows

$$J(u) = \sum_{k=1}^{\infty} x(k)^T Q x(k) + u(k)^T R u(k) + 2x(k)^T N u(k), \tag{A.5}$$

its minimization is achieved via the control law

$$u(k) = -Kx(k), \tag{A.6}$$

with K defined by

$$K = (B^T X B + R)^{-1}(B^T X A + N) \tag{A.7}$$

where X is the positive definite solution of the algebraic Riccati equation

$$A^T X A - X - (A^T X B + N)(R + B^T X B)^{-1}(B^T X A + N^T) + Q = 0. \tag{A.8}$$

A.2 Uncertainty propagation through controller design

Propagation of Markov-parameter uncertainty to state-space uncertainty
Small perturbations of the Markov parameter are considered. We denote by A_k the unperturbed matrix (computed with the true Markov parameters), take $\widetilde{A_k}$ as the perturbed matrix, and δA_k as the corresponding perturbation. We thus have

$$\widetilde{A_k} = A_k + \delta A_k. \tag{A.9}$$

Let δH_i be a perturbation of the i^{th} Markov parameter. The perturbed j^{th} Hankel matrix may then be written as

$$\delta\mathcal{H}(j) = \sum_{0}^{\mu-1} P(i+1+j)\delta H_i \tag{A.10}$$

with $P(i)$ a $r \times s$ rectangular canonical matrix with elements $P(i)_{k,l} = \delta_{k+l-1,i}$ and δ as the Kronecker symbol; μ denotes the number of Markov parameters.

Using the small-perturbation assumption $\|\delta\mathcal{H}(0)\|/\mathcal{H}(0) \ll 1$, the expression for δA_k is, to first order, given by

$$\begin{aligned} \delta A_k &\approx \delta\Sigma_k^{-1/2} U_k \mathcal{H}(1) V_k^T \Sigma_k^{-1/2} \\ &+ \Sigma_k^{-1/2} \delta U_k \mathcal{H}(1) V_k^T \Sigma_k^{-1/2} \\ &+ \Sigma_k^{-1/2} U_k \delta\mathcal{H}(1) V_k^T \Sigma_k^{-1/2} \\ &+ \Sigma_k^{-1/2} U_k \mathcal{H}(1) \delta V_k^T \Sigma_k^{-1/2} \\ &+ \Sigma_k^{-1/2} U_k \mathcal{H}(1) V_k^T \delta\Sigma_k^{-1/2} \end{aligned} . \tag{A.11}$$

The perturbed operators are made explicit in what follows. The variation of the singular values operator $\delta\Sigma_k^{-1/2}$ is,

$$\delta\Sigma^{-1/2}_{k(i,j)} = \begin{cases} -\frac{1}{2}\frac{\delta\sigma_i}{\sigma_i^{3/2}} & \text{if } j = i \\ 0 & \text{elsewhere} \end{cases} , \tag{A.12}$$

with (see Stewart, 1990),

$$\delta\sigma_i = u_i^T \delta\mathcal{H}(0) v_i. \tag{A.13}$$

Under the assumption that $\|\delta\mathcal{H}(0)\|/\Delta\sigma \ll 1$ where $\Delta\sigma$ is the minimum of the difference between two singular values of $\mathcal{H}(0)$ (true for sufficiently small perturbations), the perturbed singular vector can be expressed, using the work of Vaccaro & Kot (1987); Vaccaro (1994),

$$\delta u_i = \frac{1}{\sigma_i}\left(I - \sum_{j=1}^{k} c_j u_j u_j^T\right)\delta\mathcal{H}(0) v_i - \sum_{j=1, j\neq i}^{k} \frac{c_j}{\sigma_j} u_j u_i^T \delta\mathcal{H}(0) v_j, \tag{A.14}$$

$$\delta v_i = \frac{1}{\sigma_i}\left(I - \sum_{j=1}^{k} c_j v_j v_j^T\right)\delta\mathcal{H}(0)^T u_i - \sum_{j=1, j\neq i}^{k} \frac{c_j}{\sigma_j} v_j v_i^T \delta\mathcal{H}(0)^T u_j, \tag{A.15}$$

where

$$c_i = \begin{cases} 1 & \text{if } j = i \\ \frac{\sigma_i^2}{\sigma_i^2 - \sigma_j^2} & \text{if } j \neq i \end{cases} \tag{A.16}$$

from which the matrices δU_k and δV_k^T can readily be computed.

The uncertainty propagation towards C_k and B_k is derived in a similar fashion. We have

$$\delta C = E_{n_i} \delta U_k^T \Sigma_k^{1/2} + E_{n_i} U_k^T \delta\Sigma_k^{1/2}, \tag{A.17}$$

$$\delta B = \delta\Sigma_k^{1/2} V_k E_{n_o} + \Sigma_k^{1/2} \delta V_k E_{n_o} \tag{A.18}$$

where

$$\delta\Sigma_k^{1/2} = \begin{cases} \frac{1}{2}\frac{\delta\sigma_i}{\sqrt{\sigma_i}} & \text{if } j = i \\ 0 & \text{elsewhere} \end{cases} . \tag{A.19}$$

And finally, $\delta D_k = \delta H_0$. In this manner, perturbations of identified Markov parameters have been propagated to the state-space matrices that describe the system $\{A_k, B_k, C_k, D_k\}$.

Propagation of state-space uncertainty to controller uncertainty The final step in the uncertainty-propagation procedure is not formulated in this appendix; a related analysis may be found in Kenney & Hewer (1990); Konstantinov *et al.* (1993) that would lead to the formulation of controller uncertainty from perturbations of the state-space system.

Bibliography

Akaike, H. 1974 Fitting autoregressive models for prediction. *IEEE transaction on automatic control* **19**, 716–723. (Cited on page 15.)

Allan, Brian G, Owens, Lewis R & Lin, John C 2006 Optimal design of passive flow control for a boundary-layer-ingesting offset inlet using design-of-experiments. *AIAA paper* **1049**. (Cited on page 9.)

Apte, A, Auroux, D & Ramaswamy, M 2010 Variational assimilation for burger equations. In *U. Electronic Journal of Differential Equations* (ed. AB Conference on Differential Equations & Computational Simulations), , vol. 19, pp. 15–30. (Cited on page 87.)

Avril, S., Bonnet, M., Bretelle, A.-S., Hild, F., Ienny, P., Latourte, F., Lemosse, D., Pagano, S., Pagnacco, E. & Pierron, F. 2008 Overview of identification methods of mechanical parameters based on full-field measurements. *Experimental Mechanics* **48**, 381–402, 10.1007/s11340-008-9148-y. (Cited on page 87.)

Azamathulla, H Md & Wu, Fu-Chun 2011 Support vector machine approach for longitudinal dispersion coefficients in natural streams. *Applied Soft Computing* **11** (2), 2902–2905. (Cited on page 151.)

Barbagallo, A., Dergham, G., Sipp, D., Schmid, P.J. & Robinet, J.-C. 2012 Closed-loop control of unsteadiness over a rounded backward-facing step. *Journal of Fluid Mechanics* . (Cited on pages 13 and 23.)

Barbagallo, Alexandre, Sipp, Denis & Schmid, Peter J 2009 Closed-loop control of an open cavity flow using reduced-order models. *Journal of Fluid Mechanics* **641** (1), 1–50. (Cited on page 13.)

Bewley, Thomas R 2001 Flow control: new challenges for a new renaissance. *Progress in Aerospace sciences* **37** (1), 21–58. (Cited on page 8.)

Bukshtynov, Vladislav, Volkov, Oleg & Protas, Bartosz 2011 On optimal reconstruction of constitutive relations. *Physica D: Nonlinear Phenomena* **240** (16), 1228 – 1244. (Cited on page 87.)

Camacho, E.F. & Bordons, C. 2004 *Model Predictive Control*, 2nd edn. *Advanced Textbooks in Control and Signal Processing* XXII. (Cited on pages 8 and 23.)

Chang, Paul K 1976 Control of flow separation: Energy conservation, operational efficiency, and safety. *NASA STI/Recon Technical Report A* **77**, 11232. (Cited on page 8.)

Corke, TC, Enloe, CL & Wilkinson, SP 2010 Dielectric barrier discharge plasma actuators for flow control. *ANNUAL REVIEW OF FLUID MECHANICS* **12**, 505–529. (Cited on page 10.)

Cortelezzi, L & Speyer, JL 1998 Robust reduced-order controller of laminar boundary layer transitions. *Physical review E* **58** (2), 1906. (Cited on page 15.)

Cossu, Carlo 2007 *Retarder la transition vers la turbulence*. Ed. Techniques Ingénieur. (Cited on page 9.)

Daescu, Dacian N & Navon, IM 2007 Efficiency of a pod-based reduced second-order adjoint model in 4d-var data assimilation. *International Journal for Numerical Methods in Fluids* **53** (6), 985–1004. (Cited on page 87.)

Dovetta, Nicolas, Juillet, Fabien & Schmid, Peter J 2013 Data-based model-predictive control design for convectively unstable flows. *Underconsideration for publication in Journal of Fluid Mechanics* . (Cited on page 153.)

Gerber, A.G., Dubay, R. & Healy, A. 2006 Cfd-based predictive control of melt temperature in plastic injection molding. *Applied Mathematical Modelling* **30** (9), 884 – 903. (Cited on page 13.)

Ghil, M & Malanotte-Rizzoli, P 1991 Data assimilation in meteorology and oceanography. *Advances in Geophysics* . (Cited on page 8.)

Gonzalez, C., Bruhat, J.-F., Wainfan, B. & McKeon, B.J. 2010 Control of laminar separation on an idealized airfoil using periodic dynamic roughness actuation. In *Gallery of Fluid Motion Poster 26*, 63rd edn. Long Beach, CA. (Cited on pages 10 and 12.)

Gad-el Hak, M, Pollard, M. & Bonnet, J.P. 1998 *Flow Control: Fundamentals and Practices. Springer Lecture Notes in Physics, New Series Monographs* . Springer-Verlag. (Cited on page 9.)

Hervé, Aurelien, Sipp, Denis, Schmid, Peter J & Samuelides, Manuel 2012 A physics-based approach to flow control using system identification. *Journal of Fluid Mechanics* **702**, 26–58. (Cited on page 23.)

Huang, Shao-Ching & Kim, John 2008 Control and system identification of a separated flow. *Physics of Fluids* **20** (10), 101509. (Not cited.)

Huerre, P & Monkewitz, P 1985 Absolute and convective instabilities in free shear layers. *Journal of Fluid Mechanics* **159**, 151–68. (Cited on page 10.)

Illingworth, Simon J., Morgans, Aimee S. & Rowley, Clarence W. 2011 Feedback control of flow resonances using balanced reduced-order models. *Journal of Sound and Vibration* **330** (8), 1567 – 1581. (Cited on page 13.)

Juang, J.N. & Pappa, R.S. 1985 Eigensystem realization algorithm for modal parameter identification and model reduction. *Journal of Guidance, Control, and Dynamics* **8** (5), 620–627. (Cited on page 153.)

Juillet, Fabien, Schmid, Peter J & Huerre, Patrick 2013 Control of amplifier flows using subspace identification techniques. *Journal of Fluid Mechanics* **725**, 522–565. (Cited on pages 15 and 23.)

Kalaba, Robert E & Spingarn, Karl 1982 *Control, identification, and input optimization*. Plenum press New York. (Cited on page 15.)

Katayama, T. 2005 *Subspace Methods for System Identification*. Springer. (Cited on page 17.)

Kegerise, MA, Cattafesta, LN & Ha, C 2002 Adaptive identification and control of flow-induced cavity oscillations. *AIAA paper* **3158**, 2002. (Cited on pages 15 and 23.)

Kenney, C. & Hewer, G. 1990 The sensitivity of the algebraic and differential riccati equations. *Siam journal of control and optimization* . (Cited on page 156.)

Konstantinov, M.M., Petkov, P.. Hr. & Christov, N. D. 1993 Perturbation analysis of the discrete riccati equation. *Kybernetika* . (Cited on page 156.)

Kral, L.D. 2000 Active flow control technology. *ASME Fluids Engineering Division Technical Brief* . (Cited on pages 8 and 10.)

Lachmann, Gustav Victor 1961 *Boundary layer and flow control: its principles and application*, , vol. 2. Pergamon. (Cited on page 8.)

Ljung, Lennart 1976 On the consistency of prediction error identification methods. *Mathematics in Science and Engineering* **126**, 121–164. (Cited on page 16.)

Ljung, L. 1987 *System identification Theory for the user*. Englewood Cliffs, New Jersey: Prentice-Hall, Inc. (Cited on pages 8, 14 and 15.)

Ljung, Lennart 1988 System identification toolbox . (Cited on pages 14 and 17.)

Ljung, Lennart 2002 Prediction error estimation methods. *Circuits, Systems and Signal Processing* **21** (1), 11–21. (Cited on page 16.)

Longman, R. W., Lew, J.-S., Tseng, D.-H. & Juang, J.-N. 1988 Variance and bias confidence criteria for era modal parameter identification. *AIAA/AAS Astrodynamic conference* . (Not cited.)

Mäkilä, P. M., Partington, J. R. & Gustafsson, T. K. 2001 Worst-case control-relevant identification. *IEEE transaction on automatic control* **46** (4), 656. (Cited on page 148.)

Mckeon, Beverley J., Li, J. D., Jiang, W., Morrison, Jonathan F. & Smits, Alexander J. 2004 Further observations on the mean velocity distribution in fully developed pipe flow. *J. Fluid Mech* **501**. (Cited on page 88.)

Mehra, R.K. 1974 Optimal inputs for linear system identification. *IEEE transaction on automatic control* **19** (3), 192–200. (Cited on page 15.)

Mohammadi, Bijan & Pironneau, Olivier 2004 Shape optimization in fluid mechanics. *Annu. Rev. Fluid Mech.* **36**, 255–279. (Cited on page 20.)

Moin, Parviz & Bewley, Thomas 1994 Feedback control of turbulence. (Cited on page 13.)

Owen, John C, Bearman, Peter W & Szewczyk, Albin A 2001 Passive control of viv with drag reduction. *Journal of Fluids and Structures* **15** (3), 597–605. (Cited on page 9.)

Qin, S Joe & Badgwell, Thomas A 2003 A survey of industrial model predictive control technology. *Control engineering practice* **11** (7), 733–764. (Cited on page 8.)

Rathnasingham, Ruben 1997 System identification and active control of a turbulent boundary layer. *Tech. Rep.*. Aerospace Computational Design Lab, Dept. of Aeronautics & Astronautics, Massachusetts Institute of Technology. (Cited on page 23.)

Rissanen, J. 1983 A universal prior for integers and estimation by minimum description length. *The Annals of Statistics* **11** (2), 416–431. (Cited on page 15.)

Semeraro, O., Bagheri, S., Brandt, L. & Hennigson, D. 2011 Feedback control of three-dimensional optimal disturbances using reduced-order models. *Journal of Fluid Mechanics* . (Cited on page 13.)

Stewart, G. W. 1990 *SVD and Signal Processing, II: Algorithms, Analysis and Applications*, chap. Perturbation theory for the singular value decomposition. G. W. Stewart. (Cited on page 155.)

Thévenin, Dominique & Janiga, Gaïbor 2008 *Optimization and computational fluid dynamics*. Springer. (Cited on page 20.)

Tissot, G., Cordier, L. & Noack, B. R. 2011 Résolution d'un problème d'assimilation variationnelle 4d-var par des modèles réduits pod adaptatifs. *AFM, Maison de la Mécanique, 39/41 rue Louis Blanc, 92400 Courbevoie, France(FR)* . (Cited on page 87.)

Vaccaro, R.J. 1994 A second-order perturbation expansion for the svd. *Matrix anal. appl.* **15** (2), 661–671. (Cited on page 155.)

Vaccaro, R.J. & Kot, A.C. 1987 A perturbation theory for the analysis of svd-based alogorithms. In *Acoustics, Speech, and Signal Processing, IEEE International Conference on ICASSP '87*. (Cited on page 155.)

Wallace, R. D. & McKeon, B. J. 2012 Laminar separation bubble manipulation with dynamic roughness. *6th AIAA Flow Control Conference, New Orleans, Louisiana* (2012-2680). (Cited on page 10.)

Weyer, Erik 2001 System identification of an open water channel. *Control engineering practice* **9** (12), 1289–1299. (Cited on page 23.)

Williams, David, Kerstens, Wesley, Pfeiffer, Jens, King, Rudibert & Colonius, Tim 2010 Unsteady lift suppression with a robust closed loop controller. In *Active Flow Control II*, pp. 19–30. Springer. (Cited on page 15.)

Wu, Xiaoua & Moin, Parviz 2008 A direct numerical simulation study on the mean velocity characteristics in turbulent pipe flow. *Journal of Fluid Mechanics* **608**, 81–112. (Cited on page 149.)

Wygnanski, IsraelJ. 2006 A century of active control of boundary layer separation: A personal view. In *IUTAM Symposium on One Hundred Years of Boundary Layer Research* (ed. G.E.A. Meier, K.R. Sreenivasan & H.-J. Heinemann), *Solid mechanics and its applications*, vol. 129, pp. 155–165. Springer Netherlands. (Cited on page 8.)

Zhou, Kemin, Doyle, John Comstock, Glover, Keith *et al.* 1996 *Robust and optimal control*, , vol. 40. Prentice Hall New Jersey. (Cited on page 154.)